ISSN No. 2231-3273

INTERNATIONAL JOURNAL OF ENGINEERING SCIENCES AND MANAGEMENT

A Bi-annual Research Journal of
DRONACHARYA
GROUP OF INSTITUTIONS
GREATER NOIDA, U.P., INDIA

Vol. III | Issue II | Jul-Dec 2013

ISSN No. 2231-3273

INTERNATIONAL JOURNAL OF ENGINEERING SCIENCES AND MANAGEMENT

Vol. III | Issue II | Jul-Dec 2013

ISSN No. 2231-3273

INTERNATIONAL JOURNAL OF ENGINEERING SCIENCES AND MANAGEMENT

A Bi-annual Research Journal of
DRONACHARYA
GROUP OF INSTITUTIONS
GREATER NOIDA, U.P., INDIA

Volume III | Issue II | Jul-Dec 2013

INTERNATIONAL JOURNAL OF ENGINEERING, SCIENCES AND MANAGEMENT

Editorial Information:
For details please write to the Executive Editor, International Journal of Engineering, Sciences and Management, Dronacharya Group of Institutions, # 27, Knowledge Park-III, Greater Noida – 201308 (U.P.), India.

Telephones:
Landline: +91-120-2323854, 2323855, 2323856, 2323857
Mobile: +91-8826006878

Telefax:
+91-120-2323853

E-mail:
advisor.r&d@gnindia.dronacharya.info
director@gnindia.dronacharya.info
info@dronacharya.info

Website:
www.dronacharya.info
www.ijesm.in

 ISSN No. 2231-3273

ADVISORY BOARD

MEMBERS

FROM THE DESK OF EXECUTIVE EDITOR...

Dear Readers,

The qualitative and timely publication of Vol. III / Issue II of our esteemed International journal of Engineering, Sciences and Management (ISSN: 2231-3273) has brought great joy and happiness to the entire fraternity of the journal and honorable members of the Editorial and Advisory Board. The board members rich experience and varied expertize is providing immense succour in propelling the journal to attain an envious position in areas of research and development and accentuate its visibility. The distinctive feature is indexing of the journal by Jour Informatics, Index Copernicus and DOAJ and by others namely J-Stage, Pro-Quest, Google Scholar etc is under progress. It is a matter of great pride and honor that the journal has been viewed by researchers from twenty six countries across the globe. The aim of journal which is to percolate knowledge in various research fields with erudition and hence elevate high end research is being pursued vigorously by providing an eco-system for research and development.

Large number of research papers were received from all over the globe for publication and we thank each one of the authors personally for soliciting the journal. We also extend our heartfelt thanks to the reviewers and members of the editorial board who so carefully perused the papers and carried out justified evaluation. Based on their evaluation, we could accept sixteen research papers for this issue across the disciplines. We are certain that these papers will provide qualitative information and thoughtful ideas to our accomplished readers. We thank all the readers profusely who conveyed their appreciation on the quality and content of the journal and expressed their best wishes for future issues. We convey our deep gratitude to the Editorial Board, Advisory Board and all office bearers who have made possible the publication of this journal in the planned time frame.

We humbly invite all the authors and their professional colleagues to submit their research papers for consideration for publication in our forthcoming issue i.e. Vol. IV / Issue I / Jan-Jun 2014 as per the "Scope and Guidelines to Authors" given at the end of this issue. Any comments and observations for the improvement of the journal are most welcome.

We wish all readers meaningful and quality time while going through the journal.

Wg Cdr (Prof.) TPN Singh
Executive Editor
International journal of Engineering, Sciences and Management (IJESM)
A bi-annual Research journal of Dronacharya Group of Institutions,
Greater Noida, UP, India.

July 2013

ISSN No. 2231-3273

CONTENTS

A STRIPLINE FED DIELECTRICBASED C-BAND VIVALDI ANTENNA

(Invited Paper)

Sanjay Kumar*
Principal Advisor
Defence Avionics Research Establishment (DARE)
C.V.Ramannagar, Bangalore-560 093, India.
Tel/Fax: 91-80-25347705
E-mail: tnksk@yahoo.co.in
Corresponding Author

Saurabh Shukla
Defence Avionics Research Establishment (DARE)
C.V.Ramannagar, Bangalore-560 093, India.
Tel/Fax: 91-80-25347705
E-mail:saurabh.dare@gmail.com

ABSTRACT

A C-band stripline fed Vivaldi Antenna has been reported in this paper. This Vivaldi Antenna operates in the frequency range of 4-8 GHz with a moderate gain of 6-8 dB and return loss better than -10 dB. Due to compact size and ease of fabrication, this Antenna can be used as an individual element or can be stacked in an array for various C-Band applications like weather Radar, satellite communication and mobile military battlefield surveillance and ground Radars. A broadband stripline to slotline impedance matching has been designed and employed to achieve 2:1 bandwidth using CST Microwave Studio.

Keywords: *Travelling Wave Antenna, Slotline-Stripline Transition, Circular Cavity, Radial Stub.*

1. INTRODUCTION

Vivaldi Antenna is basically a taper slot Antenna with exponential taper and it belongs to the end fire travelling wave Antenna. As the Vivaldi Antenna is a travelling wave Antenna, the guide wavelength and the phase velocity are dependent on the substrate height, dielectric constant and taper rate. The radiation characteristics are also affected by the length, width and taper profile because the gain of the Vivaldi Antenna is proportional to the $L/\lambda g$ [1]. The tapered slot is etched out from the thin metal layer deposited on to the substrate. Moreover, the Vivaldi Antenna can work over large bandwidths with symmetric beamwidth and high efficiency. Vivaldi Antenna can be designed to achieve the bandwidth of 10:1. To achieve a wider bandwidth, the Vivaldi Antenna should have perfect impedance matching at both the feed-slotline and slotline-free space transition. Hence, the most important design aspect is to provide a suitable feeding and reduction in wave reflection at the transition regions.

2. TRANSITION REGIONS AND IMPEDANCE MATCHING

Vivaldi Antenna can be fed by a coaxial line but this mechanism doesn't provide broad bandwidth which is sought in many applications. In order to get broadband Vivaldi Antenna concept of microstrip to slotline transition is used and has been reported in literature [2]. In Microstrip-slotline transition, the microstrip feed acts as an impedance transformer and it matches 50 Ω coaxial line to a high impedance slotline. The performance of Vivaldi Antenna depends on smoothness of the transition. It is therefore essential for a designer to look into the matching aspect of transition. Transition regions in a Vivaldi Antenna are shown in Fig. 1.

The broadband impedance matching for Vivaldi Antenna employs orthogonal crossover of microstrip and slotline with radial stub at the end of microstrip and circular cavity at the end of slotline. This cavity acts as a virtual open circuit while the stub acts as virtual short at higher frequencies. This type of transition is commonly used for ultra broadband matching and the same has been reported in [3].

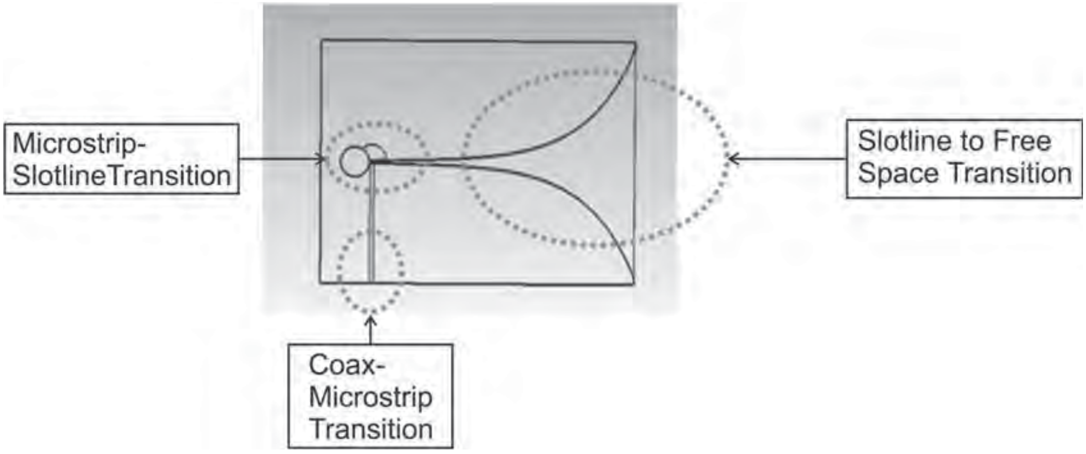

Fig 1. Transition Regions in Vivaldi Antenna

3. DESIGN OF EXPONENTIAL FLARE

The other important transition as shown in Fig 1. is exponentially flared slotline to free space transition. The return loss of a Vivaldi Antenna is greatly affected by this transition. Hence, in order to get efficient radiation in free space the width of the open end is generally kept greater than λ0/2 [4]. This criterion plays an important role in lowering the reflections at the slotline-free space transition. Moreover, the flare and the rate of flare also affect the VSWR of the Antenna. An exponential flare [5] is selected and the equation of the flare is mentioned in equation 1.

$$f(x) = x_0 + \frac{(x_1 - x_0)}{(e^{Ry_1} - 1)} \times (e^{Rx} - 1) \quad \text{------------------------}(1)$$

(x_0, y_0) = flare start point coordinates

(x_1, y_1) = flare end point coordinates

R = flare opening factor

The flare rate can be controlled by flare factor R shown in the equation.

4. STRIPLINE-SLOTLINE MATCHING

The exponentially opened slotline is generally fed by a microstrip feed because it is impossible to achieve an impedance of 50 Ω for a slotline and hence various matching networks are employed to feed slotline with microstrip. To overcome this problem the concept of balanced slotline is used and instead of microstrip feed, stripline feed is used. As the stripline transmission line requires ground plane on both the sides hence the slotline printed on both the sides appear in parallel and can be matched with a 50 Ω stripline. As explained earlier, for a broadband performance the slotline is terminated by a circular cavity and the stripline is terminated with a radial stub. This cavity-stub model is useful for designing broadband Vivaldi Antenna especially for Microwave frequencies. Cavity and radial stub cancel the reactance of each other which facilitates the impedance matching. The design of Stripline-Slotline transition is shown in Fig 2.

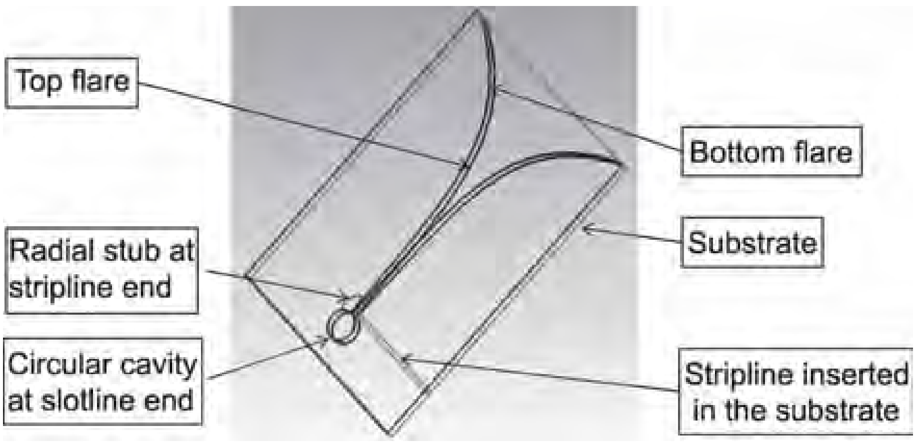

Fig 2. Stripline-Slotline transition in triplicate Vivaldi structure

5. DESIGN OF C-BAND VIVALDI ANTENNA

A theoretical model for a C-band Vivaldi Antenna has been obtained by using design equations and the model has been designed, simulated and optimized using CST Microwave Studio. As discussed earlier, the substrate height and dielectric constant plays an important role in impedance matching hence 120 mil of Rogers TMM 4 ($\varepsilon r = 4.5$) has been found appropriate to achieve the desired bandwidth. The design parameters are tabulated in Table 1.

Table 1. Design Parameters of C- Band Vivaldi Antenna

Substrate	**Slotline**	**Stripline**	**Circular Cavity**	**Radial stub**
Rogers TMM-4 ($\varepsilon r = 4.5$)	Width = 0.8 mm	Width = 1.3 mm	Radius = 4 mm	Radius = 5 mm
Substrate height = 120 mil	100 Ω	50 Ω	Open circuit	Angle = 120^0

The length of the Antenna is chosen as $1.2*\lambda 0$ at lowest frequency of operation to work as a travelling wave Antenna and the width of the Antenna is chosen as $\lambda 0$ at lowest frequency of operation[6]. These dimensions provide an efficient radiation from the Vivaldi Antenna in 4-8 GHz frequency range.

In the optimization process, the length width and the other parameters are varied in the ±10% range to check the effects of parameters on the Antenna performance. The objective is to achieve the return loss better than -10 dB for the entire C-band. The simulated return loss and VSWR results are shown in the Fig. 3 & 4.

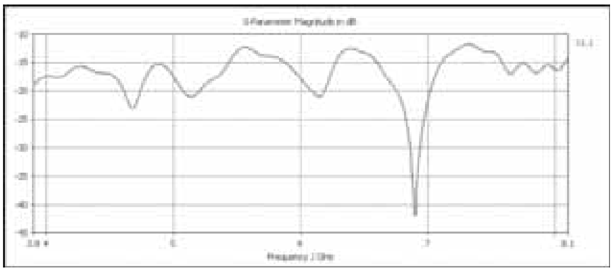

Fig 3. Return Loss of the C-band Vivaldi Antenna

In general, the acceptable range of VSWR is taken as 2:1; however it is apparent from Fig 4. that VSWR in this design has been achieved 1.8:1 that is better than the acceptable range. This helps in improving the radiation efficiency of antenna and minimizing the reflection losses.

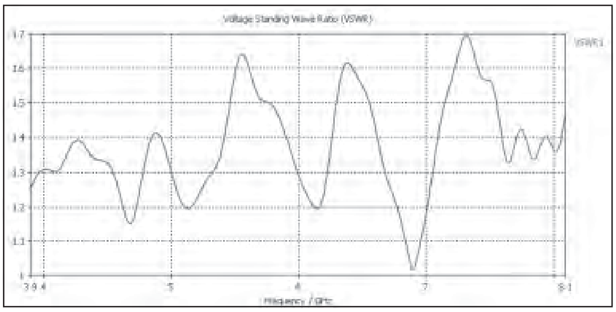

Fig 4. VSWR of the C-band Vivaldi Antenna

The designed C Band Vivaldi antenna exhibits moderate gain of 6-8 dBi over the entire frequency range. Moreover, the realized gain of the Antenna varies within 1.5 dB range with radiation efficiency greater than 85%. The Gain and radiation efficiency plots are shown in Fig 5 & 6.

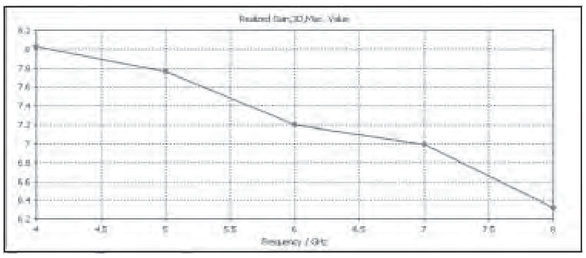

Fig 5. Gain vs. Frequency Plot of C-band Vivaldi Antenna

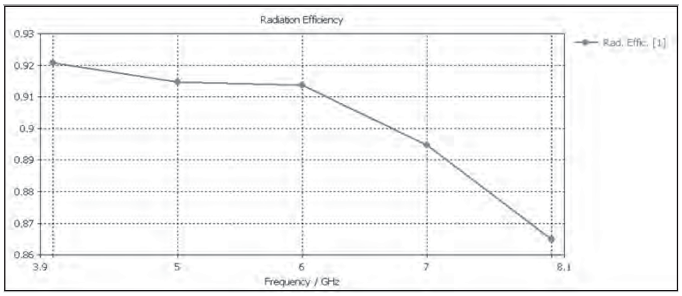

Fig 6. Radiation Efficiency over the Frequency Plot

The simulated model of dielectric based strip line fed C- Band Vivaldi Antenna has been shown in Fig 7. The antenna is quite compact in size as compared to that of available Antenna in this frequency range. This design offers exclusive advantages like lesser volume and ease of fabrication. The 3-D radiation pattern of Antenna at 4 GHz has been shown in Fig 8.

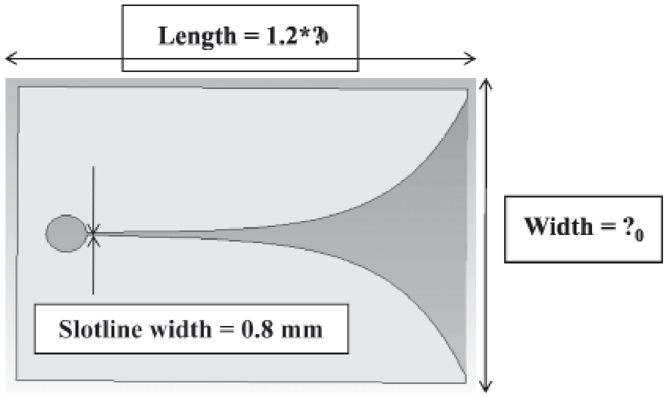

Fig 7. Simulated C-Band Vivaldi Antenna

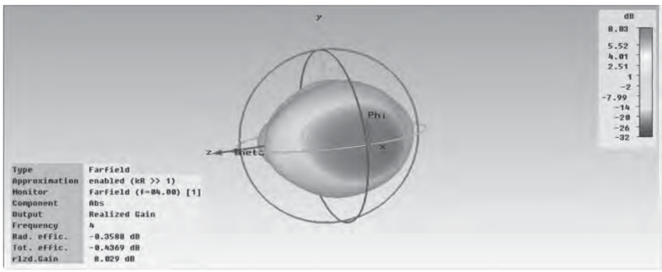

Fig 8. Simulated Radiation Pattern at 4 GHz

6. CONCLUSION

C-band Vivaldi Antenna simulation has given expected results in terms of VSWR, gain, and Radiation pattern. The Antenna presented in this paper can be used as an Antenna for low gain and limited range applications like cordless telephony and Wi-Fi communication. For high gain applications like Satellite Communication and weather Radars, an array of C-band Vivaldi Antenna can be used and the number of elements can be calculated based on the Effective Radiated Power (ERP) requirement. In case of electronically scanning Radars, the E-plane or H-plane Antenna arrays can be designed using the reported Vivaldi Antenna element where wide scan performance is required in both the principle planes. Also, this Antenna can be used in C-Band mobile military battlefield surveillance and ground surveillance radar sets with short or medium range. The compact size of Antenna offers competitive advantage of lighter weight, lesser volume, better accuracy and resolution.

ACKNOWLEDGEMENT

The authors would like to thank Director, DARE for his continuous support and encouragement for this work.

REFERENCES

1. Lewis, L.R., Fasset, M., and Hunt, J.: "A broadband stripline array element", IEEE Symp. Antenna and Propagation,Atlanta,USA, 1974, pp. 335-337.
2. P. J. Gibson, "The Vivaldi Aerial", Proc. 9th European Microwave Conference, Brighton, U.K., 1979, pp. 101-105.
3. M. M. Zinieris, " A Broadband Microstrip-Slotline Transition", Microwave & Optical Technology Letters, Vol 18, No.5, 1998, 339-342.
4. R. N. Simons and R. Q. Lee, "Linearly Tapered Slot Antenna Impedance Characteristics," in 1995 IEEE AP-S International Symposium, Vol. 1, Newport Beach, CA, pp. 170-173,1995.
5. Priya Suresh N et al., "An Ultra Wideband Wide Beam Stripline Fed Vivaldi Antenna for Active Phased Array", EWCI 2012, 23rd Feb 2012.
6. D. H. Schaubert and J. Shin, "Parameter study of Tapered Slot Antenna Array", IEEE International Antenna and Propagation, Symposium Digest, New Port Beach, CA, June 1995, pp 1376-1379.

CORRELATION BETWEEN TWO EXPERIMENTAL TECHNIQUES: RESISTIVITY AND RCPT

Pratanu Ghosh*
Assistant Professor
Civil and Environmental Engineering
California State University, Fullerton CA 92831, USA
Email: pghosh@fullerton.edu, Phone No. +1-657-278-4602
Corresponding Author

Alex Hammond
US Army Corps of Engineers
Email: hamm.alex@gmail.com

Paul J Tikalsky
College of Engineering, Architecture and Technology
Oklahoma State University, Stillwater, OK 74078, USA
Email: Paul.Tikalsky@OKState.edu

ABSTRACT

Concrete resistance to the penetration of chloride ions from deicing salts is an important performance indicator for mixture design specifications. Rapid Chloride Permeability Test (RCPT) according to ASTM C1202 specification can be used for approval of concrete mixture designs as an indicator of potential long-term behavior. However, it is time consuming and not conducive to quality control/ quality assurance (QC/QA) testing of field cured concrete. The Wenner probe device characterizes the electrical resistance of concrete, which has a role both in the initiation and propagation of chloride induced corrosion. This paper demonstrates the connected physics relationship between these two tests and the correlation of the test results with incorporation of essential adjustments due to the joule effect and geometric shape difference. Using different High Performance Concrete (HPC) and control mixtures, the electrical resistivity data is well correlated with the RCPT and provides reliable prediction of concrete resistance to chloride ingress with less effort and expense.

Keywords: *Chloride ingress, joule effect, corrosion, resistivity, RCPT, Wenner Probe*

1. INTRODUCTION

Chloride ion ingress is one of the major problems that affect the durability of concrete structures such as bridge decks, concrete pavements and other structures exposed to chloride salts during winter. Typically chloride resistance of concrete is determined by Rapid Chloride Permeability Test (RCPT) according to ASTM C1202 specification[1,2]. The total charge passed in coulomb in 6 hour of RCPT is considered a relative measure of the resistance to chloride ingress of the concrete. Feldman et al. conducted research to investigate usefulness of the RCPT as a method of testing chloride ion penetration. It was determined that the physical characteristics of the concrete specimens in the RCPT were changed by the high impressed voltage and vacuum saturation procedure of the test. Therefore, the results obtained from this test potentially leading to incorrect measurements[3]. One major limitation of the RCPT is the high current flow through permeable concrete mixtures results in a “joule effect”. The increase in temperature effectively decreases the electrical resistance and encourages the current to flow more rapidly and produce more heat which further accelerates the current flow[4].

The other existing method of determination of concrete resistance to the chloride ion penetration is the electrical resistivity by Wenner probe device. It was originally designed to determine soil resistivity in soil strata, but has been adapted for concrete[5]. Research has been conducted to investigate the effects of probe spacing and other factors on resistivity readings[6,7,8,9]. The Florida Department of Transportation has developed a method to standardize procedures for collection of resistivity readings[10].

Experimentation using the Wenner probe device on 529 sample sets was conducted by Kessler et al. at the Florida Department of Transportation to investigate whether resistivity can be used as a quality control measure in place of the RCPT. Their findings indicate that there is a good correlation between the RCPT and resistivity with the application of geometric correction factor[11]. Torri et al. found a good correlation between the charge passed in the RCPT, initial direct current and the electrical resistivity. It was observed that charge passed was one of the most effective indicators for the evaluation of chloride permeability for different set of cementitious mixtures[12]. Marriaga et al. studied the reliability of the RCPT and resistivity test on the basis of chloride resistance of Ground Granulated Blast Furnace Slag (GGBFS) mixtures with different levels of replacements. They established that electrical resistivity and the total charge passed is an indirect measure of the chloride penetration suitable for both OPC and GGBS mixtures[13]. Riding et al. developed a simplified method which is similar to RCPT procedure except the specimen and gasket size to determine concrete resistivity as an index of concrete permeability. To eliminate the gradual temperature rise problem only one current reading was taken (after 5 minutes) that could be applied to measure the concrete resistivity. An empirical correlation between the new method and the standard RCPT method established the validity and promise of the new simplified method. The disadvantage of this method is its application and suitability on core field samples as it has not yet been determined[14]. Rupnow et al. already showed that the better precision of Wenner Probe resistivity meter from their experimental investigation of single laboratory and multi laboratory measurements and surface resistivity test shows lower variability than rapid chloride permeability test[15].

Most of the existing studies for finding the correlation between the RCPT and electrical resistivity data is not based on fundamentals of physics relationship and lacks HPC mixtures data. The purpose of this research was to find scientific correlation between the RCPT results and the results obtained from a Wenner probe resistivity device by Ohm's law for several ternary, binary and control cementitious mixtures. It has been observed that there is a good correlation in the testing results based on the essential adjustments due to the joule effect and geometric shape difference. In addition, rapid test method like Electrical resistivity measurement provides a fast and reasonable approximation of the corrosion resistance of concrete.

2. EXPERIMENTAL INVESTIGATION

Different types of ternary, binary cementitious mixtures along with control mixtures with a water/cementitious materials ratio of 0.44, typical of exposed bridge deck concrete, were designed to give a wide range of values for this experimental program. All mixtures contained 256 kg of the cementitious material with a Coarse Aggregate Factor (CAF) of 0.67. Limestone coarse aggregate of size 19 mm meeting ASTM C33 No.67 gradation and ASTM C33 silica sand were used. Tests were performed on mixtures using:

- ASTM Type I cement (TI)
- Portland-pozzolan cement(TIP (20))
- Slag modified portland cement (TISM[TIS (25)])
- Limestone blended cement (E)

Mineral additives used:

- Ground granulated blast furnace slag (G120S)
- Fly ash (Types C, F and F2)
- Silica fume(SF)
- Metakaolin (M)

ASTM 595-08 version is used for blended cement specification. The basic mixture parameters were coded into the names of the mixtures with percentage of each cementitious material, e.g. 75TI/20F/5SF means 75% Type I Cement, 20% Class F fly ash and 5% Silica Fume. Table 1 shows the concrete mixture compositions. Medium range water reducing admixture and air entraining agent were also used to meet required slump flow and other durability performance specifications. Rapid Chloride Ion permeability test (RCPT) was performed with different ternary, binary cementitious mixtures including the control mixtures following ASTM C1202 specification. For each mixture, two 100 mm x 200 mm cylinders were cast and wet cured for 14 days and then they were air cured in lab conditions until the 98th day for testing. Ninety eight days (i.e. 14 weeks) were selected as sufficient time for pozzolanic reaction to develop. Experimentation with a Wenner Probe device was conducted for 26 different concrete mixtures to determine concrete cylinder resistivity on 98 days and this data was utilized to obtain correlation with the RCPT data. Concrete cylinders of 100 mm x 200 mm were cast and placed in a wet curing room in accordance with ASTM C192 specification. They were wet cured until 98-day for electrical resistivity measurements following Florida DOT method to comply with continuous Saturated Surface Dry (SSD) condition. A minimum of two specimens were tested for each of the concrete mixtures for the RCPT and electrical resistivity data measurement. The average value of the specimen readings was reported to minimize the variation.

3. ANALYTICAL DEVELOPMENT

It is necessary to determine the resistivity from the RCPT data in order to compare with the results obtained using the Wenner probe device. Both of these testing methods are related by Ohm's law as shown in ‘Eq. (1)’, which relates voltage (V), current (I), and resistance (R) in an electrical circuit.

$$I = \frac{V}{R} \tag{1}$$

The RCPT can be modeled as an electrical circuit consisting of a power source, steady voltage drop, and a resistor. The basic equation for electrical resistivity (ρ) of this resistor is expressed in 'Eq. (2)'

$$\rho = R * \frac{A}{l} \tag{2}$$

where R is the resistance of the resistor, A is the cross sectional area and l is the thickness of the specimen.

The RCPT has a constant voltage drop (60 Vdc) across the resistor with a measured current value in 6 hour time interval. As the dimensions of the specimen are also known, resistivity can be directly computed. The resistivity (ρ) of the specimen used in the RCPT can be determined by substituting the value of resistance (R) from 'Eq. (1)' into 'Eq. (2)' and it is expressed in 'Eq. (3)'.

$$\rho = \frac{V \times A}{I \times l} \tag{3}$$

3.1 Joule effect and theoretical resistivity The application of the 60 V dc in RCPT induces an increase in temperature of the electrode solution throughout the 6 hour test period. This accelerates the current flow (I) through permeable concrete mixtures during the test period resulting in a high value of charge passed. Betancourt et al. developed a temperature adjustment to reduce or eliminate this "joule effect" and improve the prediction of charge passed during 6 hour time period4. The adjusted charge during the 6 hour test can be expressed in 'Eq. (4)'.

$$Q_0 = e^{[\ln(Q_{c6hr}) + \beta\,(1/\delta T - 1/273)]} \tag{4}$$

In 'Eq. (4)', Q_0 is the adjusted charge passed through 6 hour RCPT and β is an experimental constant equal to 1245, Q_{c6hr} is the original charge passed through 6 hour RCPT test, and δT is the difference in temperature increment in Kelvin during the 6 hour test4. Table 1 depicts the 6 hour unadjusted charge and adjusted charge for 26 different cementitious mixtures. The adjusted average current is obtained by dividing the "joule effect" adjusted charge passed (Q_0) by time in seconds and it is expressed in 'Eq. (5)'.

$$I_{adj} = \left(\frac{Q_0}{t}\right) \tag{5}$$

This adjusted average electrical current is then substituted in 'Eq. (3)' to obtain theoretical resistivity as shown in 'Eq. (6)' for all the cementitious mixtures.

$$\rho_{the} = \frac{VA}{I_{adj}\, l} \tag{6}$$

3.2 Geometric correction factor and experimental resistivity The Wenner probe device measures the electrical resistivity of concrete and this technique uses a series of four probes connected to a power source. The spacing of the probes is constant (a=5.1 cm). This spacing dimension is always used in the lab to maintain uniformity of electrical resistivity measurement. A known current is passed between the two outer probes and the resulting voltage drop across the two inner probes is measured. The theoretical concept for determining the resistivity using the Wenner probe device is shown in 'Eq. (7)',

$$\rho_{measured} = 2 * \pi * a * \frac{V}{I} \tag{7}$$

where "a" is the distance between probes.

Current is not one dimensional, it is a three dimensional field. When resistivity is measured on a rounded cylinder using the Wenner probe device, the current is restrained within the concrete. Further, interference is caused by the concrete and air interface. Resistivity readings from a semi-infinite flat slab represent the standard for resistivity of the material, whereas the resistivity from the curved cylinder has interference from the edge of the cylinder. In order to account for this interference, the data needed to be converted into an equivalent semi-infinite slab resistivity where there are no curvature effects. Morris et al. developed this adjustment factor (K) to convert the experimental lab resistivity data performed on concrete cylinder to eliminate the geometrical shape difference between a wide thick slab and concrete cylinder. The experimental resistivity values obtained by using the Wenner Probe device need to be divided by the proper correction factor, which was equal to K = 2.7 for 50 mm probe spacing and 100 mm x 200 mm cylinder. Experimental resistivity data needs to be involved with this correction factor for understanding in-situ bridge deck slab data. The Florida Department of Transportation10 also used this adjustment as expressed in 'Eq. (8)'to develop the limits for the FDOT resistivity testing method[16].

$$\rho_{real} = \frac{\rho_{measured}}{K} \tag{8}$$

Using ‘Eq.(8)’, the theoretical electrical resistivity data from the RCPT method can be compared to real experimental data obtained using the Wenner probe device for all 26 different cementitious mixtures.

3.3 Comparison of RCPT charge with the charge obtained from experimental resistivity As the Wenner probe testing technique also follows Ohm’s law, current through the resistor can be computed by rearranging ‘Eq. (3)’ and it is expressed in ‘Eq. (9)’.

$$I = \frac{VA}{\rho l} \tag{9}$$

The converted coulomb value was determined by multiplying the current value (I) by the RCPT duration (6 hours = 21,600 seconds) and is shown in ‘Eq. (10)’. The resulting value is the theoretical coulomb calculated from the Wenner probe resistivity device readings.

$$Q_{the} = I * t \tag{10}$$

This theoretical coulomb value is compared with the coulomb value obtained from the RCPT for all cementitious mixtures. The results for both testing procedures can be analytically combined as an evaluation tool for concrete with the application of both geometric correction factor and the adjustment due to the joule effect.

3.4 Comparison with empirical method As the RCPT and electrical resistivity are two important parameters in durability modeling of concrete, there is always research interest to correlate the data between them. Berke et al. developed an empirical equation to obtain correlation between RCPT and experimental resistivity data as this test is frequently used in quality control and concrete specifications for construction projects[17]. ‘Eq. (11)’ was used to derive correlations between the two tests. In the study presented herein, adjustments due to the joule effect and geometric correction factor are included in the derived correlation equation for all 26 different cementitious mixtures.

$$\rho_{emp} = 4887x(Q_0)^{-0.832} \tag{11}$$

Correlation of both testing methods is presented in the Fig. 1 through Fig. 9 for both adjusted and unadjusted resistivity and experimental, theoretical and empirical methods.

4 RESULTS

Table 1. Wenner probe resistivity conversions to coulomb

Mixture	Wenner probe Method				
	Measured Resistivity ($\rho_{measured}$)	Geometric K Factor	Geometric Adjusted Resistivity(ρ_{real}) (GAR)	Calculated Coulombs from GAR (Q_{the})	Coulomb from Berke’s empirical method (Q_{emp})
	kΩ*cm (kΩ*in)		kΩ*cm (kΩ*in)	Coulombs	Coulomb
75TI/20F/5M	28.7 (11.3)	2.7	10.6 (4.2)	1711	1591
60TI/30F/10F2	8.4 (3.3)	2.7	3.1 (1.2)	5857	6972
60TI/20F2/20G120S	42.4 (16.7)	2.7	15.7 (6.2)	1158	992
75TI/20F2/5M	42.6 (16.8)	2.7	15.8 (6.2)	1152	985
67TI/30F2/3SF	36.3 (14.3)	2.7	13.4 (5.3)	1352	1200
60TI/20F/20F2	14.8 (5.8)	2.7	5.5 (2.2)	3328	3500
100TIP	20.5 (8.1)	2.7	7.6 (3.0)	2394	2373
60TI/30F2/10C	17.0 (6.7)	2.7	6.3 (2.5)	2887	2973
75TISM/25C	18.7 (7.3)	2.7	6.9 (2.7)	2630	2665
75TISM/25F2	30.6 (12.1)	2.7	11.3 (4.5)	1603	1473
97TISM/3SF	49.3 (19.4)	2.7	18.2 (7.2)	997	831
75TI/20F/5SF	36.4 (14.3)	2.7	13.5 (5.3)	1349	1190
100TI	17.9 (7.0)	2.7	6.6 (2.6)	2746	2811
65TI/30F2/5SF	64.0 (25.2)	2.7	23.7 (9.3)	767	605
65TIP/35G120S	73.8 (29.0)	2.7	27.3 (10.8)	666	510
60TI/20F/20G120S	36.3 (14.3)	2.7	13.4 (5.3)	1354	1200
100E	16.7 (6.6)	2.7	6.2 (2.4)	2938	3031
80E/20G120S	29.8 (11.7)	2.7	11.0 (4.3)	1650	1521
95E5SF	46.0 (18.1)	2.7	17.0 (6.7)	1068	902
62TI/35G120S/3SF	62.8 (24.7)	2.7	23.3 (9.2)	782	617
60TI/35G120S/5M	65.1 (25.6)	2.7	24.1 (9.5)	754	593
75TI/20F2/5SF	65.6 (25.8)	2.7	24.3 (9.6)	748	587
77TI/20F2/3SF	42.4 (16.7)	2.7	15.7 (6.2)	1158	992
65TISM/35G120S	39.2 (15.4)	2.7	14.5 (5.7)	1253	1092
50TI/35G120S/15SF	47.2 (18.6)	2.7	17.5 (6.9)	1040	871
85TIP/15F	25.8 (10.2)	2.7	9.6 (3.8)	1902	1792

Note: 75TI/20F/5M = 75% Type I cement, 20% Class F fly ash, 5% metakaolin

4.1 Wenner probe resistivity and RCPT data In order to verify a relationship using Ohm's law, three different ways of analyzing the data needed to be investigated. The first type of analysis done was to calculate equivalent coulomb values from resistivity data and compare it to the RCPT coulomb data. The second method was to compute equivalent resistivity from the RCPT data to compare with the Wenner probe resistivity data. The third type of analysis done was to compare the RCPT coulomb data and Wenner probe resistivity data.

To develop a relationship between the RCPT and resistivity, data was collected and shown in Fig. 1 through Fig. 7. Each data point represents average values of resistivity with an average of 2 specimens (8 readings per cylinder specimen) for each mixture, and at least 2 specimens for the RCPT. There is a strong need for using the joule effect adjustment and geometric correction factor to relate these two testing methods through Ohm's law. This necessity for these adjustments has been clearly observed by comparing coulomb values from the RCPT with calculated coulomb from resistivity as shown in Fig. 1 through Fig. 3 and in Table 1.

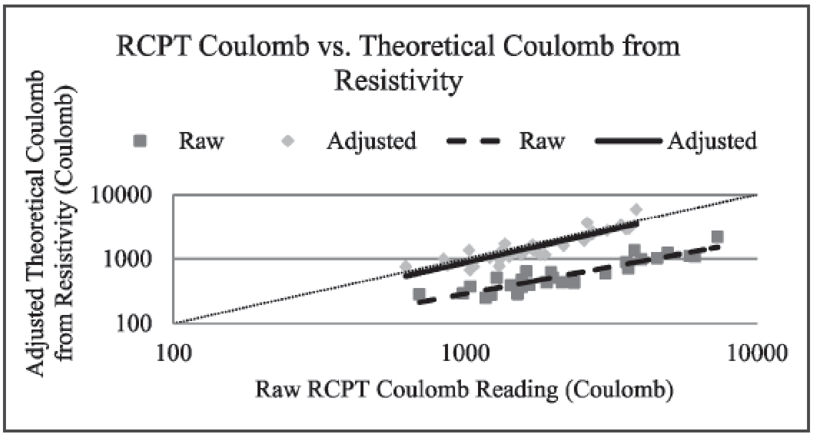

Fig. 1. Raw RCPT coulomb vs. adjusted coulomb from Wenner probe resistivity data (Joule effect and geometric shape adjustment)

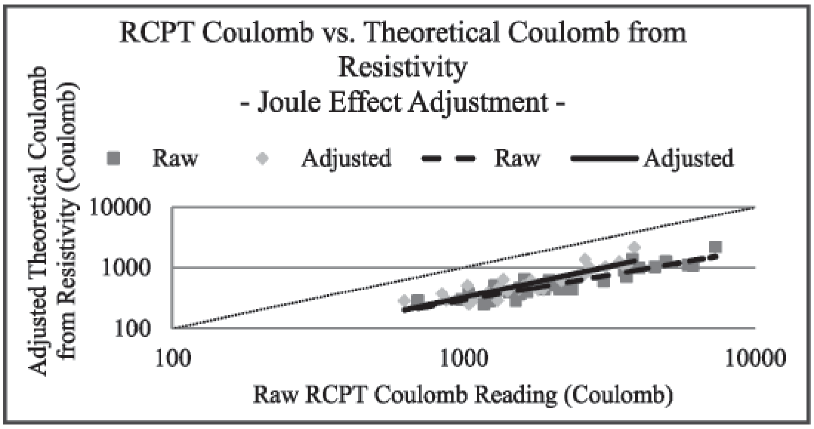

Fig. 2. Raw RCPT coulomb vs. adjusted coulomb from Wenner probe resistivity (Only joule effect adjustment)

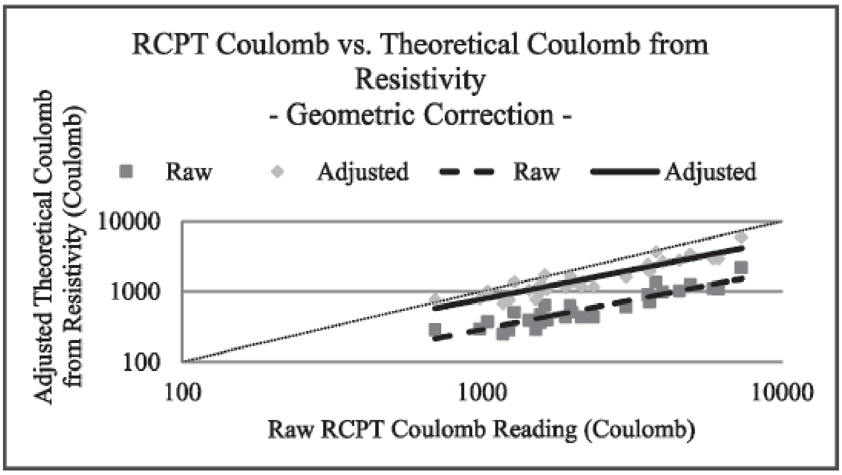

Fig. 3. Raw RCPT coulomb vs. adjusted coulomb from Wenner probe resistivity (Only geometric shape adjustment)

The closer the line is to a 1:1 relationship, the better the relationship is between these two methods using Ohm's law. Fig. 1 shows the adjusted (including joule effect and geometric correction factor) and raw (no adjustment) coulomb relationship. The correlation is close to the 1:1 relationship with the adjustments. To understand how each of these adjustments affects the data, they are plotted separately in Fig. 2 and Fig. 3, keeping the joule effect adjustment or geometric correction unchanged for each plot. The trend in Fig. 2 is due to the excessive heating of the specimens caused by the large current flow through the permeable and control mixtures. Both adjustments are incorporated to account for most of the differences in the coulomb relationship through Ohm's law for these two testing methods.

Similar trend is observed in the coulomb value comparisons for calculated resistivity in Fig. 4 through Fig. 6 and Table 2.

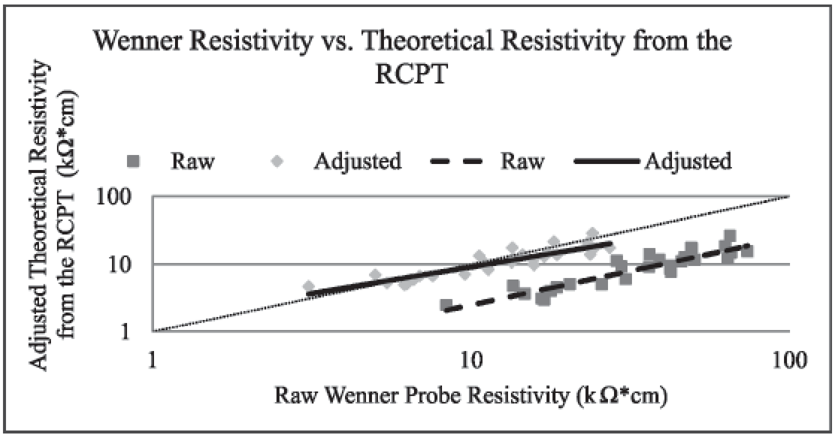

Fig. 4. Raw Wenner probe resistivity vs. adjusted resistivity from RCPT
(Both joule effect and geometric correction)

Table 2. RCPT conversions to resistivity

	RCPT data			
Mixture	Unadjusted Average RCPT charge (Q)	Joule Effect Adjusted RCPT charge (Q_0)	Calculated Resistivity(ρ_{the}) from the RCPT	Resistivity (ρ_{emp}) from Berke's empirical method
	Coulomb	Coulomb	kΩ*cm (kΩ*in)	kΩ*cm (kΩ*in)
75TI/20F/5M	1621	1369	13.3 (5.2)	12.0 (4.7)
60TI/30F/10F2	6786	3871	4.7 (1.8)	5.1(2.0)
60TI/20F2/20G120S	2316	1804	10.1 (4.0)	9.5 (3.8)
75TI/20F2/5M	2363	1877	9.7 (3.8)	9.2 (3.6)
67TI/30F2/3SF	1987	1611	11.3 (4.4)	10.5(4.1)
60TI/20F/20F2	5490	3431	5.3 (2.1)	5.6 (2.2)
100TIP	4023	2715	6.7 (2.6)	6.8 (2.7)
60TI/30F2/10C	6137	3558	5.1 (2.0)	5.4 (2.1)
75TISM/25C	4023	2725	6.7 (2.6)	6.8 (2.7)
75TISM/25F2	3032	2173	8.4 (3.3)	8.2 (3.2)
97TISM/3SF	935	845	21.5 (8.5)	17.9 (7.1)
75TI/20F/5SF	1163	1032	17.6 (6.9)	15.2 (6.0)
100TI	4562	3068	5.9 (2.3)	6.1 (2.4)
65TI/30F2/5SF	1512	1308	13.9 (5.5)	12.5 (4.9)
65TIP/35G120S	1176	1040	17.5 (6.9)	15.1 (5.9)
60TI/20F/20G120S	2000	1709	10.6 (4.2)	10.0 (3.9)
100E	5890	3649	5.0 (2.0)	5.3 (2.1)
80E/20G120S	1970	1703	10.7 (4.2)	10.0 (3.9)
95E/5SF	1656	1415	12.9 (5.1)	11.7 (4.6)
62TI/35G120S/3SF	984	872	20.9 (8.2)	17.5 (6.9)
60TI/35G120S/5M	698	627	29.0 (11.4)	23.0 (9.1)
75TI/20F2/5SF	1230	1071	17.0 (6.7)	14.7 (5.8)
77TI/20F2/3SF	1900	1555	11.7 (4.6)	10.8 (4.3)
65TISM/35G120S	1568	1318	13.8 (5.4)	12.4 (4.9)
50TI/35G120S/15SF	1437	1216	15.0 (5.9)	13.3 (5.2)
85TIP/15F	3634	2555	7.1 (2.8)	7.1(2.8)

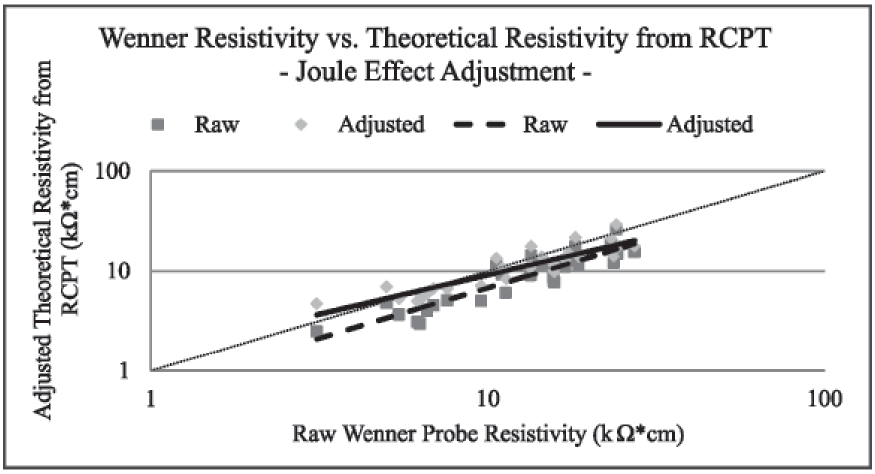

Fig. 5. Wenner probe resistivity vs. Theoretical resistivity from RCPT
(Only joule effect adjustment)

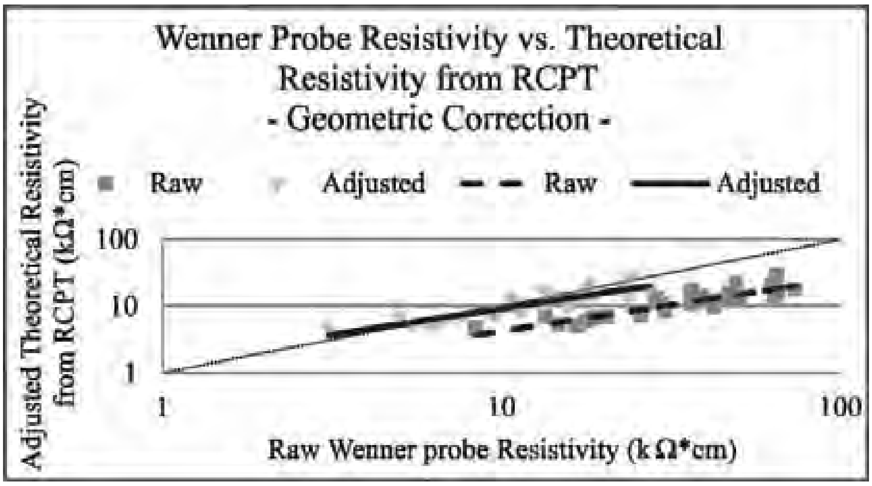

Fig. 6. Raw Wenner probe resistivity and adjusted resistivity from RCPT
(Only Geometric shape adjustment)

Similar to the coulomb comparisons, either the joule effect adjusted values or the geometric corrected values are kept the same for each plot to investigate the effect of the adjustment. With the adjustments, it is evident that the relationship is much closer to a 1:1 relationship than without these adjustments. Two sets of data are presented in Fig. 5, one showing the RCPT raw data converted to resistivity and the other showing the joule effect adjusted data in the computation for the RCPT data keeping unchanged geometrically adjusted resistivity. The relationship between the calculated resistivity from the RCPT data and the experimentally determined resistivity is closer to a 1:1 relationship with the implementation of joule effect adjustment. Fig. 6 shows the effects of varying the geometric correction factor while keeping the adjusted RCPT data unchanged. It has been observed that there is a change in slope between the joule effects adjusted values and the raw data values. The prime reason for this change in slope is due to the excessive heating of the test specimens through highly permeable mixtures requiring more adjustment.

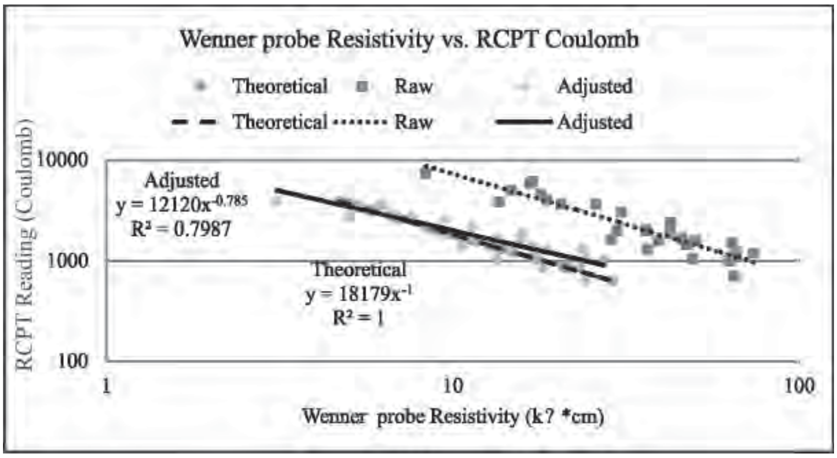

Fig. 7. Wenner probe resistivity vs. RCPT coulomb

In Fig. 7, a theoretical line is presented to represent coulomb values based on the RCPT in correlation with electrical resistivity computed from the RCPT along with the raw data for comparisons. There is a relationship between the RCPT and resistivity readings based on the fit of the trend line to the data and the proximity of the trend line to the theoretical line.

It has been observed that the adjusted predictive line in Fig. 7 is much closer to the theoretical values obtained from the RCPT with the incorporation of adjustments due to the joule effect and geometric correction factor. There still exists a variance between the theoretical and adjusted values; however, this can be explained by looking the values of surface resistivity vs. concrete resistivity. Surface resistivity is determined by the Wenner probe device and only determines the resistivity a small distance into the concrete (up to a depth equal to the probe spacing). Concrete conductivity is determined through the RCPT over the entire depth of the specimen. The difference between the theoretical and empirical readings is due to the presence of more paste at the surface of the concrete. Surface of concrete has a different resistivity than the center of the concrete where less paste exists.

4.2 Comparison with Berke's empirical method

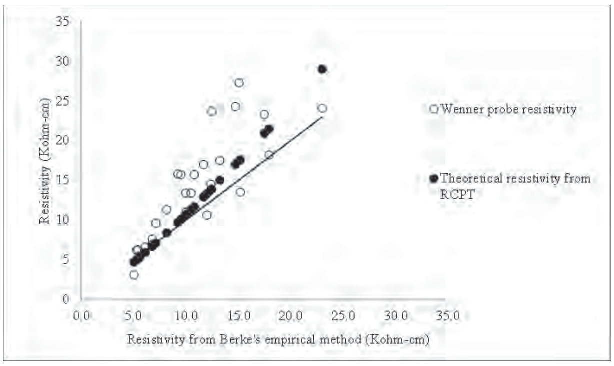

Fig. 8. Comparison of resistivity from empirical, experimental and theoretical methods

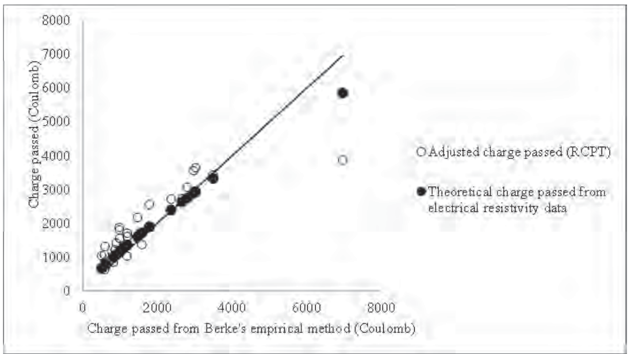

Fig. 9. Comparison of the charge passed from empirical, RCPT and theoretical methods

These Wenner probe resistivity and RCPT coulomb data were also compared with Berke's empirical method to investigate the correlation of the tests and it is expressed in Fig. 8 and 9. It has been observed that resistivity values from Berke's empirical method correlated well with Wenner probe resistivity and the theoretical resistivity from the RCPT data. There are some scattered points in case of Wenner probe resistivity values, which measures surface resistivity as compared to resistivity over entire depth of specimen in case of RCPT and Berke's empirical method.

5. CONCLUSION

In order to use chloride ion penetration as part of a durability acceptance criterion, an effective and simpler means of testing concrete test needs to be used. This research demonstrates the good correlation between the RCPT and Wenner probe data to justify the use of Wenner probe device as an expedited method for investigation of chloride ion ingress in bridge decks and other concrete structures. The RCPT results and results obtained using a Wenner probe can be related through Ohm's law for different blended and unblended cement concrete mixtures. This correlation of data becomes only reliable with the incorporation essential adjustments due to the joule effect and geometric shape factor. This is particularly true for mixtures with higher permeability. Comparison with Berke's empirical method was also necessary to obtain strong relationship between the data of two testing methods. This analysis also supports the use of Wenner probe device as a possible quality assurance/quality control (QA/QC) tool in concrete field testing. It is recommended that several external factors namely moisture, temperature of concrete, presence of rebars needs to be considered during field practice of Wenner probe device.

ACKNOWLEDGEMENT

The authors wish to express their gratitude and sincere appreciation to the Federal Highway Administration Pooled Fund Study TPF-5(117) for support of this research work.

REFERENCES

1. ASTM Standard C1202-05. Standard Method of Test for Electrical Indication of Concrete's Ability to Resist Chloride, American Society for Testing and Materials, Philadelphia, PA, 2005.
2. ASTM Standards 04.01, 04.02. American Society for Testing and Materials, Philadelphia, PA, 2007.
3. Feldman, R.F., Chan, G.W, Brousseau, R.J. & Tumidajski, P.J. Investigation of the Rapid Chloride Permeability Test, ACI Materials Journal, 91, 1994, p.246-255.
4. Julio-Betancourt, G.A, G.A. & R.D Hooton. Study of the Joule Effect on Rapid Chloride Permeability Values and Evaluation of Related Electrical Properties of Concretes, Cement and Concrete Research, 34, 2004, p.1007 - 1015.
5. Ewins, AJ. Resistivity Measurements in Concrete, British Journal of NDT, 32, 1990, p.120-126.
6. Gowers, K.R. & Millard, S.G. Measurement of Concrete Resistivity for Assessment of Corrosion Severity of Steel Using Wenner Technique, ACI Materials Journal, 96, 1999, p.536-541.
7. Sengul, O. & Gjorv, O.E. Electrical Resistivity Measurements for Quality Control During Concrete Construction, ACI Materials Journal, 105, 2008, p.541-547.
8. Stanish, K.D., Hooton, R.D., & Thomas, M.D.A. Testing the Chloride Penetration Resistance of Concrete: A Literature Review, University of Toronto, Toronto, Ontario, Canada, 2000, FHWA Contract DTFH61-97-R-00022.
9. Smith, K. Evaluating Concrete Bridge Design Factors Using Concrete Resistivity, Penn State University Master's Thesis, 2002, p. 92-113.
10. FDOT Standard FM5-578, Florida Method of Test for Concrete Resistivity as an Electrical Indicator of Its Permeability, Florida Department of Transportation, 2004, FM 5-578.
11. Kessler, R.J., Powers, R.F. & Paredes, M.A. Resistivity Measurements of Water Saturated Concrete as an Indicator of Permeability. Presented at NACE International Corrosion Conference, Houston, Texas. 2005, Paper 5261, p.1–10.
12. Torri, K, Sasatani, T. & Kawamura, M. Application of Rapid Chloride Permeability Test to Evaluate the Chloride Ion Penetration into Concrete, Durability of Concrete, ACI Special Publication 170-21, 1997, p.421-435.
13. Marriaga, J.L., Claisse, P. & Ganjian, E. Application of Traditional Techniques on Chloride Resistance Assessment of GGBS Concrete, Presented at Second International Conference on Sustainable Construction Materials and Technologies, Università Politecnica delle Marche, Ancona, Italy, June 28 - June 30, 2010, p.1911-1921.
14. Riding, K.A., Poole, J.L., Schindler, A.K., Juenger, M.C.G. & Folliard, K.J. Simplified Concrete Resistivity and Rapid Chloride Permeability Test Method, ACI Materials Journal, 105, 2008, p.390-394.
15. Rupnow, T. & Icenogle, P. Evaluation of Surface Resistivity Measurements as an Alternative to the Rapid Chloride Permeability Test for Quality Assurance and Acceptance, July, 2011, Report No. FHWA/LA.11/479.
16. Morris, W., Moreno, E.I. & Sagües, A.A. Practical Evaluation of Resistivity of Concrete in Test Cylinders using a Wenner Array Probe, Cement and Concrete Research, 26, 1996, p.1779-1787.
17. Berke, N.S. & Hicks, M.C. The Life Cycle of Reinforced Concrete Decks and Marine Piles Using Laboratory Diffusion and Corrosion Data, In corrosion forms and control of infrastructure, V.Chaker, ASTM STP 1137, American Society for Testing and Materials, Philadelphia, 1992, p.207-31.

A FUNDAMENTAL STUDY OF AN INDUSTRIAL SHAFT FOR ITS FATIGUE LIFE ESTIMATION USING STRESS LIFE ASSESSMENT TECHNIQUE

Rajesh M. Metkar*
Assistant Professor (Mechanical)
Government College of Engineering, Kathora Naka, Amravati, India
Email: rajeshmetkar@yahoo.co.in, Cell No;+ 91-9975497452
Corresponding Author

Vivek K. Sunnapwar
Principal
LokmanyaTilak College of Engineering,
Koperkhairane, Navi Mumbai, India
Email: vivek.sunnapwar@gmail.com

Subhash Deo Hiwase
Vice President
Jupiter and AAT Group, Hyderabad, India
Email:hiwases@yahoo.com

ABSTRACT

The objective of present study is to evaluate the fatigue failure and durability theories considering life prediction of a circumferentially grooved industrial shaft having adjacent notches of several crack length and loaded with a couple force at both the ends, using stress life method. A mathematical model has been developed to calculate the effect of load on stress concentration using finite element simulation techniques and then subsequently using the formulation of stress life method and its comparison in predicting the life before and after notch at the crack initiation location. The analytical derivation for nominal stress calculations have been developed to compare with numerical analysis stress values along with life prediction. The investigations conducted at different crack length on the grooved shaft shows that at a particular crack length, the fracture stress at the crack tip crosses over the endurance stress limit of the shaft material which is nothing but the failure point of the shaft with finite life value. This study shows that the fatigue life prediction technique is comparable for the present case study of grooved shaft and can be concluded that this technique could be used to estimate the life of mechanical parts involving such applications.

Keywords: *Shaft, Fatigue Life Estimation, Stress Life, Notch, Stress Analysis*

1. INTRODUCTION

It has been confirmed from host of literature that despite the existence of substantial research works in structural analysis of an industrial shaft, the studies concerning durability analysis pertaining to fatigue failure at notch location with various crack length, were rarely found. In fact, no fundamental information, relating to application of several fatigue failure theory and its comparison on a notched shaft with respect to various crack length is available till date. The present work, therefore, makes an attempt to determine the material failure due to loading, considering stress theories to evaluate the failure by comparing it on an industrial shaft with and without notch and for various crack lengths. The present theoretical model is based on finite element simulation for stress prediction and then subsequently using the stress life formulation for the comparison of predicted life before and after notch at crack initiation location. Such a work will provide fundamental information to evaluate the fatigue failure and durability theories considering life prediction of an industrial notched shaft.

2. THEORETICAL FORMULATION

The physical system refers to a simple configuration of industrial shaft with a circumferential groove at the center with and without notch, which is loaded with equal and opposite torque at both the ends forming a couple [2]. The boundary and load condition at both the ends of shaft is constrained in only axial degree of freedom and an equal and opposite torque of 12000 N-m is applied forming a couple. The following figure shows the mathematical model of the grooved shaft with the boundary condition considered for the evaluation of fatigue life.

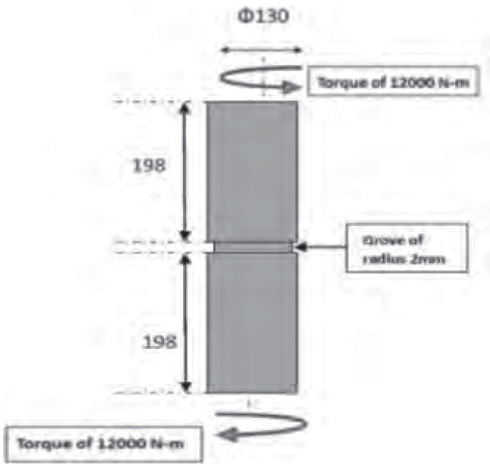

Fig. 1 Industrial shaft specimen studied under fatigue simulation.

The fatigue failure study has been carried out on an industrial shaft specimen using Stress Life (S-N) method, a prominent fatigue failure prediction technique. For studying the failure theories, the crack lengths of various dimensions have been modeled right from 0.5 mm to 8.0 mm with an interval of 0.5 mm. In stress life (S-N) method, S-N plot is used to predict the fatigue failure, wherein, life of the industrial shaft is calculated using Equation (1).

$$\text{Fatigue Strength, } S_f = \sigma_f' \,(2N_f)^b \qquad (1)$$

Where, σ_f' is fatigue strength coefficient and b is fatigue strength exponent of material

3. METHOD OF SOLUTION

The stress analysis of a shaft for different crack length has been performed numerically with the aid of finite element method. To capture the stress and deflection values very accurately, relatively, very dense mesh has been created around the groove and around the cracks of several lengths. A minimum mesh size of around 0.25 mm has been chosen around the groove and the crack, and the maximum mesh size of around 0.5 mm for the rest of the calculation domain for the numerical computation. The modified second order quadrilateral elements have been chosen to model the finite element model of shaft [7]. The test for grid independence was made to ensure that a mesh size finer than the stated one produced insignificant changes (below 3%) in stress gradients and deflections around the groove location. In accordance with the stability criteria, the implicit Hilber-Hughes-Taylor operator is used for integration of the equations of motion in ABAQUS software[4]. The shaft specimen is made up of steel material and chemical composition is shown in Table 1.

Table 1 Chemical compositions by percent weight of steel shaft

Constitution	C	Mn	P	S	Si	Al
Values	0.045	0.081	0.016	0.024	0.27	0.033
Constitution	Cr	Ni	Cu	N	O	
Values	0.1	0.005	0.13	0.008	13PPM	

4. RESULTS AND DISCUSSION

4.1 Stress analysis of industrial shaft specimen without crack The stress analysis of an industrial shaft specimen without crack features, an industrial shaft with a circumferential groove at the center, which is loaded with equal and opposite torque at both the ends forming a couple. The boundary and load condition at both the ends of shaft is constrained in only axial degree of freedom and an equal and opposite torque of 12000 N-m is applied forming a couple. The geometry of the shaft specimen and the mesh design along with boundary conditions are shown in Figure 2. A refined mesh of size around 0.25 mm has been adopted surrounding the groove region to capture the stress and deflections accurately [5].

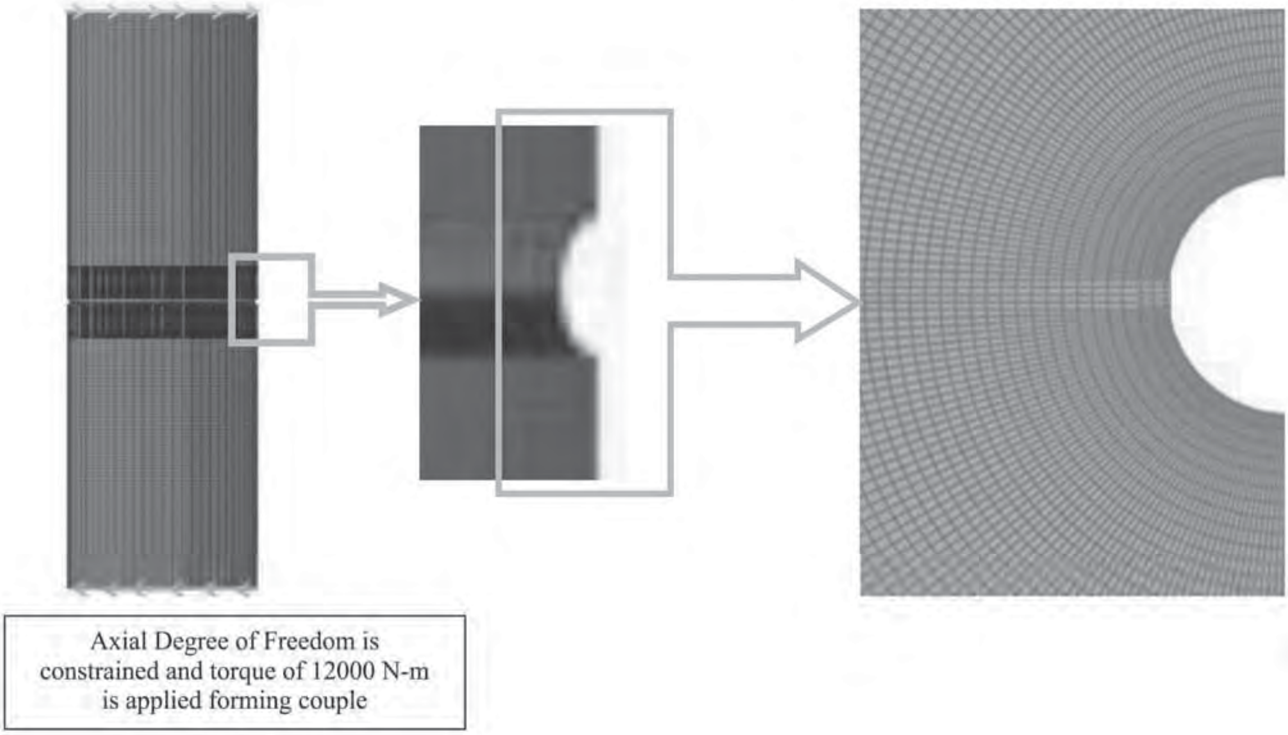

Fig.2 Mesh design and boundary condition of shaft model without crack.

The contour plots of von-mises stress, for a shaft specimen is shown in Figure 3 .It is observed that due to opposing torque load the shaft experiences torsion (twisting) and maximum von-mises stress occurs at the bottom of groove point, which is an obvious result due to minimum cross-sectional area of the shaft at that location.

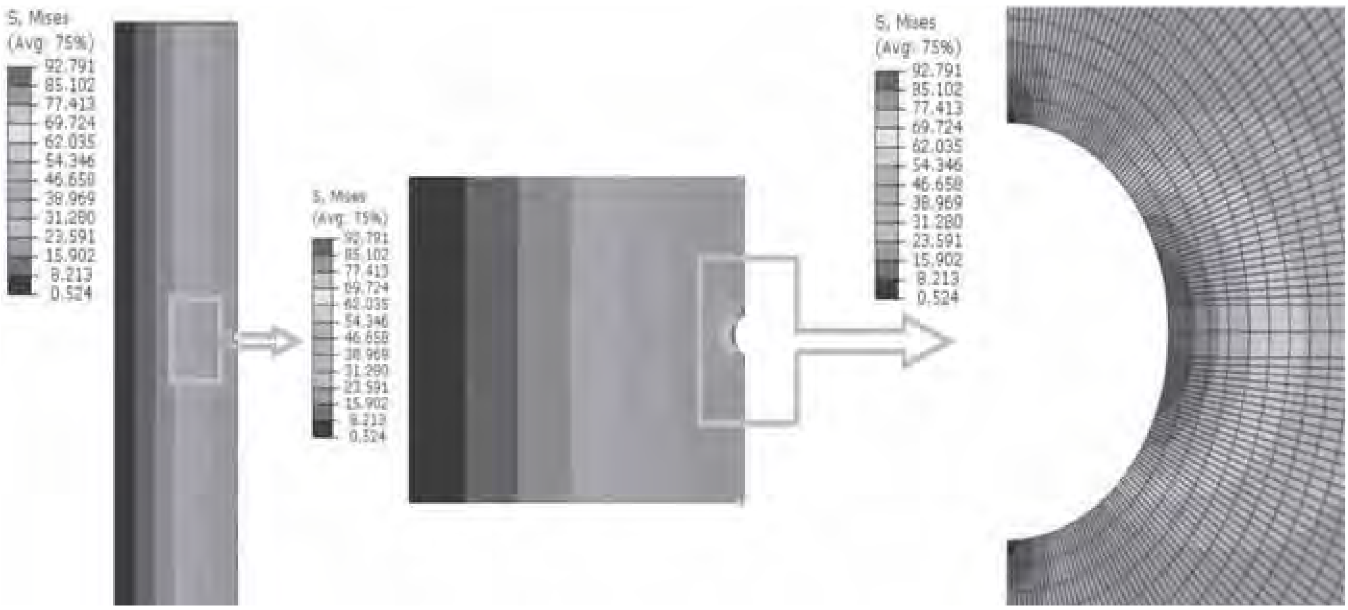

Fig.3 Von-mises stress contours of shaft specimen without crack.

4.2 Stress analysis of the shaft specimen with 0.5 mm Crack The shaft specimen with circumferential groove and a crack at the bottom of groove have been studied to understand the effect of load on stress concentration near crack region.

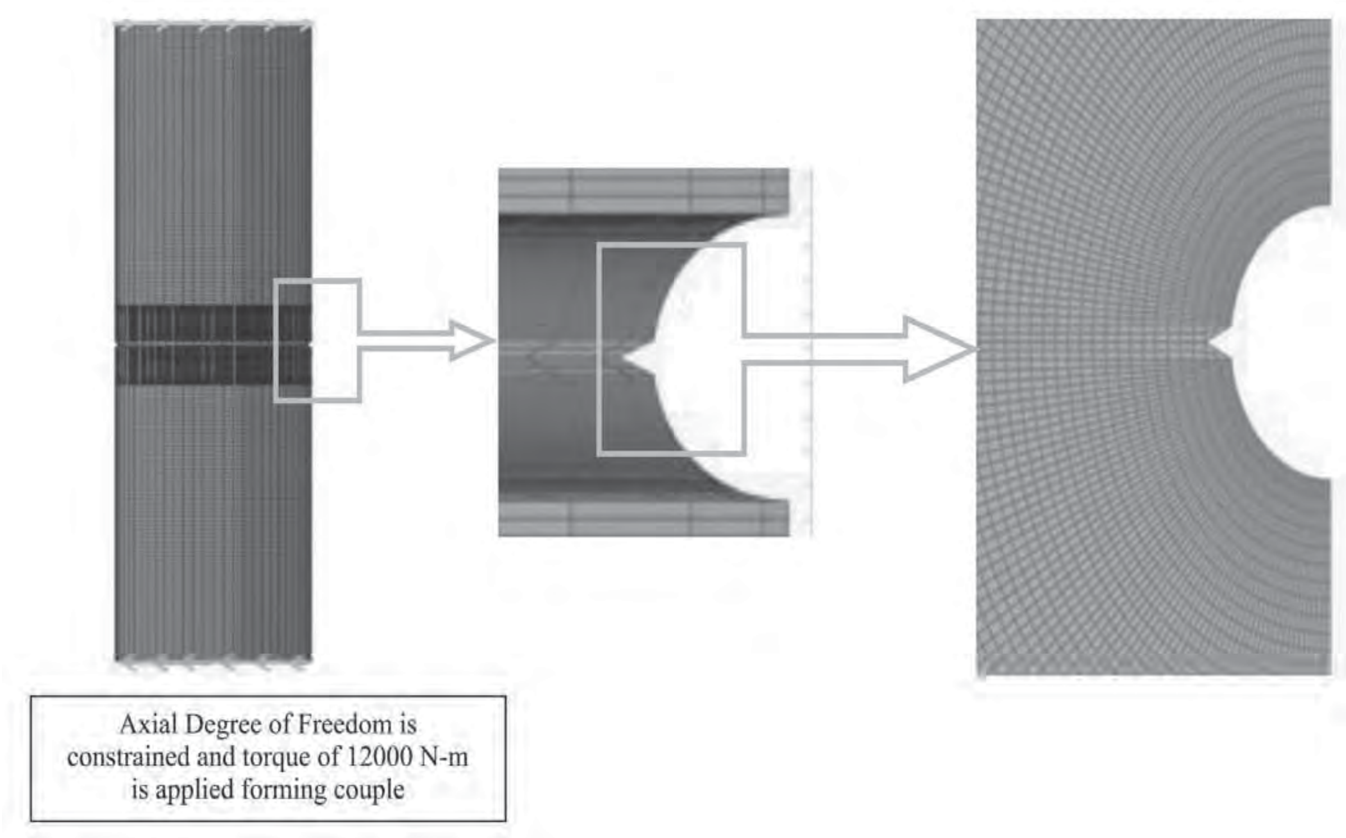

Fig.4 Mesh design and boundary condition of shaft model with 0.5 mm crack length.

The crack length of 0.5 mm to 4.0 mm with the increment of 0.5 mm, have been modeled at the bottom point of groove, where maximum von-mises and principal stress values were found. The Figure 4 shows the mesh design along with boundary and load conditions applied for the numerical stress analysis for the shaft specimen with 0.5 mm crack length.

The stress analysis of the shaft specimen with 0.5 mm crack shows that the maximum von-mises stress is developed at the crack tip and it goes on reducing with respect to the normal distance moving away from crack and can be seen through the Figure 5.

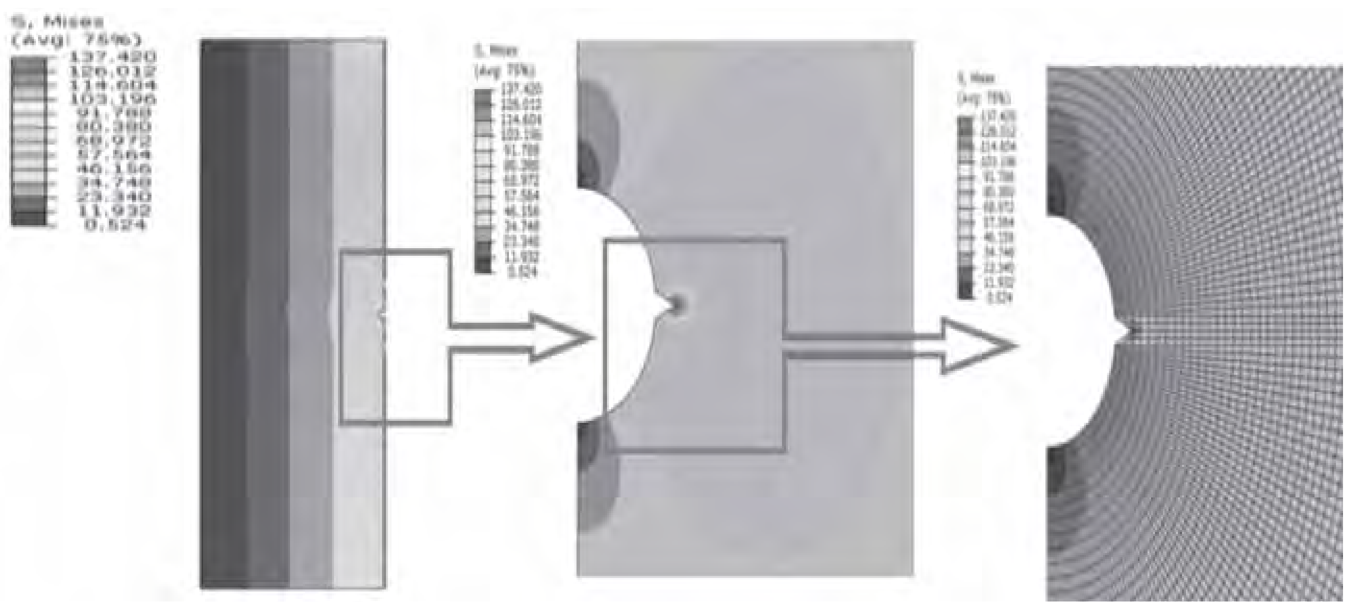

Fig.5 Von-mises stress contours of shaft with 0.5 mm of crack.

It has also been observed that the nominal loads acting on overall shaft specimen depicts elastic nature but because of geometrical discontinuities of crack, the stress concentrations at the crack tip appears to be maximum due to the reason that at the crack tip, the strain energy will be maximum, which in turn causes plastic strains at the crack tip and is responsible for the maximum von-mises stress at that location [3].

Similarly, the stress analysis results obtained for the crack length of 0.5 mm to 8.0 mm with the increment of 0.5 mm have been used for the prediction of fatigue life of the shaft specimen using life estimation technique. In stress life approach, stress life (S-N) curve is plotted on log-log scale for shaft material. Life of shaft under applied load is calculated by using stress-life curve.

4.3 Stress-life prediction of shaft The stress-life method uses the alternating stress amplitude to predict the number of cycles to failure. This method is based on comparing the stress amplitude to a stress versus fatigue life curve (S-N diagram)[1]. The S-N curves are based on empirical formulae derived from experimental data. The stress-life method is generally used for high cycle fatigue, because under low cycle fatigue the stress-strain relationship becomes nonlinear. In the present study, to establish the failure theories on industrial shaft specimen, the stress-life prediction technique is used to estimate the life of the shaft.

The predicted S-N curve for industrial shaft specimen, derived from Equation (1) is shown in Figure 6. The graph shows that with the increase in stress amplitude during cyclic loading of industrial shaft specimen, the number of reversal to failure cycles goes on decreasing [6]. Similarly, the actual S-N curve derived for the same specimen using finite element based stress amplitude values also shows the analogous variation in the number of reversal to failure and can be seen through Figure 7. From the derived S-N curve of the shaft specimen, it can be depicted that without crack the life of the specimen is found out to be in the range of 1013 number of reversal to failure, but with just initiation of crack in the specimen the life is reduced to the range of 1011 number of reversal to failure, and further increase in the crack length in the specimen it further decreases to around 105 number of reversal to failure.

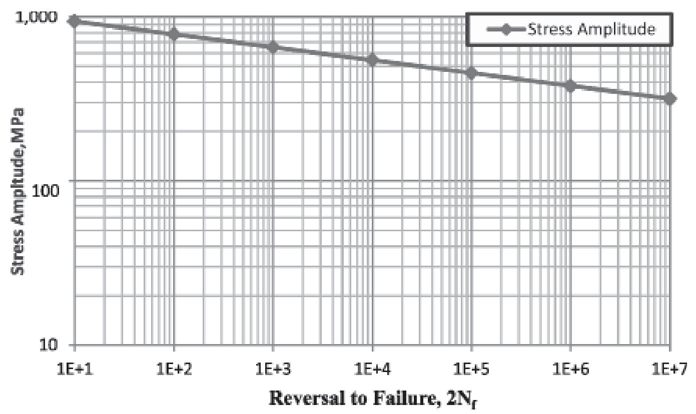

Fig.6 Stress life plot of shaft specimen using guessed reversal to failure.

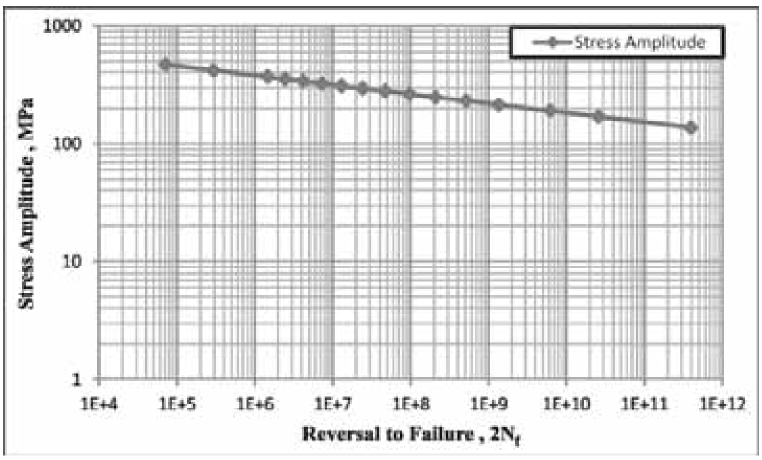

Fig.7 Stress life plot of shaft specimen using finite element derived stress amplitude.

The variation in stress amplitude with respect to change in crack length is shown in Figure 8. The graph shows that, with respect to increase in crack length the stress amplitude increases to a certain limit and then attends an asymptotic steady value. This is because of the fact that with increase in crack length, the strain energy at the tip of the crack increases and at a certain crack length, due to material property of construction, it achieves a maximum limit to hold such strain energy. Further increase in crack length has no significant changes rather a drooping effect is observed, which is clear indication of material failure[4].

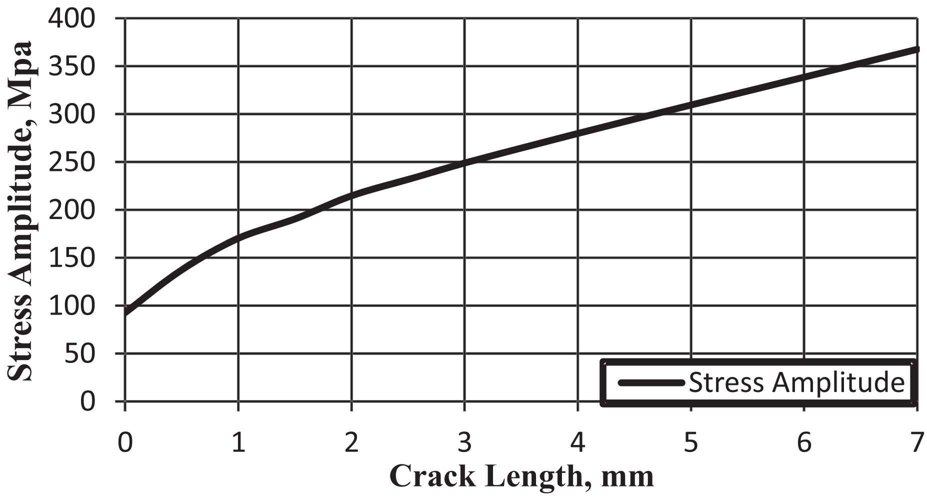

Fig.8 Stress amplitude with crack length.

Similarly, variation of fatigue notch factor, Kf with respect to change in crack length in the industrial shaft specimen is shown in Figure 9, which also shows similar trend as depicted in Figure 8, which is an obvious result, as the fatigue notch factor, Kf is directly proportional to function of stress amplitude.

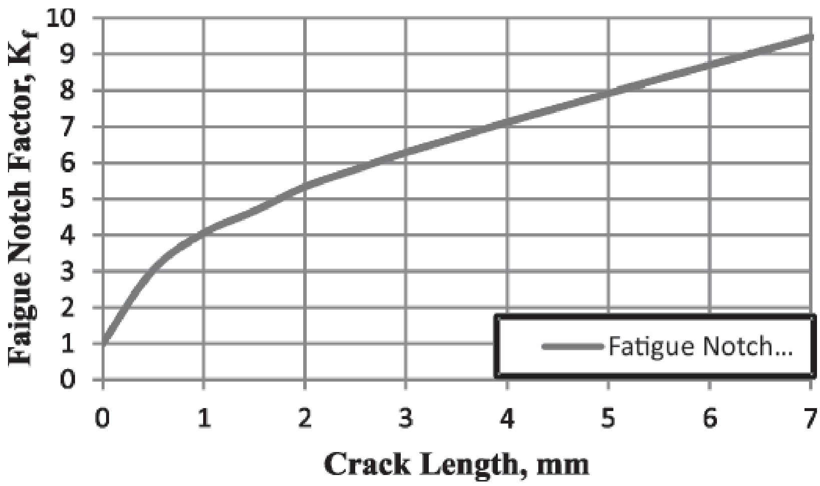

Fig.9 Fatigue notch factor verses crack length.

The estimated stress-life of the industrial shaft specimen with respect to crack lengths is presented in the Table 2. It can be observed that the life of the specimen without crack is found out to be around in the range of 1013 number of reversal to failure, but with just initiation of crack in the specimen the life is reduced to the range of 1011 number of reversal to failure, and further increase in the crack length in the specimen it further decreases to around 105 number of reversal to failure.

Table 2 Number of reversal to failure for various crack length using stress-life approach.

Sr. No	Crack Length, mm	Number of reversal to failure, ($2N_f$)
1	0.0	5.81E+13
2	0.5	3.96E+11
3	1.0	2.58E+10
4	1.5	6.22E+09
5	2.0	1.36E+09
6	2.5	5.14E+08
7	3.0	2.08E+08

8	3.5	9.66E+07
9	4.0	4.69E+07
10	4.5	2.44E+07
11	5.0	1.31E+07
12	5.5	7.29E+06
13	6.0	4.17E+06
14	6.5	2.45E+06
15	7.0	1.47E+06
16	7.5	2.95E+05
17	8.0	7.10E+04

5. CONCLUSION

- The stress plots for the shaft specimen due to bending and torsional loading of the shaft shows that the maximum von-mises stress occurs at the bottom of the groove, which is more obvious due to less cross-sectional area, and is the point of crack initiation as well.
- The stress plots for the bending and torsional loaded shaft specimen with crack at the bottom of the groove shows that the von-mises and maximum principal stresses occurs at the crack tip point, whereas the minimum principal stress also occurs at the crack tip point only.
- It has also been observed that the nominal loads overall the shaft specimen depicts elastic nature. The stress concentrations at the crack tip appears to be maximum due to geometrical discontinuities of crack. This in turn causes higher principal stresses at the crack tip and is responsible for the maximum von-mises stress at that location.
- It has been observed that the crack continues to grow as long as cyclic bending and torsional stress are present. At the point vicinity of final fracture area, the crack size becomes large enough to raise the stress intensity factor at crack tip to the level of the material's fracture toughness and sudden failure occurs in next tensile stress-cycle. At that particular crack length,stress intensity at the notch tip exceeds the critical stress intensity value. Although, overall nominal stresses in the shaft are well below the yield strength, the elevated stress at the notch tip is due to notch at circumference.
- The Stress Life method studied for the evaluation of the fatigue failure theories on an industrial shaft specimen predicts comparative results and can be used for the prediction of fatigue life of engineering components.

ACKNOWLEDGEMENT

The authors thank for the support provided by Jupiter and AAT Group, Hyderabad (India).

REFERENCES

1. Adib, H., Pluvinage, G.: Theoretical and Numerical Aspects of the Volumetric Approach for Fatigue Life Prediction in Notched Components, International Journal of Fatigue, 2003,Vol. 25, pp. 67-76.
2. Daniel, B., Taylor, D., Marco, S., Mazzeo, E.: The Fatigue Behavior of Three Dimensional Stress Concentration, International Journal of Fatigue,2005, Vol. 27, pp. 207-221.
3. Farahani, A.V., Kodric, T., Ghahramani, A.: A Method of Fatigue Life Prediction in Notched and Unnotched Components, Journal of Materials Processing Technology,2005, Vol. 169, pp. 94-102.
4. Metkar, R,M., Sunnapwar, V,K.,Hiwase, S.D.: A Fatigue analysis and Life Estimation of Crankshaft- A Review, International Journal of Mechanical and Materials Engineering, 2011,vol 6 (3),pp425-430.
5. Metkar, R.M., Sunnapwar, V.K., Hiwase, S.D.:Modal Analysis for High Cycle Fatigue Life Estimation of Crankshaft," International Journal of Applied Engineering Research, 2011,Vol.6, pp. 2485-2490.
6. Pyttal, B., Schwerdt, D., Berger, C.: Very High Cycle Fatigue- Is There a Fatigue Limit, International Journal of Fatigue,2011, Vol. 33, pp. 49-58.
7. Stamenkovic, D., Maksimovic, K.: Fatigue Life Estimation of Notched Structural Components, Journal of Mechanical Engineering, 2010, Vol. 56, Issue 12, pp. 846-852.

AN IMPROVED VIRAL SYSTEM, GENETIC ALGORITHM AND ADAPTIVE GENETIC ALGORITHM FOR SOLVING REACTIVE DISPATCH PROBLEM

K. Lenin*
Research Scholar, Jawaharlal Nehru Technological University,
Assistant Professor, Sree Sastha College of Engineering
Chennai, India.
E-mail: gklenin@gmail.com
Contact number – 09940556102
Corresponding author

B. Ravindranath Reddy
Deputy Executive Engineer
Jawaharlal Nehru Technological University
Hyderabad 500 085 India

M. Surya Kalavathi
Professor of Electrical and Electronics Engineering
Jawaharlal Nehru Technological University
Kukatpally, Hyderabad 500 085, India.

ABSTRACT

This paper presents Viral Systems (VS), a novel bio-inspired methodology based on a natural biological process taking part when the organism has to give response to an external infection when used for solving reactive power dispatch problem. VS have proven to be very efficient when dealing with problems of high complexity. Genetic Algorithm (GA) & Adaptive genetic algorithm is used for solving the multi-objective reactive power dispatch problem in power system. The virus infection expansion corresponds to the feasibility region exploration, and the optimum corresponds to the organism lowest fitness value. For such type of problems, available algorithms usually present weaknesses and exact mathematical methods cannot guarantee the optimum of the problem in a bounded time. In the adaptive genetic algorithm the probability of cross over and mutation pc and pm are varied depending on the fitness values of the solutions and the normalized fitness distance between the solutions in the evaluation process to prevent premature convergence and refine the convergence performance of genetic algorithms.

Keywords: *genetic algorithm, adaptive genetic algorithm, Viral System, bio-inspired methodology, optimization, meta-heuristic, reactive power dispatch problem.*

1. INTRODUCTION

Optimal reactive power dispatch problem is one of the difficult optimization problems in power systems. The sources of the reactive power are the generators, synchronous condensers, capacitors, static compensators and tap changing transformers. The problem that has to be solved in a reactive power optimization is to determine the required reactive generation at various locations so as to optimize the objective function. Here the reactive power dispatch problem involves best utilization of the existing generator bus voltage magnitudes, transformer tap setting and the output of reactive power sources so as to minimize the loss and to enhance the voltage stability of the system. It involves a non linear optimization problem. The reactive power can be controlled in order to improve the voltage profile and minimize the system loss. Generally, some load bus voltage might violate their upper or lower limits during system operation due to disturbances and/or system configuration changes. The power system operator can alleviate this situation and voltages can be maintained within their permissible limits by reallocating reactive power generation in the system.

Generally, the optimal VAR dispatch problem has many objectives such as: reducing the fuel costs: ameliorating the supply quality and reliability by improving the voltage profile over the system; and enhancing the system security by uploading the system equipment. The reactive power optimization problem is a nonlinear combinatorial optimization problem. Various mathematical techniques have been adopted to solve this optimal reactive power dispatch problem. These include the gradient method[1-2], Newton method[3] and linear programming [4-7].The gradient and Newton methods suffer from the difficulty in handling inequality constraints. To apply linear programming, the input- output function is to be expressed as a set of linear functions which may lead to loss of accuracy. Viral Systems is a new bio-inspired methodology simulating the natural biological process taking part when the organism has to give a response to an external infection. Natural Immune System protects the organism from dangerous extern agents such as viruses or bacteria. In this context, antibodies try to protect the organism from such pathogens. Immune systems have a lot of peculiarities that make them very attractive for computational optimization (Cutello et al., 2007[20] and Cutello et al, 2007[22]. In certain manner, Viral System (VS) makes use of the same infection-antigenic response concept from immune systems, but from the perspective of the pathogen. That is, the virus infection expansion corresponds to the feasibility region exploration, and the optimum corresponds to the organism lowest fitness value. For such type of problems, available algorithms usually present weaknesses and exact mathematical methods cannot guarantee the optimum of the problem in a bounded time. So, several generalized meta-heuristics (as genetic algorithms, tabu search or simulated annealing among others) have successfully tried to deal with such problems. Since the last decade, new research is being undertaken in order to find other natural-life inspired methods to solve these kind of problems.A genetic algorithm is a stochastic search technique based on the mechanics of natural selection. In this paper, genetic algorithm is used to solve the voltage constrained reactive power dispatch problem. The proposed algorithm identifies the optimal values of generation bus voltage magnitudes, transformer tap setting and the output of the reactive power sources so as to minimize the transmission loss and to improve the voltage stability. The adaptation mechanism provides for the alteration of operator probabilities in proportion to the fitness's of strings created by the operators. Simply stated, operators which create and cause the generation of better strings are allotted higher probabilities. The technique has been developed in the context of a steady-state GA[18], and experimental evidence has demonstrated considerable promise. Specifically, a mutation rate that decreases exponentially with generations has demonstrated superior performance for a single application. The effectiveness of the proposed approach is demonstrated through various IEEE bus systems. The test results show the proposed algorithm gives better results with less computational burden and is fairly consistent in reaching the near optimal solution.

2. PROBLEM FORMULATION

The objective of the reactive power optimization problem is to minimize the active power loss in the transmission network as well as to improve the voltage profile of the system. Adjusting reactive power controllers like generator bus voltages, reactive power of VAR sources and transformer taps performs reactive power scheduling.

$$\text{Min PL} = \sum_{i=1}^{NB} P_i(X, Y, \delta) \qquad (1)$$

Subject to

I The control vector constraints

$$X_{min} \le X \le X_{max} \qquad (2)$$

ii) The dependent vector constraints

$$Y_{min} \le Y \le Y_{max} \qquad (3)$$

And

iii) The power flow constraint

$$F(X, Y, \delta) = 0 \qquad (4)$$

Where

$$X = [V_G, T, Q_C] \qquad (5)$$

$$Y = [Qg, V_L, I] \qquad (6)$$

NB - Number of buses in the system.
δ - Vector of bus phase angles
P^i - Real power injection into the ith bus
V_G - Vector of generator voltage magnitudes
T - Vector of tap settings of on load transformer tap changer.

Q_C	-	Vector of reactive power of switchable VAR sources.
V_L	-	Vector of load bus voltage magnitude.
I	-	Vector of current in the lines.
P_L	-	Vector of power loss in the transmission network.

3. FOUNDATIONS OF VIRAL SYSTEMS

The concept of viruses' analogies has been mainly used as part of genetic algorithms. For instance, Kubota et al. (1996)[21] propose them as part of a specific operator in genetic algorithms, and Saito (2003)[19] has described the use of genetic algorithms which make use of a virus evolutionary theory (GAV), and an algorithm based on the conception of horizontal evolution caused by virus infections. GAV is carried out by attacking a chromosome by a number of viruses, and having the genes of the chromosome recombined by the attack. The infection is allowed when the evaluation value goes up, but it falls into local minima easily. In order to escape from these local minima, an infection which makes the evaluation value worse in a small rate under small probability is allowed as well.

Viruses, viral infections and organism antigenic response Viruses are intracellular parasites shaped by nucleic acids, such as DNA or RNA, and proteins. The protein generates a capsule, called a capsid, where the nucleic acid is located. The capsid plus the nucleic acid shape the nucleus capsid, defining the virus. There are a high number of different types of viruses, each of them showing a different and autonomous behavior. However, the simplest and most common type of virus is the phage, a type of virus infecting bacteria. Figure 1 depicts a traditional representation for such structure.

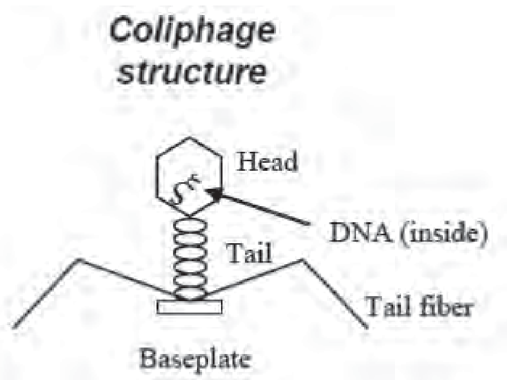

Fig. 1 Coli phage structure

One of the main characteristics of viruses is the replication mechanism. The phage (a common type of virus) does follow lytic replication process. Left side of Figure 2 depicts the biological evolution of the virus infection following the next steps:

1. The virus is adhered to the border of the bacterium. After that, the virus penetrates the border being injected inside this one, (1) and (2) in Figure 2.

2. The infected cell stops the production of its proteins, beginning to produce the phage proteins. So, it starts to replicate copies of the virus nucleus-capsids, (3a) in Figure 2.

3. After replicating a number of nucleus-capsids, the bacterium border is broken, and new viruses are released, (4a), which can infect near cells, (1), in Figure 2.

The life cycle of the virus can be developed in more than one step. Some viruses are capable of lodging in cells giving rise to the lysogenic replication.

This case is shown in the right side of Figure 2. It follows:

1. The virus infects the host cell, being lodged in its genome, (3b) in Figure 2 where a pro-phage (mutation) can arise.

2. The virus remains hidden inside the cell during a while until it is activated by any cause, for example ultraviolet irradiation or X-rays, (i) in Figure 2. During such time the cell reproduces itself normally.

3. The replication of cells altered, with proteins from the virus, starts. So, lysogenic replication produces the genome

alteration of the cell leading to a procedure similar to a mutation process.

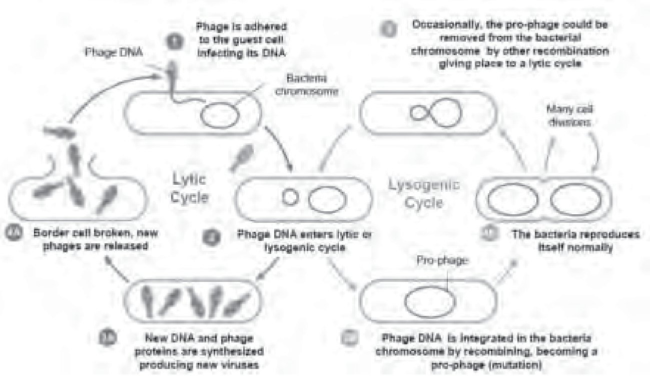

Fig. 2 Lytic (left) and lysogenic (right) replication of viruses

However, some viruses have the property of leading an antigenic response in the infected organism. In these situations an immune response is originated causing the creation of antibodies. This is the specific case of phages. So VS follows an exploration process that combines lytic replication to search the neighbourhood of the existing solutions (which is one of the main features of Tabu Search) and a mutation process (which is a characteristic of Genetic Algorithms).

3.1 Computational description of Viral Systems VS are an iterative method that runs during a maximum number of iterations, or until the optimum are reached in case of a known optimum. VS define the clinical picture of an infected population as the description of all the cells infected by viruses. Computationally, it includes the encoding of the solution that is being explored (the genome of the cell that is infected, in biological terms) and the number of nucleus-capsids being replicated, NR, (for lytic replications) or the number of hidden generations, IT, (for lysogenic replications). Thus the state of each virus is given by the three-tuple “cell genome-NR-IT”. All these three-tuples corresponding to the cells infected by viruses define the clinical picture.

Every cell infected by a virus develops a lytic or a lysogenic replication according to a probability *plt* (for lytic replication) or *plg* otherwise, where *plt* + *plg* = 1. In case of lysogenic replications, the activation of the mutation process takes place after a limit of iterations has passed (LIT). The value of LIT depends on the cell’s health conditions, so a healthy cell (high value of the objective function being minimised, f(x)) will have a low infection probability, i.e. the value of LIT will be higher. An unhealthy cell, on the contrary, will have a lower value of LIT. In case of lytic replications, a number of virus replications (NR) is calculated for each iteration as a function of a binomial variable, Z, adding its value to the current NR in the clinical picture. Z is calculated using a Binomial distribution given by the maximum level of nucleus-capsids replicated, LNR, and the single probability of one replication, pr,: Z = Bin (LNR , pr). LNR represents the limit to break the cell border and to release the lodged viruses. As in the lysogenic cycle, the value of LNR is set depending on the value of the objective function being minimised, f(x).

Thus cells with higher f(x) have lower probability of getting infected, and therefore the value of LNR will be higher. Two infections process have been defined for VS: massive infections where a devastating infection reaches a high number of cells, and selective infection where a parsimonious infection following a like-elitist process takes place. An example of the first case is the Ebola virus with a rapid and massive infection that very often produces the death of the patient in a few days, and an example of the second one is the HIV virus, which through a step-by-step evolution destroys the immune system during a process that can take years.

3.2 Massive infection Once a massive infection takes place and viruses are liberated inside the organism, each liberated virus will have a probability, *pi*, of infecting other new cells of the neighbourhood. If the neighbourhood cardinality of x is defined as |*V(x)*|, the number of cells infected by the virus in the neighbourhood can be calculated as a binomial distribution given by Y = Bin (|*V(x)*|, *pi*). On the other hand, in order to defend itself from the growth of the viral infection, the Organism (the set of cells) responds by releasing antigens.

In the clinical picture, each one of the infected cells generates antibodies according to a Bernoulli probability distribution A(x) = Ber (*pan*), where *pan* is the unitary probability of generating antibodies by the cell x in the clinical picture. Hence, the total population of infected cells generating antibodies is characterized by a Binomial distribution of parameters: the size of the clinical picture, *n*, and the probability of generating antibodies, *pan*: A(population) = Bin (*n*, *pan*). Also, the antigenic response for every cell in the neighbourhood of an active virus is estimated as a Bernoulli probability distribution given by the probability of generating antibodies, *pan*: A(x’) = Ber (*pan*) : x’∈V(x).

Therefore, the total number of cells with antibodies in the neighbourhood will follow a Binomial probability distribution given by the total size of the neighbourhood for all the active viruses, |V(x)|, and the probability of generating antibodies, pan: A = Bin (|V(x)|, *pan*). In this situation, a Markovian Process defines the evolution of the clinical picture (Cortés *et al*. 2008).

Let, $\pi = (\pi_0, \pi_1, .., \pi_{LNR})$ be the probability of a cell with 0, 1, …, LNR nucleus-capsids replicated. Equations (1-3) are satisfied in steady state.

$$\pi = \pi .p \tag{7}$$

$$\pi_J = \frac{1}{1-P_0}\left(\sum_{K=0}^{J-1} P_{J-K}.\pi_K\right) \forall J = 1,2, \ldots, LNR \tag{8}$$

$$\pi_0 + \pi_1 + .. + \pi_{LNR} = 1 \tag{9}$$

To ensure computational control of the infection evolution, we can give (10) as an adequate value for *pan.*

$$P_{an} > \frac{n.\pi_{LNR}.\left(P_i.\left|\overleftrightarrow{v(x)}\right| - 1\right)}{n.\pi_{LNR}.\left(P_i.\left|\overleftrightarrow{v(x)}\right| - 1\right) + n} \tag{10}$$

Where |V (x) | is the average neighbourhood size for a specific problem. However, we do not use the same value of pan for all the cells. In fact, a higher value of f(x) implies a healthy cell and therefore this cell will have a higher probability of developing an antigenic response. On the contrary, a cell with an low value of f(x) represents an unhealthy cell with a lower probability of developing an antigenic response. Thus we define for each cell its specific pan(x). Figure 3 describes the algorithmic process. The original state is depicted by the clinical picture on the left-hand side. The viruses reaching the level of nucleus capsids (LNR) break the border and start infecting new cells in their neighbourhoods.

The response of the Organism is characterized by the antigenic response, liberating space in the clinical picture, and by creating antibodies in cells located in the virus neighbourhood. This situation leads to a new clinical picture, depicted on the right-hand side of the figure, with new infected cells lodging viruses.

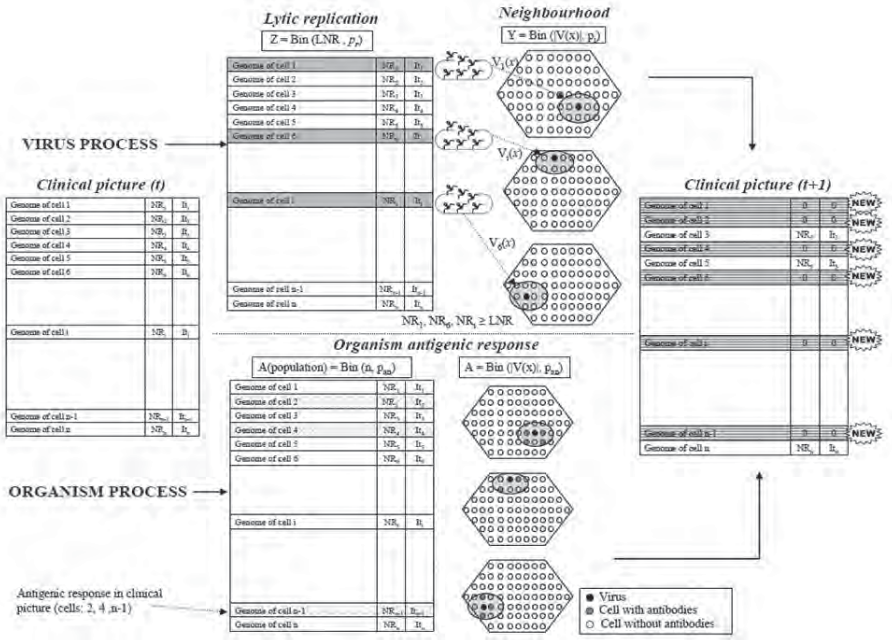

Fig. 3 Algorithmic for lytic replication case in massive infections

3.3 Selective infection Once a selective infection takes place and viruses are liberated inside the organism, the virus selects a cell with a low value of f(x) in the neighbourhood. However, the virus will not be able to infect those cells that have developed antigens. Higher values of f(x) imply healthy cells and therefore cells that have a higher probability of developing antigenic responses. On the contrary, cells with low value of f(x) imply unhealthy cells with lower probability of developing antigenic responses. This effect is represented by the previously introduced hyper geometric function. Then, if the probability of generating antibodies for the case of cell x is pan(x),nA(x) is defined as a Bernoulli random variable: A(x) = Ber (pan(x)). If cell x generates antibodies, the cell is not infected and it is therefore not included in the new clinical picture. For recording this clinical picture we use the original cell (that was infected by the virus and that reached the LNR limit) and we initiate a lysogenic cycle for that cell. Figure 4 defines the algorithm evolution for the infection. The initial state is on the left-hand side: the virus process starts with viruses breaking the border and starting the infection of new cells in their neighbourhoods. Each virus selects the most promising cell, which is the least healthy cell. The Organism process is characterized by the probability of antigenic response in the least healthy cell. Those cells developing antibodies are not infected. Finally, the interaction (right hand side of the figure) defines the new clinical picture, with new infected cells lodging viruses. The cells generating antibodies follow a new lysogenic replication.

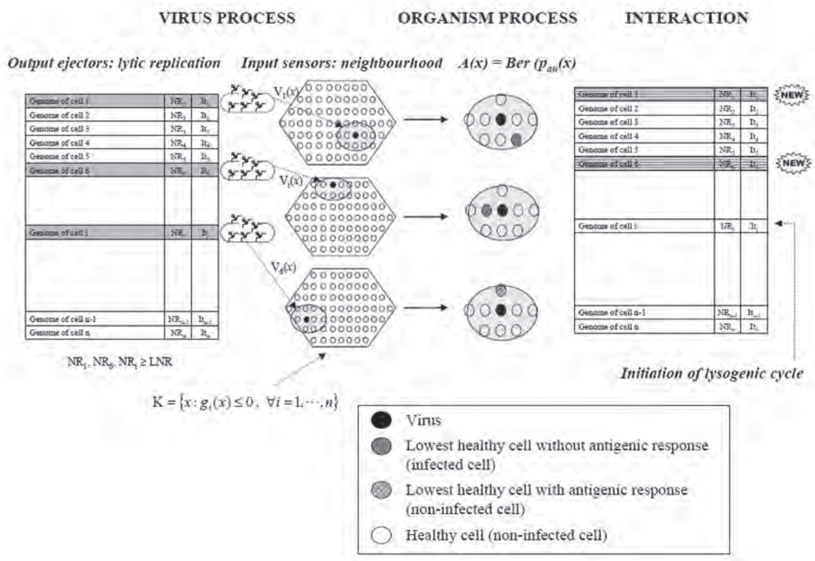

Fig. 4 Algorithm for lytic replication case in selective infection

The main difference between massive and selective infection processes is the infection activity every time the algorithm makes iteration. In the selective infection case, only a single cell is infected whereas in the massive one, all cells are infected at each iteration. However, lytic and lysogenic replications are the same for both processes. Therefore, the differences in the pseudo code of the massive process respect to the selective process only appear in the main procedure.

3.4. Algorithm for Virus System

1. Determine the required inputs for the problem

2. Determine the value of Viral Systems parameter, i.e. the maximum number of iterations (ITER), the size of clinical picture (POB), the probability of occurring lytic replication (plt), the probability of infecting a neighboring cell (pi), the probability of replicating a virus (pr), probability of producing antigene (pan), the constant multiplier for computing LNR (LNR0), and the constant multiplier for computing LIT (LIT0).

3. Create infected cells as many as POB and put them in the initial clinical picture. Each infected cell has a unique genome, has NR equals 0 and IT equals 0.

4. Start the first iteration; t = 1.

5. Start checking the objective function value and antigene production for the first infected cell, m = 1.

6. Compute the objective function value for cell m. Update the best objective function value found so far , if the objective function value of cell m is better (lower) than the previously recorded .

7. Check the ability of cell m to produce antigene, based on the probability of producing antigene is pan. If cell m is able to produce antigene, the cell is deleted from the clinical picture.

8. If m ≠ POB, then m = (m+1) and go back to step 6. Otherwise, go to the next step.

9. Start the replication for the first cell in the clinical picture, m = 1.

10. Determine the replication type for the virus inside cell m, based on the probability of occurring lytic replication is plt. If the replication type is lytic, then go to the next step. Otherwise, go to Step 15 for lysogenic replication.

11. Update the NR of cell m; NR = NR + Z.

12. Compute the LNR for cell m. If its NR is larger than or equal to LNR, then go to the next step. It means, the replicated viruses break the cell’s border. Otherwise, go to Step 19.

13. Delete cell m from clinical picture. Start infecting neighboring cells, based on the probability of infecting a neighboring cell is pi.

14. For each infected neighboring cell, check whether it is able to produce antigene. Keep the neighboring cells that are unable to produce antigene. Go to Step 18.

15. Update the IT of cell m; IT = IT + 1.

16. Compute the LIT for cell m. If LIT is larger than or equal to LIT, then go to the next step. It means, the virus is activated and thus it will mutate the cell's genome. Otherwise, go to Step 19.

17. Delete cell m from clinical picture. Perform the mutation procedure by selecting the first gene and another gene randomly. Swap those genes and conform the last gene to the new first gene.

18. Store either neighboring cells or mutated cell in a temporary storage.

19. If m ≠ POB, then m = (m+1) and go back to step 10. Otherwise, go to the next step.

20. If there is any duplication between the genome of cells in the temporary storage, remove the duplicates. If there is any duplication with the cells in the clinical picture, delete the duplicates as well.

21. Insert the cells in the temporary storage into the clinical picture. If the number of cells in the temporary storage is larger than POB, then delete all cells in the clinical picture and select cells from the temporary storage starting from the best to enter the new clinical picture.

22. If t ≠ ITER, then t = (t+1) and go back to step 5. Otherwise, the algorithm stops with the best solution found is the one whose objective function value is recorded.

4. GENETIC ALGORITHM

GA is search algorithms based on the mechanics of natural genetics and natural selection.The GA is a population search method. A population of strings is kept in each Generation. The simulation of the natural processes of reproduction, gene crossover and mutation produces the next generation.

4.1. Reproduction Reproduction is simply an operation whereby an old chromosome is copied into a "mating pool" according to its fitness value. More highly fitted chromosomes receive a greater number of copies in the next generation. Copying chromosomes according to their fitness values means that chromosomes with a higher value have a higher probability of contributing one or more offspring in the next generation.

4.2. Crossover Crossover is the primary genetic operator, which promotes the exploration of new regions in the search space. It is a structured, yet randomized mechanism of exchanging informing between strings. This operation is similar to that of two scientists exchanging information. Crossover begins by selecting at random two members previously placed in the mating pool during reproduction. A crossover point is then selected at random and information from one parent, up to the crossover point is exchanged with the other member, thus creating two new members for the next generation. An example of the crossover operator is depicted

	Parent A:	1 0 1 1 0 0 0 1
	Parent B:	0 1 0 0 0 0 1 1
Crossover site		↑
	Child A :	1 1 0 1 0 0 0 1
	Child B :	1 0 1 0 0 0 1 1

Fig 5 .Crossover Operator

4.3 Mutation Although reproduction and crossover effectively search and recombine existing chromosomes, they do not create any new genetic material in the population. Mutation is capable of overcoming this shortcoming. It is an occasional (with small probability) random alternation of a chromosome position as shown in Figure 2.

Child A	:	1 1 0 1 0 0 0 1
New Child A	:	0 1 0 1 0 1 0 1

Fig. 6 Mutation Operator

4.4 Fitness Function The fitness function is the one which gives a raw measure amongst the fit to each possible candidate solution in the problem space.

For a minimization function,, the fitness function is taken as

4.5 Selection Method Here, Roulette wheel selection method is followed. This is fitness proportional selection mechanism.

$$\text{FIT} = 1/1 + \phi \tag{11}$$

The better fit strings get selected often to pass on their information to their off springs.

5. ADAPTIVE STRATEGY OF ADAPTIVE GENETIC ALGORITHM

This consists of an n-tuple of binary strings bi of length l, where the bits of each string are considered to be the genes of an individual chromosome and where the n-tuple of individual chromosomes is said to be a population. In a multiple variable optimization problem, the individual variable coding is usually concatenated into a complete string. To decode a string, bit strings with specified string length are extracted successfully from the concatenated string and the sub strings are then decoded and mapped into the value in the corresponding search space. There are three main GA operators: reproduction, crossover, and mutation.

The reproduction operator allows highly productive chromosomes (strings) to live and produce off springs in the next generation. The crossover operator, used with a specified probability, exchanges genetic information by splitting two chromosomes at a random site and joining the first part of one chromosome with second part of another chromosome. Mutation introduces occasional changes of a random string position with a specified mutation probability.

5.1 Reproduction, Crossover and Mutation The significance of P_c and P_m in controlling GA performance has long been acknowledged in GA research. The crossover probability Pc controls the rate at which solutions are subjected to crossover. The higher value of P_c, the quicker are the new solutions introduced into the population. As P_c increases, however, solutions can be disrupted faster than selection can exploit them. Mutation is only a secondary operator to restore genetic material. Nevertheless, the choice of Pm is critical to GA performance. Large values of Pm transform in the GA into a purely random search algorithm, while some mutation is required to prevent the premature convergence of the GA to sub optimal solutions. Identifying optimal settings for P_c and P_m is an important problem for improving the convergence performances of GAs and has been studied by many researchers.

The key idea of the adaptive GA is to adapt the probabilities of crossover and mutation based on the fitness statistics of population at each generation. In Ref.[8], it has been observed that the difference between the maximum fitness value and average fitness value of the population. fmax - f, like to be less for a population scattered in the solution space. Therefore, the values of Pc and Pm should be varied depending on the value of fmax - f. On the other hand, if Pc and Pm have the same values for all the solutions of the population, which means solutions with high fitness values as well as the solutions with low fitness values are subjected to the same level of mutation and crossover, this will certainly deteriorate the performance of GAs. The adaptive strategy for updating Pc and Pm developed in [8] takes the following forms.

$$P_c = \begin{cases} k_1(f_{\max} - f_c)/(f_{\max} - f), & f_c > f \\ \mathrm{k}_{3,} & \mathrm{f_c} \le \mathrm{f} \end{cases} \tag{12}$$

And

$$P_m = \begin{cases} k_2(f_{\max} - f_i)/(f_{\max} - f), & f_i > f \\ \mathrm{k}_{4,} & \mathrm{f_i} \le \mathrm{f} \end{cases} \tag{13}$$

Where k_1, k_2, k_3 and k_4 have to be less than 1.0 to constrain P_c and P_m to the range 0.0 - 1.0 f_c is the larger of fitness values of the individuals selected for crossover and f_i is the fitness of the i^{th} chromosome to which the mutation with probability

P_m is applied.

5.2 ALGORITHM FOR RPO PROBLEM

a. Start.

b. Read line data, bus data.

c. Generate random variables for V,G, T, QC for NP.

d. Decode the nh population and carryout load flow and get the solution.

e. The fitness function is calculated as:

$$f_n = P^n{}_L + \alpha \sum_{j=1}^{NG} Q_{G,j}^{lim,n} + \beta \sum_{j=1}^{NL} V_{L,j}^{lim,n} \quad ; n = 1,2.., \quad N_n \tag{14}$$

α, β = penalty factors

$P^n{}_L$ = total real power losses of the n^{-th} population

$$Q_{G,j}^{lim,n} = \begin{cases} Q_{G,min} - Q_{G,j}^n & \text{if } Q_{G,j}^n < Q_{G,min} \\ Q_{G,j}^n - Q_{G,max} & \text{if } Q_{G,j}^n > Q_{G,max} \end{cases} \tag{15}$$

And

$$V_{L,j}^{lim,n} = \begin{cases} \left| V_{L,j}^n \right| - V_{L,max} , & \text{if } \left| V_{L,j}^n \right| > V_{L,max} \\ 0 & \text{otherwise} \end{cases} \tag{16}$$

f. By Roulette wheel selection from the mating pool.

g. Carry out crossover, Mutation and form new children.

h. Repeat steps (e) and (f) until the child population of size is generated.

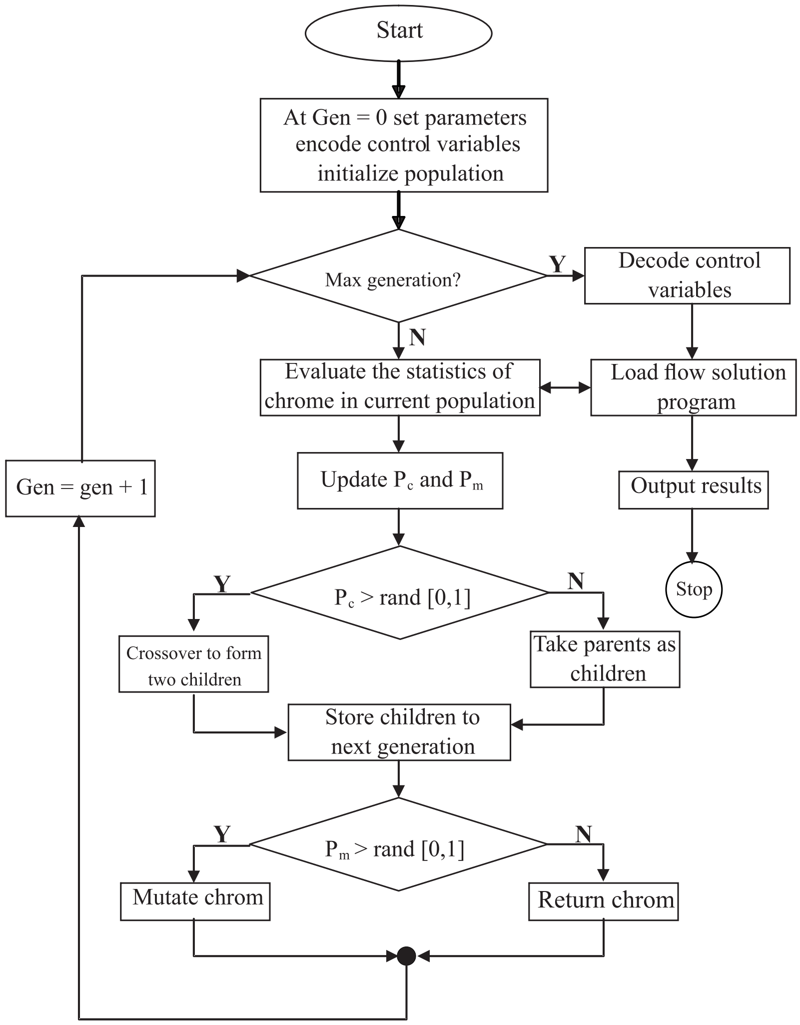

Fig. 7 Flow Chart of Adaptive GA Algorithm for Reactive Power Optimization Problem

6. SIMULATION RESULTS

The proposed GA , AGA & VS based RPO problem has been tested on standard IEEE 57, 191 (practical) bus test systems.

V_{min} - 0.95, V_{max} - 1.05, T_{min} - 0.9, T_{max} - 1.1,
P_C - 0.83 P_m - 0.018 k_1 - 0.85 k_2 - 0.5 k_3 - 1.0 k_4 - 0.04.

For IEEE 57-Bus

NG = 7, NB = 57, NTR = 17 NQ = 5

Table 1. Optimum Reactive Power schedule values obtained For IEEE 57-bus system

	GA	AGA	VS
No. of iteration	125	100	95
Population size	24	24	24
Time (sec.)	22.7	18.9	16.82
Loss (MW)	26.7890	25.0012	24.6815

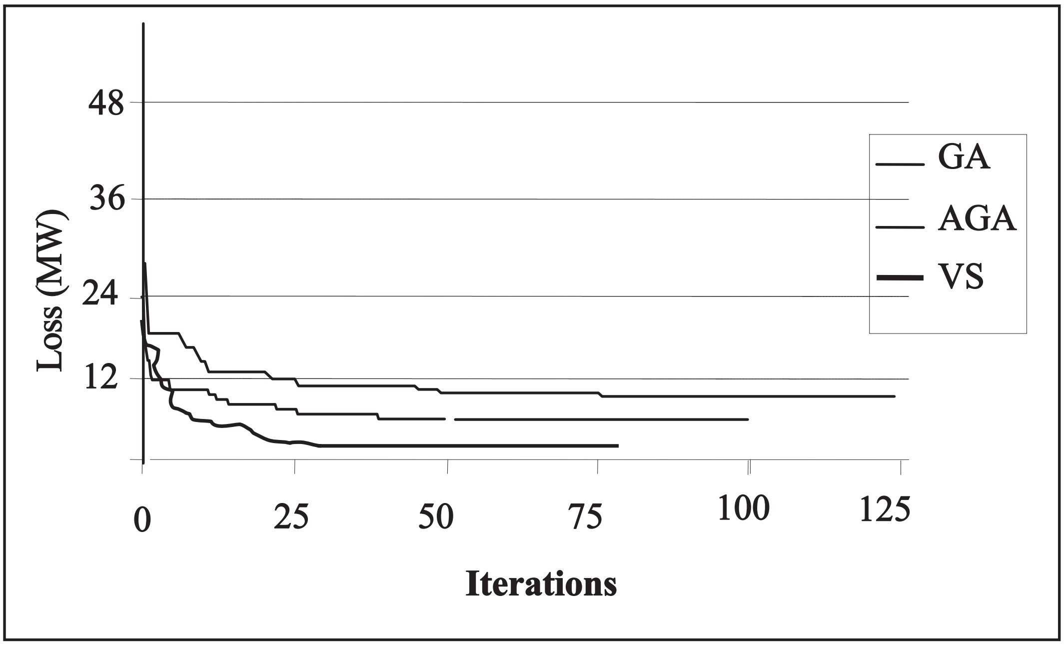

Figure 8. Convergence characteristics of IEEE 57-bus system

For Practical 191-Bus

NG = 20, NL = 200, NB = 199 NTR = 55

Table 2. Optimum Reactive Power schedule values obtained for practical 191 utility (Indian) systems.

	GA	AGA	VS
No. of iteration	149	125	121
Population size	24	24	24
Time (sec.)	59.7	45.7	36.010
Loss (MW)	149.772	149.001	138.532

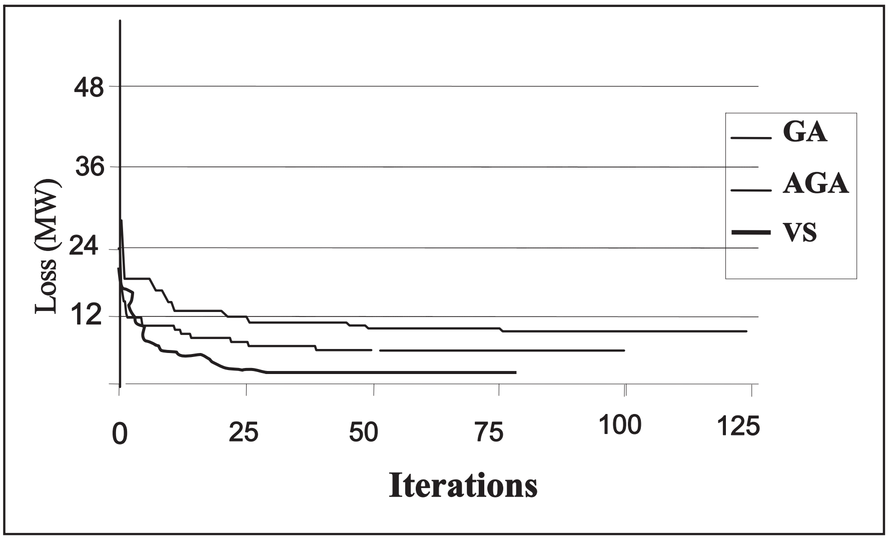

Figure 9. Convergence characteristics of practical 191 utility system

V_{min} - 0.95, V_{max} - 1.05, T_{min} - 0.9, T_{max} - 1.1, sus_{max} - 0.15, sus_{min} - 0.0

Table 3. Optimal Control values of Standard IEEE 57-bus system

VG1	1.05
VG2	1.03
VG3	1.04
VG4	1.03
VG5	1.03
VG6	1.02
VG7	1.02

T1	1.05
T2	0.93
T3	0.92
T4	0.93
T5	0.93
T6	0.90
T7	0.92
T8	0.91
T9	0.93
T10	0.91

T11	0.99
T12	0.94
T13	0.90
T14	0.93
T15	0.94
T16	0.93
T17	0.97

Q1	**Q2**	**Q3**	**Q4**	**Q5**
0.04	0.02	0.05	0.04	0.07

Table 4. Optimal Control values of Practical 191 utility (Indian) systems

VG1	1.19
VG 2	0.83
VG 3	1.07
VG 4	1.01
VG 5	1.11

VG 11	0.91
VG 12	1.02
VG 13	1.06
VG 14	0.99
VG 15	1.01

VG 6	1.19
VG 7	1.13
VG 8	1.03
VG 9	1.11
VG 10	1.06

VG 16	1.09
VG 17	0.90
VG 18	1.01
VG 19	1.14
VG 20	1.11

T1	1.02
T2	1.08
T3	1.09
T4	1.10
T5	1.03
T6	1.08
T7	1.05
T8	1.07
T9	1.06
T10	1.03
T11	0.98
T12	1.07
T13	1.09
T14	1.04
T15	1.01

T21	0.90
T22	0.98
T23	0.99
T24	0.98
T25	0.95
T26	1.00
T27	0.97
T28	0.94
T29	1.07
T30	0.93
T31	0.97
T32	0.94
T33	1.07
T34	0.93
T35	0.90

T41	0.90
T42	0.93
T43	0.97
T44	0.99
T45	0.98
T46	0.92
T47	0.98
T48	1.06
T49	0.95
T50	0.96
T51	0.99
T52	0.97
T53	1.03
T54	0.94
T55	0.91

7. CONCLUSION

In this paper, a new approach VS, GA & AGA has been demonstrated and applied to solve optimal reactive power dispatch problem. Here VS is an iterative method that runs during a maximum number of iterations to reach optimum value. AGA approach is different from the previous techniques for adapting operator probabilities as Pc and Pm , are not predefined, they are determined adaptively for each solution of the population. The values of Pc and Pm, range from 0.0 to 1.0 and 0.0 to 0.5 respectively.The problem has been formulated as a constrained optimization problem. Different objective functions have been considered to minimize real power loss, to enhance the voltage profile. The proposed approach is applied to optimal reactive power dispatch problem and tested on the IEEE 57, practical 191 bus power systems. The simulation results indicate the effectiveness and robustness of the proposed algorithms to solve optimal reactive power dispatch problem.

REFERENCES

1. Lee K.Y., Park Y.M. and Ortiz J.L. ‘ A united approach to optimal real and reactive power dispatch’ IEEE, Trans. Power System, vol.1 No.2, pp.1147 - 1153, May 1985.
2. Hong, Y.Y. Sun, D.I., Lin, S.Y., Lin, C.J.(1990), ‘ Multiyear Multi case optimal AVR planning’ IEEE, Trans. Power System, vol.5 No.4, pp.1294 – 1301.
3. Deeb, N, Shaidepour, S.M. ‘ Linear reactive power optimization in large network using the decomposition approach’, IEEE, Trans. Power System, vol.5 No.2, pp.428 - 435, May 1990.
4. Man Lovini, J.R.S, Garcaa, A.V. ‘ A heuristic method for reactive power planning, IEEE, Trans. Power System, vol.11 No.1, pp.68 - 74, Feb. 1995.
5. Granville, S ‘Optimal reactive dispatch through interior point methods’ IEEE, Trans. Power System, vol.9 No.1, pp.136 - 146, Feb. 1994.
6. Mamoh J.A, Geo, X.S. ‘ The quadratic interior point method solving power system optimization problems’, IEEE, Trans. Power System, vol.9 No.3, pp.1327 - 1336, Aug. 1994.
7. Wu, Y.C. Debs, A.S. ‘ A direct non-linear predictor corrector primal dual interior point algorithm for optimal power flows’, IEEE, Trans. Power System, vol.9 No.2, pp.876 - 883, May 1994.
8. Srinivas, M and Patnaick, L.M. ‘Adaptive probabilities of crossover and mutation in genetic algorithms’, IEEE, Trans. On System, Man and Cybernetics vol.24 No.4, pp.656 - 667, May 1994.
9. Kazarlis, S.A Bakirtzis, A.G and Petridis, V (1996), ‘ A Genetic Algorithm solution to the unit commitment problem’,

IEEE Transactions on Power Systems, Vol.11, pp.83 – 92,.

10. Orero, S.O. and Irbing, M.R. 'A genetic algorithm for generator scheduling in power systems electrical power and energy system', IEEE, Trans. Power System, vol.18 No.1, pp.19 - 26, May 1996.

11. Thiemo Krink, Jakob S. Vesterstrom and Jacques Riget, ' Particle Swarm Optimization with Spatial Particle Extension', Procs. of CEC_2002.

12. Fukuyama, Y. et al., "Practical Distribution State Estimation Using Hybrid Particle Swarm Optimization", Proc. of IEEE Power Engineering Society Winter Meeting, Columbus, 2001.

13. Eberhart R. C.and Shi, Y."Comparing Inertia Weights and Constriction Factors in Particle Swarm Optimization", Proc. of CEC 2000.

14. Fukuyama, Y. 'A Particle Swarm Optimization for Reactive Power and voltage control in Electric Power System', IEEE Trans. on Power Systems, pp. 87 – 93, 2001.

15. J. D. Schaffer and A. Morishma, "An adaptive crossover mechanismfor genetic algorithms," in Proc. Second Int. Con$ Genetic Algorithms ", 1987, pp. 3640.

16. L.Davis, "Adapting operator Probabilities in genetic algorithms," Proc.Third Int. Genetic Algorithms, 1989, pp. 61-69.

17. D. E. Goldberg, "A note on Boltzmann tournament selection for genetic algorithms and population-oriented simulated annealing,"Complex Syst.,vol. 4, pp. 445-460, 1990.

18. D. Whitley and D. Starkweather, "Genitor-I1 A distributed genetic algorithm," J.. Expt. Theor. Art$ Int., vol. 2 , pp. 189-214, 1990.

19. Saito, S. 2003: A Genetic Algorithm by Use of Virus Evolutionary Theory for Combinatorial Problems. Optimization and Optimal Control, Vol.1, World Scientific Publishing Co.; 10: 251-268.

20. Cutello V., Nicosia G. and Pavone M.2007: An Immune Algorithm with Stochastic Aging and Kullback Entropy for the Chromatic Number Problem. Journal of Combinatorial Optimization 14 (1), 9-33.

21. Kubota, N., Fukuda, T., Shimojima, K. 1996: Virus-evolutionary genetic algorithm for a self-organizing manufacturing system. Computers and Industrial Engineering 30 (4), 1015-1026.

22. Cutello V., Nicosia G., Pavone M. And Timmis J. 2007: An Immune Algorithm for Protein Structure Prediction on Lattice Models. IEEE Transaction on Evolutionary Computation 11(1), 101 117.

ANALYSIS OF ENERGY SAVING FOR EXTERNAL WALLS USING DIFFERENT ENERGY SOURCES

Subhash Mishra*
Ph.d Scholar, Department of Mechanical Engineering
Jamia Millia Islamia, New Delhi, India
E-mail: subhashmishra.2008@rediffmail.com
Contact No. 9953432708
Corresponding Author

J A Usmani
Professor
Mechanical Engineering Department,
Jamia Millia Islamia, New Delhi, India,
E-mail: jausmani@yahoo.com

ABSTRACT

The energy strategy of any country is to save energy. Energy consumption for heating has higher value in cold region of India due to buildings having no insulation and energy is saved by reducing consumption. In this paper, a systematic approach is developed for optimization of insulation material thickness. The Optimum insulation thickness, Energy saving and Payback period are calculated by using life cycle cost analysis over 10 years of the building life. Also the optimum insulation thickness of external wall for the five different fuel sources (Fuel oil, LPG, Coal, Natural gas and Electricity) and two different insulation materials (Expended Polystyrene and Glass wool) are calculated for Leh (74.83E, 34.08N), Srinagar, Jammu and Kashmir ,India. As a result, the optimum insulation thickness vary between 0.0445 and 0.1255m, Energy saving vary between 997.37 Rs/m^2 and 3031.04Rs/m^2, and Payback periods very between 1.385 and 2.018 years for different fuel sources.

Keywords: *Degree-days; Energy saving; life cycle cost analysis; optimum insulation thickness; payback period.*

1. INTRODUCTION

This paper aims to investigate the conservation of energy through building walls for five different energy sources and two different insulation materials. We know that day by day, the rate of energy consumption is gradually increasing. Due to limited energy sources and pollution from burning of fuel, we need to save energy at any cost. Mainly, the energy consumption is distributed among industrial sector, building sector, transportation and agricultural areas. Where the building sector is second larger energy consumption area. Heat loss from buildings generally occurs through external walls and roof. In this analysis, the heat loss through external wall is considered. From energy conservation point of view, the most important method of reducing heat and cooling loads of the building is achieved by applying thermal insulation to the building envelope. The annual heating and cooling requirements of buildings in cold regions can be obtained by means of the heating Degree-Days concept. The number of Degree-Days is the difference between the base temperature and the mean outdoor ambient temperature. The life cycle cost analysis (LCCA) is used to calculate the optimum insulation thickness.

To fulfill the outline of this analysis a literature review followed with scope of paper is given as follows. Turki and Zaki[1] investigated the effect of insulation and energy storing layers upon the cooling load. A mathematical model to study the thermal response of multilayer building components is presented. Bolatturk[2] calculated the optimum insulation thicknesses, energy savings and payback periods. The annual heating and cooling requirements of building in different climates zones were obtained by means of the heating degree-days concept.Durmayaz et al.[3] estimated the heating energy requirement in building based on degree-hours method on human comfort level. For an illustration we have considered the city of Istanbul in Turkey and presents a detailed account for practical energy requirements and fuel consumption calculations. Hasan[4] optimized the insulation thickness for wall by using the life cycle cost analysis. In his study, transmission load was estimated by using the degree-days concept. Generalized charts for selecting the optimum insulation thickness as a function of degree days and wall thermal resistance are prepared. Farhanieh and Sattari[5] studied the effects of insulation on the energy saving in Iranian building. For this purpose, an integrative modeling is used for simulation of the energy consumption in buildings.Bakos[6] evaluated the energy saving by comparing the energy consumption (in KWH) for space heating before and also after the application of thermal insulation in the structure envelope. A performance comparison is done in cost and energy saving is studies.Weir and Muneer[7] studied embodied energy of raw materials, manufacturing and associated CO_2,SO_2 and No_x contents have been estimated for a double- glazed, timber framed window containing an inert gas filled cavity.Sarak and Satman[8] determined the natural gas consumption by residential heating in Turkey by heating degree-day method. The authors also present a case study for the calculations of residential heating natural gas consumption in Turkey in terms of degree-days. Sofrata and Salmeen[9] developed a consistent and more general mathematical model for optimum insulation thickness. He also introduced a program flow chart to select the best insulation thickness. In this study, the life-cycle cost analysis (LCCA) is used to calculate the costs of heating over the life time. Ozkahraman and Bolatturk[10] calculated the amount of energy conserved by using porous tuff stone in external walls of buildings. Due to porous structure, tuff stone is a good heat insulator. So considerable energy savings can be achieved by using tuff stone for facing buildings in cold climate zone. Mohammed and Khawaja[11] determined the optimum thickness of insulation for some insulating materials used in order to reduce the rate of heat flow to the buildings in hot countries. Important factor that affects the optimum thickness of insulation is the solar radiation energy flowing into the house. In this paper, a solar radiation calculation is done.Sallal[12] explored the effect of different climates on the decision of selecting the insulation type and thickness. It shows the importance of using the life-cycle cost model on the decision of adding more insulation levels and knowing when to stop.Comakli and Yuksel[13] investigated the optimum insulation thickness for the three coldest cities of Turkey by using the degree -days values. Their study was based on the life cycle cost analysis.Papakostas and kyriakis[14] determined the heating and cooling degree-hours for the two main cities in Greece, namely Athens and Thessaloniki ,using hourly dry bulb temperature. Lollint et al.[15] demonstrated the significant economic advantages come out from high-performance building envelope. In this paper, economic analysis and evaluation of the envelope components based on the optimization of the insulating materials thickness.Ozel and Pihtili[16] obtained the optimum location and distribution of insulation for all wall orientations in both summer and winter by consideration of maximum time lag and minimum decrement factor. The investigation was carried out by using an implicit finite difference method for multilayer walls during typical summer and winter days in Elazig, Turkey. Ozel and Pihtili[17]developed a numerical model based on implicit finite difference scheme was applied for 12 different roof configurations during typical winter and summer days.Mohsen and Akash[18] evaluated the energy conservation in residential buildings of Jordan. This paper is intended to provide some insights into the general state of energy consumption in the residential sector and its trends in Jordan. Daouas et al.[19] determined the optimum insulation thickness under steady periodic conditions. Estimated loads are used as inputs to a life-cycle cost analysis in order to determine the optimum thickness of the insulation layer. The optimum insulation thickness is calculated, based on the estimated cooling transmission loads.Sisman et al.[20] determined the optimum insulation thickness for different degree-days (DD) regions of Turkey (Izmir, Bursa, Eskisehir & Erzurum) for a lifetime of N years. In this study, the optimum insulation thickness for a given building envelope was determined by considering the thermal conductivity and price of the insulation material, average temperature in the region, fuel price for the heating and the present worth factor (PWF). Buyukalaca et al.[21] studied the heating and cooling degree-days for Turkey by using long-term recent measured data. The monthly cooling and heating requirements of specific building in different locations can be estimated by means of the degree-days concept.Dombayci[22]investigated the environment impact of optimum insulation thickness. In the calculations, coal was used as the fuel source and the Expanded Polystyrene(EPS) as the insulation material.Al-Sanea et al.[23] investigated the effect of the average electricity tarrif on the optimum insulation thickness in building walls by using a dynamic heat-transfer model and an economic model based on the present-worth method.Mahlia et al.[24] developed correlation between thermal conductivity and the thickness of selected insulation materials for building wall.Lu et al.[25] developed a new analytical method, which provides close-formed solutions for both transient indoor and envelope temperature changes in building. Time-dependent boundary temperature is presented as Fourier Series.

2. DESIGN OF EXTERNAL WALL STRUCTURE

Brick, varieties of concrete (light weight and reinforced) and Stone are the common material used for the construction of external walls. For minimizing the heat loss the insulation can be placed inside, to the outside or in between (sandwich wall). In this analysis the insulation is placed outside. In cold region of India, the external wall insulation applications are generally made by the sandwiches wall types. The structure of external wall is made by 3 cm internal plaster, wall materials (Brick) , insulation material and 2 cm external plaster. In this paper, the calculations were carried out for Brick (20 cm) wall. The surfaces of the wall are insulated on the external side and plastered on both sides is as shown in Fig. 1.

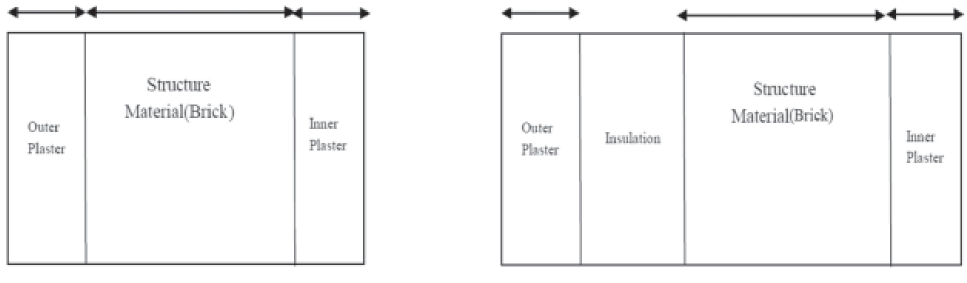

Fig.1 Cross Sectional View Of External Walls : (a) Uninsulated Wall (b) Insulated Wall

2.1 ANNUL FUEL CONSUMPTION CALCULATION FOR EXTERNAL WALLS Heat loss from buildings occurs through surface of external wall, window, ceiling and air infiltration. In this analysis, heating loss is observed only on the external wall surface.

The heat loss per unit area of external wall is given by

$Q= U (T_b – T_a)$ (1)

Where U is the overall heat transfer coefficient. T_b is the base temperature and T_a is mean air temperature.

Annual heating loss per unit area from external wall in the terms of degree-days is given by

$Q_A = 86400\ DD\ U$ (2)

Where DD is the Degree- Days. The annual energy requirement is given by

$E_A = 86400\ DD/ (R_{tw}+ x/k)\eta_s$ (3)

Where η_s is the efficiency of space heating system.

And the annual fuel consumptions is given as

$Mfa= 86400\ DD/ (R_{tw}+ x/k)\ LHV.\ \eta_s$ (4)

Where LHV is lower heating value of fuel.

2.2 ENERGY SAVING AND OPTIMUM INSULAION THICKNESS The life-cycle cost analysis (LCCA) is used in this analysis that determines the cost analysis of a system. The total cost of heating over the life time of the insulation material which was taken as 10 years. Total heating cost is indicated together with life cycle (N) and presents worth factor (PWF). PWF can be calculated by using inflation rate g and interest rate i. Inflation and the interest rate are taken as 10 % and 8 % respectively.

The interest rate adapted for inflation rate r is given by

If i>g then,

$r = (i – g)/ (1+ g)$

If i<g then,

$r = (g – i)/ (1+ i)$

and

$PWF = (1 + r)^N – 1 / r (1 + r)^N$

If i = g then,

$PWF = N /(1+ i)$ (5)

The total heating cost of the insulated building is given as

$C_t = C_A\ PWF + C_i\ x$ (6)

The optimum insulation thickness is obtained by minimizing total heating cost of insulation building (C_t). So the derivative of C_t with respect to x is taken and equal to zero from which the optimum insulation thickness X_{opt} obtained.

$X_{opt} = 293.94(DD\ C_t\ PWF\ K / HU.\ C_i\eta_s)\ 0.5 – K\ R_{tw}$ (7)

Pay-Back Period(PP) is calculated by solving the equation (8)

$C_{ins}/ A_s = (1 + r)^{PP} -1 / r (1 + r)^{PP}$ (8)

Where C_{ins}/ As is the simple Pay-Back Period. Energy saving obtained during the lifetime of insulation material can be calculated as follow:

$E_s = C_{to} - C_{ins}$ (9)

3. RESULTS

Insulation application is one of the most important methods to conserve energy in buildings. So choosing the appropriate insulation material and determining the optimum insulation thickness is very important for energy saving. The optimum thickness of insulation material (Expended polystyrene &Glass wool)is calculated with a outside insulation wall types building. The optimum insulation thickness for different fuel types is given in table 2. Optimum insulation thickness varies between 0.08 m and 0.1255 m for glass wool and for Expended polystyrene it varies between 0.044 m and 0.072 m depending on the type of fuel used for heating.

All the unit's prices, heating values and efficiencies of heating systems for different fuel that is used in the analysis are given in tables 1.

Table 1: Properties of fuel and its efficiency

Fuel Type	Fuel Oil	LPG	Coal	Natural Gas	Electricity
Cost	30 Rs/kg	70Rs/kg	18Rs/kg	26Rs/m3	3.50 Rs/kwh
Heating Value	40.59x106J/kg	46.04x106J/kg	29.29x106 J/kg	34.53x106J/m3	3.6x 10 6J/kwh
System Efficiency (%)	80	90	65	93	99

Table 2: Optimum insulation- thickness for different fuel types

Fuel types	Optimum Insulation Thickness (m)	
	Expended Polystyrene(EPS)	Glass Wool(GW)
Fuel Oil	0.0488	0.087
LPG	0.07268	0.1255
Coal	0.04965	0.0883
Natural Gas	0.0445	0.08008
Electricity	0.0509	0.09045

Table 3 shows the payback period and energy saving over 10 years for insulated building in Leh for different fuel types.

Table 3:Payback period and Energy saving for different type of fuel in India

Fuel Type	Payback Period (Years)		Energy Saving (Rs/m2)	
	EPS	GW	EPS	GW
Fuel Oil	1.914	1.57	1200.074	1457.06
LPG	1.582	1.385	2654.8715	3031.04
Coal	1.89	1.56	1238.9452	1499.866
Natural Gas	2.018	1.6332	997.37	1232.7584
Electricity	1.87	1.55	1305.23	1572.71

The optimum insulation thicknesses for different types of fuel specified in table 2 were calculated by using equation (7) and the values of the parameter are shown in table 4.

Table 4: Parameters used in the calculation of insulation- thickness

Parameter	Value
Degree day, ^{o}c days Interest Rate Inflation Rate PWF Lifetime R_{wt}	1863,Leh(74.831 E, 34.08 N), Srinagar, J.K,INDIA. 8% 10% 9.05 10 0.5858 m^2k/w
Insulation- Glass Wool(GW)	
Cost Conductivity	4279 Rs/m^3 0.038 w/m k
Insulation-Expended Polystyrene(EPS)	
Cost Conductivity	9421 Rs/m^3 0.032 w/m k

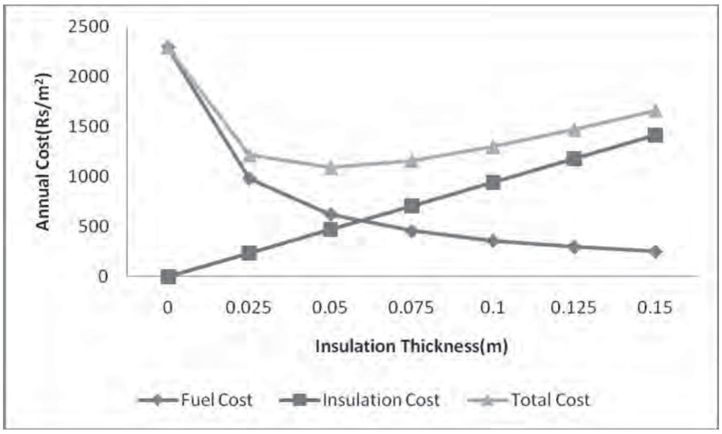

Fig. 2(a) Variation of annual cost with insulation- thickness for EPS insulation and fuel oil is selected as heating source

Fig.2 (a&b) Shows variation of total cost, fuel and insulation cost versus the insulation thickness for expended polystyrene (EPS) and Glass wool (Gw) insulation material. If the insulation thickness is increased, the fuel cost and heat load decreases but the total cost is increased. Total cost is the sum of insulation and fuel cost. Total cost decreases up to a certain value of the insulation thickness, beyond this value the total cost is increased. It means total cost is minimum at optimum insulation thickness. The results show that optimum insulation thickness is 0.0488m for EPS white it is 0.087m for Glass wool(GW) for brick wall.

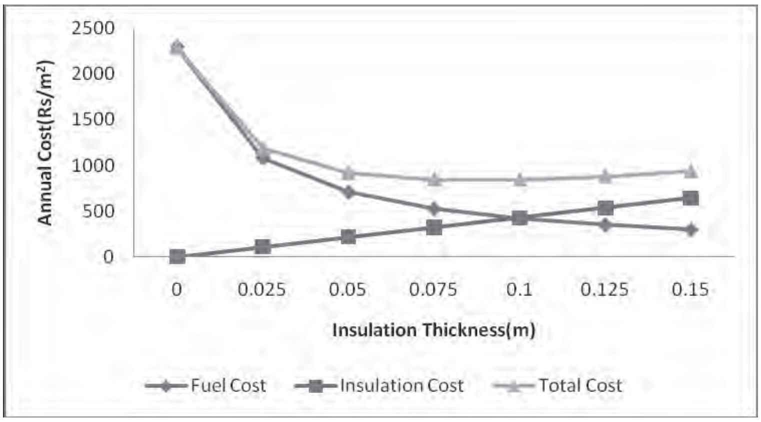

Fig. 2(b) Variation of annual cost with insulation- thickness for GW insulation and fuel oil is selected as heating source

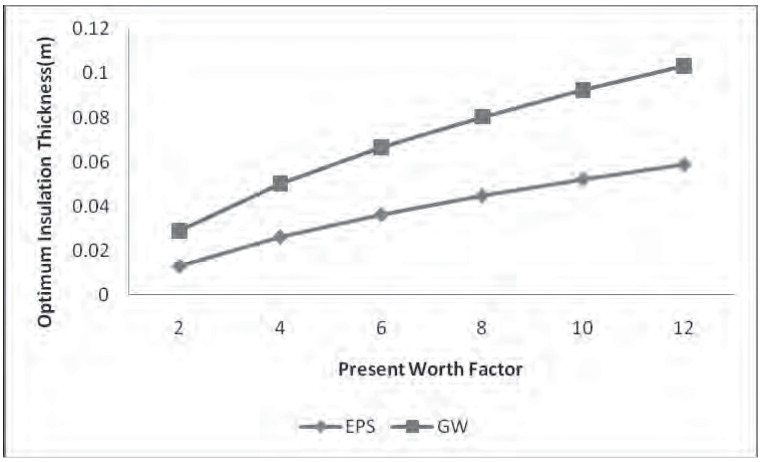

Fig.3 Effect of present worth factor on optimum insulation thickness for fuel oil heating source.

The effect of PWF on optimum insulation thickness for fuel oil heating source is shown in Fig.3 for two types of insulation materials. When the value of PWF is increased, then optimum insulation thickness is also increased. It means that the inflation and interest rate have also affect on optimum insulation thickness. From Fig.3, it can be concluded that for a given value of PWF, building insulated with GW requires more insulation thickness. EPS insulation requires less insulation thickness as compared to GW insulation for a given value of PWF. Therefore it can be concluded that EPS insulation is more effective as compared to GW insulation .

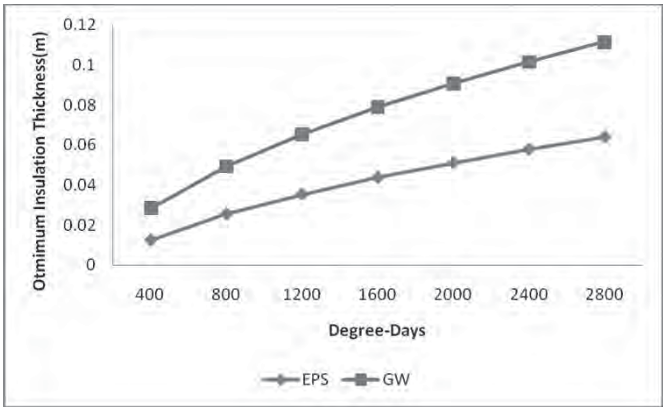

Fig.4 Optimum insulation thickness versus Degree-Days value.

Fig.4 shows the effect of Degree-Days on optimum insulation thickness for Fuel oil heating source. The optimum insulation- thickness increases for increasing Degree-Days. Colder climates have higher Degree-Days values. So it requires more insulation thickness. Leh has less Degree-Days values (1863). It means it requires less insulation thickness.

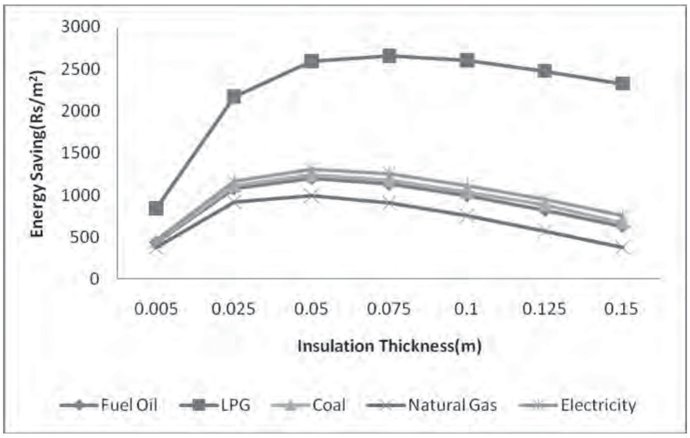

Fig.5 Effects of insulation- thickness on annual energy saving for different energy types.

Fig.5 shows the effects of different fuel types on energy saving. When insulation thickness is increased, then energy saving is gradually increased and reaches its maximum value at optimum insulation thickness, and after that energy saving decreases. Lowest value of energy saving is obtained for Natural gas fuel,and highest value of energy saving is obtained for LPG energy source. As shown in Fig.5, the application of insulation thickness increases the energy saving up to optimum insulation thickness. Energy saving is more important for the expensive fuel and mainly depended upon the cost of fuel and climatic condition. Higher value of energy saving is obtained as 2654.33 Rs/m^2, when LPG is taken as fuel source and EPS as the insulation material.

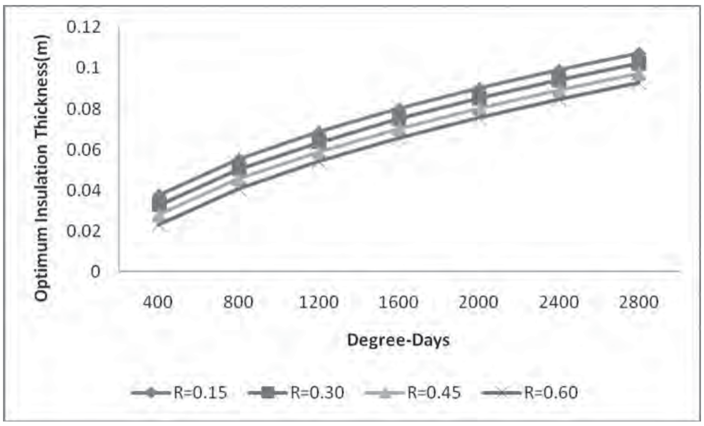

Fig.6 Effect of Degree-Days and wall thermal resistance on optimum insulation thickness for LPG fuel source- EPS insulation

Fig.6 shows the effect of Degree-Days and wall thermal resistance on optimum insulation thickness. Colder climates having higher Degree-Days require larger insulation thickness. From Fig.6, it can be concluded that for a given value of Degree-Days, building having lower thermal resistance require higher insulation thickness.

4. CONCLUSION

The optimum insulation- thickness, Energy Savings and Payback Periods are calculated for the different energy types and two different insulation materials. The optimum result is obtained, when fuel oil as an energy sources and Expended polystyrene as the insulating material is used. At optimum insulation thickness, the energy saving is maximum and total annual cost of heating is minimum. As seen from Fig. 2(a and b), choosing a thickness value apart from optimum thickness will increase the total cost. So according to economic view point, optimum insulation thickness must be applied to the building. From Fig. 4, it is observed that the optimum insulation- thickness increases for increasing Degree-Days. For finding the optimum insulation thickness, life cycle cost analysis is used. As a result, the Optimum insulation thickness vary between 0.0445 and 0.1255m, Energy saving vary between 997.37 Rs/m^2 and 3031.04 Rs/m^2 , and Payback Periods vary between 1.385 and 2.018 years for different fuel sources.

Scopes of future work in above field are as follows:

1. To compare the energy saving and optimum insulation thickness for different Wall materials.
2. To develop a method that would find out the most economical insulation material used in the wall construction.

REFERENCES

1. Turki, A. Al.;&ZakiG.M. Cooling load response for building walls comprising heat storing and thermal insulating layers.Journal of Energy Conversion Management, Volume. 32, 1991, p.235-247.
2. Bolatturk,A. Determination of optimum insulation thickness for building walls with respect to various fuels and climate zones in Turkey. Journal of Applied Thermal Engineering, Volume. 26, 2006, p. 1301- 1309.
3. Durmayaz,A.;Kadioglu,M. &Sen,Z. An application of the degree-hours method to estimate the residential heating energy requirement and fuel consumption in Istanbul. Journal of Energy, Volume. 25, 2000, p.1245-1256.
4. Hasan,A.Optimizing insulation thickness for buildings using life cycle cost. Journal of Applied Energy, Volume.63, 1999, p.115-124.
5. Farhanieh,B. &Sattari,S. Simulation of energy saving in Iranian buildings using integrative modeling for insulation. Journal of Renewable Energy, Volume. 31, 2006,p.417-425.
6. Bakos,G.C. Insulation protection studies for energy saving in residential and tertiary sector.Journal of Energy and Buildings, Volume. 31, 2000, p. 251-259.
7. Weir,G.&Muneer,T. Energy and environmental impact analysis of double-glazed windows. Journal of Energy Conservation Management,Volume. 39, 1998, p.243-256.
8. Sarak,H.&Satman,A.The degree-day method to estimate the residential heating natural gas consumption in Turkey; a case study. Journal of Energy,Volume. 28, 2003, p.929-939.
9. Sofrata,H. &Salmeen,B.Selection of thermal insulation thickness.Fourth Saudi Engineering conference, Volume. 5, 1995, p.389-399.
10. Ozkahraman, H.T.& Bolatturk, A.The use of tuff stone cladding in buildings for energy conservation. Journal of construction and Building Materials,Volume. 20, 2006, p.435-440.
11. Mohammed,J.&Khawaja,A.L.Determination and selecting the optimum thickness of insulation for buildings in hot countries by accounting for solar radiation.Journal of Applied Thermal Engineering, Volume. 24, 2004, p.2601-2610.
12. Sallal,K.A. Comparison between Polystyrene and Fiberglass roof insulation in warm and cold climates. Journal of Renewable Energy, Volume. 28, 2003, p.603-611.
13. Comakli, K.& Yuksel, B. Optimum insulation thickness of external walls for energy saving. Journal of Applied Thermal Engineering, Volume. 23, 2003, p.473-479.
14. Papakostas,K. &kyriakis,N. Heating and cooling degree-hours for Athens and Thessaloniki, Greece.Journal of Renewable Energy, Volume. 30, 2005, p. 1873-1880.
15. Lollint; Barozzi; Fasano; Meroni&Zinzi. Optimization of opaque components of the building envelope, energy economic and environmental issues. Journal of Building and Environment, Volume. 41, 2006, p.1001-1013.
16. Ozel,M.&Pihtili,K. Optimum location and distribution of insulation layers on building walls with various orientations. Journal of Building and Environment, Volume. 42, 2007, p.3051-3059.
17. Ozel,M.&Pihtili,K. Investigation of the most suitable location of insulation applying on building roof from maximum load levelling point of view. Journal of Building and Environment, Volume. 42, 2007, p. 2360-2368
18. Mohsen,M.S&Akash B.A. Some prospects of energy savings in buildings. Journal of Energy Conversion and

Management,Volume. 42, 2001, p.1307-1315.

19. Daouas,N.;Hassen,Z. &Aissia H.B. Analytical periodic solution for the study of thermal performance and optimum insulation thickness of building walls in Tunisia. Journal of Applied Thermal Engineering, Volume. 30, 2010,p.319-326.

20. Sisman,N.;Kahya,E;Aras, N. & Aras, H.Determination of optimum insulation thickness of the external walls and roof (ceiling) for Turkey's different degree-day regions.Journal of Energy Policy, Volume. 35, 2007, p.5151-5155.

21. Buyukalaca, O.,Bulut,H., &Yilmaz,T.Analysis of variable- base heating and cooling degree-day for Turkey.Journal of Applied Energy, Volume.69,2001,p. 269-283.

22. Dombayci,O.A. The environmental impact of optimum insulation thickness for external walls of buildings.Journal of Building and Environment, Volume. 42, 2007, p.3855-3859.

23. Al-Sanea, S.A.,Zedan,M.F,Al-Ajlan,S.A.Effect of electricity tarrif on the optimum insulation- thickness in building walls as determined by a dynamic heat -transfer model.Journal of Applied Energy, Volume. 52, 2005, p.313-330

24. Mahlia,T.M.I, ;.Taufi,B.N., Ismail, &Masjuki, H.H.Correlation between thermal conductivity and the thickness of selected insulation materials for building wall. Journal of Energy and Buildings, Volume. 39, 2007, p.182-187.

25. Lu, X.;Lu,T., &Viljanen, M.A new analytical method to simulate heat transfer process in buildings.Journal of Applied Thermal Engineering, Volume. 26, 2006, p.1901-1909.

INFLUENCE OF CEMENT CONTENT AND CURING PERIOD ON THE GEOTECHNICAL PROPERTIES OF CEMENT-MODIFIED SOIL

Binod Tiwari, PhD., PE*
Associate Professor, Civil and Environmental Engineering Department,
California State University, Fullerton, 800 N State College Blvd.,
E-419, Fullerton, CA 92831, USA
E-mail: btiwari@fullerton.edu
Corresponding author

Kaushlendra Lal Das, EIT
Former graduate student, Civil and Environmental Engineering Department,
California State university, Fullerton, 800 N State College Blvd.,
E-419, Fullerton, CA 92831, USA
E-mail: kkld@csu.fullerton.edu

ABSTRACT

In general weak soils, especially clays are not suitable for building civil engineering structures to be supported by those soils. These soils are often modified with cement to increase the soil bearing capacity and strength so that foundations can be designed cheaply for structures to be supported by those weak clays. Studies pertinent to the appropriate curing time for such soils have not been in sufficient detail. This study mainly focuses on the variation in geotechnical properties of weak clays with the addition of different amount of cement and also different time of curing. The study result shows that 2% cement gives the highest dry density and compressive strength for cement-modified clays if it is not cured. Likewise, 7 days curing period is sufficient to gain enough compressive strength in cement-modified clays.

Keywords- : *Clay, cement-modification, liquid limit, unconfined compression strength, curing, maximum dry density.*

1. INTRODUCTION

A heavy structure needs a decent amount of bearing capacity in the soil for its foundation. Weak soils do not possess sufficient strength to provide appropriate bearing capacity for those structures. Such soils are generally mixed with different admixtures to gain their shear strength and stiffness. Some of those admixtures are – cement, lime, kiln dusts, etc. Loose soil becomes slightly stiff immediately after using small amount of cement. Curing those cement mixed soils for some days increases the strength and stiffness of soil. The end result is similar to that in concrete and the gain in strength depends on the ratios of the soil and the cement. Field and laboratory tests show that changes in the physical properties of cement modified soil arenon-reversible for several decades. However, after many years of weathering, it may come to the original state. Although the effect of soil modification is well known to geotechnical community, it is still unknown that what type of clay mineral can be best modified using cement, lime or fly ash.In the United States, first time soil mixing was used by Intrusion-Prepakt, Inc. of Cleveland Ohio in the 1950's, where as in the late 1960's and early 1970's the Swedes used mixed-in-place lime stabilization process. Japanese and Scandinavians continue to refine the soil mixing technology in various foundation applications since 1970's.Baghdadi et al. (1995)[1]and Miller andZaman (2000)[2] did studies pertinent to the effect of Portland cement and Cement Kiln Dust (CKD) on engineering properties of soils. Atterberg limits, standard Proctor and Unconfined compressive tests were measured by adding different amount Portland cement and CKD by weight.From the lab experiment, they showed that the cement or CKD mixture increases the optimum moisture content, but decreases the maximum dry unit weight. They also found that unconfined compressive strength and modulus of elasticity of CKD treated soils were lower than that achieved by Portland cement treatment. They reported that - optimum water content (%) for the CKD treated soil is more than Cement treated soil; maximum dry unit weight of cement treated soil is greater than CKD treated soil; unconfined compressive strength of cement treated soil is muchlarger than the CKD treated soil; soil treated with 10% cement by weight gives the maximum unconfined compressive strength and modulus of elasticity; soil treated with 20% CKD by weight gives maximum unconfined compressive strength and modulus of elasticity; modulus of elasticity of the cement treated soil is much higher than CKD treated soil. Miller and Zaman (2000)[2], with experimental studies on physical models with 3m width, 10m length, and 230 slope, showed that higher the CKD content, less the soil erosion. soil slope models.

There are several factors that governs the hardening characteristics of the cement treated soil. Some of the predominant factors that affect the strength of cement treated soil are - amount and type of cement, curing time, soil characteristics etc.

This study is mainly focused on how the compressive strength and other geotechnical properties of different types of soil change with the addition of cement and with curing.

2. MATERIALS AND METHODS

2.1 STUDY MATERIALS: Four types of soils were used in this study – a) mixture of 30% montmorillonite and 70% quartz (referred as sample 1 from now onwards), b) mixture of 20% montmorillonite and 80% quartz (referred as sample 2 from now onwards), and c) mixture of 50% kaolinite and 50% quartz (referred as sample 3 from now onwards). Montmorillonite, kaolinite and quartz used for this study were obtained from Wards's Natural, USA. Ordinary Portland cement was used as the modifying agent. Distilled water was used for all tests.

2.2 SOIL TESTING METHODS: Liquid Limit and Plastic limit were measured for untreated sample as well as the samples treated with different percentage of cement ranging from 2% to 10% for all of the tested soil samples.ASTM D4318 (2008)[3] was strictly followed while measuring the liquid limit, plastic limit and calculating the plasticity index of the soil sample (Figure 1). Sample 1 was used to measure maximum dry density and optimum moisture content for all cement contents ranging from 2% through 10%. Harvard miniature compaction device (Figure 2) was used to measure the compaction parameters. The device had 1.4 inch internal diameter, 2.8 inch height and 20 pound capacity spring hammer. Total number of tamping required to produce the energy equivalent to the Standard Proctor Compaction test was difficult to calculate. Therefore, two compaction tests were performed using the Standard Proctor Device and Miniature Compaction tests were performed for different number of tamping for 5 different layers of soil. The number of tamping that gave closest maximum dry density was utilized for rest of the tests. Compressive and shear strength of compacted soil sample was measured with unconfined compression device (Figure 3). ASTM D 2166 (2008)[4] was strictly followed to measure the unconfined compression strength. The samples were sheared at the shearing rate of 0.5%/minute. Unconfined compaction tests were performed on the soil samples after – a) no curing, b) 7 days of curing and c) 14 days of curing. The data obtained from different soil tests were compiled to evaluate the change in geotechnical properties with the addition of cement.

Figure 1:Left – Liquid limit test method and right – plastic limit test method

Figure 2: Harvard Miniature Compaction device used for this study

Figure 3: Unconfined Compression device used for this study

3. SOIL TEST RESULT AND ANALYSIS

3.1 ATTERBERG LIMIT: Shown in Table 1 are the variations in Atterberg limit with the addition of cement. Although there was no drastic change in Atterberg limit and activity, there was an increase in Atterberg limits with the addition of cement upto 2%. After that, Atterberg limit decreased or remained constant. This shows that cement content doesn't have significant influence in the Atterberg limits and activities of soil.

Table 1: ATTERBERG LIMITS OF TESTED SAMPLES

SAMPLE	Cement (%)	Liquid Limit	Plastic Limit	Activity	Plasticity Index
	0	185.3	19.4	6.1	165.9
	2	209.7	28.2	6.7	181.5
1	6	193.7	24.8	6.2	168.9
	8	205.9	21	6.8	184.9
	10	176.1	20	6.0	156.1
	0	129.9	20.8	6.0	109.1
	2	149.8	24.4	6.9	125.4
2	6	100.8	24.5	4.2	76.3
	8	98.1	22.9	4.1	75.2
	10	86.4	19.1	3.7	67.3
	0	43.8	19.4	0.57	24.4
	2	49	26.5	0.52	22.5
3	6	45.1	25.8	0.45	19.3
	8	43.4	27.6	0.37	15.8
	10	45.2	21.9	0.54	23.3

3.2 COMPACTION: Shown in Figure 4 is the Compaction Curve for sample no. 1. ZAV is the zero air-void line. The maximum dry unit weight was 109 pounds per cubic ft (pcf) at the optimum moisture content of 17.4%. These parameters were measured for all soil samples and presented in Table 2. Data presented in Table 2 are the data immediately after the compaction. The data shows that the maximum dry unit weight decreases as the cement content increases when the cement content was higher than

6%. This shows that adding cement doesn't always increase the dry unit weight.

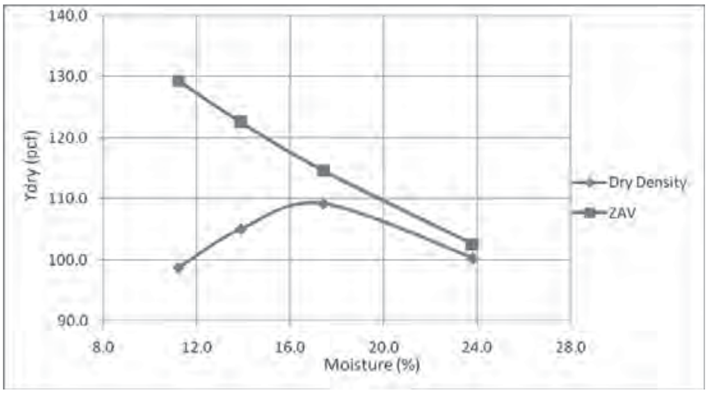

Figure 4: Compaction characteristics of sample 1 without cement treatment

Table 2: VALUES OF MAXIMUM UNCONFINED COMPRESSIVE STRENGTH, MAXIMUM DRY UNIT WEIGHT AND CORRESPONDING MOISTURE CONTENTS

Cement %	Max. unconfined compressive strength (psi)	Corresponding Moisture Content (%)	Max. dry unit weight(pcf)	Corresponding Moisture Content (%)
0	55	17.4	109.15	17.4
2	106.9	14.05	110.5	18.07
6	100.91	13.54	109.5	16.98
8	53.897	16.45	103.48	21.5
10	52.34	18.17	97.73	22.48

Psi: pounds/square inch

3.3 COMPRESSIVE STRENGTH: The stress-strain characteristics of the compacted sample 1 are presented in Figure 5. Y-axis is unconfined compressive stress and x-axis is axial strain. The data shows that maximum unconfined compression strength was obtained at the moisture content of 17.4%, which is same for the maximum dry unit weight. The values of maximum compressive strength of soil added with different percentage of cement are presented in Table 2. As observed in the case of dry unit weight, unconfined compressive strength increased with an increase in cement up to 2% cement. This doesn't justify the importance of soil-cement stabilization.

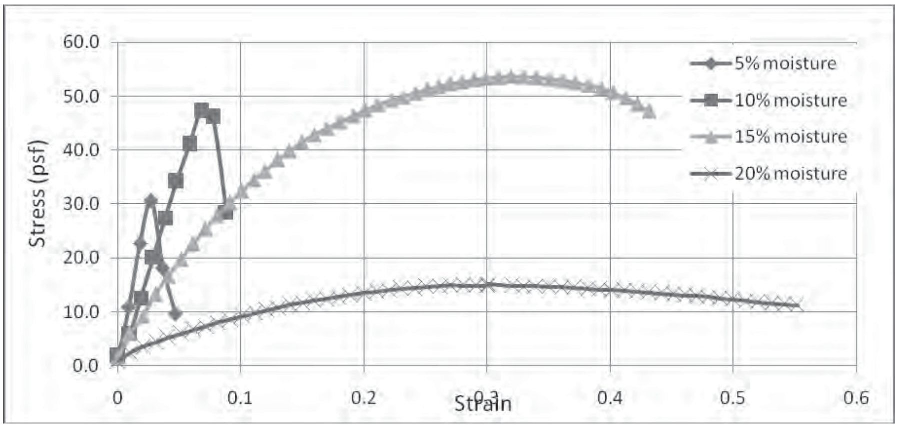

Figure 5: Stress-strain characteristics of sample 1 without cement treatment

To evaluate the effect of curing on the compressive strength of soil, soil samples 1 was mixed with 10% cement but at different moisture contents. Unconfined compressive strengths were measured immediately after compaction, after 7 days of temperature controlled curing, and 14 days of temperature controlled curing. The results of the unconfined compression test are presented in Table 3. The moisture content that yielded maximum compressive strength without curing was 28.2%. Compressive strength of that soil increased significantly after 14 days of curing. For samples compacted at moisture contents other than the optimum moisture content, the unconfined compressive strength increased by 4 to 5 times after 7 days of curing, but did not change significantly after 7 days of curing. This shows that 7 day curing is sufficient for majority of soil modification projects.

Table 3: MAXIMUM UNCONFINED COMPRESSIVE STRENGTH (IN PSI) AT DIFFERENT MOISTURE CONTENTS – RIGHT AFTER COMPACTION, AT 7 DAYS OF CURING, AND AT 14 DAYS OF CURING

Molding Moisture Content (%)	NO CURING	7 Days of Curing	14 Days of Curing
10.8	23.1	157.1	151.5
13.1	26.7	272.0	196.5
15.1	38.9	258.4	223.8
24.0	60.6	508.8	357.0
28.2	60.7	245.1	435.2
32.5	20.0	205.5	219.4

4. CONCLUSION

Atterberg limit tests, compaction test and unconfined compression tests were conducted in different soil samples to evaluate the improvement of soil unit weight and compressive strength with the addition of cement. The test results and the analysis show that the dry unit weight and compressive strength doesn't change for cement content higher than 2%. However, if the soil sample is cured for more than 7 days at controlled temperature, the unconfined compressive strength increases by 4 to 5 times. This increase in compressive strength can save the construction cost significantly.

ACKNOWLEDGEMENT

The authors would like to thank California State University Fullerton, Office of the Provost for providing research assistantship to the second co-author for this study. We would also like to appreciate the support provided by the IRA Funding at the California State University, Fullerton to purchase research materials.

REFERENCES

1. Baghdadi, Z.A., Fatani, M.N., and Sabban, N. A. 1995. Soil Modification by Cement Kiln Dust. *Journal of Materials in Civil Engineering*, 7(4), 218-222.
2. Miller, G.A., and Zaman. M. 2000.Field and Laboratory Evaluation of Cement Kiln Dust as a Soil Stabilizer. *Transportation Research Boardof the National Academies,*Washington DC, 25-32.
3. ASTM D4318. 2008.Standard Test Method for Liquid Limit, Plastic Limit, and Plasticity Index of Soils. *ASTMInternationalAnnual Book of Standards.*West Conshohocken, PA.
4. ASTM D 2166. 2008.Standard Test Method for Unconfined Compressive Strength of Cohesive Soil. *ASTMInternationalAnnual Book of Standards.*West Conshohocken, PA.

PYTHOCRYPT- A CRYPTO SYSTEM FOR MEDICAL IMAGES

Harsha S*
Assistant Professor, CS&E,
Vidya Vikas Institute of Engineering & Technology (VVIET),
Mysore, India.
E-mail: harshahassan@gmail.com
Corresponding author

N Bhaskar
Professor & Head
Mathtea, Vidyavardhaka College of Engineering (VVCE),
Mysore, India.
E-mail: bhasiyer@gmail.com

Chandan CM
Dept. of Graphics and Animation
CIST, University of Mysore
Mysore, India.
E-mail: catchchandan@gmail.com

ABSTRACT

Providing security for Medical data such as X-Ray, ECG, MRI, etc. has gained immense importance due to their sensitive nature. The penetration of Internet in all walks of life has made data sharing a necessity amongst hospital networks all over the globe which are in need of security system for their online data exchange. The usage of geometrical objects for encryption is a young area. The present research work explores one such option; the use of Pythagoras's theorem for right-angled triangle to encrypt medical images. The work proposes a crypto-system with considerable security with one requirement – the use of a secure channel for key exchange.

Key Words: *Medical Images, Cryptosystem, Pythagoras, Symmetric, Private key.*

1. INTRODUCTION

Medical images are some of the greatest source of information and hence needs a strong security system for transit. They contain sensitive information about an individual which require confidentiality. This research proposes a new method that is based on Pythagorean triplets to encrypt the images; especially the medical images that have uniform backgrounds and confined regions of interest.

2. RELATED STUDY

The survey includes the study of some of the most eloquently described algorithms for medical image encryptions and a study of their performances under different circumstances. Most of the papers that have done research in this area propose the use of pixel positions and/or chaotic sequences of one dimension[1-3] Because of the nature of the Pseudo Random Number Generators (PRNG) used in these systems, the security provided becomes weak over largely varying sizes. Also the time taken becomes a proportionate variable to size and hence vulnerable to timing attack. Some algorithms use selective position encryption which provides a powerful security system. But the regional approach makes it slightly more vulnerable to brute force attack by a untrusted/system with prior knowledge of the type of images that are shared. An analysis of the boundary of encrypted region may divulge very useful information to the cryptanalyst. Some researchers have proposed the technique of dividing the images in multiple sub images based on the information pixel data and position iec [6]. These systems target a very limited section (black and white) of medical images only. Most systems concentrate on monochrome or grey scale images and some are specifically designed for some standard available formats such as JPEG[2].

3. PROPOSED METHOD

Any given image with smaller well defined regions of interest and large uniform backgrounds such as X -rays, MRI scans etc. will have a high correlation among consecutive pixels. This creates it difficulty to encrypt. Even large blocks of such files may have correlation with their neighbors. This method proposes that they have encrypted in such a way that the correlation is hidden or avoided as far as possible. We propose the use of Pythagorean triplets[1].

The mapping function is as follows.

$$C[i] = \text{floor}\,(F(P[j], K[i])) = \text{floor}(\sqrt{P[j]^2 + K[i]^2}\,) \qquad (1)$$

$$\text{Where } K[i] = F\,(P[i], K_0) \qquad (2)$$

and K_0 is the secret key selected by user.

The decryption function will simply be the inverse of the mapping function. The key K_0 is used to generate subsequent keys. Plain text will be rounded up after computation to generate the actual pixel values.

4. JUSTIFICATION

This research work was carried out because it was felt that the use of general purpose cryptosystems such as RSA, DES, 3-DES [7] etc for medical image encryption would diminish their sanctity due to the nature of the images. Medical images have a very small region of interest and rest will be monochromatic. That would lead to the same data repeatedly encrypted with same key on any existing standard cryptosystem. The cryptanalyst would easily recognize the region of interest and he/she would also get a large amount of plain text to cipher text relation. Hence it was an idea to design an algorithm that can be specifically used for images with highly sensitive information concentrated in a small region of the image. The use of Pythagorean triplets was conceived as an idea for its divergence in backtracking and it can be substituted as the standard factorization problem.

5. EXPERIMENTATION AND ANALYSIS

The algorithm was implemented in Python© and the input files were some of the normally available medical images[1]. The results are shown below in figures 1-3. The cipher text is unintelligible in any publicly available text, image or any multimedia handling software package. It has been opened as a binary file and numbers have been formed using normal ASCII conversion.

Figure 1

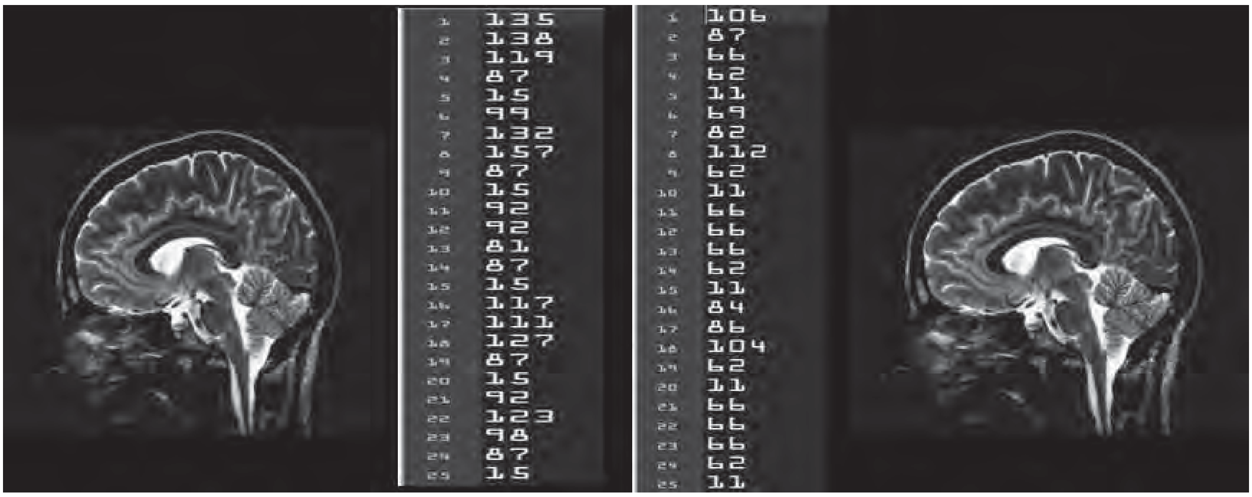

1. The images used are freely available online and do not have any sensitive/personal data attached.

Figure 2

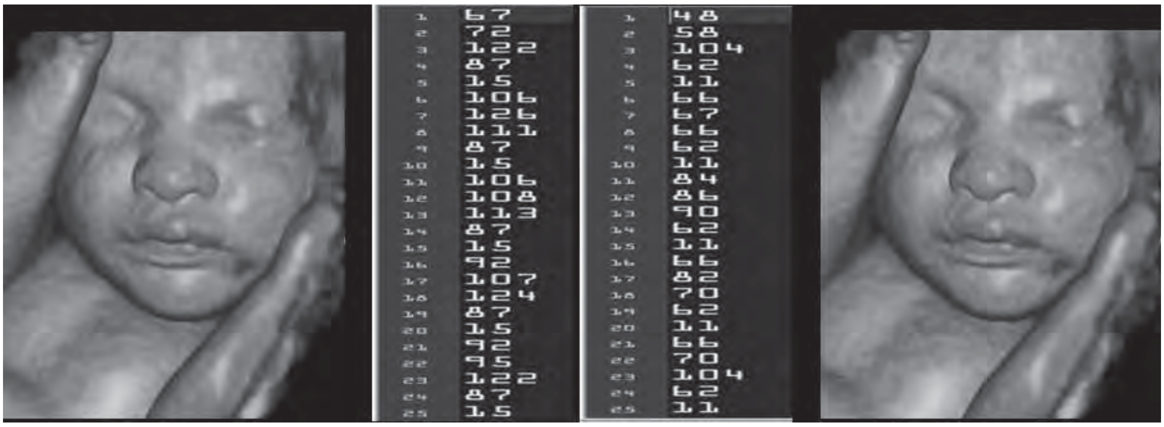

Figure 3

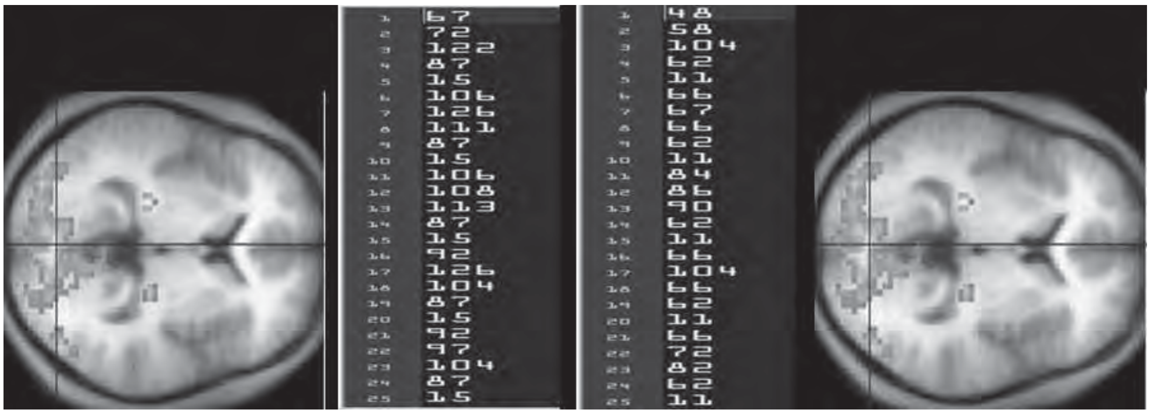

Figures 1-3. Set of Medical images and PythoCrypt files: Plain text, Cipher text, Key file and Decrypted file

The cipher text and key generated at the encryption phase makes our algorithm work on lines of OTP[7]. This is added with the advantage of a pass phrase to enhance the security. The cipher text file is bloated up with non-finite size ratio. The maximum size during the experimentation was CT : PT= 4 : 1R Minimum ratio was 1.7 : 1. This shows that the backtracking methods of cryptanalysis can not be used against PythoCrypt. The cipher text generated was tested for correlation against plain text. The plotted graphs are shown in figure 4. From this it is evident that the two files have very low correlation. Even for pixels having same value (background and uniform colored regions), the cipher text values vary to quite a good extent. This behavior is due to the fact that PythoCrypt can be used on any random sized word every time.

Figure 4.

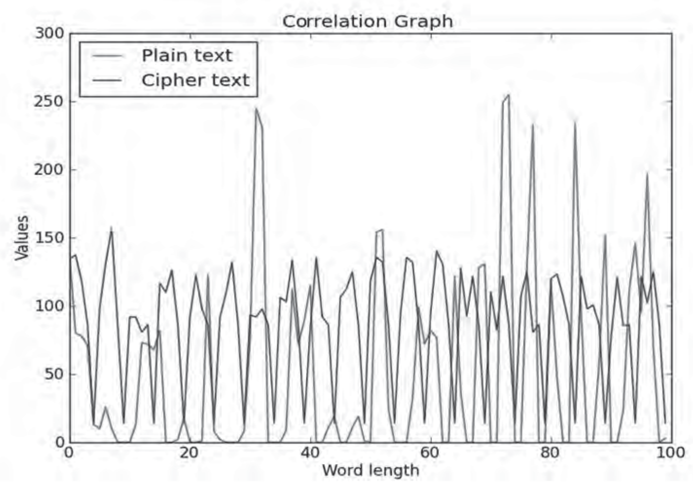

The plot of plain text and cipher text as a test for correlation taken from results of figure 1.

6. ADVANTAGES OF PYTHOCRYPT

- It can be seen from the analysis that the proposed system produces a cipher text file that can not be rendered in any standard application for images or text.
- It works better under noisy conditions because of the bloating up of the file during encryption.
- The system can be easily modified to work with any other file types such as text, numerical data etc.
- It provides very strong protection against most available cryptanalysis techniques because of the multi-level encryption.
- Use of random sized words ensures varying cipher text values for same pixels as observed in multi character encryption [7]

7. CONCLUSION

PythoCrypt as is a unique promising cryptosystem particularly powerful when used on medical images and frequency based transformation sensitive data. It fares well in noisy conditions and with the protected sharing of key assured, it offers a stable and robust security system.

REFERENCES

1. Pythagorean theorem, Pythagoras, 570-495 BC.
2. Medical Image Encryption Based on Pixel Arrangement and Random Permutation for Transmission Security, Usman, K. Sch. of Med., Tokai Univ., Tokai Juzoji, H.; Nakajima, I.; Soegidjoko, S.; Ramdhani, M. ; Hori, T.; Igi, S
3. A Chaos-based Visual Encryption Mechanism in JPEG2000 Medical Images Chin-Feng Lin, Wen-Thong Chang, Ching-Yi Li
4. Chaos-Based Medical Image Encryption Using Symmetric Cryptography, Ashtiyani, M. Electr. Eng. Dept., IHU, Tehran, Birgani, P.M. ; Hosseini, H.M.
5. Region-based selective encryption for medical imaging, Yang Ou, Department of Information Security, Chul Sur, Kyung Hyune Rhee, Division of EC and TE, Pukyong National University, Busan, Republic of Korea
6. Analysis of security problems in a medical image encryption system. Alvarez G, Li S, Hernandez L., Instituto de Física Aplicada, Consejo Superior de Investigaciones Científicas, Serrano 144, 28006 Madrid, Spain. gonzalo@iec.csic.es
7. Cryptography and Network Security. William Stallings, 4th Edition, Pearson Publications.

USE OF GENETIC ALGORITHM IN MULTI-OBJECTIVE OPTIMIZATION OF A REAL WORLD PROBLEM USING SCILAB GENETIC TOOL

Saurabh Vishnoi*
M.Tech Scholar
Department of Computer Science and Engineering
Ajay Kumar Garg Engineering College, Ghaziabad, India.
Email: svish18@gmail.com
Corresponding author

Shiva Tyagi
Assistant Professor
Department of Computer Science and Engineering,
Ajay Kumar Garg Engineering College, Ghaziabad, India.
Email: tyagishiva1@gmail.com

ABSTRACT

In this challenging world, where the time and space complexity is a very critical issue, the optimization of a problem plays a vital role in achieving the real time goals. In an industry, we always want the cost incurred to be as low as possible thus producing high quality product at that very cost. Here comes the role of optimization process. In this paper we have illustrated a real world problem and solved it using multi-objective optimization of the problem. It has been seen that the solution of a real world problem is somewhat different as compared to the solution of a general problem in the sense that they require more optimization than one objective function in parallel. We have used mathematical equations to represent any real world problem. The objective can be maximizing or minimizing of the function. The objective function determines how effective should be the solution and what can be the criteria to judge the solution. This paper aims to stress the importance of multi-objective optimization of real world problem so that we can have an effective design cycle of the process. We have also given a step by step procedure that can be followed to solve any real world problem represented using objective functions. We have used Scilab[11][12] which is a scientific software package for numerical computations providing a powerful open computing environment for engineering and scientific applications.

Keywords: *Multi-objective optimization, Genetic Algorithm, Scilab.*

1. INTRODUCTION

From the time, we are able to solve a optimal problem that have the solution of the problem which continues to be a matter of great concern. Whenever we design an algorithm, we have used approaches like greedy method or dynamic programming to have optimized solution vectors. We can use formulation of mathematical equations to represent a real world problem and its objective functions. Here we consider, without the loss of generality, the minimization of two objectives are equally important, where no additional information about the problem is available[2][3][4]. A solution of the problem can be described by a "decision vector" $\vec{x}$ of the form $\vec{x}$ =(x1,x2…xn) lying in the design space . The evaluation of the two objective functions on $\vec{x}$ produces a solution $\vec{y} = (y1, y2)$ in the objective space Y, i.e. f is a vector map of the form $f{:}X \rightarrow Y$. Comparing these two solutions $\vec{x}1$ and $\vec{x}2$ requires to define a dominance criteria. In modern multi-objective optimization[2][5][6][7] the Pareto[9] criteria is the most used. This criteria states:

An objective vector $\vec{y}1$ is said to dominate another objective vector $\vec{y}2$ (i.e. $\vec{y}1 < \vec{y}2$,) if no component of $\vec{y}1$ is greater than the corresponding components of $\vec{y}2$ and at least one component is greater; accordingly the solution $\vec{x}1$ dominates $\vec{x}2$, if f($\vec{x}1$) dominates f($\vec{x}2$) ; all non-dominated solutions are the optimal solutions of the problem, solutions not dominated by any others. The set of these solutions is named Pareto set while its image in objective space is named Pareto front[9].

Fig. 1 Representation of function f(mapping from design space to objective space)

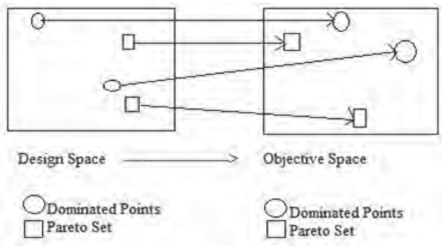

Optimizing a real world problem requires finding a set of decision variables that satisfies constraints and optimizes simultaneously a vector function. The objective functions of all decision makers are represented by the elements of the vector function. The optimization of this vector function leads to non-unique solution of the problem. For example, when selecting a car that maximizes the comfort and minimizes the cost, the solution may be represented by a segment of cars not by a single car only. This paper gives a procedure to find out the most optimal solution vector of a problem that may require optimizing more than two functions simultaneously.

2. MULTIOBJECTIVE OPTIMIZATION PROBLEM

The problems of the real world which requires simultaneous optimization of more than two objective functions at the same time are put in this category. The solution to these problems is not a single solution instead is a set of non-dominated solutions for multi-objective optimization problem. The non dominated solutions are usually referred as Pareto Optimal Set[9]. A solution belonging to this very set is called Pareto optimum and its graphical representation is called Pareto Front[9]. To obtain the Pareto front[9] is the main goal of a multi-objective optimization problem[2][5][6][7].

An example of real world problem is ZDT1[2][3][6] problem that consists of solving the following multi-objective optimization problem[2][5][6][7]:

$$\min\{ f_1 , f_2 \}$$

, where the objective functions are:

$$f_1 = x_1$$

$$f_2 = g.(1 - (f_1/g)^{1/2})$$

and

$$g(x_2,\ldots,x_n) = 1 + (9/n-1).\sum_{i=2}^{n} xi$$

$$0 <= x_i <= 1$$

The optimal Pareto front[9] is decided by $(f_1, 1- (f_1)^{1/2})$

3. USE OF GENETIC ALGORITHM IN OPTIMIZATION PROBLEM

We used the following steps to optimize our problem. We first define a memory that contains current solutions of the problem. Then we have used a selection module to determine which type of the previously determined solutions we can keep in memory or we can discard. For this purpose we can use mating or environmental selections. In mating we use a fitness selection phase in which the promising solutions are picked for variation. In environmental selection we decide which of stored solutions can be kept into the memory. A variation module is then defined that takes a set of solutions and modifies these solutions to generate more promising solutions using crossover and mutation operators. The Crossover operator produces new individuals by combination of information of two or more parents. The mutation operator alters individuals that have low probability of survival. The terminologies that we use, call solutions of the problem as candidates and the set of candidates as population. A fitness function is used to represent a particular objective function for the characterization of the problem. Considering all problem constraints, the fitness function measures how much a given solution is closed to achieve the target[1][3][5][6][7]

4. SCILAB GENETIC TOOL

Scilab[11][12] is an open source scientific software package for numerical mathematics and scientific visualization. It is a powerful framework capable of interactive calculations and automation of calculations through programming. It provides a number of tools for doing scientific and engineering task. It has an inbuilt multi-objective Niched Sharing Genetic Algorithm version 2(NSGA2)[1].

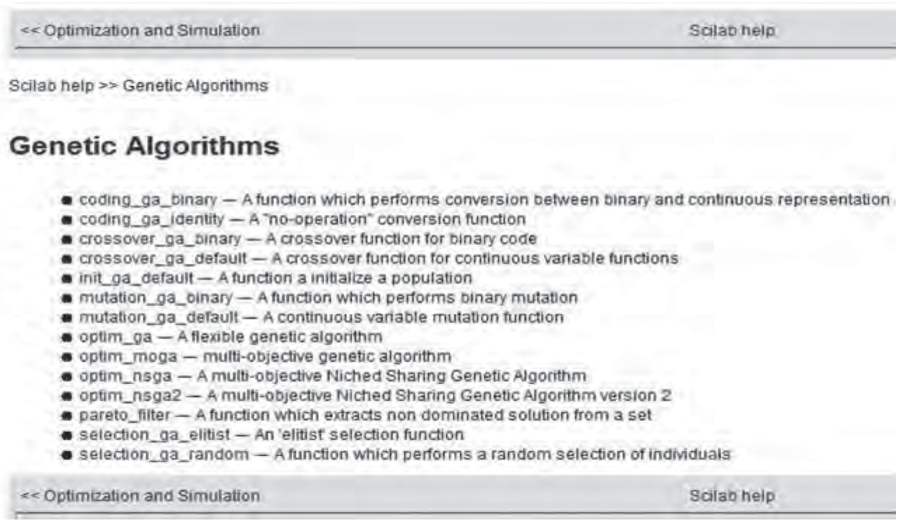

Fig. 2 Scilab genetic algorithm's functions

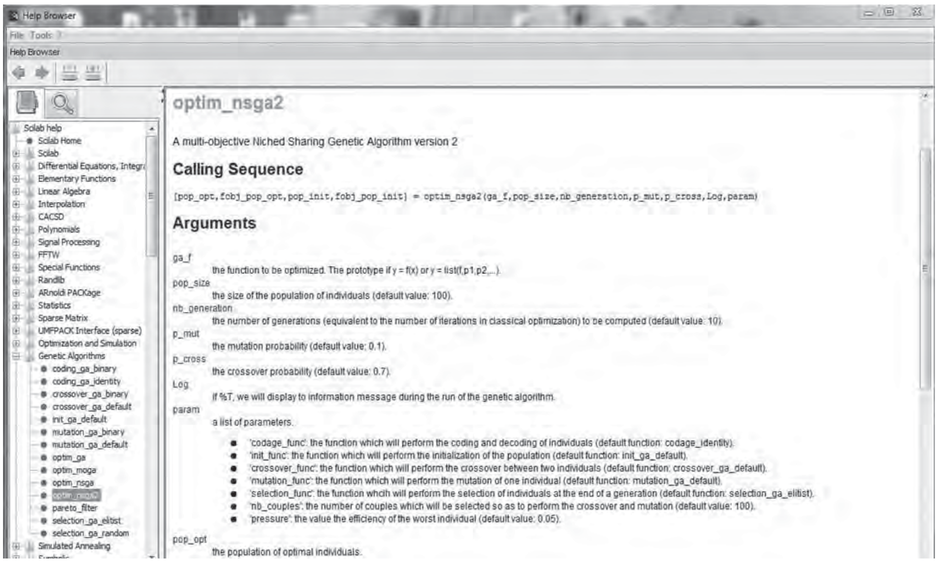

Fig. 3 Scilab NSGA2 genetic algorithm function syntax

5. PROCEDURE AND SYSTEM DESIGN

Procedure:

//Defining a test problem.

PROCEDURE ZDT1

1. f1=x(1)
2. g(x2,….,xn) = 1 + (9/n-1).$\sum_{i=2}^{n} xi$
3. h(x)=(1 – (f1/g)1/2
4. f = [f1,,g(x)*h(x)]
5. return f

//Define Minimum boundary function

PROCEDURE MINBDZDT1(n)

1. Create a matrix of zeros having of n rows and 1 column and store into Res variable.
2. Return Res

//Define maximum boundary function

PROCEDURE MAXBDZDT1(n)

1. Create a matrix of ones of n rows and 1 column and store into Res variable.
2. Return Res

//Starting NSGA2 algorithm

1. Set problem dimension= No. of objectives
2. Set name of the function to the test problem function.
3. Set Population Size.
4. Set Crossover probability
5. Set no. of generations
6. Set other parameters of NSGA2 algorithm
7. Compute optimal Pareto front
8. Declare current population as global variable.
9. //performing optimization
10. for i=1 to No. of Generations do
11. Set location of Generation no. to 1.
12. Compute optimal population and Optimal function object using crossover and mutation operation.
13. if(i>1) then change initial population generation function.
14. Readjust NSGA2 parameters.
15. Save population by setting current population to optimal population.
16. Compute Pareto front and filter
17. Plot final population.

The complexity of NSGA2[1] algorithm is O(MN2)[1] as compared to O(MN3) of other evolutionary algorithms where M is the number of objectives and N is the population size[1][3][8][10]. Thus more the population size, the more will be the computational time. A more complex problem has more objective functions that are needed to be optimized simultaneously. It will also account for increase in computational time.

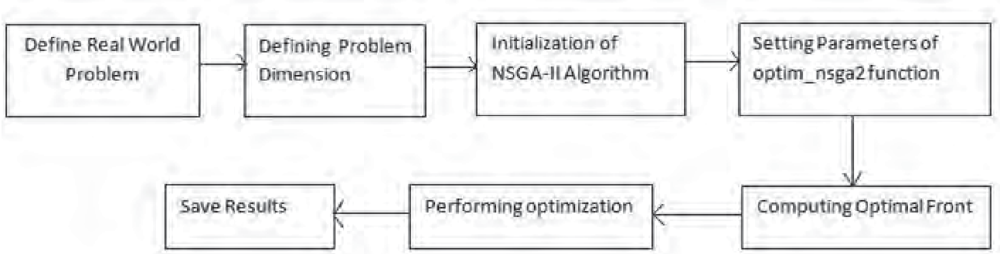

Fig. 4 System design

6. RESULTS

On implementation of the above algorithm[1] we see that after almost 20 generations we have our solution vectors lying on the Pareto front[9]. The results are shown :

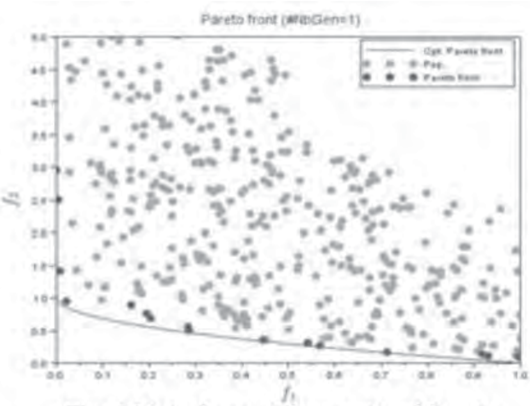

Fig. 5 Plot of population, optimal Pareto front and Pareto front (1st Generation)

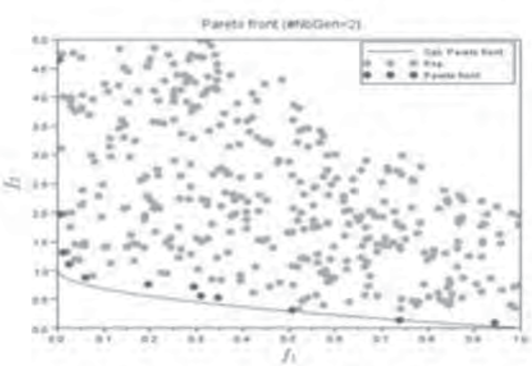

Fig. 6 Plot of population, optimal Pareto front and Pareto front (2nd Generation)

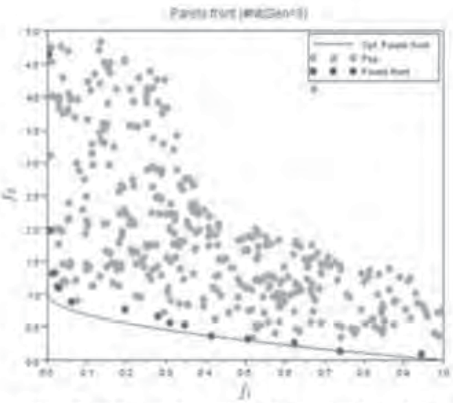

Fig. 7 Plot of population, optimal Pareto front and Pareto front (3rd Generation)

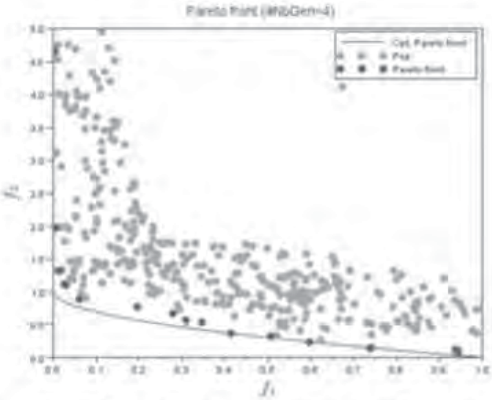

Fig. 8 Plot of population, optimal Pareto front and Pareto front (4th Generation)

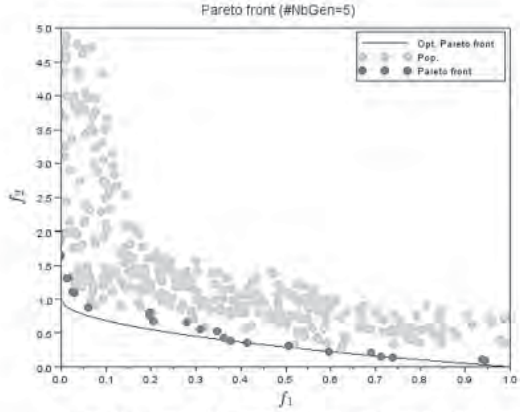

Fig. 9 Plot of population, optimal Pareto front and Pareto front (5th Generation)

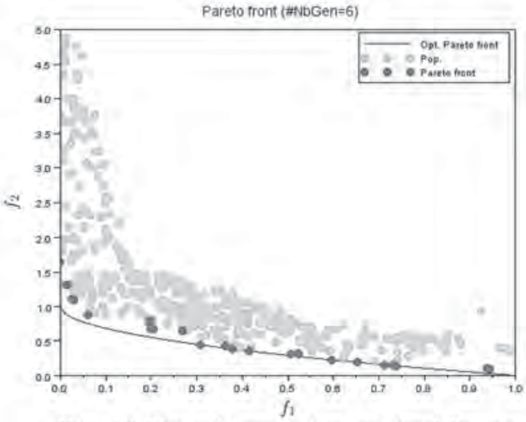

Fig. 10 Plot of population, optimal Pareto front and Pareto front (6th Generation)

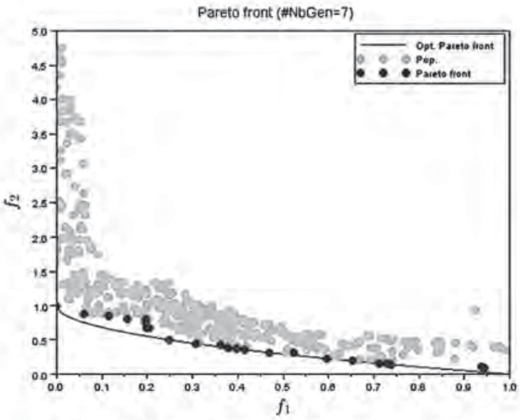

Fig. 11 Plot of population, optimal Pareto front and Pareto front (7th Generation)

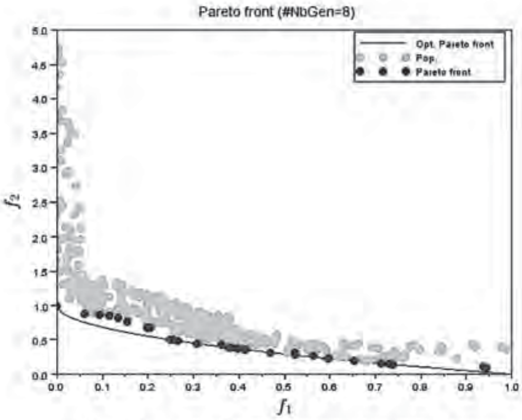

Fig. 12 Plot of population, optimal Pareto front and Pareto front (8th Generation)

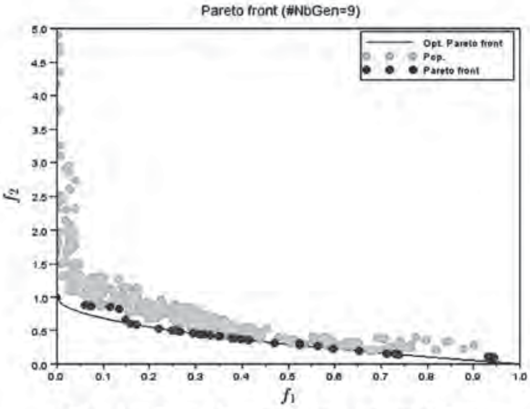

Fig. 13 Plot of population, optimal Pareto front and Pareto front (9th Generation)

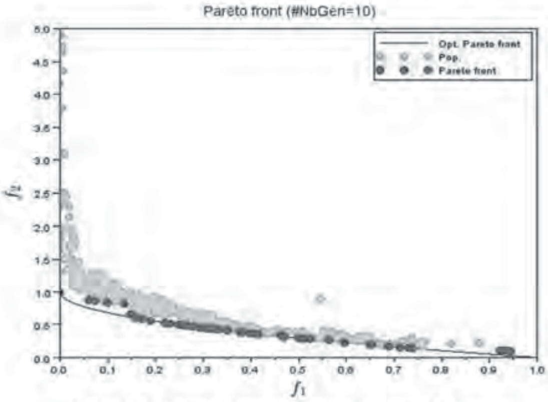

Fig. 14 Plot of population, optimal Pareto front and Pareto front (10th Generation)

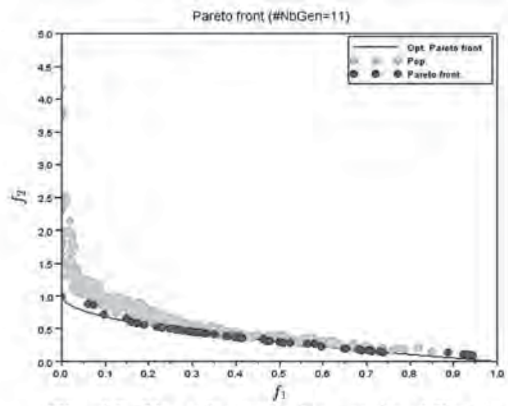

Fig. 15 Plot of population, optimal Pareto front and Pareto front (11th Generation)

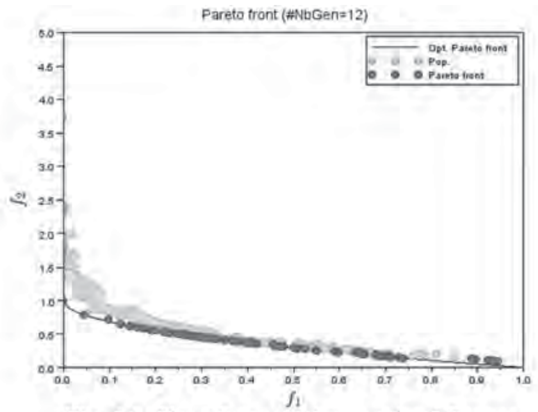

Fig. 16 Plot of population, optimal Pareto front and Pareto front (12th Generation)

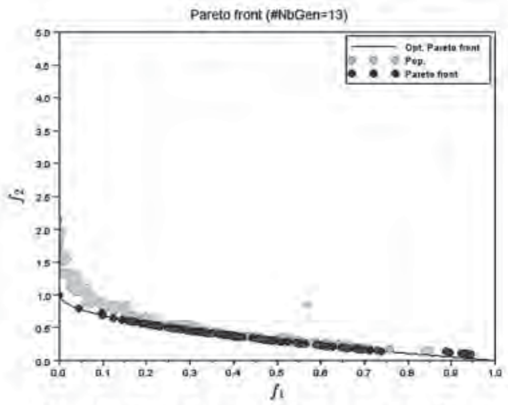

Fig. 17 Plot of population, optimal Pareto front and Pareto front (13th Generation)

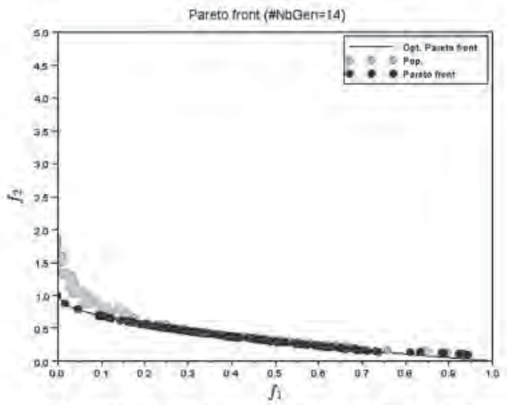

Fig. 18 Plot of population, optimal Pareto front and Pareto front (14th Generation)

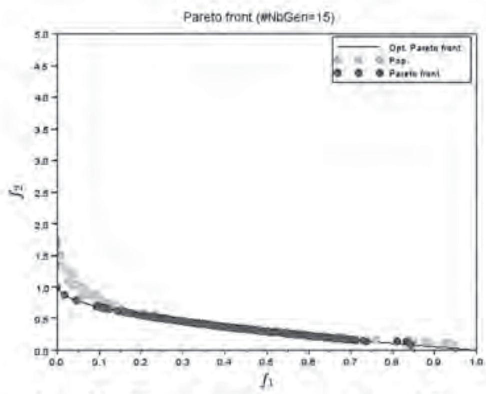

Fig. 19 Plot of population, optimal Pareto front and Pareto front (15th Generation)

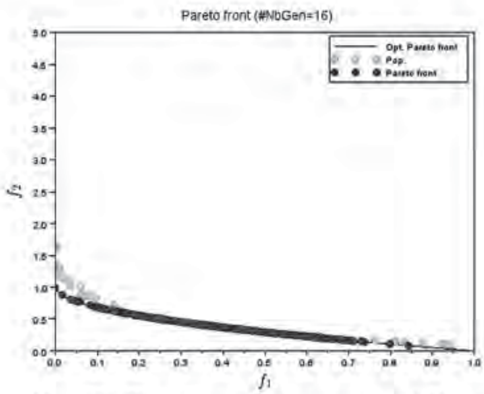

Fig. 20 Plot of population, optimal Pareto front and Pareto front (16th Generation)

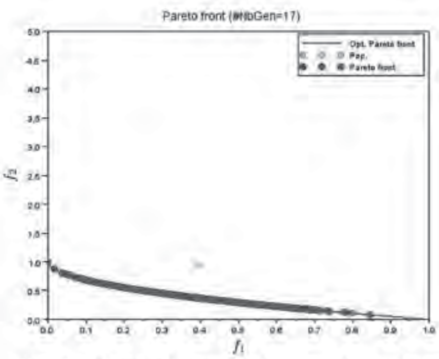

Fig. 21 Plot of population, optimal Pareto front and Pareto front (17th Generation)

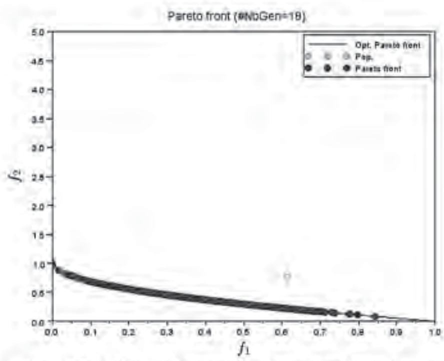

Fig. 22 Plot of population, optimal Pareto front and Pareto front (18th Generation)

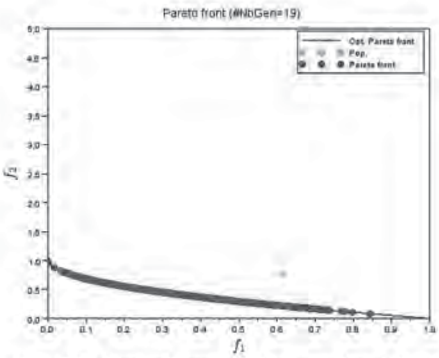

Fig. 23 Plot of population, optimal Pareto front and Pareto front (19^{th} Generation)

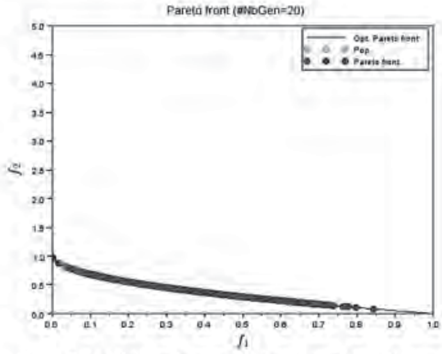

Fig. 24 Plot of population, optimal Pareto front and Pareto front (20^{th} Generation)

7. CONCLUSION

In this paper we have shown the multi-objective optimization[2][5][6][7] of a problem that requires the simultaneous optimization of more than one objective function. Thus, it becomes somewhat difficult to optimize functions simultaneously. Scilab[11][12] has a very powerful genetic tool that having. Scilab[11][12] functions used for implementing NSGA2[1] algorithm for optimization. The complexity of the algorithm is determined by using probablistic approach which depend on the size of the population and on the number of objectives that are need to be optimized simultaneoulsy[1][3][8][10]. Thus, we can say if a real world problem can be decomposed into equations representing its objective function then we can easily find out the solution of the problem using multi-objective optimization of the problem.

REFERENCES

1. K. Deb, A. Pratap, S. Agarwal, and T. Meyarivan, *A fast and elitist multi-objective genetic algorithm: NSGA-II*, IEEE Trans. Evol. Comput., vol. 6, no. 2, pp. 182–197, Apr. 2002.
2. K. Deb, L. Thiele, M. Laumanns, and E. Zitzler, *Scalable test problems for evolutionary multi-objective optimization,* A. Abraham, L. Jain, and R. Goldberg, editors, Evolutionary Multi-objective Optimization, pages 105{145. London: Springer-Verlag, 2005.
3. Eckart Zitzler, Kalyanmoy Deb, and Lothar Thiele , Comparison of Multiobjective Evolutionary Algorithms: Empirical results, IEEE Explore
4. Kalyanmoy Deb, Ankur Sinha and Saku Kukkonen, MultiObjective Test Problems, Linkages, and Evolutionary Methodologies, Kanpur Genetic Algorithms Laboratory (KanGAL), Indian Institute of Technology Kanpur
5. Juan J. Durillo, Student Member, IEEE, Antonio J. Nebro, Carlos A. Coello Coello, Senior Member, IEEE, Jos´e García-Nieto, Francisco Luna, and Enrique Alba, A Study of Multi-objective Meta heuristics When Solving Parameter Scalable Problems.
6. K. Deb., *Multi-objective genetic algorithms: Problem difficulties and construction of test problem*, Evolutionary Computation Journal, 7(3):205-230, 1999.
7. K. Deb, Multi-objective optimization using evolutionary algorithms, Chichester, UK: Wiley, 2001.
8. K. Deb, A. Anand, and D. Joshi, *A computationally efficient evolutionary algorithm for real-parameter optimization,* Evolutionary Computation Journal, 10(4):371{395, 2002.
9. K. Deb and D. Saxena, On finding Pareto-optimal solutions through dimensionality reduction for certain large-dimensional multi-objective optimization problems, Technical Report KanGAL Report No. 2005011, Department of Mechanical Engineering, IIT Kanpur, India, 2005.
10. C. M. Fonesca and P. J. Fleming. On the performance assessment and comparison of stochastic multiobjective optimizers, in Proceedings of Parallel Problem Solving from Nature IV (PPSN-IV), pages 584{593, 1996.
11. Satish Annigeni, SCILAB-A hands on introduction.
12. Claude Gomaz, Engineering and scientific computing with SCILAB.

PLATFORM INTEGRATION IN SUBMICRON TECHNOLOGY WITH IPXACT: A REVIEW

Naresh C Sharma*
Post Graduate Student
Department of Electronics and Communication
Noida Institute of Engineering and Technology, Greater Noida, India
Email: nareshc.sharma@gmail.com
Phone no.+91- 9810284466
Corresponding Author

Suvendra Sahoo
Assistant Professor
Department of Electronics and Communication
Noida Institute of Engineering and Technology,Greater Noida, India
Email: suvendra.sahoo@gmail.com

Satyendra Sharma
Professor and Head
Department of Electronics and Communication
Noida Institute of Engineering and Technology, Greater Noida, India
Email: satyendracommn@gmail.com

ABSTRACT

System-on-Chip (SoC) designs are getting more complex, including many IP components and with time-to-market pressures rising, EDA and VLSI companies are looking for ways to build and update designs easily. An effective SoC integration needs extensive IP (intellectual property) re-use, doing thousands of interconnections quickly without any error. The IEEE-1685 standard (IP-XACT) was designed to fit this requirement. An IPXACT standard is developed by a consortium of VLSI and EDA companies to agree upon a common standard for IP-exchange and develop a generic re-use methodology. In this paper, we will focus on some key IP-XACT feature and proposed methodology used extensively for IP reuse and SoC integration.

Keywords: *System-on-chip (SoC), Electronic Design Automation (EDA), Platform Integration, IP Re-Use, IPXACT, reduce design cycle time*

1. INTRODUCTION

IP-XACT is a standard for the description of electronic Intellectual Property (IP). This standard is intended for use by Electronic Design Automation (EDA) and Electronic System Level (ESL) tools. It was created and is owned by the SPIRIT Consortium. IP-XACT is an XML schema for language and vendor-neutral IP descriptions that includes a generator interface for "plug-in" functionality. It is design language neutral, design tool neutral, efficient, and proven. The primary goals of the standard are to:

- Enable IP vendors to provide a single description of their components to all of their customers, regardless of the design language or tools that they use

- Enable developers to transfer designs between environments that use different design languages.

A schema is built on the existing XML (W3C) standard with a standardized API for generator integration called the Tight Generator Interface (TGI). The schema, first released by the SPIRIT Consortium, is now an IEEE standard that is validated and released in accordance with the IEEE policies published as IEEE-1685.

XML schemas are used to define the legal building blocks of an XML document or document structure. An XML schema defines:

- Elements and attributes that can appear in a document
- Which elements are child elements
- The number and order of child elements
- Whether an element is empty or can include text
- Data types for elements and attributes
- Default and fixed values for elements and attributes

It is important to note that xml does not do anything. It was created to structure, store and transport information. XML is just plain text. Software that can handle plain text can also handle XML. However, XML-aware applications can handle the XML tags specially. The functional meaning of the tags depends on the nature of the application. With XML, you invent your own tags, as XML has no pre-defined tags and is designed to support schemas like IP-XACT [1].

1.1 WHAT IP-XACT PROVIDES: IP-XACT provides XML descriptions of components and systems. A component has several attributes that can map directly to XML. These include:

- Memory maps
- Registers
- Bus interfaces
- Ports
- Views (additional data files)
- Parameters
- Generators
- File sets

When multiple components are connected, it becomes an IP-XACT design file. This includes the attributes above, as well as the interconnect information of all the components in the design. Fig 1 shows how IP-XACT is mapped to a component. Think of the IP-XACT files and generators as simply “another view” of an IP block[1].

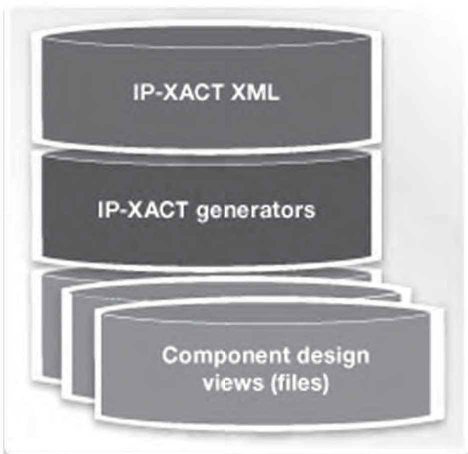

Fig 1: IP-XACT Component

2. IPXACT / SPIRIT PLATFORM

The SPIRIT Consortium provides a unified set of high quality IP-XACT™ specifications for documenting IP using meta-data. This meta-data is used to configure, integrate, and verify IP in advanced SoC design environments. External tools, called generators, interface to such design environments using the LGI: Loose Generator Interface (database access through file exchange) and/or the TGI: Tight Generator Interface (database access through software API). The IP-XACT standard can be applied in various parts of a typical SoC design flow as depicted in Fig 2.

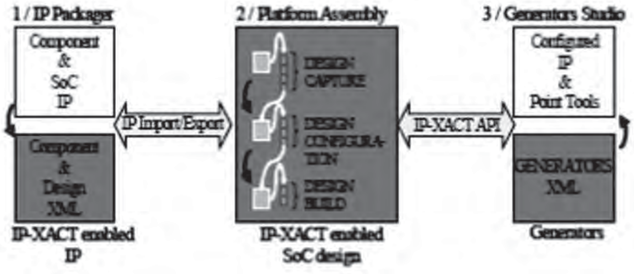

Fig 2: IP-XACT Flow

2.1 IP PACKAGING: The goal is to package all the components of an IP library into XML files in accordance with the IP-XACT schema, which describes the syntax and semantic rules. It includes IP attributes such as physical ports, interfaces, parameters, generics, register map, etc. An important part of the schema is dedicated to referencing the various files related to the different views of a component: e.g. simulation model in a specific language or documentation[2] [3].

Many EDA companies provide highly configurable digital IP for reuse, so customers can easily integrate the IP into their designs configured for the target application. EDA companies generate the IP-XACT file based on the users' configuration. This allows designers to have an XML master view of their various configurations without having to deal with IP-XACT limitations related to configurable IP. Fig 3 shows how a single component can be configured to generate many different components, each of which has its own IP-XACT representation[1].

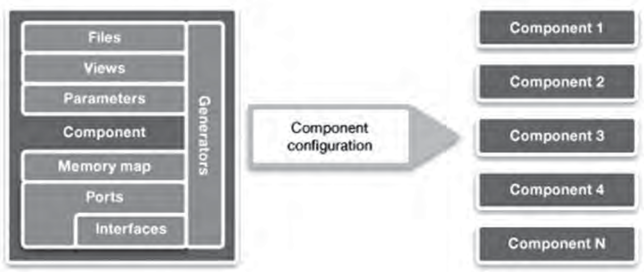

Fig 3: Component configuration

2.2 PLATFORM ASSEMBLY: After the packaging step, it is possible to import, configure and integrate components into the system, assemble the design, resolve connection issues, and automate design tasks. An examples of the use of IP-XACT at this level is the partial or full automation of design assembly and configuration through TGI-based generators that can instantiate, configure and connect components according to chosen design parameters (e.g. abstraction levels of components)[3]. To achieve all stated above, SPIRIT provides a design environment. A SPIRIT Design Environment (DE) is the co-ordination of a set of tools and IP, or expressions of that IP (e.g., models) such that the system-design and implementation flows of an SoC are efficiently enabled and re-use centric. Co-ordination is managed through creation and maintenance of a meta-data description of the SoC. Fig 4 shows the use of the SPIRIT consortium specified formats and interfaces[4] [3]. Using the above mentioned design environment, generators, views, tools etc. a VLSI company assembles a platform, which is used by an SoC integrator to integrate chip. On comparing Fig 4 with Fig 2 we can have a direct resemblance of various blocks of the SPIRIT provided design environment and deployed IPXACT flow.

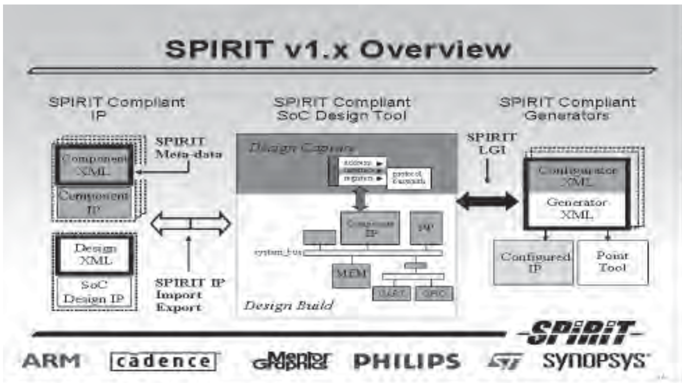

Fig 4: IP-XACT Platform/Design Environment

2.3 TOOL FLOW: The goal is to link the design activities around the centric IP-XACT database by means of a dedicated environment that provides access to the IP-XACT information. A typical platform provides an IP Packager, a Platform Assembly tool, as well as a Generator Studio to develop and debug additional TGI-based generators as explained above briefly. An example in Fig 5 shows using IP-XACT, how you can automatically connect components with associated interfaces? Consider a simple example of an AMBA™ APB master connecting through an APB bus to an APB slave. As the APB interface has been defined, the three components can automatically connect.[3][1]

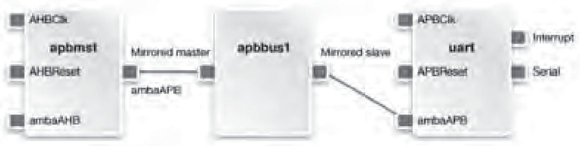

Fig 5: APB Master to Slave connection using IP-XACT interface

2.4 IP INTEGRATION FLOW AT STMicroelectronics: ST uses the flow shown in Fig 6 for the design and verification of its IPs, subsystems and chips. This flow uses IP-XACT as a common format from which design groups can generate automatically e.g. the RTL netlist, the SystemC netlist, the register test and header files that are used in design verification and software development, the register documentation for the product datasheets. The IP-XACT database is made of IP-XACT compliant IPs and sub systems both from ST and from external suppliers. IPs built within ST, are made IP-XACT compliant through a combination of conversion tools extracting the IP-XACT information from legacy formats e.g. the HDL files or the specifications. IPs from external suppliers are either provided in IP-XACT format or made IP-XACT compliant within ST. Whatever the source of the IP it needs to pass a QA (Quality Assurance) step before entering the IP-XACT database. This QA step is fundamental to the flow as it guarantees the time won through design automation will not be lost debugging IP-XACT IP representations. It is also very illustrative of the type of flow automation achieved with IP-XACT as it uses many of the tools used around IP-XACT[2] [3].

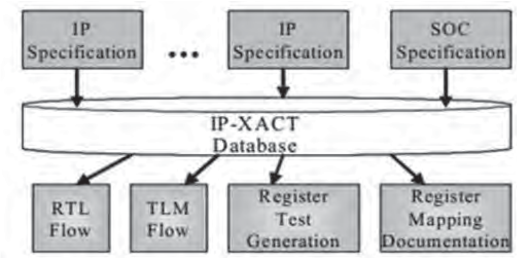

Fig 6: SPIRIT design and verification flow at ST

Hence in Fig 6 the IP specification is capturing the IP and configurability of the IP which would be used for SoC integration. SoC specification have implemented generators and register bank information etc. All this has been captured uniquely and is fed to SPIRIT platform which will have various parallel paths one for integration under the heading of "RTL flow" and verification under the heading of "TLM flow" and Register bank generation and testing under the "Register test generation" and documentation etc. under "Register Mapping and Documentation".

3. DISCUSSION

Using IPXACT based approach is enabling design teams to boost their productivity while lowering development costs. At the same time, these advance approaches are helping the design teams to meet the stringent time-to-market requirements. The objective is to rely on a single description of the target which also allows automating in various dimensions of SoC integration. One such use model is using IP-XACT description for configuring memory mapped resource handling from a debugger offers speed-up in the integration of an external IP. From a user point of view, it provides both easy to read description of memory mapped resource fields, as well as a calculation of register addresses and a generation of the debugger commands. This reduces risks of human errors and increases the productivity of the firmware developer. There are tools which propose IP-XACT extensions for interpreting the data contained in the registers from a software point of view[3].

4. CONCLUSION

IP-XACT components basically create an electronic data book for the core. EDA companies provide generated IP-XACT which includes: Filset information, different views, configuration documentation, IP versions, memory and register maps, and a batch script that allows you to recreate your component or design configuration at any time. Whether you are using a single IP core or building a subsystem with multiple components, you will see the benefits of the generated files that reduce your design and verification time. Existing industrial IP integration flows already benefit from applying the IP-XACT standard. These benefits are in various areas such as: Automated System C IP Packaging, Integration and Configuration and Virtual Prototype generation, IP Integration Verification, both formal and simulation based, IP Quality Assurance and many more. In the future more elements of the SoC design flow such as verification, integration verification and debug environment configuration can be automated using next versions of IP-XACT. Several of the required extensions are currently prototyped.

REFERENCES

1. Building an IP-XACT Design and Verification Environment with DesignWare IP By John A. Swanson, senior marketing manager, DesignWare IP, Synopsys, 12 Feb 2013.
2. O. Florent ,"Spirit-based IP Assembly and SDC Promotion for a 65-nm System-on-Chip using coreAssembler", in Proceedings of SNUG Europe 2006.
3. WidoKruijtzer, Pieter van der Wolf, Erwin de Kock, Jan Stuyt (NXP Semiconductors, The Netherlands) Wolfgang Ecker, Albrecht Mayer (Infineon Technologies), Serge Hustin, Christophe Amerijckx, Serge de Paoli (STMicroelectronics), Emmanuel Vaumorin(Magillem Design Services, France), wido.kruijtzer@nxp.com " Industrial IP Integration Flows based on IP-XACT™ Standards".
4. SPIRIT user guide version 1.0.

APPLICATION OF ADAPTIVE WAVELET TRANSFORM FOR ECG SIGNAL ENHANCEMENT

Rajiv Ranjan*
Associate Professor
Department of Electrical & Electronics Engineering
Dronacharya Group of Institutions, Greater Noida, U.P., India
Email: rajiv_ee_rex@yahoo.com
Contact No. 9891262550
Corresponding Author

V.K. Giri
Professor
Electrical Engineering Department
Madan Mohan Malaviya Engineering College, Gorakhpur, U.P., India

Ajit Kumar Ranjan
System Engineer
CETPA, Noida, India

ABSTRACT

Electrocardiogram (ECG) signal has been widely used in cardiac pathology to detect heart disease. The ongoing trend of ECG monitoring techniques to become more ambulatory and less obtrusive generally comes at the expense of decreased signal quality. To enhance this quality, consecutive ECG complexes can be averaged triggered on the heartbeat, exploiting the quasi-periodicity of the ECG. However, this averaging constitutes a trade-off between improvement of the SNR and loss of clinically relevant physiological signal dynamics. Recent work has attempted to utilize wavelet techniques in the analysis of biomedical signals including ECG. In this paper Multi- Resolution Analysis property of wavelet transform is used to enhance ECG signal quality by denoising the signal.

Keywords: *Electrocardiogram (ECG), Adaptive Wavelet Transform (AWT), Multi- Resolution Analysis (MRA), Signal to Noise Ratio (SNR), Daubechies 6 (db 6).*

1. INTRODUCTION

The electrocardiogram is a graphic recording or display of the time variant voltages produced by the myocardium during the cardiac cycle. The P, QRS and T-waves reflect the rhythmic electrical depolarization and repolarization of the myocardium associated with the contractions of the atria and ventricles. This ECG is used clinically in diagnosing various abnormalities and conditions associated with the heart. The normal value of heart beat lies in the range of 60 to 100 beats/ minute. A slower rate than this is called bradycardia (slow heart rate) and a higher rate is called tachycardia (fast heart rate). If the cycles are not evenly spaced, an arrhythmia may be indicated. If the P-R interval is greater than 0.2 seconds, it may suggest blockage of the AV node. The horizontal segment of this waveform preceding the P-wave is designated as the baseline or the isopotential line. The P-wave represents depolarization of the atrial musculature. The QRS complex is the combined result of the repolarization of the atria and depolarization of the ventricles, which occur almost simultaneously. The T-wave is the wave of ventricular repolarization, where as the U-wave, if present is generally believed to be the result of after potentials in the ventricular muscle. So, the duration amplitude and morphology of the QRS complex is useful in diagnosing cardiac arrhythmias, conduction abnormalities, ventricular hypertrophy, myocardial infection and other disease states.

In general, ECG signals have unique morphological characteristics (P-QRS-T complex) and it is highly significant than other biological signals. It is possible to diagnose many cardiac diseases by analyzing the variations of this morphology visually. However, the presence of noises in ECG signals will severely affect the visual diagnosis and feature extraction of various applications. Many digital signal processing algorithms have been used to process the ECG Signal [1]-[6]. A Kalman filter with adaptive noise-covariance estimation has been developed and evaluated on a variety of ECG signals to assess whether the filter is capable of enhancing the SNR of these signals, while at the same time reserving clinically relevant morphological variations in the ECG [1]. Detecting QRS complexes in the ECG is one of the most important tasks that need to be performed. This stage is crucial in basic ECG monitoring systems and also is important for all other ECG processing applications. Enhancement of the ECG is also important in a stress test[5], [6]. The stress ECG is prone to various types of noise, and it is important to reduce the noise without distorting the morphology of the ECG. Arrhythmia classification is another important task in interpretive systems which provide a diagnostic classification of the ECG. Another useful processing task is a noise alert algorithm which determines the fidelity of the ECG by indicating the level and type of noise in the signal. Many of the researchers have used digital Infinite Impulse Response (IIR) filter to remove the effects of power line interference and baseline wander from ECG signals[7, 8]. Because, the design of IIR filter is simple, on other hand, higher order IIR filters are performing well to remove the noises from the signals. However, it has the drawback of increased filtering time, memory and incapable to filter the highly non-linear signals in the entire ECG range. Some of the SNR and artifact problems that arise during these recordings can be suppressed by simple, frequency-selective filtering[9]–[10].Wavelet transform (WT) is a very promising technique for time frequency analysis. By decomposing signals into elementary building blocks that are well localized both in time and frequency, the WT can characterize the local regularity of signals[4]. This feature can be used to distinguish ECG waves from serious noise, artifacts and baseline drift. In this paper, we have used Multi Resolution Analysis (MRA) technique of WT to denoise ECG signal and enhance signal quality by increasing SNR.

2. WAVELET TRANSFORM

2.1 Continuous Wavelet Transform (CWT) Let x(t) be a signal defined in L2(R) space, which denotes a vector space for finite energy signals. R is a real continuous number system. Such signals satisfy:

$$\int_{-\infty}^{+\infty} \left| x(td)t \right|^2 \leq 0$$

The Wavelet Transform or Continuous Wavelet Transform (CWT) of a continuous time domain signal x(t) is given by X(a,τ) which is defined as :

Forward CWT:

$$X(a,\tau) = \int_{-\infty}^{+\infty} x(t).\frac{1}{|a|^{1/2}}\psi^*\left(\frac{t-\tau}{a}\right)dt \tag{1}$$

Inverse CWT:

$$x(t) = \frac{1}{c}\int_{\tau=-\infty}^{\infty}\int_{a=-\infty}^{\infty} X(a,\tau).\frac{1}{|a|^{5/2}}\psi\left(\frac{t-\tau}{a}\right)da.d\tau \tag{2}$$

The analyzing wavelet Ψ(t) term can be written as -

$$\psi_{a,\tau}(t) = \frac{1}{|a|^{1/2}}.\psi\left(\frac{t-\tau}{a}\right) \tag{3}$$

$$\psi_{1,0}(t) = \psi(t)$$

Notice that

Then above equations can be written as:

$$X(a,\tau) = \int_{-\infty}^{\infty} x(t)\psi_{a,\tau}*(t)dt \tag{4}$$

Forward CWT:

Inverse CWT:

$$x(t) = \frac{1}{c}\int_{\tau=-\infty}^{\infty}\int_{a=-\infty}^{\infty} X(a,\tau).\frac{1}{a^2}\psi_{a,\tau}(t)da.d\tau \tag{5}$$

Where a , $\tau \in R$ and $a \neq 0$ and 'c' is a constant($0 < c < \infty$) that depends on the wavelet used. The success of the reconstruction depends on this constant called, admissibility constant, to satisfy the following admissibility condition

$$c = \int \frac{|\psi(\omega)|^2}{|\omega|} d\omega$$

Where $\Psi(\omega)$ is the Fourier transform and $\Psi^*(t)$ is the complex conjugate of the mother wavelet $\Psi(t)$, x(t) the signal to be transformed, a and τ the dilations (scaling) and translations (time-shift) parameters, respectively. With a suitable choice of the mother wavelet, the scale parameter is proportional to the reciprocal of frequency; the translation parameter stands for time.

2.2 Discrete Wavelet Transform (DWT) The corresponding discrete wavelet transform (DWT) of a time domain signal x(t) is given by X(j,k) which is defined as:

$$X(j,k) = \int_{-\infty}^{+\infty} x(t).\frac{1}{|a_0|^{j/2}} \psi^* \left(\frac{t - k\tau_0 a_0{}^j}{a_0{}^j} \right) dt \tag{6}$$

The analyzing wavelet $\Psi(t)$ term can be written as

$$\psi_{jk}(t) = \frac{1}{|a_0|^{j/2}} .\psi \left(\frac{t - k\tau_0 a_0{}^j}{a_0{}^j} \right) \tag{7}$$

Then the expression of Eq. (6) can be written as:

$$X(j,k) = \int_{-\infty}^{+\infty} x(t).\frac{1}{|a_0|^{j/2}} \psi^*{}_{j,k}(t) dt \tag{8}$$

We can define the DWT of a signal x(t) to be the set of analysis coefficients:

Analysis : $$c_{j,k} = \int_{-\infty}^{\infty} x(t) \psi_{j,k}(t) dt \tag{9}$$

From these we can recover the signal as:

Synthesis: $$x(t) = \sum_j \sum_k c_{j,k} \psi_{j,k}(t) \tag{10}$$

Assuming existence of a scaling function, $\varphi(t)$ we can modify this definition as follows:

Since the spaces are getting larger and larger as j goes to $+\infty$ we can approximate any signal x(t) closely by choosing a large enough value of j = J and projecting the signal into VJ using the basis , (for all values of k).

$$cA_0(m) = \int_{-\infty}^{\infty} x(t) \phi_{J,m}(t) dt \tag{11}$$

From these we can approximately recover the signal as:

$$x(t) \approx \sum_m^n cA_0(m) \phi_{J,m}(t) \tag{12}$$

In effect, we replace the signal x(t) by the approximate signal given by the projection coefficients, cA0(m). From Eq. (10), (11) and (12), we can write

$$\begin{aligned} x(t) &= \sum_m cA_0(m).\phi_{Jm}(t) \\ &= \sum_k cA_1(k).\phi_{J-1,k}(k) + \sum_k cD_1(k).\psi_{J-1,k}(t) \\ &= A_1(t) + D_1(t) \end{aligned} \tag{13}$$

As before, we call the signals A1(t) and D1(t) the approximation and the detail at level-1. We call the coefficients cA1(k) and cD1(k) the approximation-coefficients and the detail-coefficient at level-1

We can further decompose A1(t) to get:

$$x(t) = A_1(t) + D_1(t)$$
$$= \sum_k cA_2(k).\phi_{j-2,k}(t) + \sum_k cD_2(k).\psi_{j-2,k}(t) + \sum_k cD_1(k).\psi_{j-1,k}(t) \tag{14}$$
$$= A_2(t) + D_2(t) + D_1(t)$$

We call the signals A2(t) and D2(t) the approximation and the detail at level-2. We call the coefficients cA2(k) and cD2(k) the approximation-coefficients and the detail-coefficients at level-2.

2.3 Multi-resolution Analysis Define Wj to be set of all signals x(t), which can be synthesized from the daughter wavelets ψj,k(t), $-\infty < k < \infty$. These spaces are orthogonal to each other and we can synthesize any (energy) signal x(t) as

$$x(t) = \sum_{j=-\infty}^{\infty} x_j(t) \tag{15}$$

where $$x_j(t) = \sum_{k=-\infty}^{\infty} c_{j,k}\psi_{j\,k}(t)$$

This leads to various decompositions:

$$\begin{aligned} x(t) &= A_1(t) + D_1(t) \\ &= A_2(t) + D_2(t) + D_1(t) \\ &= A_3(t) + D_3(t) + D_2(t) + D_1(t) \\ &= A_4(t) + D_4(t) + D_3(t) + D_2(t) + D_1(t) \end{aligned}$$

where Di(t), in Wi, is called the detail at level i and Ai(t), is called the approximation at level i.

The approximate coefficients can be computed as below:

$$\begin{aligned} cA_1(k) &= \left\langle x(t)\ \phi_{j-1,k}(t)\right\rangle \\ &= \left\langle \sum_n cA_0(n)\phi_{j,n}(t)\ \phi_{j-1,k}(t)\right\rangle \\ &= \sum_n cA_0(n)\left\langle \phi_{j,n}(t)\ \phi_{j-1,k}(t)\right\rangle \end{aligned} \tag{16}$$

To complete this calculation we have to compute the inner product:

$$\begin{aligned} \left\langle \phi_{j,n}(t), \phi_{j-1,k}(t)\right\rangle &= \int_{-\infty}^{\infty} \sqrt{2^j}\phi(2^j t - n)\sqrt{2^{j-1}}\phi(2^{j-1}t - k)dt \\ &= \int_{-\infty}^{\infty} \sqrt{2^{2j-1}}\phi(2^j t - n)\phi(2^{j-1}t - k)dt \quad \text{(substitute } s = 2^{j-1}t - k\text{)} \\ &= \int_{-\infty}^{\infty} \sqrt{2}\phi(2s + 2k - n)\phi(s)ds \quad \text{(Use the 2-scale equation for } \phi(s)\text{)} \\ &= \int_{-\infty}^{\infty} \sqrt{2}\phi(2s + 2k - n)\sum_m h_0\ m\ \sqrt{2}\phi(2s - m)ds \\ &= \sum_m h_0(m)\int_{-\infty}^{\infty} \phi(2s + 2k - n)\phi(2s - m)2ds \quad \text{(integral is 0 unless m=n-2k)} \\ &= h_0(n-2k) \end{aligned}$$

The detail coefficients can be computed similarly:

$$\begin{aligned} cD_1(k) &= \left\langle x(t)\ \psi_{j-1,k}(t)\right\rangle \\ &= \left\langle \sum_n cA_0(n)\phi_{j,n}(t)\ \psi_{j-1,k}(t)\right\rangle \\ &= \sum_n cA_0(n)\left\langle \phi_{j,n}(t)\ \psi_{j-1,k}(t)\right\rangle \end{aligned}$$

The Equations (16) and (17) are used for decomposing the signal into approximation and detailed coefficients.

3. DATA ACQUISITION AND DEMARCATION OF INDIVIDUAL ECG COMPLEXES

To evaluate the used technique AWT, a diversity of arrhythmic ECG signals is used. The signals are obtained from the Massachusetts Institute of Technology–Beth Israel Hospital. To map the AWT's performance as a function of the SNR of the recorded signals as well, the ECG signals are corrupted with additive Gaussian noise of various amplitudes, yielding ECG signals with SNRs ranging from −3 to 24 dB. The TWA signals comprise a rather ideal dataset for evaluating the performance of the AWT. They exhibit relatively high SNR values that can be made smaller by additive Gaussian noise, and that moreover facilitate quantitative assessment of the processed ECG signals. Before defining the individual ECG complexes, the QRS complexes need to be detected. To facilitate this detection, the SNR of the ECG signals is a priori enhanced by linearly combing the signals in such a way as to maximize the variance. The linear combination with maximum variance is referred to as the principal component. The QRS complexes are subsequently detected in the principal component as local extrema that exceed an adaptive threshold. This adaptive threshold is updated continuously by means of a AWT and depends on the SNR of the ECG signals complexes in the principal component, when the SNR changes, the threshold is adapted to prevent noise from exceeding it, in the mean time ensuring that the QRS complexes still exceed the threshold.

4. RESULTS AND DISCUSSIONS

Noisy signal is shown in figure (1) which is analysed with Daubechies 6 Wavelet as best suited mother wavelet at level 4 with the help of Wavelet tool of MATLAB R2012a. Figure 2 shows approximation signal a_4 having lower frequency and figure (3) to figure (6) depicts detailed signal d_4, d_3, d_2, and d_1 which contains higher frequency component of the signal . From the waveform shown in figure 3 it is clear that detailed coefficient d1 is having higher frequency than that of d2, detailed coefficient d2 is having higher frequency than that of d3 and detailed coefficient d3 is having higher frequency than that of d4.

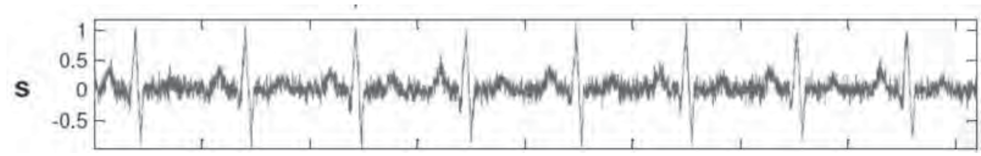

Figure 1

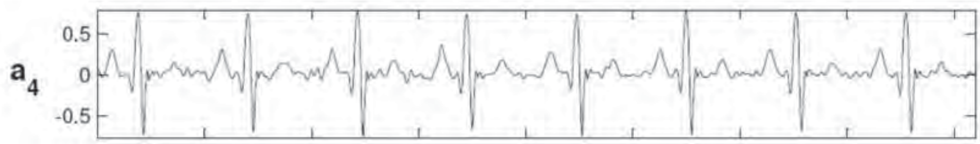

Figure 2

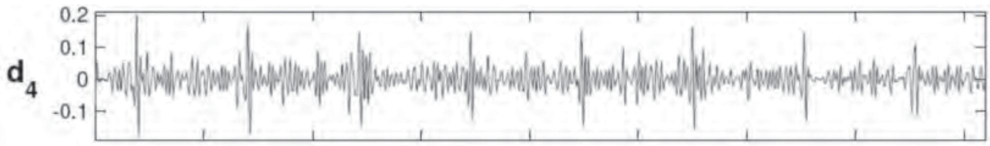

Figure 3

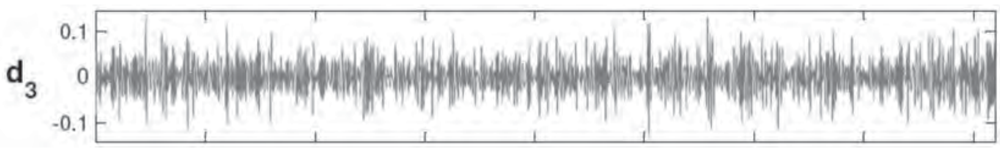

Figure 4

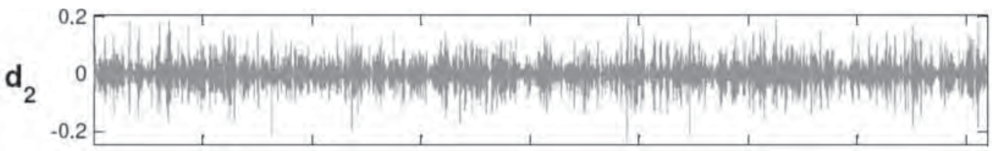

Figure 5

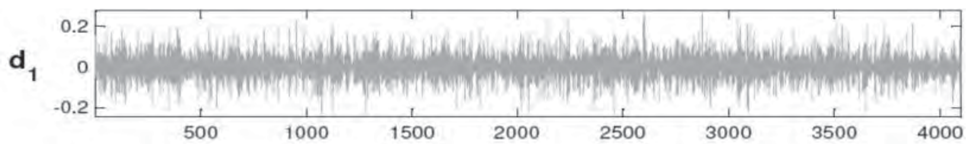

Figure 6

Signal is denoised with Wavelet transform and denoised signal is plotted which is shown in figure 7. For analysis many mother wavelet like Haar, Coiflet, Symlet,Morlet, Maxican Hat, Daubechies 2, Daubechies 4, Daubechies 6 and Daubechies 8 have been tried but Daubechies 6 (db 6) provides high SNR.

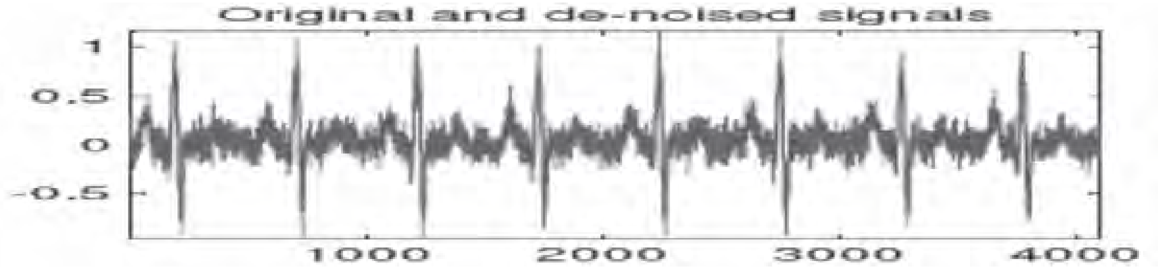

Figure 7

5. CONCLUSION

An approach to study ECG signal based on adaptive wavelet transform is investigated in this paper. Computer simulation results show this approach is promising for ECG signal noise reduction and signal enhancement. To extract the quality ECG signal from the raw noisy ECG signal WT based denoising were employed by using eight wavelet function. In order to identify the performance of denoising, SNR were investigated and results are discussed. The morphology of ECG signals not deviates as well in all three wavelets. However, the morphology "db4"and "sym7" wavelets based ECG signals are infinitesimally difference from the actual PQRST and the "db6" wavelet function holds the excellent morphology. The "db4" wavelet gives the more suppressed "T" wave and "sym7" gives the disturbed ECG pattern. The overall performance of "db6" is better than other wavelet based on morphological characteristics preservation and produces the excellent ECG signal even though the signal contaminates power line noise, baseline wander, and low and high frequency noises. More tests will be conducted to investigate further its performance in the future.

REFERENCES

1. Rik Vullings, Bert de Vries and Jan W.M. Bergmans, "An Adaptive Kalman Filter for ECG Signal Enhancement" IEEE Trans. Biomed. Eng., vol.-58, pp. 1094–1103, 2011.
2. P. S. Hamilton and W. J. Tompkins, "Quantitative investigation of QRS detection rules using the MIT/BIH arrhythmia database," IEEE Trans.Biomed. Eng., vol. BME-33, pp. 1157–1165, 1986.
3. C. Li, C. Zheng, and C. Tai, "Detection of ECG characteristic points using wavelet transforms," IEEE Trans. Biomed. Eng., vol. 32, pp. 21–28, 1995.
4. S. Barro, R. Ruiz, D. Cabello, and J. Mira, "Algorithmic sequential decision-making in the frequency domain for life threatening ventricular arrhythmias and imitative artifacts: A diagnostic system," J. Biomed. Eng., vol. 11, pp. 320–328, 1989.
5. V. X. Afonso, W. J. Tompkins, T. Q. Nguyen, K. Michler, and S. Luo., "Comparing stress ECG enhancement algorithms: With an introduction to a filter bank based approach," IEEE Eng. Med. and Biol., Mag., vol.15, no. 3, pp. 37–44, 1996.
6. V. X. Afonso, W. J. Tompkins, T. Q. Nguyen, S. Trautmann, and S. Luo, "Filter bank-based processing of the stress ECG," in Proc. Annu.Int. Conf. IEEE Eng. Med. Biol. Soc., Sept. 1995.
7. S. C. Mahesh, et al., "Suppression of noise in the ECG signal using digital IIR filter," presented at the Proceedings of the 8th WSEAS International Conference on Multimedia systems and signal processing, Hangzhou, China, 2008.
8. M. C.B, et al., "Processing ECG Signal with Kaiser Window- Based FIR Digital Filters " International Journal of Engineering Science and Technology (IJEST), vol. 3, pp. 6775 - 6783, 2011.
9. J. H. V. Bemmel and H. van derWeide, "Detection procedure to represent the foetal heart rate and electrocardiogram," IEEE Trans. Biomed. Eng., vol. 13, no. 4, pp. 175–82, Oct. 1966.
10. M. Oehler, V. Ling, K. Melhorn, and M. Schilling, "A multichannel portable ECG system with capacitive sensors," Physiol. Meas., vol. 29, pp. 783–793, 2008.

MARKOVIAN QUEUING MODEL WITH HETEROGENEITY IN ARRIVAL PROCESS RULED BY A SECOND ORDER STOCHASTIC MATRIX

Gajendra K. Saraswat*
Assistant Professor
Department of Mathematics
Sanjay Institute of Engineering & Management
Chaumuhan, Mathura-281406, Uttar Pradesh, India
E-mail: telllakshya@yahoo.co.in
Contact No. 8958791371
Corresponding author

R.K. Agarwal
Ex-Reader
Department of Mathematics
B.S.A. (P.G.) College, Mathura-281004, Uttar Pradesh, India

ABSTRACT

This paper studies a two-level modification of the M/M/1 model where the rate of arrival and service capacity experiences Poisson distribution. The problem is discussed by using probability generating function and matrix method technique. The transient and steady state probabilities are obtained and some special cases are also analyzed.

Keywords: *Queuing Theory, Markovian Process, Matrix Method Technique, Probability Generating Function Technique, Poisson distribution, Exponential Distribution.*

1. INTRODUCTION

In queuing theory, a great number of probabilistic models possessing a variety of properties have been discussed. In these models the parameters describing arrival intensity and/or service capacity possesses one of the following characteristics: (a) the parameters are homogeneous in time, (b) the parameters vary with time, (c) the parameters are homogeneous, but heterogeneity is introduced by control action, e.g., passengers are refused admittance in a lift if the number of passengers reaches a certain limit, or, again, service capacity is reinforced for the same reason.

A queuing problem possessing characteristics of service heterogeneity was discussed by GAVER[1] and AVI ITZHAK AND NAOR[2]. In their model the service rate alternates in a random fashion between a fixed arbitrary positive level and zero. YECHIALI AND NAOR[3] analyzed a model where both arrival intensity and service capacity undergo Poissonian jumps between two levels.I. M. PREMCHANDRA AND LILIANA GONZALEZ[4] consider a queuing system with a multipurpose counters in which service mechanism consists of three stages I, II and III performed in sequence by two servers. MURARI AND AGARWAL[7] discussed in his model explicit results in heterogeneous queues with general distribution. A model with two stages heterogeneous service and deterministic server vacations for a single server queue was analyzed by MADAN[11] . The monitoring of network congestion was discussed by WANG AND HUANGYONG[13] based on queuing theory. In his research, KRISHNA KUMAR, MADHESWARI AND VENKATAKRISHNA[14] obtained transient solutions of an M/M/2 queue with heterogeneous servers subject to catastrophes.

The problem under consideration possesses the following characteristics: a stream of Poisson-type customer arrive at a single service station. The arrival pattern is non-homogeneous. There exists two arrival intensities at which the input source is capable of operating. The time interval during which the input function at any one level is an exponentially distributed random variable. The system is Markovian. Further, service time is taken to be exponentially distributed.

We have a single service queuing system wherein the arrival process remains in two stages, (i) state I, (ii) state II. The arrival and service rates in state I are λ_1 and μ respectively. It can jump to state II with Poisson intensity η_{12} , where 1 and 2 are written for state I and state II respectively. The arrival rate of the customers or units in state II is λ_2 . Further, it is assumed that λ_2 lower λ_1.

2. FORMULATION OF THE PROBLEM

(i) A stream of Poisson-type units arrive at a single service station. There exists two different arrival rates λ_1 and λ_2 , only one of which is operative at any instant.

(ii) The queue discipline is first-come-first-served.

(iii) The system has Poisson service rate μ is corresponding to arrival rate λ_1 and λ_2. The state of the system operating with arrival rate λ_1 and service rate μ is denoted by P whereas the second with arrival rate λ_2 and service rate μ is denoted by L.

(iv) The Poisson rate at which the system moves from the state P to L or L to P are denoted by η_{12} and η_{12} respectively. The transitions from one state to another are ruled by second order stochastic matrix.

$$\begin{array}{ccc} \text{State} & I & II \\ \begin{array}{c} I \\ II \end{array} & \multicolumn{2}{c}{\begin{bmatrix} 1-\eta_{12} & \eta_{12} \\ \eta_{21} & 1-\eta_{21} \end{bmatrix}} \end{array}$$

and the way how the transit is depicted by the following diagram.

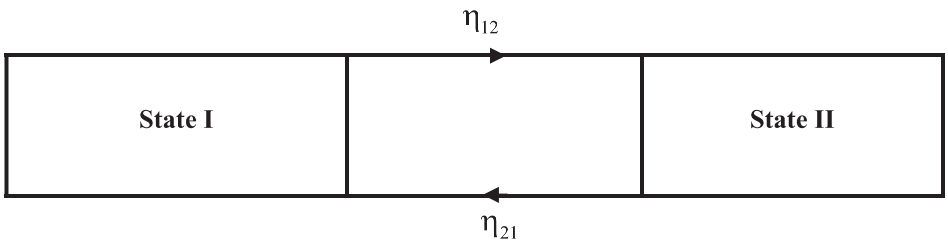

(v) If at any instant the queue length is N, then the arriving customers will be considered lost for the system.

(vi) The service is instantaneous.

A number of areas suggest that this model is of practical use. For example, consider a factory producing certain items of consumers interest is functioning towards its full capacity and sending items with rate λ_1 to the sales depot of that factory. But for various reasons like go-slow practice of the workers, it may not manufacture items with that capacity i.e., it is forced to reduce the supply or the arrival rate of units/items to λ_2 (λ_2 is considerably lower than λ_1). However, after the persuasion of the management workers increases the supply and mean arrival rate may reach to λ_1 from λ_2.

The paper is divided in two sections. In section A, the steady state behavior of the queuing system in limited space is discussed with the help of probability generating function, and some particular cases are also discussed. In section B, we analyze the transient behavior of the system using matrix method technique.

3. SOLUTION OF THE PROBLEM

Let us define

$P_n(t) \equiv$ the probability, that at time t, the system is in the state I and n units are in the queue including the one in service.

$L_n(t) \equiv$ the probability, that at time t, the system is in the state II and n units are in the queue including the one in service.

$R_n(t) \equiv$ the probability, that n units are in the queue at time t including one in service.

Obviously

$$R_n(t) = P_n(t) + L_n(t)$$

Let the time t be reckoned from the instant when queue length is zero, and the system is in the state I. Initial conditions are,

$$P_n(0) = \begin{cases} 1, & n = 0 \\ 0, & otherwise \end{cases}$$

$$L_n(0) = 0, \quad n \geq 0$$

SECTION 'A' The equilibrium equations in steady state governing the system are;

For State I

$$(f - \mu)P_0 = \mu P_1 + \eta_{21} L_0 \tag{1}$$

$$fP_n = \mu P_{n+1} + \lambda_1 P_{n-1} + \eta_{21} L_n, \ 1 \leq n < N \tag{2}$$

$$(f - \lambda_1)P_N = \lambda_1 P_{N-1} + \eta_{21} L_N, \tag{3}$$

Where , $f = (\lambda_1 + \mu + \eta_{12})$

For State II

$$(g - \mu) L_0 = \mu L_1 + \eta_{12} P_0 \tag{4}$$

$$gL_n = \mu L_{n+1} + \lambda_2 L_{n-1} + \eta_{12} P_n, \ 1 \leq n < N \tag{5}$$

$$(g - \lambda_2)L_N = \lambda_2 L_{N-1} + \eta_{12} P_N, \tag{6}$$

Where, $g = (\lambda_2 + \mu + \eta_{21})$

Define the probability generating functions of P_n and L_n by

$$P(z) = \sum_{n=0}^{N} z^n P_n \tag{7}$$

$$L(z) = \sum_{n=0}^{N} z^n L_n \tag{8}$$

Multiplying (1) to (6) by suitable powers of z and using (7) and (8), we have

$$K_1(z)P(z) = \mu(z-1)P_0 + z\eta_{21}L(z) - z^{N+2}\lambda_1 P_N \tag{9}$$

$$K_2(z)L(z) = \mu(z-1)L_0 + z\eta_{12}P(z) - z^{N+2}\lambda_2 L_N \tag{10}$$

Where,

$$K_1(z) = [z\{\lambda_1(1-z) + \mu + \eta_{12}\} - \mu] \tag{11}$$

$$K_2(z) = [z\{\lambda_2(1-z) + \mu + \eta_{21}\} - \mu] \tag{12}$$

Solving equations (9) and (10), we get

$$P(z) = \frac{\mu(z-1)\{P_0 K_2(z) + z\eta_{21}L_0\} - z^{N+2}\lambda_1 P_N K_2(z) - z^{N+3}\lambda_2\eta_{21}L_N}{K_1(z)K_2(z) - z^2\eta_{12}\eta_{21}} \tag{13}$$

$$L(z) = \frac{\mu(z-1)\{L_0 K_1(z) + z\eta_{12}P_0\} - z^{N+2}\lambda_2 L_N K_1(z) - z^{N+3}\lambda_1\eta_{12}P_N}{K_1(z)K_2(z) - z^2\eta_{12}\eta_{21}} \tag{14}$$

From R(z) = P(z) + L(z)

Therefore,

$$R(z) = \frac{[P_0\{K_2(z) + z\eta_{12}\} + L_0\{K_1(z) + z\eta_{21}\}] - z^{N+2}\{\lambda_1 P_N K_2(z) + \lambda_2 L_N K_1(z)\} - z^{N+3}\{\lambda_2\eta_{21}L_N + \lambda_1\eta_{12}P_N\}}{K_1(z)K_2(z) - z^2\eta_{12}\eta_{21}}$$

R(z) is a polynomial. The four zeros of its denominator must vanish its numerator, which is of (N+4) degree, giving rise to set of four equations in four unknowns, viz., P_0, L_0, P_N and L_N. Solving the four equations, the four unknowns can be known.

Hence R(z) can be determined completely.

PARTICULAR CASES: The following particular cases are arises

(i) When from stage II the system does not go to stage I, the corresponding solution can be obtained by making η_{21} equal to zero i.e., $\eta_{21} = 0$

$$P(z) = \frac{\mu(z-1)\{P_0K_2(z)\} - z^{N+2}\lambda_1 P_N K_2(z)}{K_1(z)K_2(z)}$$

$$L(z) = \frac{\mu(z-1)\{L_0K_1(z) + z\eta_{12}P_0\} - z^{N+2}\lambda_2 L_N K_1(z) - z^{N+3}\lambda_1\eta_{12}P_N}{K_1(z)K_2(z)}$$

Where $K_1(z) = [z\{\lambda_1(1-z) + \mu + \eta_{12}\} - \mu]$

$K_2(z) = [z\{\lambda_2(1-z) + \mu\} - \mu]$

(ii) When from stage I the system does not go to stage II, the corresponding solution can be obtained by making η_{12} equal to zero i.e., $\eta_{12} = 0$

$$P(z) = \frac{\mu(z-1)\{P_0K_2(z) + z\eta_{21}L_0\} - z^{N+2}\lambda_1 P_N K_2(z) - z^{N+3}\lambda_2\eta_{21}L_N}{K_1(z)K_2(z)}$$

$$L(z) = \frac{\mu(z-1)\{L_0K_1(z)\} - z^{N+2}\lambda_2 L_N K_1(z)}{K_1(z)K_2(z)}$$

Where $K_1(z) = [z\{\lambda_1(1-z) + \mu\} - \mu]$

$K_2(z) = [z\{\lambda_2(1-z) + \mu + \eta_{21}\} - \mu]$

SECTION 'B' KOLMOGOROV'S forward equations describing the model lead to the following:

Differential equations for stage I

$$P_0^{'}(t) = (f+\mu)P_0(t) + \mu P_1(t) + \eta_{21}L_0(t) \tag{15}$$

$$P_1^{'}(t) = \lambda_1 P_0(t) + fP_1(t) + \mu P_2(t) + \eta_{21}L_1(t) \tag{16}$$

$$P_n^{'}(t) = \lambda_1 P_{n-1}(t) + fP_n(t) + \mu P_{n+1}(t) + \eta_{21}L_n(t), \quad 1 \le n < N \tag{17}$$

$$P_N^{'}(t) = \lambda_1 P_{n-1}(t) + (f+\lambda_1)P_N(t) + \eta_{21}L_N(t), \tag{18}$$

Where $f = -(\lambda_1 + \mu + \eta_{12})$

Differential equations for stage II

$$L_0^{'}(t) = (g+\mu)L_0(t) + \mu L_1(t) + \eta_{12}P_0(t) \tag{19}$$

$$L_1^{'}(t) = \lambda_2 L_0(t) + gL_1(t) + \mu L_2(t) + \eta_{12}P_1(t) \tag{20}$$

$$L_n^{'}(t) = \lambda_2 L_{n-1}(t) + gL_n(t) + \mu L_{n+1}(t) + \eta_{12}P_n(t), \quad 1 \le n < N \tag{21}$$

$$L_N^{'}(t) = \lambda_2 L_{N-1}(t) + (g+\lambda_2)L_N(t) + \eta_{12}P_N(t), \tag{22}$$

Where $g = -(\lambda_2 + \mu + \eta_{21})$

Employing matrix notation, equations (15 to 18) and (19 to 22) give

$$\vec{P}^{'}(t) = A_1\vec{P}(t) + \eta_{21}I_{N+1}\vec{L}(t) \tag{23}$$

$$\vec{L}(t) = B_1\vec{L}(t) + \eta_{12}I_{N+1}\vec{P}(t) \tag{24}$$

Where

$$\vec{P}(t)=\begin{bmatrix} P_0(t) \\ P_1(t) \\ .... \\ .... \\ P_{N-1}(t) \\ P_N(t) \end{bmatrix}, \qquad \vec{L}(t)=\begin{bmatrix} L_0(t) \\ L_1(t) \\ .... \\ .... \\ L_{N-1}(t) \\ L_N(t) \end{bmatrix}$$

I_{N+1} = Identity matrix of order (N+1)

$\vec{P}'(t) = D\vec{P}(t)$ etc., $D \equiv \dfrac{d}{dt}$

$$A_1=\begin{bmatrix} f+\mu & \mu & 0 & 0 & .. & .. & .. & 0 & 0 & 0 & 0 \\ \lambda_1 & f & \mu & 0 & .. & .. & .. & 0 & 0 & 0 & 0 \\ 0 & \lambda_1 & f & \mu & .. & .. & .. & 0 & 0 & 0 & 0 \\ .. \\ .. \\ .. \\ .. \\ 0 & 0 & 0 & 0 & .. & .. & .. & 0 & \lambda_1 & f & \mu \\ 0 & 0 & 0 & 0 & .. & .. & .. & 0 & 0 & \lambda_1 & (f+\lambda_1) \end{bmatrix}$$

$$B_1=\begin{bmatrix} g+\mu & \mu & 0 & 0 & .. & .. & .. & 0 & 0 & 0 & 0 \\ \lambda_2 & g & \mu & 0 & .. & .. & .. & 0 & 0 & 0 & 0 \\ 0 & \lambda_2 & g & \mu & .. & .. & .. & 0 & 0 & 0 & 0 \\ .. \\ .. \\ .. \\ .. \\ 0 & 0 & 0 & 0 & .. & .. & .. & 0 & \lambda_2 & g & \mu \\ 0 & 0 & 0 & 0 & .. & .. & .. & 0 & 0 & \lambda_2 & (g+\lambda_2) \end{bmatrix}$$

tri-diagonal matrix of order (N+1) with main diagonal and super diagonal. Solving equation (23) and (24), we get a four – order differential equations. In order to apply matrix notation, we will express it in a form that involve first order differential coefficients.

$$D^4\vec{P}(t)-aD^3\vec{P}(t)-bD^2\vec{P}(t)-cD\vec{P}(t)+d\vec{P}(t)=0 \tag{25}$$

$$\left.\begin{aligned} a &= A^* \\ b &= C^* \\ c &= (B^*)^3+B^*C^* \\ d &= \{A^*(B^*)^3-(B^*)^2C^*\} \end{aligned}\right\}, \text{ and } \left\{\begin{aligned} \boldsymbol{A}^* &= \boldsymbol{A}_1 \\ \boldsymbol{B}^* &= \boldsymbol{B}_1 \\ \boldsymbol{C}^* &= \eta_{21}\eta_{12}\boldsymbol{I}_{N+1}^2 \end{aligned}\right.$$

In order to solve (25), we follow PIPES AND HARVILL (1970)

Let $\vec{S}_1(t) = \vec{P}'(t)$ (26)

$$\vec{S}_2(t) = \frac{d}{dt}\vec{S}_1(t) = \vec{P}''(t) \tag{27}$$

$$\vec{S}_3(t) = \frac{d}{dt}\vec{S}_2(t) = \vec{P}'''(t) \tag{28}$$

$$\vec{S}_3(t) = \frac{d}{dt}\vec{S}_3(t) = \vec{P}''''(t) \tag{29}$$

Therefore (25) assumes in the form

$$\vec{S}_3^{'}(t) - a\vec{S}_3(t) - b\vec{S}_2(t) - c\vec{S}_1(t) + d\vec{P}(t) \tag{30}$$

From (1.26) to (1.30),we have

$$\vec{v}^{'}(t) = A\vec{v}(t) \tag{31}$$

Where

$$\vec{v}^{'}(t) = \begin{bmatrix} \vec{P}(t) \\ \vec{S}_1(t) \\ \vec{S}_2(t) \\ \vec{S}_3(t) \end{bmatrix},$$

a (4N+4) column vector whose first (N+1) elements are $\vec{P}(t)$, second (N+1)elements are of $\vec{S}_1(t)$ and so on and whose last (N+1) elements are of $\vec{S}_3(t)$

$$A = \begin{bmatrix} o & I_{N+1} & o & o \\ o & o & I_{N+1} & o \\ o & o & o & I_{N+1} \\ -d & c & b & a \end{bmatrix},$$ a square matrix of (4N+4)th order

Where $o \equiv$ null matrix of order (N+1)

$I_{N+1} \equiv$ identity matrix of order (N+1)

The set of initial conditions associated with (31) are

$$\vec{P}(0) = \begin{bmatrix} P_0(0) \\ P_1(0) \\ P_2(0) \\ .... \\ .... \\ P_{N-1}(0) \\ P_N(0) \end{bmatrix} = \begin{bmatrix} 1 \\ 0 \\ 0 \\ .. \\ .. \\ 0 \\ 0 \end{bmatrix}, \qquad \vec{L}(0) = \begin{bmatrix} L_0(0) \\ L_1(0) \\ L_2(0) \\ .... \\ .... \\ L_{N-1}(0) \\ L_N(0) \end{bmatrix} = \begin{bmatrix} 0 \\ 0 \\ 0 \\ .. \\ .. \\ 0 \\ 0 \end{bmatrix},$$

$$P'(0) = S_1(0) = \begin{bmatrix} P_0^{'}(0) \\ P_1^{'}(0) \\ P_2^{'}(0) \\ .... \\ .... \\ P_{N-1}^{'}(0) \\ P_N^{'}(0) \end{bmatrix} = \begin{bmatrix} -(\lambda_1 + \eta_{12}) \\ \lambda_1 \\ 0 \\ .... \\ .... \\ 0 \\ 0 \end{bmatrix},$$

$$P'''(0) = S_3(0) = \begin{bmatrix} P_0'''(0) \\ P_1'''(0) \\ P_2'''(0) \\ P_3'''(0) \\ P_4'''(0) \\ .... \\ .... \\ P_{N-1}'''(0) \\ P_N'''(0) \end{bmatrix} = \begin{bmatrix} (\lambda_1+\eta_{12})^3 - 2\mu\lambda_1(\lambda_1+\eta_{12}) - \mu(\lambda_1+\mu+\eta_{12}) \\ -f\lambda_1(2\lambda_1+\mu+2\eta_{12}) - \lambda_1(\lambda_1+\eta_{12})^2 + 2\mu\lambda_1^{\,2} \\ -\lambda_1^{\,2}(3\lambda_1+\mu+2\eta_{12}) + f\lambda_1^{\,2} \\ \lambda_1^{\,3} \\ 0 \\ .... \\ .... \\ 0 \\ 0 \end{bmatrix},$$

$$P''''(0) = S_3'(0) = \begin{bmatrix} P_0''''(0) \\ P_1''''(0) \\ P_2''''(0) \\ P_3''''(0) \\ P_4''''(0) \\ P_5''''(0) \\ .... \\ .... \\ P_{N-1}''''(0) \\ P_N''''(0) \end{bmatrix} = \begin{bmatrix} (f+\mu)P_0'''(0) + \mu P_1'''(0) \\ fP_1'''(0) + \mu P_2'''(0) + \lambda_1 P_0'''(0) \\ \lambda_1 P_1'''(0) + fP_2'''(0) + \mu P_3'''(0) \\ \lambda_1 P_2'''(0) + fP_3'''(0) \\ \lambda_1^{\,4} \\ 0 \\ .... \\ .... \\ 0 \\ 0 \end{bmatrix},$$

Combining the above four sets are, we have

$$\vec{v}(0) = \begin{bmatrix} \vec{P}(0) \\ \vec{S}_1(0) \\ \vec{S}_2(0) \\ \vec{S}_3(0) \end{bmatrix}, \quad \text{a (4N+4) column vector}$$

For the solution of (31), we consider the following two cases:-

CASE I :

When the coefficient matrix A has distinct eigenvalues. Consider the linear transformation from $\vec{v}(t)$ to a new dependent vector $\vec{z}$ by means of the modal matrix of A,

$$w = (\vec{w}_1, \vec{w}_2, \vec{w}_3, ..., \vec{w}_k, ..., \vec{w}_{4N+4})$$

Where $\vec{w}_k$, is the k^{th} eigen vector of A.

Therefore $\vec{v}(t) = w\vec{z}$ (32)

Substituting (1.32) into (1.31) and pre-multiplying by w^{-1}

$$w^{-1}\vec{v}\,'(t) = w^{-1}Aw\vec{z}$$

Or $\vec{z}\,' = w^{-1}Aw\vec{z}$ (33)

Since w is a modal matrix of A, the term $w^{-1}Aw$ is a diagonal matrix with the eigenvalues of A on the diagonal

$$\vec{z}\,' = \begin{bmatrix} \ddots & & \\ & \lambda_i & \\ & & \ddots \end{bmatrix} \vec{z} \qquad (34)$$

Where x_i represents the eigenvalues of A on the diagonal. The result is that the transformed system is uncoupled, that is (34) may be represented by the single scalar differential equation.

x_i

$$\vec{z}_M^{'} = x_M \vec{z}_M, \qquad M=1, 2, \ldots\ldots\ldots, \quad 4N+4 \tag{35}$$

Its general solution is

$$z_M = C_M e^{tx_M} \tag{36}$$

Where C_M is an arbitrary constant. Hence, general solution of (34) may be written as.

$$\vec{z} = \begin{bmatrix} C_1 e^{tx_1} \\ C_2 e^{tx_2} \\ C_3 e^{tx_3} \\ \ldots. \\ \ldots. \\ C_{4N+4} e^{tx_{4N+4}} \end{bmatrix} \tag{37}$$

From (32) the general solution of (31) in terms of eigenvector expansion

$$\vec{v}(t) = (\vec{w}_1, \vec{w}_2, \vec{w}_3, \ldots\ldots., \vec{w}_{4N+4}) \begin{bmatrix} C_1 e^{tx_1} \\ C_2 e^{tx_2} \\ C_3 e^{tx_3} \\ \ldots. \\ \ldots. \\ C_{4N+4} e^{tx_{4N+4}} \end{bmatrix} \tag{38}$$

Or

$$\vec{v}(t) = \sum_{M=1}^{4N+4} \vec{w}_M C_M e^{tx_M} \qquad C_M$$

This equation shows that the general solution may be expressed as a linear combination of the eigenvectors. By applying the initial condition t=0, the (4N+4) constants C_M may be evaluated from (38)

$$\vec{v}(0) = \sum_{M=1}^{4N+4} \vec{w}_M C_M \tag{39}$$

$$= (\vec{w}_1, \vec{w}_2, \vec{w}_3, \ldots\ldots\ldots., \vec{w}_{4N+4}) \begin{bmatrix} C_1 \\ C_2 \\ C_3 \\ \ldots. \\ \ldots. \\ C_{4N+4} \end{bmatrix} = Cw$$

Therefore $\quad C = \vec{w}^{1} \vec{v}(0)$

The eigenvalues x_i (I = 1, 2, 3, ………,4N+4) of the matrix A can be computed from its characteristic equation:

$$\left| A - xU \right| = 0 \tag{40}$$

If the numerical values of the parameters $\lambda_1, \lambda_2, \mu, \eta_{12}, \eta_{21}$ and N are given, the actual solution of the equation (40) can be known.

CASE II :

When the coefficient matrix A has some multiple eigenvalues. Whenever multiple eigenvalues occur, a modified approach is employed since by usual methods we can not find all the eigenvectors associated with the multiple roots. When this situation occurs, the alternate method is based on the method of undetermined coefficients.

For convenience, consider that the first eigenvalues of an (4N+4)th order system has a multiplicity of 4; that is $x_1 = x_2 = x_3 = x_4 = x$ (say) and $x_5, x_6, \ldots\ldots, x_{4N+4}$ are distinct.

To solve (31) assumes a solution in the form$

$$\vec{v}(t) = (\vec{w}_1 + t\vec{w}_2 + t^2\vec{w}_3 + t^3\vec{w}_4)e^{xt} + \sum_{M=5}^{4N+4} C_M e^{tx_M}\vec{w}_M \tag{41}$$

Substituting this assumed solution into (31) gives

$$\begin{aligned} &x(\vec{w}_1 + t\vec{w}_2 + t^2\vec{w}_3 + t^3\vec{w}_4)e^{xt} + (\vec{w}_2 + 2t\vec{w}_3 + 3t^2\vec{w}_4)e^{xt} + \sum_{M=5}^{4N+4} C_M e^{tx_M}\vec{w}_M \\ &= A(\vec{w}_1 + t\vec{w}_2 + t^2\vec{w}_3 + t^3\vec{w}_4)e^{xt} + \sum_{M=5}^{4N+4} C_M e^{tx_M} A\vec{w}_M \end{aligned} \tag{42}$$

By employing the definition of eigenvectors and eigenvalues the summations on each side of the equality may be cancelled. The remaining expression becomes

$$\begin{aligned} &x(\vec{w}_1 + t\vec{w}_2 + t^2\vec{w}_3 + t^3\vec{w}_4) + (\vec{w}_2 + 2t\vec{w}_3 + 3t^2\vec{w}_4) \\ &= A(\vec{w}_1 + t\vec{w}_2 + t^2\vec{w}_3 + t^3\vec{w}_4) \end{aligned} \tag{43}$$

Equating like powers of t

$$\begin{aligned} x\vec{w}_1 + \vec{w}_2 &= A\vec{w}_1 \\ x\vec{w}_2 + 2\vec{w}_3 &= A\vec{w}_2 \\ x\vec{w}_3 + 3\vec{w}_4 &= A\vec{w}_3 \\ x\vec{w}_4 &= A\vec{w}_4 \end{aligned}$$

which may be solved sequentially for the four unknown eigenvectors. Once the unknown eigenvectors have been evaluated, the general solution becomes

$$\vec{v}(t) = (C_1\vec{w}_1 + C_2 t\vec{w}_2 + C_3 t^2\vec{w}_3 + C_4 t^3\vec{w}_4)e^{xt} + \sum_{M=5}^{4N+4} C_M e^{tx_M}\vec{w}_M \tag{44}$$

Arbitrary constants have been omitted from the terms involving the unknown eigenvectors since at most an eigenvector is known up to an arbitrary constant.

For which the (4N+4) arbitrary constants may be evaluated in the usual manner by application of the initial conditions. The solution for $\vec{v}(t)$ will give the solution of $\vec{P}(t)$ and $\vec{S}_1(t) = \vec{P}'(t)$ Substituting the values of $\vec{P}(t)$ and $\vec{P}(t)$ in (23), we get L(t).

Thus $P_n(t)$ and $L_n(t)$ are completely known. Hence $R_n(t)$ can be determined.

4. CONCLUSION

Evidently, the above discussed M/M/1 model for two states give explicitly results to find out the probability of the system. In this model, we discussed both steady and transient solutions. Many organizations can use this model to improve their capacity and utilize the resources properly. In future research, this model can be modified for two states in service process and also be evaluated for three states in arrival process. Numerical and graphical areas may be major part for further research work.

REFERENCES

1. GAVER, D.P.J.R(1962): A waiting line with interrupted service including priorities, J.Roy. Statist. Soc. B(24) 73-90
2. AVI-TZHAK, B., and P. NAOR(1961): On a problem of preemptive priority queuing, Operations Res. 9 664-672.
3. YECHIALI, U., and P. NAOR (1971): Queuing problems with heterogeneous arrivals and services, J. Operations Res. Soc. Am. 19, 722-734.
4. PREMCHANDRA, I.M. and LILIANA GONZALEZ(1994): System with multipurpose counters, Ops. Res. Vol.21. No.9 969-977
5. SAATY, T.L.; Elements of Queuing Theory with applications. Mc-Graw Hill Book Company, Inc.
6. D. GROSS and M. HARRIS(1974): Fundamentals of Queuing Theory, Wiley, New York,.
7. MURARI, K. and AGARWAL, R.K. (1981): Explicit results in heterogeneous queues with general distribution, `Cahiers du Centre d' Etudes de Recherché Operationalle, Bruxelles Volume 23.
8. PIPES, LOUIS A. and LAWRENCE R. HARVILL (1970) : Applied mathematics of Engineers and Physicists, McGRAW-HILL kogakusha Ltd., London .
9. PRABHU, N. U. (1965): Queues and Inventories, John Wiley & Sons.
10. FELLER, W. (1973): An introduction to Probability Theory and Its Applications,Vol. II, Wiley, New York.
11. MADAN, K.C. (2001) : On a single server queue with two stages heterogeneous service and deterministic server vacations, International journal of systems Science, 32, 113-125.
12. SUNDARI, S. MARAGATHA and SRINIVASAN, S. (2011): M/M/C Queuing model for waiting time of customers in Bank sectors, Int. j. of Mathematical Sciences and Applications, Vol. 1, No. 3, 1569-1575.
13. WANG JIANG-PING, HUANG YONG (2008) : The monitoring of the network traffic based on queuing theory, ISORA 'O8, ORSC & APORC, pp. 60-65.
14. KRISHNA KUMAR, B., MADHESWARI PAVAI, S. and VENKATAKRISHNAN(2007) Transient solution of an M/M/2 queue with heterogeneous servers subject to catastrophes, Information and Management Sciences Vol.18(1) 63-80.

EQUIVALENCE OF EXTERNAL ELECTRIC FIELD TO THE SUPER SATURATION RATIO IN PARTICLE NUCLEATION

Shivani Avasthi*
Research Scholar
Department of Physics, Gurukula Kangri University
Hardwar, 249404, Uttrakhand, India
Email: avasthi.s2@gmail.com
Contact no.: 09899654677
Corresponding Author

P. P. Pathak
Professor
Department of Physics, Gurukula Kangri University
Hardwar, 249404, Uttrakhand, India
Email: pathakpp77@yahoo.co.in

ABSTRACT

Under suitable conditions of temperature and external electric field, theory of drop growth has been applied to water vapor condensation and nucleation. The radius of critical nucleus is found to depend upon external electric field and relaxation time. In further studies, in absence of electric field, Helmholtz free energy of for-mation of minute water droplets and ice crystals about a critical nucleus is found to be greater than that in presence of electric field; but equilibrium concentration of nuclei is found to be much large. Consequently, observations at different conditions suggest that a small value of electric field has similar effect as very high super saturation ratio to find a nucleus of given size under similar conditions of temperature.

Keywords: *Atmospheric electricity, atmospheric particles, Helmholtz free energy, heterogeneous nucleation, homogeneous nucleation, nucleation rate*

1. INTRODUCTION

Electric field estimation in troposphere clouds show that super cooled liquid water drops and fro-zen drops can coexist at very low temperatures down to -400 C[1] with an incidence of ice particles already at rather warm temperatures of -40 C [2]. Homogeneous freezing of solution drops formed on soluble cloud condensation nuclei will not play an important role at temperatures above -350 C [3].

It is well known fact that there exists an electric field in atmosphere during fair weather which influences many atmospheric processes[4]. Thunderclouds are known to have additional strong electric fields. The electric field so generated may affect the rate of condensation of water vapour and ice nucleation. Various mechanisms of cloud electrification have been reviewed which infer that the thundercloud electrification is still not a resolved problem[5].

Wang studied about the collection efficiency of atmospheric aerosols or rain drops[2]. The collec-tion of charged aerosols by a conducting sphere in an external electric field and enhancement in the collection efficiency of various shaped aerosol particles by hydrometeors under thunderstorm conditions (as compared with fair weather electric field) throw light on the importance of the electric fields[6] [7]. It has been reported that the electric field influences the nucleation process[8].

Large positive cluster ions (mass ≤ 2500amu) were detected in the upper troposphere for the first time using a large ion mass spectrometer[9]. The most common ions measured were composed of water, acetone, and proton. Two larger modes were also detected. The lesser of these could be explained by the uptake of sulphuric acid but there were insufficient amounts of condensable gases to explain the largest measured particles by any other means than attachment of small aerosols to the ion clusters. The required concentration of these aerosols was 2.5 104 cm-3 which strongly indicated that the ions participated in the formation of nuclei. Many years of work on ions in the free troposphere and stratosphere was summarized and major cluster ions were reported containing sulphuric acid, nitric acid, acetone and water[10].

Nucleation is basically a competition between the growth and evaporation of molecular clusters. For a stable cluster to be formed, an initial energy barrier must be overcome and this barrier is due to surface tension of cluster[11]. The height of this barrier is determined by the temperature and concentration of the nucleating clusters[12]. Nucleation is a thermally activated process which leads to a stable fragment of the condensed phase.

2. THEORETICAL CONSIDERATION

Near the ground, ions are produced mainly by ionizing radiations of radioactive substances such as thoron and radon. Ions play an important role in cloud condensation and ice nucleation in the atmosphere. In the process of nucleation the fundamental quantity of importance is the Helmholtz or Gibb's free energy of germ formation. At normal electric fields, the electrostatic energy of germ formation is very small compared to the volume and surface energy terms. It becomes appreciable only at high electric field at which breakdown of air might occur. The critical size of the droplet is achieved quickly.

Whenever droplets are formed inside the cloud, strong updrafts try to give them a vertical motion. All the drops are not of the same size and they have a downward vertical motion under gravity, resisted by the viscosity of air. The viscosity is given by the equation

$$6\,\pi\eta\, r\, vT = mg = 4\pi r^3\, \rho w\, g/3 \qquad (1)$$

Where η is the viscosity of air, r is the radius of the drop, vT the terminal velocity, ρW the density of water, m the mass of the drop and g the acceleration due to gravity. From Eq. (1), we have

$$vT = 2\, r^2\, \rho w\, g/9\eta \qquad (2)$$

Thus terminal velocity depends on square of radius of droplet; the bigger drops have a tendency to fall down faster than the smaller ones. So, the drops in the updraft have different velocities and they sweep past each other.

Consequently, the larger hydrometeor comes down and the smaller is taken up by updraft. The cloud thus becomes negatively charged at its bottom and positively at its top.

In the present paper, we examined, theoretically, the effect of external field on water vapour con-densation to estimate the radius, number of water molecules, Helmholtz or Gibb's free energy of germ formation of nucleus and the equilibrium concentration of critically sized nuclei. Further, equivalence has been made between electric field and super saturation ratio.

3. HOMOGENEOUS NUCLEATION

3.1. In absence of ion and electric field In classical liquid drop model, the Gibb's function has been taken into account for the formation of a drop. Abraham and Dufour have shown that the Helmholtz or free energy is the proper ther-modynamic potential and Gibb's function is only the approximation of Helmholtz's function[13]. Practically the differences turn out to be negligible at constant temperature. However, it is not a constant pressure process. We may assume that the required phase change occurs at constant temperature. Thus, the energy for the formation of nucleus is given by

$$\Delta F_w = 4\pi r2_w \sigma_{w/v} - 4\pi r3_w \Delta F_{vol.} / 3 \qquad (3)$$

Where, r_w is the radius of the spherical water nucleus, σw/v surface free energy per unit area of water nucleus in water vapour (surface tension), ΔFvol, the volume free energy of condensate per unit volume per mole.

Here $\Delta F_{vol} = {}_{\rho w} R\, T \ln S_{V.W} / M_w$

With ρ_w, density of water, T the temperature, M_w the molecular weight of water, R the universal gas constant and SV.W the super saturation ratio of water vapour over water surface

The critical radius for the uncharged case is obtained to be

$$rc = 2\, M_w\, \sigma_{w/v} / (\rho_w R\, T \ln S_V.W) \qquad (4)$$

And the number of water molecules in a critical nucleus is given by

$$n_c = 4\pi r3_c \ \rho N / 3 M \quad (5)$$

$$S_{V.W} = e/ e_{sat.w}$$

Corresponding to the maximum Helmholtz free energy for the critical radius of nucleus, we have

$$\partial \Delta F_w / \partial r_w = 0 \quad (6)$$

N, being the Avogadro number.

Therefore, critical free energy for uncharged droplet can be written as

$$\Delta F_c = 4\pi r2_c \ \sigma_{w/v} /3 \quad (7)$$

The equilibrium concentration of these nuclei is given by

$$C(n_c) = C\,(1)_0 \exp [- \Delta F_c / kT] \quad (8)$$

Where, C (n_c) represents the concentration of nuclei with nc water molecules in critical nuclei, $C(1)_0$ the concentration of monomers, and k the Boltzmann constant.

Table 1

values of r_c , n_c, F_c and $\ln[C(1)_0/C(n_c)$ as the function of temperature and supersaturation ratio (in absence of electric field)

S_{vw}	r_c ($\times 10^{-10}$m)	n_c	ΔF_c ($\times 10^{-19}$ J)	$\ln[C(1)_0/C(n_c)]$
		T = 273 K		
1.1	119.78	240966	432.88	11490.15
1.2	62.61	34414	118.27	3139.30
1.3	43.51	11549	57.12	1516.16
1.4	33.93	5477	34.73	921.86
1.5	28.15	3128	23.91	634.66
		T = 260K		
1.1	125.76	278889	477.22	13300.45
1.2	65.74	39838	130.40	3634.34
1.3	45.69	13374	62.99	1755.57
1.4	35.62	6337	38.28	1066.89
1.5	29.56	3622	26.37	734.95
		T =250 K		
1.1	130.79	313709	516.16	14961.16
1.2	68.37	44813	141.05	4088.41
1.3	47.51	15037	68.11	1974.20
1.4	37.05	7131	41.42	1200.58
1.5	30.75	4077	28.53	826.96
		T = 240 K		
1.1	136.24	354583	560.07	16910.33
1.2	71.22	50654	153.05	4621.07
1.3	49.49	16996	73.90	2231.28
1.4	38.59	8058	44.93	1356.58
1.5	32.03	4608	30.96	934.78

3.2. In presence of electric field Eisenberg and Hobbs reported that water is strongly polarizable medium with electric dipole moment 1.83×10^{-21} C.m-1[7]. Applications of an electric field will induce an electric dipole moment on embryo of water as well as the surrounding water vapour molecules. The moment induced on drop is given[14]

$$P = E\, r_w^{\ 3} \quad (9)$$

Where, r_w is the radius of droplet and E the inducing electric field. The moment P_1 induced on the water vapour molecule is given by

$$P_1 = \alpha E_1 \qquad (10)$$

Where, α is the polarizability.

Comparing Eqs. (9) and (10), α is written in units of r^3C (m^3), although, it is very correct that α has units of dipole moment per electric field as is evident from Eq.(10).

The expression for rate of increase has been derived as

$$dr'_C /dt = (\rho v/\rho w) [9\alpha\lambda E^2 /(m_w \; r,_C)]^{1/2} \qquad (11)$$

Where, λ is the mean free path, E the electric field, mw the mass of water vapour molecule, ρv the density of water vapour and r,c the radius of water nucleus in electric field.

Integrating the above equation within limits

$r,_C = 0$ to $r,_C = r^*_C$ (critical radius of nucleus)

and $t = 0$ to $t = \tau$ (relaxation time)

we get,

$$r^*_C = [3 \rho_v \tau (9\alpha\lambda E^2 /m_w)1/2 / 2 \rho w]^{2/3} \qquad (12)$$

Analogically in electric field, Eqs. (5), (6) and (7) for the energy of formation and equilibrium concentration, become

$$N^*_c = 4\pi r^*3c .\rho N /3 M \qquad (13)$$

$$\Delta F^*_C = 4\pi r^{*2}_C .\sigma_{w/v} /3 \qquad (14)$$

And

$$C (n^*_C) = C (1)_0 \exp [- \Delta F^*_c / kT] \qquad (15)$$

Table 2

values of r^*_c, n^*_c, F^*_c and $\ln[C(1)_0/C(n^*_c)$ as the function of temperature and supersaturation ratio (in presence of electric field)at T= 273 k

$E \times 10^5 Vm^{-1}$)	$r^*_c (\times 10^{-10}$ m)	n^*_c	$\Delta F_c (\times 10^{-19}$ J)	$\ln[C(1)_0/C(n^*_w)]$
		$\tau = (5\times 10^{-6}$ S)		
1.5	5.75	27	0.99	26.38
1.8	6.49	38	1.27	33.71
2.1	7.19	52	1.56	41.41
2.4	7.86	68	1.86	49.37
		$\tau = (6\times 10^{-6}$ S)		
1.5	6.49	38	1.27	33.71
1.8	7.33	55	1.62	43.00
2.1	8.12	75	1.99	52.82
2.4	8.88	98	2.38	63.17
		$\tau = (7\times 10^{-6}$ S)		
1.5	7.19	52	1.56	41.41
1.8	8.12	75	1.99	52.82
2.1	8.99	102	2.44	64.77
2.4	9.84	133	2.92	77.51
		$\tau = (8\times 10^{-6}$ S)		
1.5	7.86	68	1.86	49.37
1.8	8.88	98	2.38	63.17
2.1	9.84	133	2.92	77.51
2.4	10.76	174	3.49	92.64

3.3. Equivalence between electric field and super saturation ratio In absence of external electric field, a critical nucleus of a particular radius is obtained from Eq. (4) whereas in presence of electric field the radius is given by Eq. (12). If the same size of nucleus is obtained in two cases, then R.H.S. of these two Eqs. [i.e. Eqs (4) and (12)] may be equated to get

$$2\,M\,\sigma_{w/v} / (\rho_w\, RT \ln S_{V.W}) \quad = \quad [3\,\rho_v\,\tau\,E\,(9\alpha\lambda/m_w)^{1/2} / 2\,\rho_w\,]^{2/3} \qquad (16)$$

This reduces to

$$E_{eq}^{2/3} \ln SV.W \;=\; 2\,M\,\sigma_{w/v}\,[3\rho_v\,(9\alpha\lambda/m_w)^{1/2}/2]^{-2/3}/\,R\,\rho_w 1/3\,T\tau^{2/3} \qquad (17)$$

Equation (17) may be written as

$$E_{eq}^{2/3} \ln S_{V.W} \;=\; K, / T\tau^{\,2/3} \qquad (18)$$

Where, E_{eq} is equivalent electric field and K, is a constant which is given by

$$K, = 2M\,\sigma_{w/v}[3\,\rho_v\,(9\alpha\lambda/m_w)^{1/2}/2]^{-2/3}/\,R\rho_w^{\,1/3} \qquad (19)$$

For a given value of temperature and relaxation time, Eq. (18) becomes

$$E_{eq}^{\,2/3} \ln S_{V.W} \;=\; K,, \qquad (20)$$

where, $\quad K,, \;=\; K, / T\tau^{2/3}$

From Eq. (20), we have

$$\ln S_{V.W} \;=\; K,,/\,E_{eq}^{\,2/3} \quad \text{or } S_{V.W} = \exp\,[K,,/E_{eq}^{\,2/3}] \qquad (21)$$

Which shows that the super saturation ratio varies exponentially with equivalent electric field.

Table 3

values of E_{eq} corresponding to $S_{v,w}$ for given r'^*_c as the function of τ and T

$S_{v,w}$	r'^*_c ($\times 10^{-10}$m) and E_{eq} ($\times 10^5$ Vm^{-1}) at temperature							
	273 K		260 K		250 K		240 K	
	r'^*_c	E_{eq}	r'^*_c	E_{eq}	r'^*_c	E_{eq}	r'^*_c	E_{eq}
				$\tau = (5\times 10^{-6}$ S)				
1.1	119.78	142.69	125.76	153.54	130.79	162.84	136.24	173.12
1.2	62.61	53.94	65.74	58.03	68.37	61.55	71.22	65.43
1.3	43.51	31.24	45.69	33.62	47.51	35.65	40.49	37.91
1.4	33.93	21.51	35.62	23.15	37.05	24.55	38.59	26.09
				$\tau = (6\times10\text{-}^{6}$ S)				
1.1	119.78	118.92	125.76	127.94	130.79	135.70	136.24	144.27
1.2	62.61	44.95	65.74	48.36	68.37	51.29	71.22	54.53
1.3	43.51	26.04	45.69	28.01	47.51	29.71	40.49	31.59
1.4	33.93	17.93	35.62	19.29	37.05	20.46	38.59	21.75
				$\tau = (7\times10\text{-}^{6}$ S)				
1.1	119.78	101.93	125.76	109.67	130.79	116.32	136.24	123.67
1.2	62.61	38.53	65.74	41.45	68.37	43.96	71.22	46.74
1.3	43.51	22.32	45.69	24.01	47.51	25.47	40.49	26.27
1.4	33.93	15.37	35.62	16.53	37.05	17.54	38.59	18.64
				$\tau = (8\times 10\text{-}^{6}$ S)				
1.1	119.78	89.18	125.76	95.96	130.79	101.77	136.24	108.20
1.2	62.61	33.71	65.74	36.27	68.37	38.47	71.22	40.89
1.3	43.51	19.53	45.69	21.01	47.51	22.28	40.49	23.69
1.4	33.93	13.44	35.62	14.46	37.05	15.34	38.59	16.32

Table 4

values of $(S_{V,W})_{eq}$ corresponding to E for a given r'^*_c as the function of τ and T

E ($\times 10^5$ Vm^{-1})	r'^*_c ($\times 10^{-7}$ m)	Equivalent supersaturation ratio $(S_{V,W})_{eq}$ at			
		273 K	260 K	250 K	240 K
		$\tau = (5 \times 10^{-6}$ S)			
1.5	5.75	7.30	8.00	8.76	9.58
1.8	6.49	5.80	6.29	6.82	7.39
2.1	7.19	4.89	5.31	5.64	6.05
2.4	7.86	4.27	4.62	4.90	5.21
		$\tau = (6 \times 10^{-6}$ S)			
1.5	6.49	5.80	6.29	6.82	7.39
1.8	7.33	4.75	5.16	5.26	5.92
2.1	8.12	4.08	4.34	4.62	4.95
2.4	8.88	3.62	3.89	4.09	4.39
		$\tau = (7 \times 10^{-6}$ S)			
1.5	7.19	4.89	5.31	5.64	6.05
1.8	8.12	4.08	4.34	4.62	4.95
2.1	8.99	3.55	3.78	4.01	4.26
2.4	9.84	3.19	3.39	3.56	3.74
		$\tau = (8 \times 10^{-6}$ S)			
1.5	7.86	4.27	4.62	4.90	5.20
1.8	8.88	3.62	3.89	4.09	4.39
2.1	9.84	3.19	3.39	3.56	3.74
2.4	10.76	2.89	3.06	3.19	3.35

4. RESULTS AND DISCUSSION

In the present calculations the constant values used are:

$\lambda = 10^{-7}$ m., $\rho_v = 10^{-2}$ kg . m^{-3} at 10^0 c, $\alpha = 5 \times 10^{-29}$ m.^{3}, $\rho_w = 1000$ kg.m^{-3}, $m_w = 3.0 \times 10^{-26}$ kg., R = 8.314 J.mole-^{1}K-^{1} , $\sigma_{W/V} = 72 \times 10$-3 j.m^{-2}, N = 6.023 10^{23}, k = 1.38 10^{-23} J.K-^{1} and constant K, = 447.6.

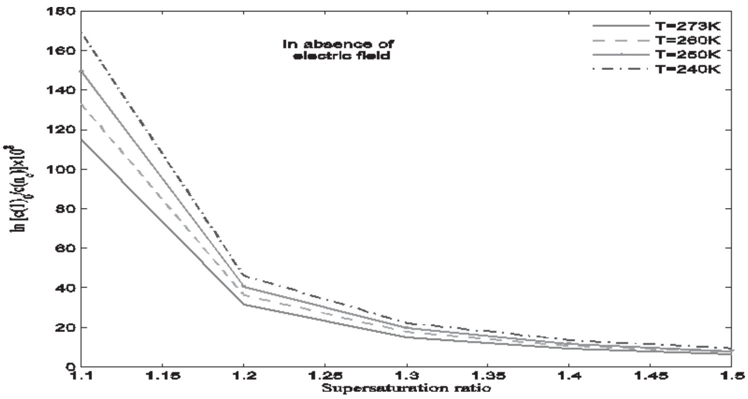

Fig 1- Variation of natural log of ratio of equilibrium concentration of mono-mers and critical nuclei with super saturation ratio as the function of temp, in absence of electric field

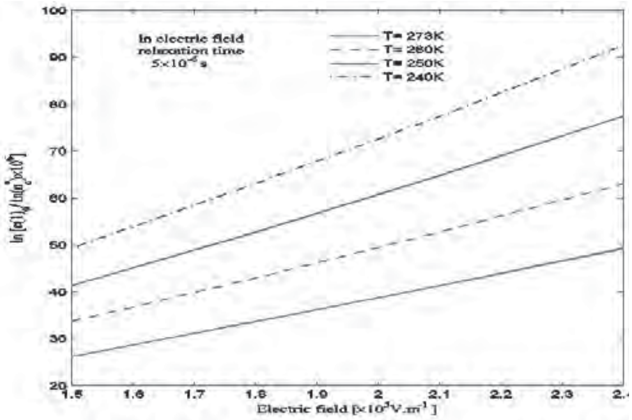

Fig. 2- Same as Fig 1, but for the variation with electric field at relaxation time 5 ×10^{-6} s, in presence of electric field

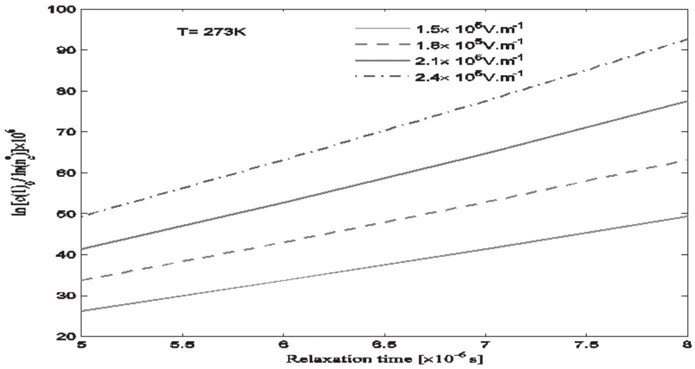

Fig. 3 - Same as Fig. 1, but for the variation with relaxation time as the function of electric field at T=273k

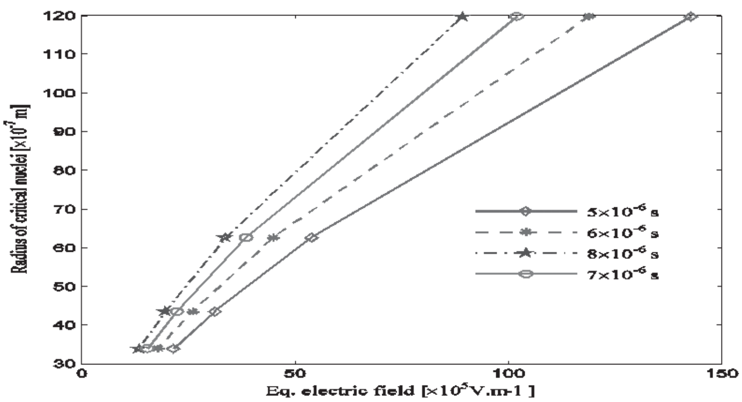

Fig 4- Variation of radius of critical nucleus with equivalent electric field as the function of relaxation time and super saturation ratio at T=273k , in absence of electric field

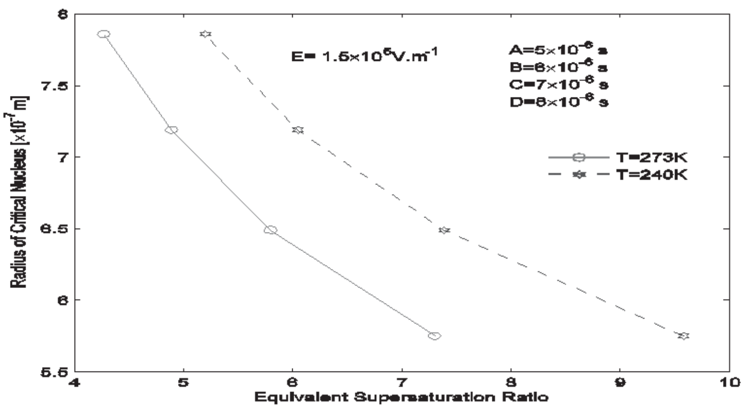

Fig 5- Variation of radius of critical nucleus with equivalent super saturation ratio as the function of temp. and relaxation time at E=1.5 × 105 V.m^{-1}

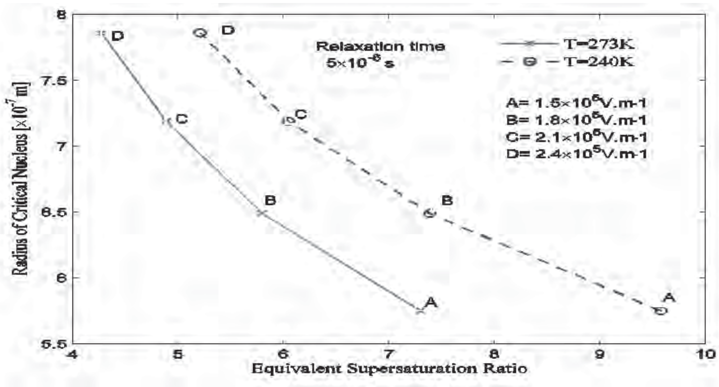

Fig. 6 - Same as Fig. 5, but as the function of temp. and electric field at τ= 5×10^{-6} s

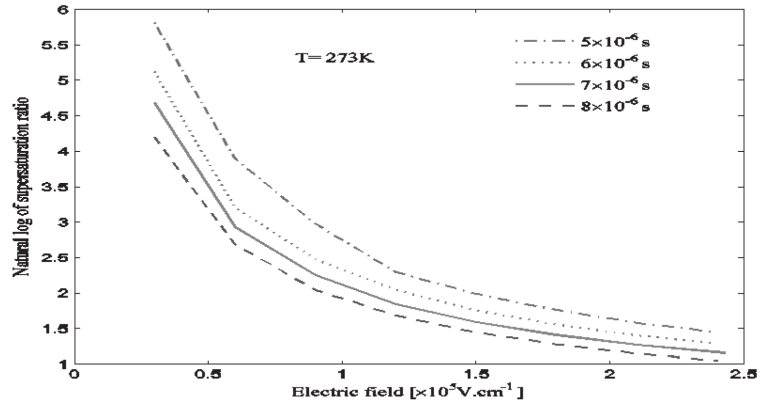

Fig.7- Variation of natural log of super saturation ratio with equivalent electric field s the function of relaxation time at T= 273k

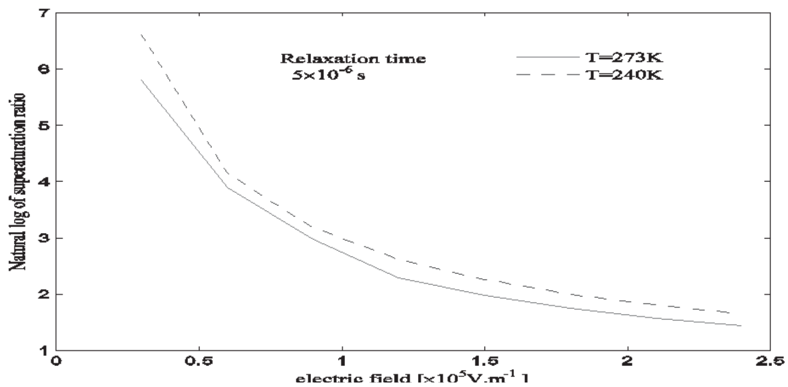

Fig. 8 - Same as Fig. 7, but as the function of temp. at τ= 5×10^{-6} s

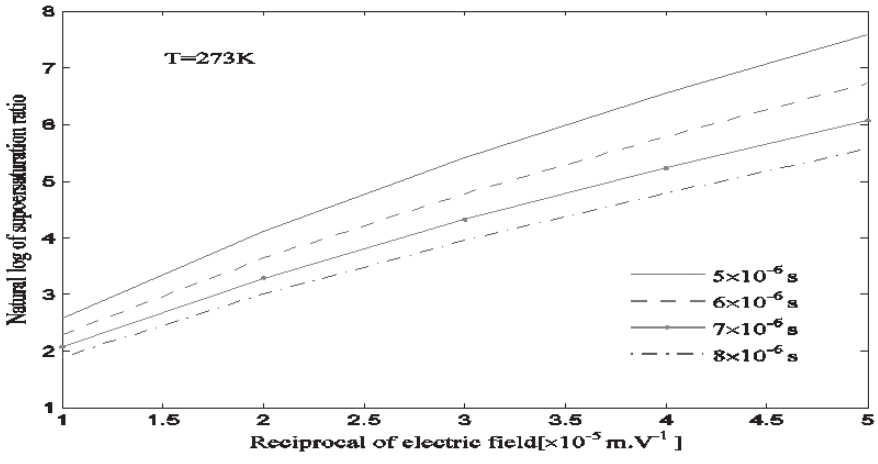

Fig.9- Variation of natural log of super saturation ratio with reciprocal of electric field as the function of relaxation time at T=273k

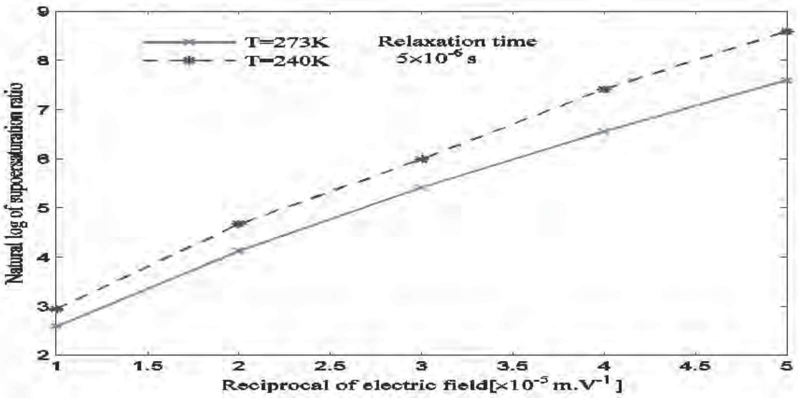

Fig. 10 - Same as Fig. 9, but as the function of temp. at τ= 5×10^{-6} s

Table (1) and (2) express the radius, number of water molecules in a critical nucleus, Helmholtz free energy of formation, and the equilibrium concentration of critical nuclei as the function of temperature and the super saturation ratio in absence and in presence of electric field, respective-ly.

From these tables we observe that at a given temperature, r^*_c, n^*_c, ΔF^*_c and ln[C $(1)_0$/C(n^*_c)] de-crease with increase in super saturation ratio [Table (1)], whereas they increase with increase in electric field [Table (2)]. [Table (1)] also shows that at $S_{V.W}$ =1.1, the values of r^*_c are (119.78, 125.76, 130.79 and 136.24) × 10^{-7}m at 273, 260, 250 and 240 K, respectively.

In presence of electric field, as is obvious from [Table (2)], the values of r^*_c, n^*_c, and ΔF^*_c for a given relaxation time increase with the increase in electric field. They are also found to increase with the increase in relaxation time. Eq (8) gives the equilibrium concentration of critical nuclei of given Helmholtz free energy at a given temperature. This equation may be further written as

$$\ln[C(1)_0/ C(n^*_w)] = \Delta F^*_c / kT \qquad (22)$$

Thus ΔF^*_c / kT measures the natural logarithm of the reciprocal of the equilibrium concentration of critical nuclei to the concentration of water monomers. From [Table (1)] we observe that, in absence of electric field, the quantity ΔF^*_c/ kT decreases with the increase of super saturation ratio and increases with the decrease of temperature, whereas in presence of electric field [Table (2)] it increases with the increase in electric field and relaxation time.

Figure (1) represents the variation of natural logarithm of ratio of equilibrium concentration of water super saturation ratio in absence of electric field as the function of temperature. Fig. 2 and 3 represent, in presence of electric field, the variation of natural logarithm of ratio of equilibrium concentration of monomers and the critical nuclei with electric field and the relaxation time. Fig 4- represent variation of radius of critical nucleus with equivalent electric field as the function of relaxation time and super saturation ratio at T=273k , in absence of electric field respectively.

Table (3) represents the equivalence of super saturation ratio with the electric field. The equiva-lence depends on temperature and relaxation time as well. For example, in absence of electric field, a critical nucleus of radius 119.78 $\times10^{-7}$m is formed at temperature 273 K and at super saturation ratio 1.1 [using Eq. (4)]. The same size of the nucleus would have been obtained in presence of electric field of 142.69×10^5 Vm^{-1} with relaxation time 5 $\times10^{-6}$ s [using Eq. (12)]. Thus, we note that super saturation ratio 1.1 at 273K is equivalent to an electric field of 142.69×10^5 V m^{-1} with relaxation time 5 $\times10^{-6}$ s. For a given relaxation time and temperature the equivalent electric field decreases with increase in super saturation ratio. At a given temperature increases with decreasing relaxation times. [Table (3)] also shows that the equivalent electric field increases with decrease in tem-perature corresponding to a given super saturation ratio at constant relaxation time. At a given relaxation time, corresponding to a super saturation ratio, the equivalent electric field increases with decrease in temperature. e. g. for τ = 6×10^{-6} s and $S_{v\,w}$ =1.1, E_{eq} =118.92×10^5, 127.94×10^5 and 135.70×10^5 and 144.27 V.m^{-1} at T=273,260 and 250 and 240 K, respectively (Table 3).

Similarly, Table (4) compares the equivalence of electric field with super saturation ratio as the function of temperature and relaxation times. From [Table (4)], it is clear that at a given relaxation time and temperature, the equivalent super saturation ratio decreases with increase in electric field. Also, the equivalent super saturation ratios increase with decrease in temperature corresponding to a given electric field at constant relaxation time. [Table (4)] also shows that the equivalent super saturation ratio at a given temperature and electric field decrease with increasing relaxation time. The variation of radius of critical nucleus with equivalent super saturation ratio has been shown in fig 5 and 6 as the functions of temperature and relaxation times' and 'temperature and electric field', respectively.

Equations (3.15)-(3.20) represent the equivalence between electric field and super saturation ratio for the formation of a given size of the critical nucleus, although, the equivalence depends on tem-perature and the relaxation time.

Figs. 7 and 8 represent the variation of super saturation ratio with electric fields as the functions of relaxation time and temperature, respectively. Fig. 7 shows that at a given temperature and electric field, the values of equivalent super saturation ratio decrease with increase in relaxation times. At T = 273K and E =3×10^4 V.m^{-1} the values of ln $(s_{vw})_{eq}$ are ,5.81, 5.12, 4.68, 4.20 at relaxation times 5×10^{-6} s , 6 $\times10^{-6}$ s, 7 $\times10^{-6}$ s and 8$\times10^{-6}$ s, respectively. Similarly, Fig. 8 exhibits that a given relaxation time and electric field, the natural logarithm of super saturation ratio varies inversely as the temperature. For example, at τ = 5×10^{-6} s, E= 1.2 $\times10^5$ V m^{-1} , the values of ln$(s_{vw})_{eq}$ Are 2.30 ,2.62 at T= 273 and 240 K, respectively. The values corresponding to 250 and 260 K are not shown in Fig 8.

At a given temperature and relaxation time Eq. (18) becomes as

$E_{eq}^{2/3}$ ln SV.W = K” (23) Where, K” is constant depending upon the temperature and relaxation time. The variation of natural logarithm of super saturation ratio with reciprocal of electric field has been shown in Figs 9 and 10 as the function of relaxation time and temperature, respectively.

5. CONCLUSION

From the above study, it is concluded that the nucleation of water droplets in electric field is very much effective. A small external electric field is equivalent to very large value of super saturation ratio, which, otherwise, never exists in the clouds. Also, in electric field induced nucleation, the critical nuclei of smaller size are found pertaining to smaller number of water molecules and require less energy for formation. Hence, equilibrium concentration of critical nuclei is enhanced as compared to the electric field-free case of nucleation. Also, from the equivalence of super satura-tion ratio with electric field, it is evident that electric field is more efficient than super saturation. This explains the rain gush after lightning.

REFERENCES

1. Abraham, F. F., A re-examination of homogeneous nucleation theory: Thermodynamic aspects. J. Atmos. Sci., **25**, 1968, p.47-53.
2. Arnold, F., Atmospheric aerosol and cloud condensation nuclei formation: a possible in-fluence of cosmic rays?, Space Sci. Rev., **125**, 2006, p.169–186.
3. Eichkorn, S., Wilhelm, S., Aufmhoff, H., Wohlfrom, K. H. & Arnold, F., Cosmic ray-induced aerosol-formation: First observational evidence from aircraft-based ion mass spectrometer measurements in the upper troposphere, Geophys. Res. Lett., **29**, 2002, p.43.
4. Enghoff , M. B. & Svensmark, H., The role of atmospheric ions in aerosol nucleation – a review, Atmos. Chem. Phys., **8**, 2008, p.4911–4923.
5. Harrison, R. G. & Ambaum H. P. M., Observed atmospheric electricity effect on clouds, Enviro. Res. Lett. **4**, 2009, p.1-5.
6. Hobbs, P.V., Ice physics. Oxford Uni. Press, Oxford, 1974.
7. Heymsfield, A. J. & Sabin, R.M., Cirrus crystal nucleation by homogeneous freezing of solution droplets. J. Atmos. Sci. **46**, 1989, p.2252-2264.
8. Heymsfield, A. J., Sabin, R. M. & Miloshovich, L. M., Homogeneous ice nucleation and super cooled liquid water in orographic wave clouds, J. Atmos. Sci., **50**, 1993, p.2335- 2353.
9. Jensen, E.J., Ice nucleating processes in upper tropospheric wave-clouds Observed dur-ing SUCCESS. Geophy. Res. Lett., **25**, 1998, p.1363- 1366.
10. Kittel, C., Introduction to solid state physics. John Wiley and sons, New York, 1977, p.401-409.
11. Parmar, D.S. & Jalaluddin, A. K., Determination of the limit of absolute Thermodynamic stability of liquid using external electric field as perturbation. Phy. Lett.. **42 A**, 1973, p.497-498.
12. Wang, P. K., Grover, S. N. & Pruppacher, H. R., On the effect of electric charges on the scavenging of aerosol particles by clouds and small raindrops. J. Atmos. Sci. 35, 1978, p.1735-1743.
13. Wang, P.K., Collection of aerosol particles by a conducting sphere in an external elec-tric field continuum regime approximation, J. Colloid. Interface Sci., **94**, 1983, p.301-318.
14. Williams, E. R., Large-scale charge separation in thunderclouds. J. Geophy. Res., **90**, 1985, p.6013- 25.

EXPERIMENTAL INVESTIGATION ON 3D-FIN UNDER NATURAL AND FORCED CONVECTION

Rupali Tupkar*
Assistant Professor
Department of Mechanical Engineering
Priyadarshini College of Engineering, Nagpur, India
E-mail: rupali_tupkar@rediffmail.com
Contact No. 9420959437
Corresponding author

Manisha Lande
Assistant Professor
Department of Mechanical Engineering
Priyadarshini College of Engineering, Nagpur, India
E-mail: landemanisha@yahoo.com
Contact No. 9665843292

Sneha Tahilyani
Assistant Professor
Department of Aeronautical Engineering
Priyadarshini College of Engineering, Nagpur, India
E-mail: snehatahilyani@gmail.com
Contact No. 8983431586

ABSTRACT

Cooling fins are devices that enhance the heat dissipation from a hot surface to a cooler ambient, usually air in the case of heat generating component. All electronic components generate heat during the course of their operations. Both the performance reliability and life expectancy of electronic equipment are inversely related to the component temperature of the equipment. The relationship between the reliability and operating temperature of a typical electronic device shows that a reduction in the temperature corresponds to an exponential increase in the reliability and life expectancy of the device.

In this work, 3D-fin made up of aluminum is used to find out the temperature distribution, heat transfer, efficiency and convection coefficient experimentally in natural and forced convection. Then 3D-fin model is analyzed on the ANSYS Software. The temperature distribution in natural and forced convection are obtained experimentally and the results are validated by using ANSYS software to find out the temperature distribution in natural and forced convection .From the graph, the results of temperature obtained from experimental and simulations in natural and forced convection correlate rather well with each other.

Keywords: *ANSYS, dissipation, 3D-fin, convection*

1. INTRODUCTION

Fins are used to enhance convective heat transfer in a wide range of engineering application. Fins are commonly applied for heat management in electrical appliances such as computer power supplies or substation transformer. Other application include I.C. engine cooling such as fins in a car radiator. It is important to predict the temperature distribution within the fin in order to choose the configuration that offer maximum effectiveness.[1].

An electronic component such as microprocessor chip generates considerable amount of heat. Hence the best way for cooling it is by using a heat sink with fins.

Heat sink is a device usually made of metal brought into contact with the hot surface of a component, such as microprocessor chip, to help cool that component through the thermal dissipation by convection, Typically made of aluminum, heat sinks are widely used in electronics and computers, and have become almost essential to modern central processing unit. [3] We choose the fin cooling of an electronic component as it is economical and helps dissipating large amount of heat from the component, we decided aluminum as the material because of low cost, also, aluminum can be easily milled and is very light.[4]

In this project we find out that, the temperature distribution, heat dissipation from the fin in both natural and forced convection and then validating the temperature distribution in natural & forced convection by using ANSYS

2. EXPERIMENTAL WORK

Body frame made up of M.S. Sheet having the size of 450 x 450 x 600mm. Front portion of the frame is cut by machine having size of voltmeter and ammeter size of 45 x 90mm. Temperature indicator having size of 90 x 90mm. Dimmer having Ø 150mm. Toggle switch having Ø 15mm. All this components fit into the gap.

Figure 1 shows the 3D. fin used in electronic cooling. Base plate is of 0.1015m x 0.048m x 0.0035m and the thickness of the fin is 0.0015m and L is length of the fin and W is the width of the fin. Which is to be fabricated with extrusion of aluminum.[7]

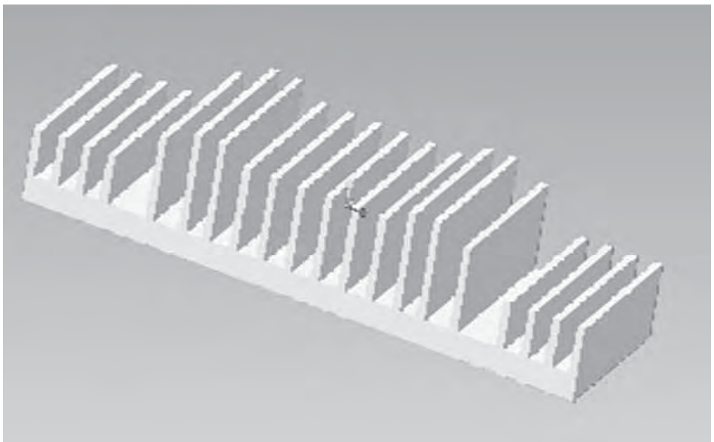

Figure1: 3D-Fin Used In Electronic Cooling

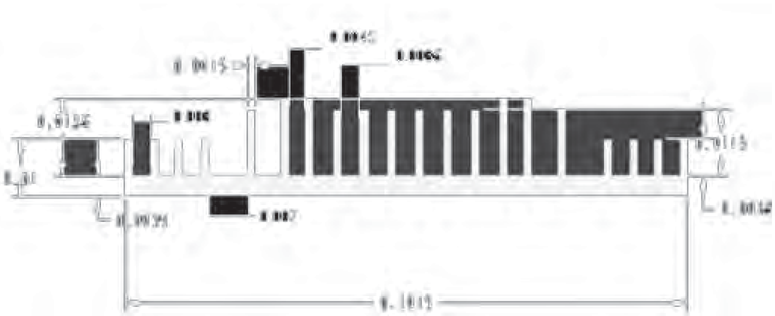

Figure2: Front View

Figure 3:Top View

All Dimensions Are In Meter

Detail information of 3D fin is summarised in “table 1”

Table 1. Information of 3D Fin

Property Name	Symbol	Property value	Unit
fin length	L	0.0065 0.0115 0.0135	m m m
Fin Width	W	0.048	m
Fin Thickness	t	0.0015	m
Distance between the fins	S	0.003 0.007 0.0045 0.0035	m m m m
Number of fins	N	20	
Thermal conductivity of Aluminum	K_{Al}	235	w/mk
Height of plate	H	0.1015	m

Asbestos sheet is cut. To this sheet hole is drawn in such way that horizontal distance between the two holes is 0.003m up to the length of 0.1015m and vertical distance between the two holes is 0.048m (means the same size of base plate of the 3D-Fin). Then mica is put on that asbestos sheet and tungsten wire drawn from this hole as shown in figure 4

Figure 4 : Heater

Then 3D-fin is put on that heater and tightened with screw as shown in figure 5

Figure 5 : 3D Fin With Heater

Exhaust fan (50 watt) is put at a height of 10cm from the 3D-fin in such way that the airflow is perpendicular to the width of the fin. For that four strips is welded from the side of 3D-fin. Fan having five number of blades which is shown in figure 6.

Figure 6 : 3D Fin With Fan

Thermocouple (K type copper constant) is attached to the temperature indicator (0-400°c) to find out the temperatures. Input is given to the heater with the help of voltmeter (0-230volt) and ammeter (0-20 Ampere) and input is varied with the help of dimmer-stat (0-2Amp). Complete set up is shown in figure 7.

Figure 7 : Experimental Set Up

3. OBSERVATION TABLE

3.1 Natural Convection

Table 2. Observation Table For Natural Convection

Sr. No	Voltage (Volt	Current (Amp)	Temperature in º C											
			T1	T2	T3	T4	T5	T6	T7	T8	T9	T10	T11	T12
1)	17	0.3	44	42	42	42	42	42	44	49	50	49	52	39
2)	24	0.42	50	48	48	48	48	48	50	61	63	61	65	44
3)	29	0.52	58	55	55	55	55	55	58	73	75	73	78	49
4)	34	0.59	65	61	61	61	61	61	65	84	87	84	91	54
5)	38	0.66	74	70	70	70	70	70	74	96	100	96	104	59
6)	42	0.71	84	81	81	81	81	81	84	110	115	110	117	64
7)	45	0.78	93	90	90	90	90	90	93	120	125	120	130	69

3.2. Forced Convection

Table 3. Observation Table For Forced Convection

Sr. No	Voltage (Volt	Current (Amp)	Temperature in o C												Velocity (m/sec.)
			T1	T2	T3	T4	T5	T6	T7	T8	T9	T10	T11	T12	
1)	17	0.3	37	37	37	37	37	37	37	44	45	44	46	36	0.5
2)	24	0.42	41	41	41	41	41	41	41	52	54	52	56	39	0.5
3)	29	0.52	44	44	44	44	44	44	44	57	59	57	61	42	0.5
4)	34	0.59	47	47	47	47	47	47	47	64	61	64	69	45	0.5
5)	38	0.66	50	50	50	50	50	50	50	67	69	67	73	48	0.5
6)	42	0.71	54	54	54	54	54	54	54	71	74	71	77	51	0.5
7)	44	0.78	56	56	56	56	56	56	56	76	79	76	83	54	0.5

where

T_1 --- Temp. at the tip of 3rd fin
T_2 -- Temp. at the tip of 5th fin
T_3 --- Temp. at the tip of 7th fin
T_4 --- Temp. at the tip of 10th fin
T_5 --- Temp. at the tip of 13th fin
T_6 --- Temp. at the tip of 15th fin
T_7 --- Temp. at the tip of 17th fin
T_8 --- Base temp of the 1st fin
T_9 --- Base temp of the middle fin
T_{10} --- Base temp of the last fin
T_{11} --- Base temp of the plate
T_{12} --- Ambient temperature

4. ANALYTICAL CALCULATION

Rayleigh number is given by

$$Ra_L = \frac{g\,\beta\,(T_S - T\infty)\,L^3}{\nu^2}$$

Nusult Number in Natural Convection is given by

$$Nu_L = 0.68 + \frac{0.67\ Ra}{[1 + (0.492/pr)^{9/16}]^{4/9}}$$

The average heat transfer coefficient (h)

$$h = \frac{K}{L} \times Nu_L$$

Total heat transfer from the fin

$$Q_{(fin)} = h\,A_t \left[1 - \quad (1\text{-}\eta_f)\right] (T_b - T\infty)$$

Where:

η_f = efficiency of the fin

A_t = Total surface area = $NA_f + A_{un}$

A_{un} = Area uncovered = S x w

A_f = Area of the fin = 2 wLc

L_c = Characteristic length

Reynolds number in forced convection is given by

$$Re = \frac{\rho v L}{\mu}$$

μ is Dynamic Viscosity v is velocity of air

The average Nusult Number in forced convection is given by

$$Nu_L = 0.664\ (Re)^{0.5}\ (pr)^{1/3}$$

% Increase in heat transfer rate due to forced convection[5]

$$= \frac{Q_{fin(Forced\ convection)} - Q_{fin(Natural\ convection)}}{Q_{fin(Natural\ convection)}}$$

5. TASKS IN THERMAL ANALYSIS

The procedure for doing thermal analysis involves the main tasks[2]

Build the model

Apply the environment

Solve

Obtain the result

5.1. Input Geometry

(a) Creating model geometry

(b) Set scale in meter

(c) Sketching > Draw > rectangle

Rectangle shows the dimension of Horizontal distance (H) and vertical distance (v).

(d) Modify dimensions

Modify the horizontal distance (H) and vertical distance (v) according to model geometry.

(e) Sketching > Draw > rectangle the size of length of fin.

(f) Modify the dimension according to model geometry.

(g) Extrude that part by giving the length of extrusion.

(h) In this way model geometry is created

5.2. Define Simulation

(a) Define New Material > Thermal conductivity.

5.3 Generate Mesh

(a) Mesh is crated automatically at the solve time.

(b) Element used is quadrilateral in the mesh.

5.4. Apply Environment

12. Apply convection at the tip of the fins.

13. Apply heat flow at the base of model geometry.

5.5 Obtain Solution

(a) Define analysis type.

(b) Solve.

5.6 Obtain Result

(a) Temperature Plot.

(b) Generate report.

(c) Exit the program.

6. ANSYS RESULT IN NATURAL & FORCED CONVECTION

Apply Boundary condition as convection at the tip of the fin is 6.28W/m^2 ^{o}C and ambient temperature as 44^{o}C, heat flow at base of the plate 10.08 Watt in natural convection & model with temperature plot in natural convection as shown in figure 8[6]

Apply Boundary condition as convection at the tip of the fin is 12.56 W/m^2 ^{o}C and ambient temperature as 39 ^{o}C, heat flow at base of the plate 10.08 Watt in forced convection. The thermal conductivity of aluminum 235w/mk. & model with temperature plot in forced convection as shown in figure 9

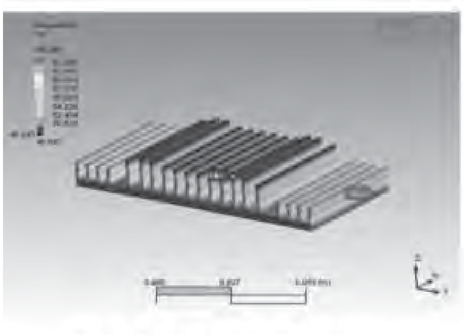

Figure 8 : Model With Temperature Plot In Natural convection

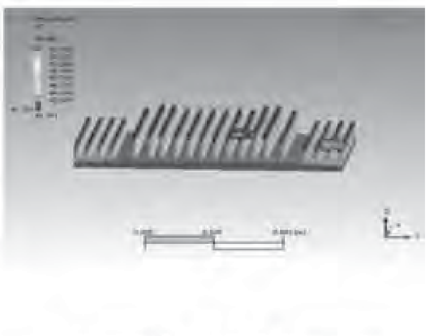

Figure 9 : Model With Temperature Plot In Forced convection

7. RESULT & DISCUSSION

Natural convection

1. Heat transfer coefficient in natural convection h = 6.28 w/m2 oc

2. Efficiency of the fin in natural convection η_{fin} = 0.97

3. Total heat transfer from the fin $Q_{fin(Natural\ Convection)}$ = 2.717 watt

Forced convection

1. Heat transfer coefficient in forced convection h = 12.56 w/m2 oc

2. Efficiency of the fin in forces convection ηfin = 0.95

3. Total heat transfer from the fin $Q_{fin(Forced.\ Convection)}$ = 4.298 watt

% Increase in heat transfer rate due to fins in forced convection =58.18%

Temperatures In Natural & Forced Convection

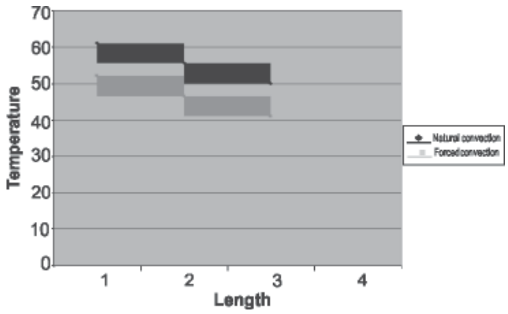

Figure10: Experimental Temperature In Natural And Forced Convection

Temperature IN Natural Convection

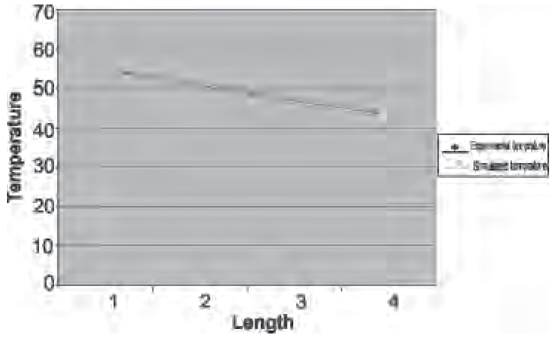

Figure11: Comparison Of Temperature From Experimental,ANSYS In Natural Convection

Temperature In Forced Convection

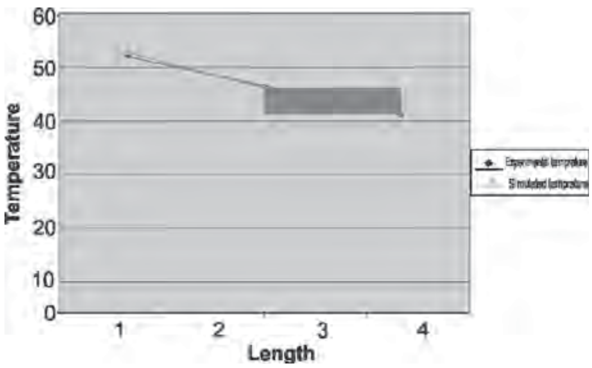

Figure 12 : Comparison Of Temperatures FromExperimental ANSYS In Forced Convection

8. CONCLUSION

From the experiment conducted on 3D-fin, it is found that,

- Giving the same heat input to the 3D-fin in natural and forced convection, temperature distribution decreases in forced convection.
- Convection coefficient increases in forced convection.
- % Increase in heat transfer rate due to fins in forced convection is 58.18%.

The 3D-fin model is analyzed on the ANSYS Software. The temperature distribution in natural and forced convection is obtained experimentally and the results are validated by using ANSYS software to find out the temperature distribution in natural & forced convection.

Also from the graph, the result of temperature obtained from experimental and simulations in natural and forced convection shows good agreement with each other. It is concluded that decreasing the temperatures, the life of the component increases. In a nutshell, forced convection in electronic cooling is more efficient than natural convection

REFERENCES

1. David P. Dewill, Frank P. Incropera “Fundamentals of Heat and Mass transfer” Fifth edition.
2. D.V. Hutton “Fundamentals of finite element analysis”
3. Incropera and Dewitt D.P. “Fundamentals of heat and mass Transfer.” 4th Edition.
4. Lee, serri“How to select a heat sink, Advid thermal technologies Inc. Laconia, new Hampshire”
5. S.B. Thombre“Data book of thermal Engineering”Green Brains Publication.
6. D.A. Anderson, J.C. Tannehill and R.H. Pletcher, computational fluid mechanics and heat transfer, Hemisphere, washington D.C. 1984.
7. Lee, serri “Optimum design and selection of heat sinks” IEEE Transactions on Components, packaging and manufacturing part A, Volume 18, No.4, December 1995.

QUANTIFICATION OF RIVERBED EXTRACTION AND MORPHOMETRIC CHARACTERIZATION OF TINAU RIVER, NEPAL

Khet Raj Dahal*
PhD Scholar
Kathmandu University, Department of Environmental Science and Engineering, Nepal
Head of Department (Civil)
Kantipur Engineering College, Lalitpur, Kathmandu, Nepal
E-mail: dahal.khetraj@gmail.com
Corresponding author

Chandra Prakash Poudyal
Assistant Professor
Kathmandu University, Department of Civil and Geomatics Engineering
P.O. Box: 6250, Dhulikhel, Kavre, Nepal
E-mail: cppoudyal@ku.edu.np

Hari Prasad Guragain
Sub-Division Chief
Department of Irrigation, Sub-division Office, Udaypur, Nepal
E-mail: hari.guragain1@hotmail.com

ABSTRACT

The study was conducted in the Tinau River during the period of March, 2011 to April, 2012. The detailed leveling survey was carried out to find the longitudinal and cross-sectional profiles of the river. The length of the selected reach was 25.54 Km. The study showed that the river morphology has been changed during the period of 2004 to 2012. The massive extraction of riverbed materials in the Tinau River has also occurred during this period. The effects of extraction were river incision, exposure of bridge piers and wash out of minor river training structures. The average incision of the Tinau River was found to be 3.31 m. Similarly, the width of the river was found to be narrowed in different changes of the study reach due to over extraction and encroachment of flood plain area.

Key words: *Riverbed materials, encroachment, river incision, Tinau River, Nepal.*

1. INTRODUCTION

BACKGROUND: Rivers and river banks reflect the cultural heritage and economic prosperity of the people living along their course. They also reflect the respect that the people have towards nature, environment, and an understanding of the ecological process[1]. Standing on this concept, Tinau reflects the cultural and historical heritage of Butwal and the surrounding villages and towns of this area.

The Tinau River is a perennial river originated from Lemthem Phant of Palpa district. The highest elevation of its watershed is 1496 m (Okharkot) and the lowest elevation is 175 m. The basin area of the Tinau is 1081 Km2.The River lies in Terai, Siwaliks and the Mahabharat range of west Nepal[2]. The headwaters of the Tinau River lie on the southern slopes of the Mahabharat range in Palpa district. The head reach is covered with mixed forest and settlements of Madi Phaant. There are several tributaries of Tinau river system. However, the major tributaries of Tinau River are Dobhan Khola, Sisne Khola, Bhaiskatta Khola, and Jhumsa Khola. The majority of these tributaries join the main Tinau before the confluence of Dobhan Khola. Then the river flows from north to south through a gorge section of Churia hills before entering into the Terai plain at Butwal. In this reach, the slope of the river is significantly steep. As the river debouches into Terai plain, it spreads into a wet piedmont fan and splits into two distributaries viz. Tinau and Dano[3].

As the river passes through the mountains and hills of the Palpa district, it carries plenty of sandy sediments with it. The major sources of sediments in Tinau are landslides, erosion and rock falls. As the Tinau enters into the Terai plain the stream power decreases significantly further downstream causing wide spread deposition of sediments in the form of alluvial fan. The sediments are useful for the construction of engineering infrastructures and are being used since the time of immemorial. The sediment faces in the fan includes channel bar and point bar, which serve as natural levees of around 3 m high.

During the normal flow regime of the river, sedimentation process proceeds through the sedimentation of bedload, but during extreme hydrological condition and massive inundations, the sedimentation is sheet flood, suspended load of finer sediments. Sediments are particulate inorganic materials transported by water from upstream sources to downstream areas of deposition. These materials are produced by the process of weathering and Erosion of Mountains or rocks. Then these are carried in rivers or streams as suspended load or bed load. The flood, carrying heavy sediment from the catchment area, drops down the sediments when it comes out of the gorges to the plains at nearby Butwal city[4]. Extraction of construction materials starting from the downstream of Butwal city heavily affects sedimentation process , which causes change in river morphology.

There are no systematic and official records of riverbed extraction. The history differs from country to country and depends on other development activities too. But the riverbeds were extracted in ancient times for the collection of Gold, Diamond and Gem[5]. However, the history of riverbed extraction for using the raw materials started since 1963-1964[1]. Riverbed extraction is a practice that has been found to have extreme impact in aquatic environment or in river environment [6]. The damage to the existing ecosystem caused mining needs to be properly adaptive to river dynamics.

River morphological processes refer to the interaction between water and sediment. The capability of the water in the river to transport the sediment supplied to it determines the dominant river processes for a specific reach of the river. If there is a disequilibrium between supply and transport capacity the river needs to adjust new hydraulic characteristics as width, depth, slope, affecting the process of aggradations (deposition) and degradation[7]. This indicates that the extraction of riverbed materials must be coherent with river morphology and sedimentology to conserve overall river morphology. However, the annual extracted volume of riverbed materials was much more than the volume of deposition in the Tinau River during last decade. Thus, the objectives of this study is to know the changing pattern of sedimentation and river morphology, existing bed level dynamics, and variation in depth, width caused by extraction, and subsequent deposition in downstream as bars.

2. MATERIALS AND METHODS

FIELD WORK: The field survey was conducted by a team. The work was carried out during the period of March 2011 to April 2012. The level survey was done to find the longitudinal profile and cross section of the selected reach of the river. The selection of the first station (upstream) was considered as less disturbed site and the intermediate stations especially from downstream of Tinau Bridge at Butwal to the Tinau Bridge at Bethari as much disturbed sites. A 25.540 Km stretch of the Tinau River was selected for the detail survey (Figure 1). The level of all the stations was recorded and calculated the reduced level referring locally developed bench mark. Nine numbers of chainages (Figure 1) were selected to measure the width and cross-sections of the river. The longitudinal profile and cross-sections of the selected stations were prepared. The bed level obtained from the field survey was compared with the past level.

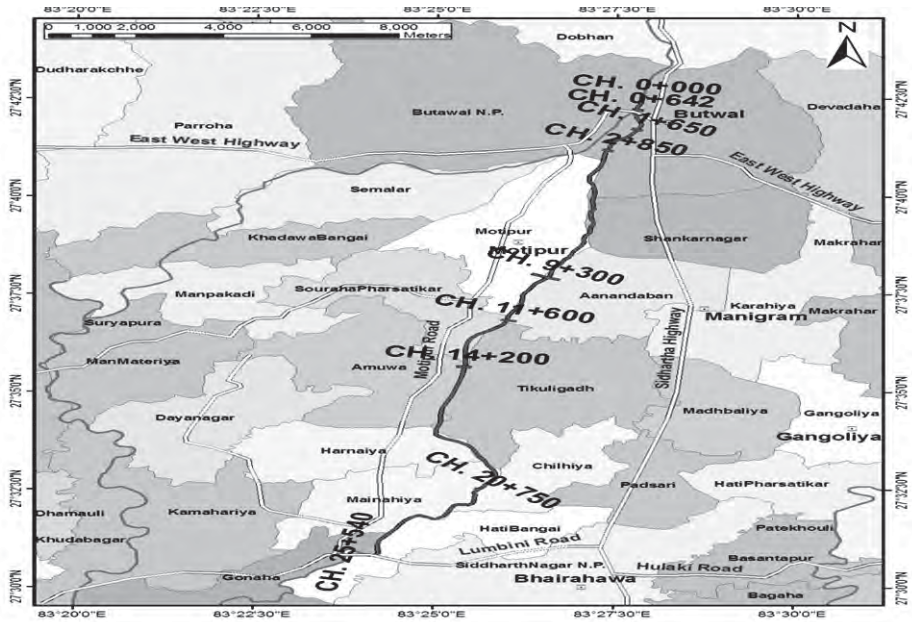

Figure 1: Map showing study reach along with the selected chainages

The survey was started at Chainage 0+000 and ended at Chainage 25+540. The details of the stations and chainage are presented in Table 1.

Table 1: Name of the station and chainage selected for the field survey

S.N.	Chainage(CH)	Name of the Station
1	0+000	Kanyadunga
2	0+642	Tinau Bridge at Butwal
3	1+650	Itiyabhode
4	2+850	Hattisund Suspension Bridge
5	9+300	Manigram Bridge axis (under construction)
6	11+600	Near Manigram
7	14+200	Amuwa Bridge axis (under Construction)
8	20+750	Near Sonare Suspension Bridge
9	25+540	Tinau Bridge at Bethari

Similarly the present width of the river was measured and compared with the past width. The past width was obtained from Google earth, 2003.

3. RESULTS AND DISCUSSIONS

The river is degraded due to extraction. However, the degradation is different from station to station (Table 2). The higher the degradation, higher is the rate of extraction and quantity of withdrawal materials.

Table 2: Details of river degradation due to extraction

Chainage	**Old bed level, m**	**Present bed level, m**	**Degradation, m**	**Station**
0+000	182.04	180.26	1.78	Kanyadunga
0+642	177.31	172.72	4.59	Tinau Bridge at Butwal
1+650	169.76	165.42	4.34	Itiyabhode
2+850	160.34	152.04	8.3	Hattisund Suspension Bridge
9+300	124.71	122.25	2.46	Manigram Bridge axis (under construction)
11+600	118.68	116.76	1.92	Near Manigram
14+200	117.61	115.13	2.48	Amuwa Bridge axis (under Construction)
20+750	106.83	103.97	2.86	Near Sonare Suspension Bridge
25+540	100.13	99.08	1.05	Tinau Bridge at Bethari
Average degradation = 3.31 m.				

Local Self Governance Act and Regulation (1999 and 2000)[9, 10] has provided the right for Local Administrative Bodies (LAB) to use the natural resources within their territory for their development. Thus, the LABs started to use the riverbed materials in a huge quantity without any restriction and consideration of sensitive area. They collected a considerable amount of money from riverbed materials. An overview of income generation from the riverbed materials during past six years (2005-2010) is presented in Table 3

Table 3: Income Generated by Local Bodies from Riverbed Materials.

S. N.	**Local Body**	**2005**	**2006**	**2007**	**2008**	**2009**	**2010**	**Total Income (NRs.)**	**Income, USD ($)**
1	**P. Amawa**	1444082	1013203	3397268	3226775	1526950	3676500	14284778	160521
2	**Shankarnagar**	4661150	4512528	6645561	3288742	4320880	7424110	30852971	346702
3	**Aanandaban**	4697530	5598399	5703860	7924000	7957953	10665265	42547007	478110
4	**Tikuligadh**	4560000	3688000	4483700	6700000	8196000	9180090	36807790	413617
5	**Chilhiya**	805000	1246832	1317753	1460425	1725000	2431000	8986010	100978

6	**HatiBangai**	1246100	1040000	2120500	1152500	1924060	1745000	9228160	103699
7	**Motipur**	550688	768938	1371570	1767000	1458159	1775200	7691555	86432
8	**Farsatikar**	587666	848316	1950878	648000	1682500	972000	6689360	75170
9	**Mainahiya**	366900	123622	430915	448399	568516	272000	2210352	24838
10	**Gonaha**	449700	470617	469508	389667	2320200	2345000	6444692	72420
11	**Butwal Municipality**	75098308	75915110	96363923	77479638	162355008	155145847	642357834	7218315
12	**DDC Rupandehi**	59451551	60720688	64918062	69969900	161794140	158705120	575559461	6467687
Total (NRs.)		153918675	155946253	189173498	174455046	355829366	354337132	1383659970	15548489
Equivalent, USD (1 $=NRs. 88.39)		1729618	1752402	2125784	1960389	3998532	3981763	15548488	

Source: DDC (2011) modified by Dahal et al. (2012)

The natural resources like sand, gravel and boulders are the good sources of income and revenue generation. Many districts of the Terai (15 districts) and some of mid-hills like Makawanpur, Kavre, Udayapur, Bhaktapur, Kathmandu, Dhading, Kaski and Nuwakot are also the potential districts for riverbed materials. However, it raises the external cost too. The total revenue from the riverbed materials in the last fiscal year (2009/10) was 1 billion, whereas the repair and maintenance cost of the road was 11 billion[11]. Due to over extraction of riverbed materials, has caused steeping of longitudinal profile in upstream, which gradually decreases to downstream (Figure 2).

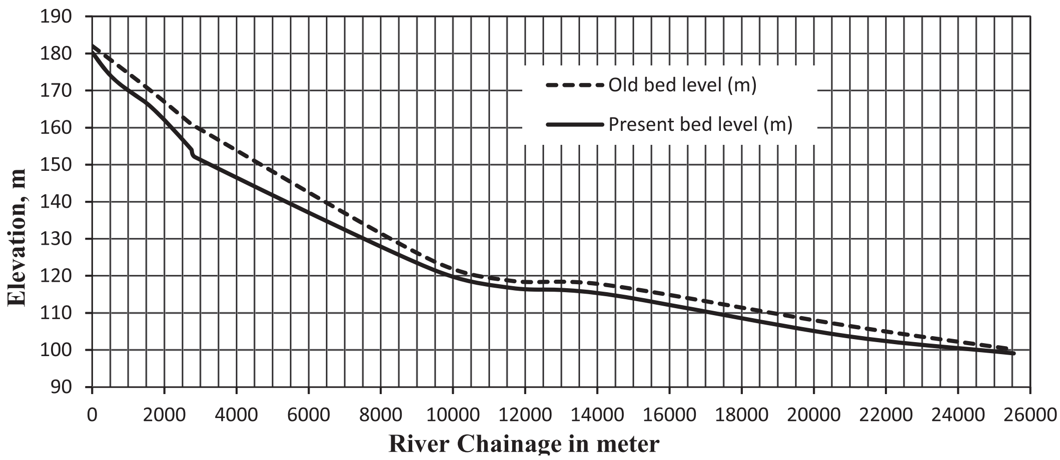

Fig. 2: Longitudinal degradation of river morphology (Source: field survey, 2012 and Guragain, 2012)

Tinau being a potential for riverbed materials, mining of these materials started (in a massive way) from last decade using excavators. Though there existed the mining of riverbed materials since quarter of century[2]. However, heavy machines entered into the river only in 2004. From 2004, the contractors and crusher mill owners used excavators to extract the raw materials from the river. The riverbed materials also exported to India in a huge quantity since the period of 2004-2011[9]. The deficit of sediment in the river obtained about 53.50 % (Figure 3).

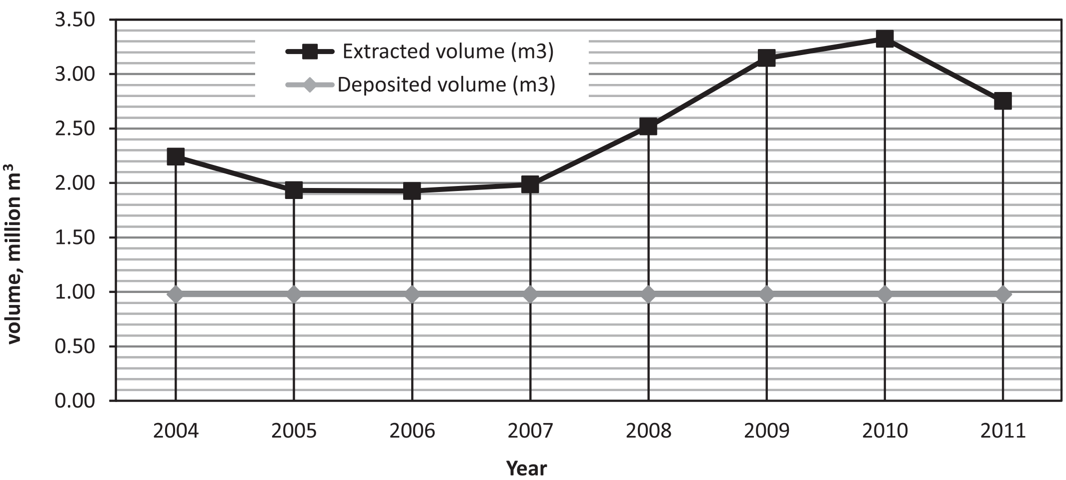

Figure 3: River-bed extraction during the period of 2004-2011 (Source: DDC).

During field survey nine stations were chosen to quantify the size of the river widths at various points. The level was taken for each section. According to the survey data the width and depth curve was plotted (Figure 4, Figure 5, Figure 6, Figure 7, Figure 8, Figure 9, Figure 10 and Figure 11 and Figure 12). It shows that the river floodplain area is encroached and the construction industrialists confined to extract the materials in a narrow width of the river. Thus the river incised. As the river incised, it became safe to live the river dwellers. In the past, when there was no active riverbed extraction, the encroachment of the flood plain area was not seen along the bank of the Tinau. After 2004 to date the landless and land broker increased in geometric series. As a result, there are about 4000 households settled in the flood plain area along the study reach[2].The average land occupied by one household is 0.5 ha[11, 12]. According to this rate of land holding, the total sum of land comes to a quantity of 2000 ha. In reality, it is the flood plain area of the Tinau River.

The width of the river has decreased consistently throughout the chainages (stations) except for chainage 1+650, where special riverbed use practice was adopted. In this station, there was canal headwork (temporarily) of Sorha Mauja Farmer Managed Irrigation System (FMIS) located and the area was protected from encroachment. The construction materials of good quality and quantity could be found there. However, the illegal extraction was heavy in depth and width causing to anomalous widening of the river valley. As a result, extra widening and deepening of river took place during the course of time causing functional damage of the headwork. The length of such stretch is about 300 m. The river width seemed constant in chainage 0+000 during this period because there is a heavy protection measures on either sides of the river.

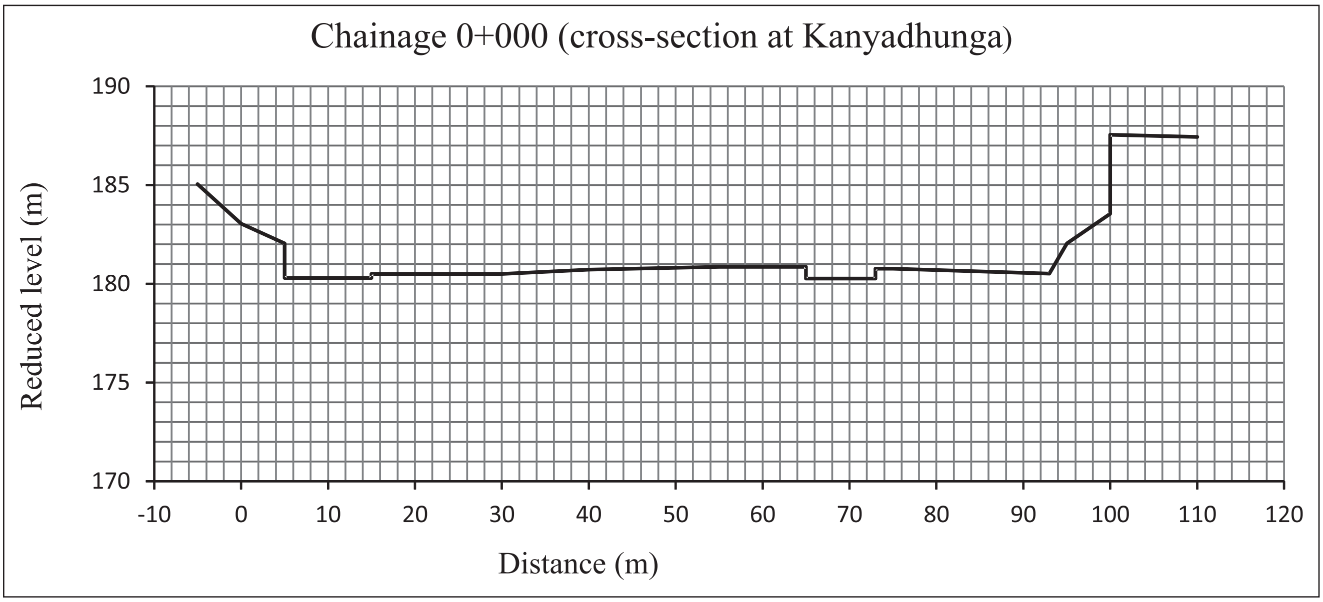

Figure4: Cross section at chainage 0+000 (Source: field survey, 2012)

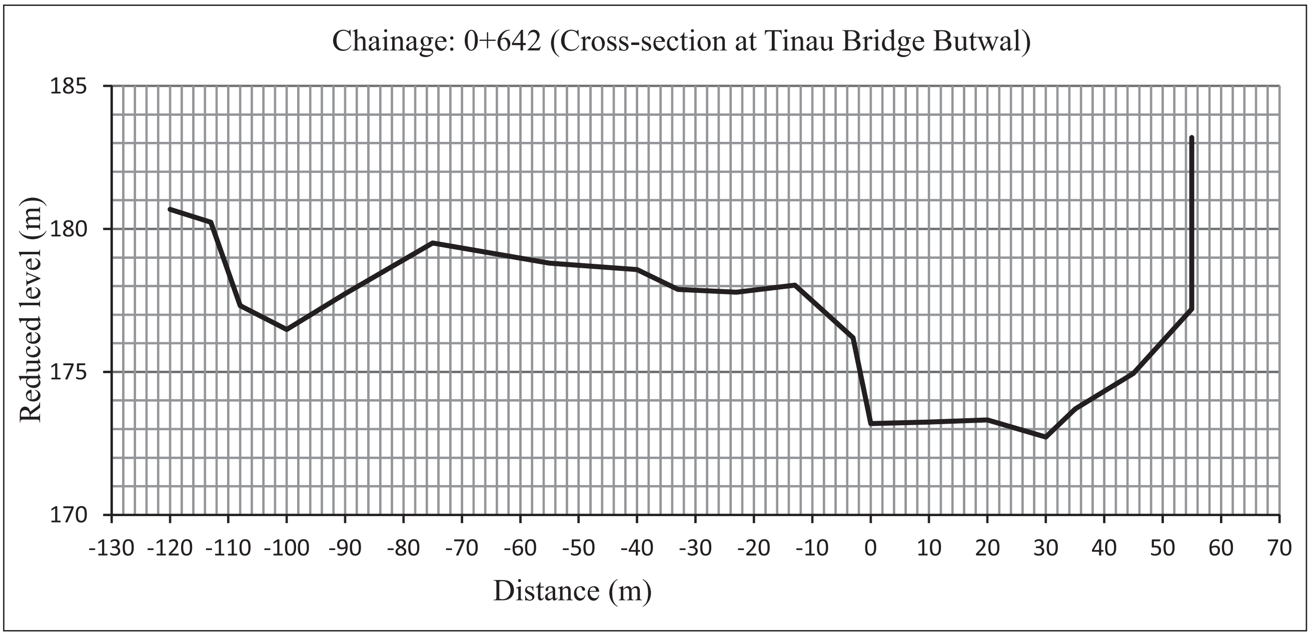

Figure 5: Cross section at chainage 0+642 (Source: field survey, 2012)

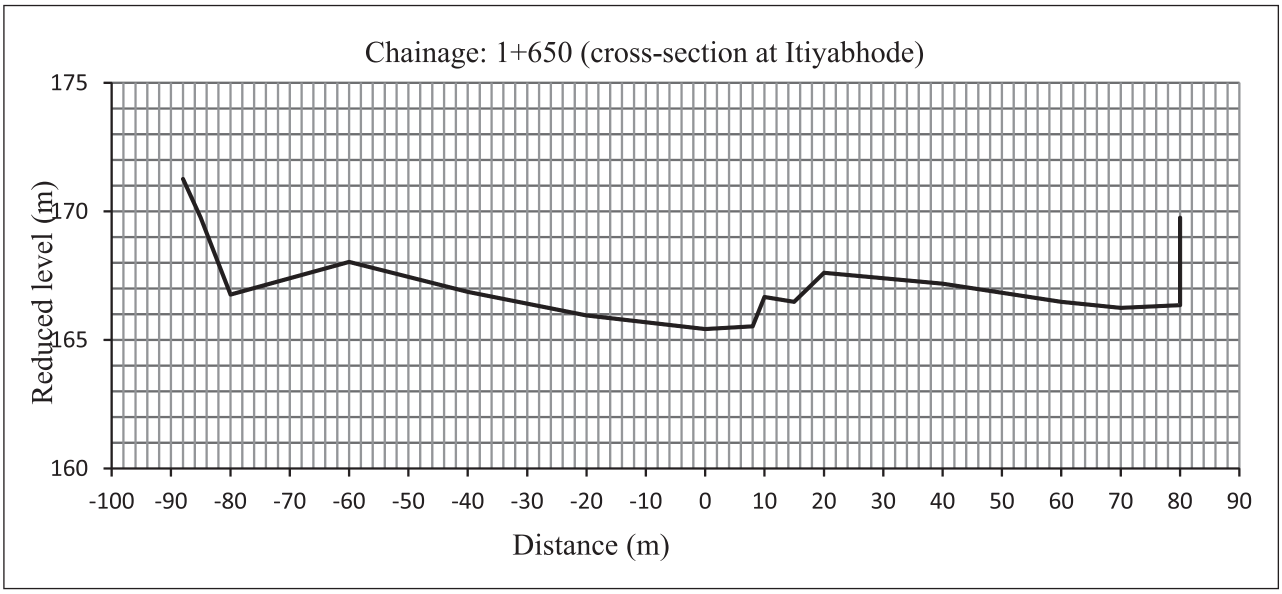

Figure 6: Cross section at chainage1+650 (Source: field survey, 2012)

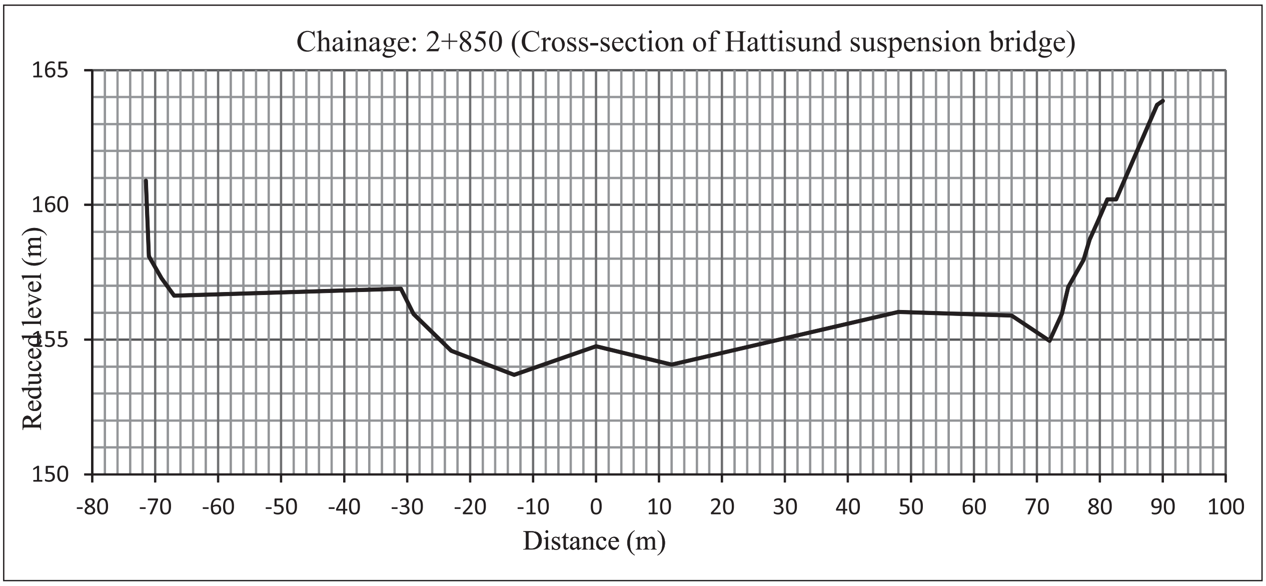

Figure 7: Cross section at chainage 2+850 (Source: field survey, 2012)

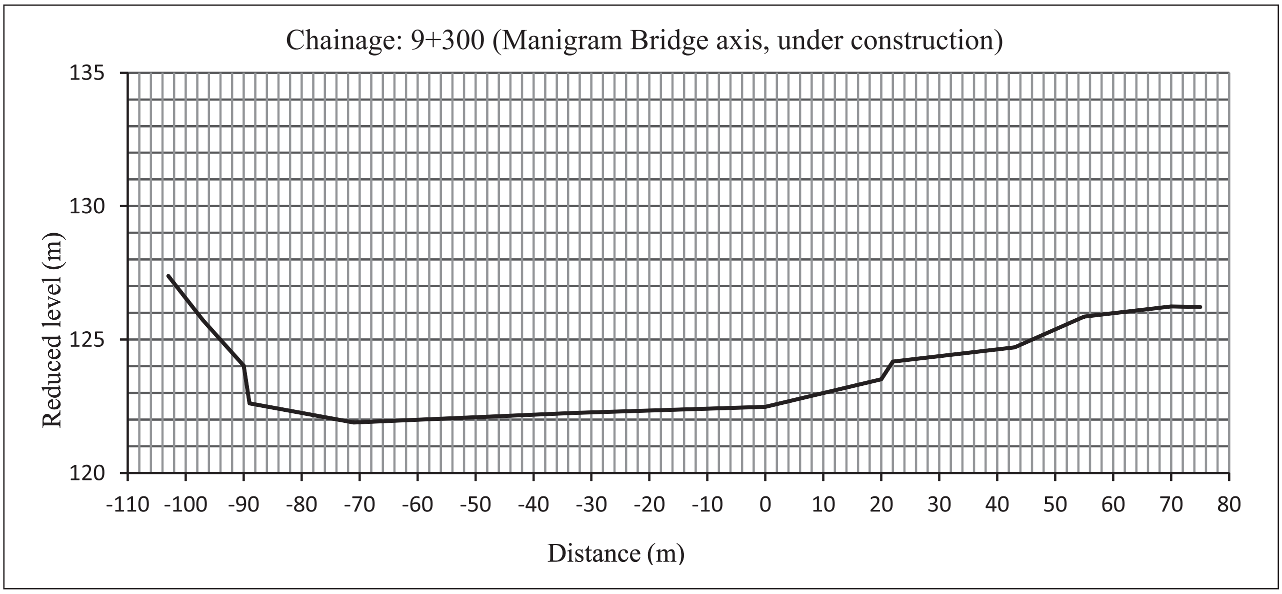

Figure 8: Cross section at Chainage9+300 (Source: field survey, 2012)

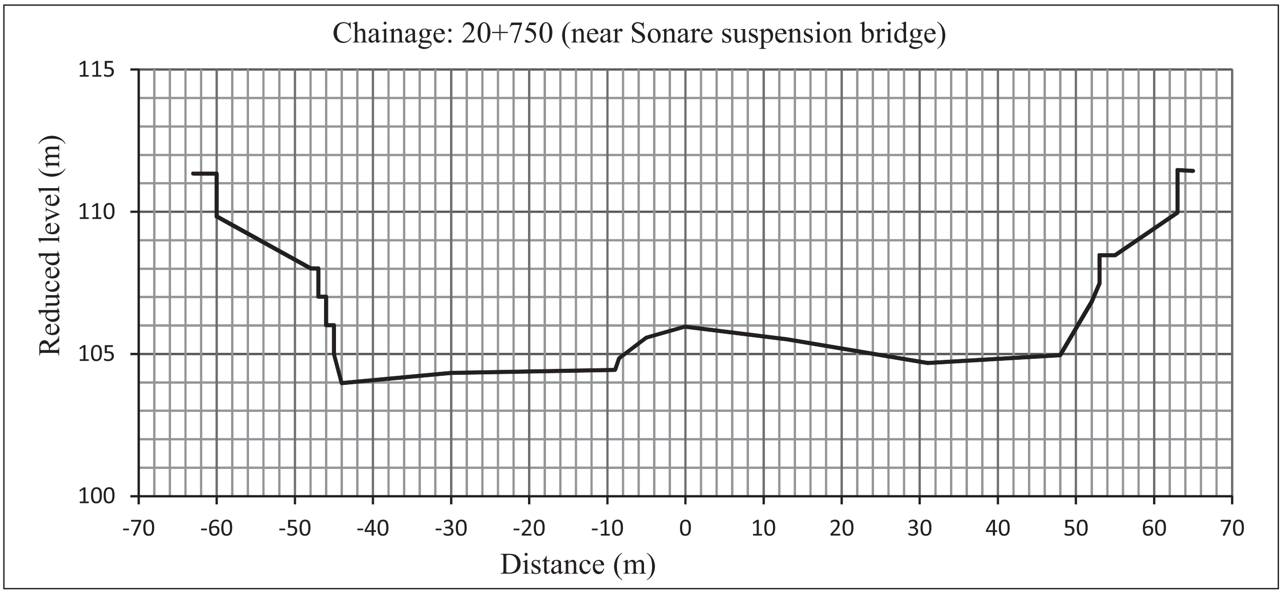

Figure 9: Cross section at Chainage 11+600 (Source: field survey, 2012)

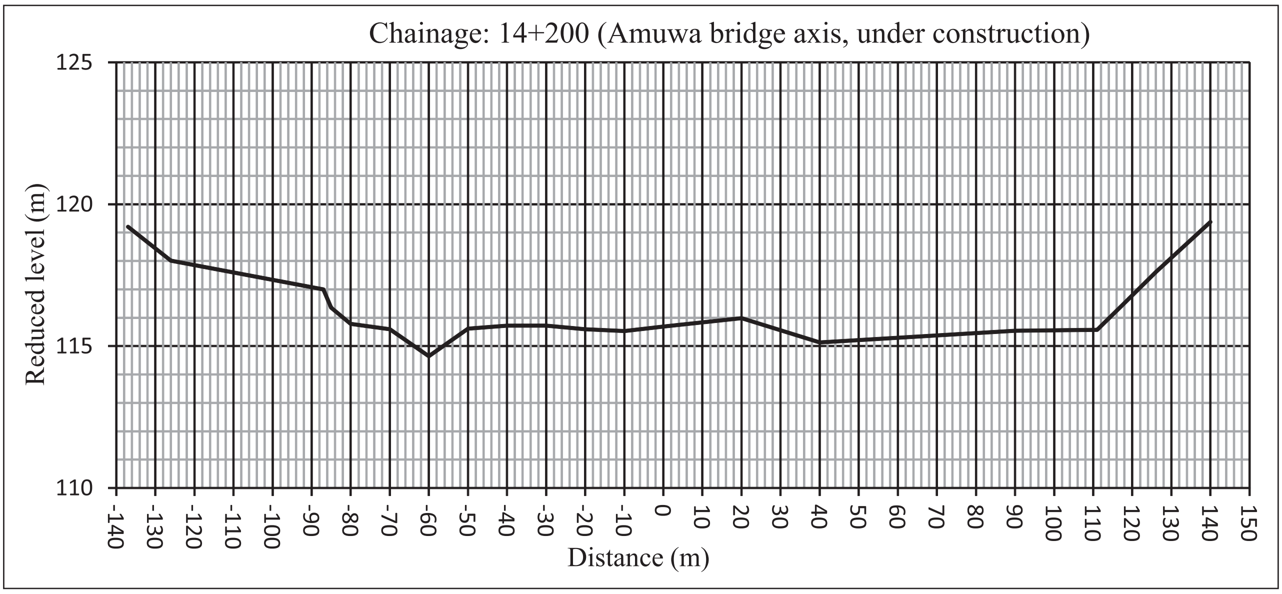

Figure 10: Cross section at Chainage 14+200 (Source: field survey, 2012)

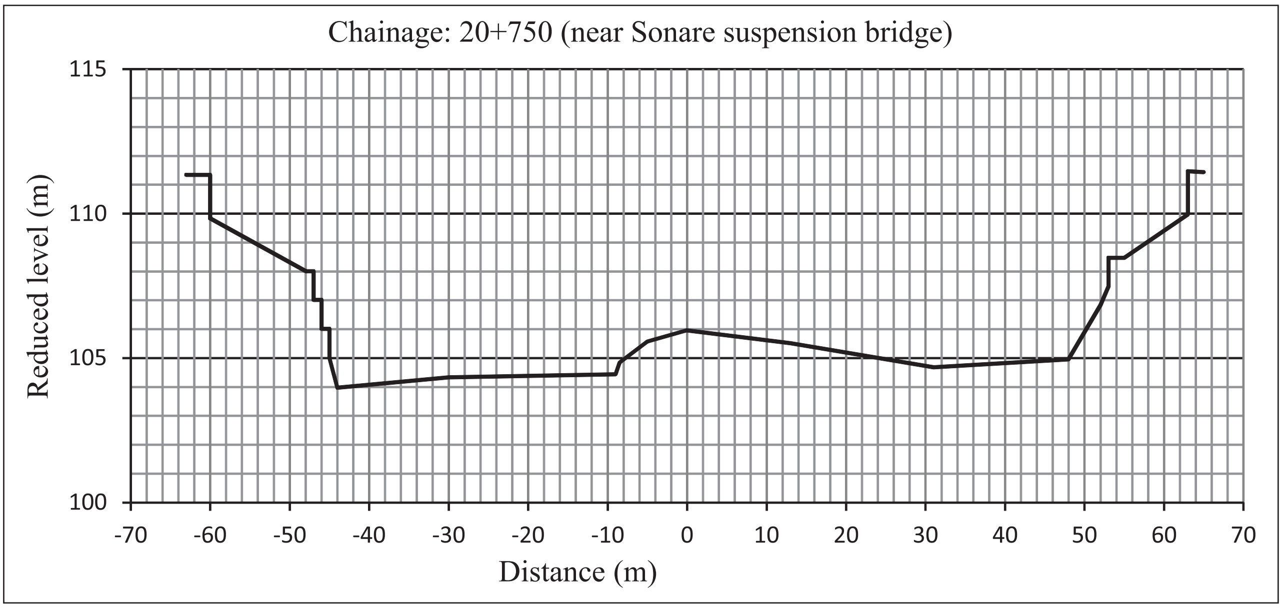

Figure 11: Cross section at Chainage20+750 (Source: field survey, 2012)

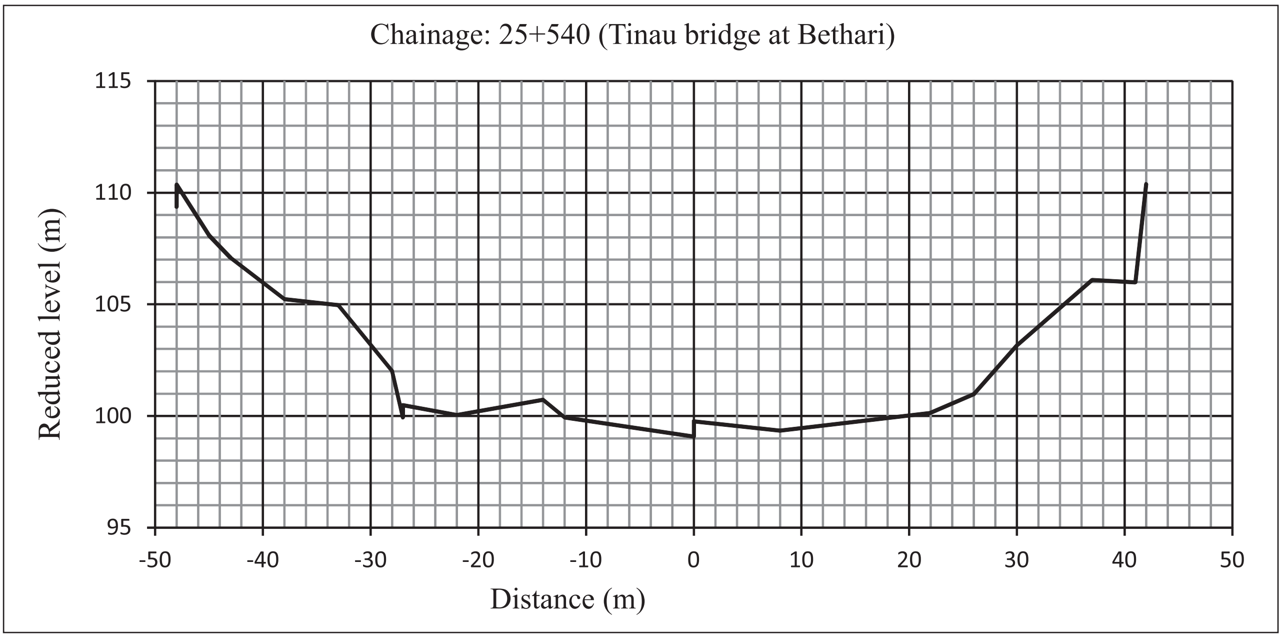

Figure 12: Cross section at chainage 25+540 (Source: field survey, 2012)

The above cross-sections of chainage 0+000 to chainage 25+540 were compared with the past width obtained from the Google earth. The details of the comparison is presented in Table 4.

Table 4: Comparison of present width of the river with the past

S.N.	**Chainage (km+m)**	**Longitude**	**Latitude**	**Width, m**			**Name of the station**
				In 2003	**In 2012**	**Difference, m**	
1.	0+000	83027’05”	27042’34”	100	100	0	Kanyadunga
2.	0+642	83027’47”	27047’13”	178	175	-3 (1.68%)	Tinau Bridge at Butwal
3.	1+650	83027’47”	27041’42”	127	170	+43 (33.86%)	Itiyabhode
4.	2+850	83027’21”	27041’11”	189	91	-88 (46.56%)	Hattisund Suspension Bridge
5.	9+300	83026’33”	27037’56”	160	127	-33 (20.63%)	Manigram Bridge axis (under construction)
6.	11+600	83026’00”	27030’50”	207	200	-7 (3.38%)	Near Manigram
7.	14+200	83025’24”	27035’38”	280	150	-130 (46.42%)	Amuwa Bridge axis (under Construction)
8.	20+750	83025’37”	27052’30”	133	103	-30 (22.56%)	Near Sonare Suspension Bridge
9.	25+540	83024’06”	27030’49”	58	45	-13 (22.41%)	Tinau Bridge at Bethari

Source: Google Earth and Field survey, 2012.

Minus (-) symbol represents the decrease in width (during the period of 2003 to 2012) while plus (+) symbol represents the increase in width during the same period.

Riverbed materials are extracted in the Tinau River for internal and external purpose. The internal purpose mostly includes construction of roads, buildings, canals, drains, Bridges and culverts and so on; whereas the external use includes the materials export to India. The major portion of the extracted volume is being used mostly for the purpose of export to India (60%) and only a small portion of this volume (40%) is being used in internal purpose[2]. Substrate extraction basically means the removal of sand and different sizes stones from the Riverbank, floodplain and river channel. Boulders were also removed and processed into appropriate size gravel. The extraction is done manually or by machines. A large number of work force exceeding 2000, are associated in this process. Extraction of substrate is a common feature in Nepalese rivers in these days. In fact, it has become one of the easy methods of livelihood for very poor people in many parts of Nepal[13]. However; the case in the Tinau River is different as compared to the rivers in other places of the country. The process of sand and gravel extraction from the Tinau has been doing by the crusher mill owners using excavators massively even the labors are using the old techniques[14].

The Tinau River was extracted massively since 2004 generating high incomes by the Village Development Committees (VDCs), Municipalities and District Development Committee (DDC)[15]. The income of local bodies (i.e. VDCs, DDC and Municipalities) is given in Table 3.

Tinau River is deepening every year. The replenishment rate is lower than the extraction rate of riverbed materials from the river. The details of sediment deposit and extraction is given in Table 5.

Table 5: Details of Deposits, Extraction and Deficits of Riverbed materials

Year	Yearly Extracted Volume, M3	Yearly Deposited Volume, M3	Deficit or Surplus Volume, M3	Remarks
2004	1,263,169	977,647.06	-285,521.94	29.2 % over extraction
2005	955,241	977,647.06	+22,406.06	2.29% surplus
2006	949,154	977,647.06	+28,493.06	2.91% surplus
2007	1,008,867	977,647.06	-31,219.94	3.19% over extraction
2008	1,540,366	977,647.06	-562,718.94	57.6% over extraction
2009	2,168,263	977,647.06	-1,190,615.94	121.8% over extraction
2010	2,345,723	977,647.06	-1,368,075.94	140% over extraction
2011	1,774,943	977,647.06	-797,295.94	81.6% over extraction
Total, M^3	12,005,726	7,821,176.48	-4,184,549.52	53.50% over extraction

Source: Guragain (2012), DWIDP (2011), DDC (2011) and modified by Dahal et al. (2012)

Sediment deposition in river channel and floodplain depend on many factors like land use, vegetation cover, climate and geo-tectonic activity in watershed [15].The supply of sediment can be either in the form of suspended load or bed load. The bed load is taken as 15 % in the case of Tinau River [16]. This rate or quantity must be matched with the extraction rate from the river channel or flood plain. However, the supply rate does not match with the extraction rate of sediment supply in the case of Tinau.

Construction industry mainly depends upon the natural riverbed materials, which are extracted in quarry (open pit mining). The mining of aggregates in the Terai region of Nepal concentrated in river channel, flood plain, bed and banks of Holocene age. Unless and otherwise, the process of extraction is not properly managed, the infrastructures build near the river bank, across the river like highway bridge, weirs and barrages will fall in danger[2]. However, the extraction of construction materials has not been done in a proper way. As the quality of aggregate improves in upstream, the mining activities tend to concentrate over there. The general information of riverbed materials of the study reach is presented in Table 6.

Table 6: Details of materials available in the study reach

Chainage	Type of Materials	Remarks
0+000	Boulder: 50%, Gravel: 30% and Sand: 20%	Kanyadunga
0+642	Boulder: 50 %, Gravel: 30% and Sand: 20%	Tinau Bridge at Butwal
1+650	Boulder: 50%, Gravel: 30% and Sand: 20%	Itiyabhode
2+850	Boulder: 50%, Gravel: 30% and Sand: 20%	Hattisund Suspension Bridge
9+300	Pebble: 30%, Gravel: 30% and Sand: 40%	Manigram Bridge axis (under construction)
11+600	Pebble: 20%, Gravel: 20% and Sand: 60%	Near Manigram

14+200	Gravel: 20%, Sand: 70% , Silt and Clay: 10%	Amuwa Bridge axis (under Construction)
20+750	Sand: 80%, Silt and Clay: 20%	Near Sonare Suspension Bridge
25+540	Sand: 80%, Silt and Clay: 20%	Tinau Bridge at Bethari

Source: Field survey (2012) (protocol used from USEPA, 1995)

The extraction of riverbed materials is more concentrated at riverbeds with bigger size aggregates for its easiness to load and transport. Bigger size materials are significantly distributed in the upper reaches and gradually decreases downwards. The extraction is done mostly by excavators. There are 70 crusher industries along the bank of the Tinau River and the employment generated by them are 2228. The total production of these crusher plants is 28, 001, 302.55 M3 per annum with 2 m average thickness of river bars, the surface area is consumed by 14000.65 M2, which is a significant area of river channel and floodplains[17].

Till now, Government of Nepal (GON) has not developed a clear rules and regulations in order to enhance the appropriate and comprehensive use of natural resources like river bed materials to ensure multiple uses of these vital resources among various users. Thus, preparation of detailed guidelines is felt necessary from all aspects of development to address the problem of the supply-demand gap of riverbed materials[1]. Tinau River is facing this problem. Thus, the engineering activity in the riverbed requires legal procedures for mining riverbed materials.[11].

Long term runoff erodes the surface and transports the products to the depositional area from the basin[15].The sediments deposition in the Tinau river is mainly heavy erosion in the catchment area. The sediments are transported from Palpa to Terai plain and deposition starts from Butwal to Marchawar. These materials are important for the development of infrastructure and could be extracted in an optimal way. If not extracted through an optimal way, it would reflect the adverse river valley environmental problems[4; 18]. In the case of Tinau, sediment is not being extracted through a designed optimal mining scheme. As a result, about1000 shallow tube wells stopped discharging water especially in the winter and dry season along the banks of the river[2]. Extraction of riverbed materials has both direct and indirect effects on ecology and environment. It disturbs the water flow, introduces the fine sediment to the water column, and removes riparian vegetation along with the natural beauty of the river[19].

Sediment transport capacity is directly proportional to the stream power[20]. If the discharge is higher; higher will be the sediment carrying capacity of a river. The Tinau flows through a gorge section in the upstream and has high slope and stream power[21]. Thus the sediment could be transported in the Terai plain. As the river flows downwards, the water is distributed in distributaries and reduces the discharge and velocity along with the carrying capacity. The sediment sizes also decreases along the length of the river[16]. Observing the environmental degradation of the Tinau river valley, the house of representative (HoR) of Nepal banned the extraction from the Tinau River, especially for the purpose of export to India[22]. Then there appeared the conflict between the builders, construction industrialists, local administrative bodies and general people. In fact, there will be always problems with the experienced people if they cannot communicate the actual situation and complexities of rivers with those who are not experienced[23]. In Tinau, there are both types of people and the problem remains as unsolved.

ANNEX

PHOTOGRAPHS OF THE SURVEY AT TINAU

Damaged Headwork

Level Survey at Tinau River

Measurement of Pole Exposure

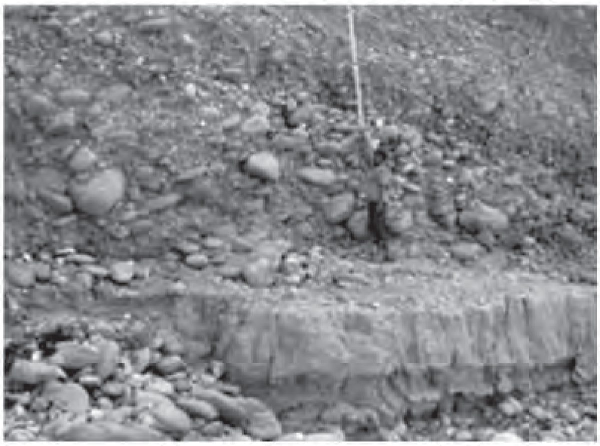

Measurement of Erosion and Incision

Encroachment in Downstream

Encroachment in Upstream

[Source: Field survey, 2012]

4. CONCLUSION

The extraction of riverbed materials from the river channel and the floodplains of the Tinau River have been started for a long period of time. However, the massive extraction was started from past decade. The contract of riverbed materials does not include the external cost. Therefore, there is a burden of road repair and maintenance due to heavy loaded vehicles in the region of Rupandehi district and also in the surrounding districts too. Thus the cost of road repair and maintenance and other environmental cost must be included while awarding the contract for extracting riverbed materials.

The extraction resulted in lowering of bed level on an average of 3.31 m along the 25.540 Km stretch of the river. The disequilibrium extraction of riverbed materials from the river has caused incision. Similarly, there is a variation in width throughout the selected reach of the river. The encroachment of floodplain area is also one of the causes of decrease in width. Encroachment floodplain area is higher in upstream as compared to downstream. The Tinau is encroached for various economic causes. One of them is being the urbanization. As Butwal is the industrial and commercial centre located at the midpoint of East-West highway and near to Indian Border (Sunauli), it is the attractive place for all types of businesses. Out of the Kathmandu Valley, it is one of the important cities facilitated with all infrastructures. The price of the land is high in this area and poor people want to take risk building their residence on the bank of the river. As the extraction activities increased, the danger of inundation on the floodplain reduced and people started to settle on the banks and floodplains. The study concluded that the further investigation on the Tinau River is needed. However, the present study could be useful for the policy makers, geologists, and environmentalists including future researchers in the area of river morphology.

ACKNOWLEDGEMENT

We would like to acknowledge Prof. Subodh Sharma, Prof. Prakash Chandra Adhikari, Prof. Bidur Prasad Upadhyay, Er. Vijay Chandra Kathiwada, and Mr. Mahesh Pathak for their contribution during the preparation of this paper.

REFERENCES

1. Baidya, H., 2003, Twelve years struggle for the conservation of Bagmati River. Nepal Water Conservation Foundation, Kathmandu.
2. Guragain, H., 2012, Impacts on Hydraulic Structure due to Riverbed Extraction. Thesis Submitted to Lumbini Engineering, Management and Science College, Pokhara University, Nepal.
3. DWIDP, 2011, Feasibility Study for Tinau Integrated Development Project. Report prepared by Environment and Resource Management Consultant (ERMC) and submitted to Department of Water Induced Disaster Prevention, Kathmandu, Nepal.
4. Sharma, C. K., 1997. A Treatise on Water Resources of Nepal. Mass printing press, Kathmandu, Nepal.
5. Timothy, M..N.1993. A Brief History of California's Gold. Cited : http://goldfever.com/ghistory.htm
6. Bruce Melton, P.E., 2009, Instream gravel mining impacts and environmental degradation feedback associated with gravel mining on the Rio Tigre of the OSA Penunsula, Costa Rica, and the proposed ADI. Jimenez Gravel Mining Concession. Report prepared by Melton engineering services, Austin, Texas.
7. WECS, 1987, Erosion and sediment in the Nepal Himalaya.Water and Energy Commission Secretariat (WECS).JICA, 1987.
8. Google Earth, 2003. Accessed on January 7, 2013.
9. Local Self-Governance Act, 1999, Government of Nepal, Ministry of Law, Justice and Parliamentary Affairs.
10. Local Self-Governance Rules, 1999, Government of Nepal, Ministry of Law, Justice and Parliamentary Affairs.
11. United Nations Development Programme (UNDP), 2011, A review of current practices of revenue generation from natural resources for the local bodies of Nepal. Ministry of local development, local governance and community development project (LGCDP), Nepal.
12. Sapkota, B., 2011. The dwellers along the bank of Tinau River. Unpublished paper presented in a national level seminar on "Tinau, Integrated Water Resource Management and Conservation" at Manigram, July 22-23, Rupandehi, Nepal.
13. Ghimire, D. R, 2011. The landless people on the bank of Tinau River in Butwal Municipality area. Unpublished paper presented in a national level seminar on "Tinau, Integrated Water Resource Management and Conservation" at Manigram, July 22-23, Rupandehi, Nepal.
14. Khanal, Sanjay Nath, 2001, Effects of Human Disturbances in Nepalese Rivers on the Benthic Invertebrate Fauna. Phd Thesis: University of Agricultural Sciences (BOKU), Vienna.
15. Dahal, K.R., Sharma, S., Sharma C.M, 2012. A review of riverbed extraction and its effects on aquatic environment with special reference to Tinau river, Nepal. Hydro-Nepal, Issue No. 11, pp.49-56.
16. Kondolf, G. Mathias, 1997, Hungry Water: Effects of Dams and Gravel Mining on the River Channels. Environmental Management vol. 21 no. 4, pp 533-551.
17. Collins , B., and T. Dunne, 1990. Fluvial geomorphology and river gravel mining. A guide for planners, case studies included. California Division of mines and Geology Special Publication 98, Sacramento.
18. District Cottage and Small Industries Office (DCSIO, 2012). Official records of registration of industries.
19. Brown, V. and Brown, B., 1998. Impacts of gravel mining on gravel bed streams. Transactions of the American Fisheries Society 127: 979-994.
20. Kondolf, G. Mathias, 1994. Geomorphic and environmental effects of instream gravel mining. Landscape Urban planning 28: pp. 225-243.
21. Richards, K.1982. Rivers: Forms and process in alluvial channels. Methuan, London, 358 pp.
22. House of Representative (HoR) of Nepal, 2010. Decisions collection from the parliamentary committee, committee for the distribution of natural resources, Singh Durbar, Kathmandu, Nepal.
23. Rosgen, D., 1996. Applied River Morphology. Wildland Hydrology, USA.

ANALYSIS OF MIXED CONVECTION HEAT TRANSFER FROM FLUSH-MOUNTED DISCRETE HEAT SOURCES

Himangshu Bhowmik
Associate Professor
Department of Mechanical Engineering
Dhaka University of Engineering & Technology (DUET)
Gazipur - 1700, Bangladesh
Email: bhowmik2005@yahoo.com
Contact No. +880-01199-377305

ABSTRACT

Numerical and experimental analysis have been performed using water to determine the single-phase mixed convection heat transfer from an in-line four simulated electronic chips, which are flush mounted to one wall of a vertical rectangular channel. The heat flux ranges from 0.1 W/cm2 to 0.6 W/cm2, Reynolds number based on channel hydraulic diameter and based on heater length, ranges from 56 to 2220, and 70 to 2775, respectively. The mixed convection heat transfer region is determined from the experimental data. To develop the empirical correlations, the appropriate value of the exponent n of Re_D is determined to collapse all the lines into a single line in the mixed convection regime. The results are also compared with reported air-cooling studies and verified by numerical simulation, with or without conjugate modelling, to gauge the extend of the conjugate effects.

Key words: *Discrete heat sources, Mixed convection, Conjugate effects, Channel flow, Electronics cooling.*

1. INTRODUCTION

Almost all of the electrical energy consumed by the electronic chips appears as heat. With increasing power density within the chips, as well as the attendant tendency to design chips closely in planar arrays, more stringent requirements in thermal management are needed. This has prompted the consideration of liquid cooling, instead of the prevalent air-cooling, to remove the increasing cooling load from high-power electronic chips [1-3]. From the heat transfer viewpoint, electronics cooling has created emphasis on understanding the basic convective fluid flow over discrete heat sources, which have different characteristics from the traditionally studied convection from a heated whole wall.

Although forced convection has proven to be reliable to remove heat from high-power chips, it necessitates a pump and there may be accompanied undesirable noise and vibration, especially for a liquid coolant. Hence mixed convection may offer the potential for significant cooling enhancement with only modest penalty in system pressure losses, and such flow condition may be well-suited to electronics cooling. Under low forced convection conditions, with increase in heat fluxes within the device, the buoyancy effect assumes greater importance, leading to a mixed convection situation. Also, for vertical channel orientation, the stream-wise component of the buoyancy force may be predicted to significantly enhance the heat transfer. And in view of the geometry, three-dimensional modelling is desirable in analysis.

Braaten and Patankar [4] studied numerically for two-dimensional situation, the mixed convection from a shrouded array of 3 1 in-line heat sources in the horizontal orientation using air, and showed the effects of buoyancy and Prandtl number on the Nusselt number. Türkoğlu and Yücel [5] examined numerically for two-dimensional laminar mixed convection for air-cooling in a vertical channel with a single discrete heat source. The experimental results obtained by Wang and Vafai [6] for the 4 1 in-line in air in a horizontal rectangular channel show that the mixed convection play an important role in the total heat transfer process. Meinders et al. [7] investigated mixed convection experiments for air from a 6 1 in-line protruded elements mounted on the wall of a horizontal wind tunnel. Du et al. [8] numerically simulated for two-dimensional idealization, the mixed convection for air in open-ended vertical channels for various arrangements of protruding heaters.

Based on the survey, no work has been reported for discrete heat sources in channel liquid cooling under mixed convection conditions. Furthermore, none of the above worked on a 4 1 vertical rectangular channel. In the authors' laboratory, forced convection through a vertical channel with a 4 × 1 in-line heaters have been studied [9,10]. Since this basic arrangement has not been studied in the mixed convection mode, there is motivation to extend the work to cover the mixed convection regime. Therefore the main contribution in the present work is on the experimental investigation on steady-state mixed convective heat transfer from a linear array of flush-mounted heat sources in a vertical up-flow channel, using water as the working fluid. The results are also compared with three-dimensional numerical simulation.

2. EXPERIMENTAL APPARATUS AND PROCEDURE

The experimental facilities consist of a test section apparatus and instrumentation similar to those employed by Tso et al.[9] and for convenience reproduced in Figs. 1(a) and 1(b). The experiments are conducted in a closed-loop liquid-cooling flow facility with a vertical upflow, Plexiglas test section. The flow loop consists of a reservoir, pump, heat exchanger, filter, rotameters, flow channel and degassing facility. The temperature at the test section inlet is maintained constant by means of the heat exchanger and the immersion heater in the reservoir, and is measured just prior to the test section by a K-type thermocouple. Through the majority of the 120 mm-long-channel is constructed from Plexiglas, the multichip module is machined from high-temperature Teflon (low thermal conductivity of 0.4 W/m K) and surface-mounted on the rectangular duct with 20 mm width and 5 mm height. The first chip is located 700 mm downstream of the channel inlet, providing a minimum hydrodynamic entry length of 50 mm hydraulic diameters. This allows the fluid laminar boundary layer to be fully developed before the first chip.

The surfaces of the chips are mounted in the Teflon substrate module, and the chips are positioned in the centre of the channel wall with a spacing of 5 mm between the edges of the chip and the channel side walls. Each chip was fabricated from Oxygen-free Copper such that the cross-sectional dimensions of the chip surface in contact with the liquid are 10 mm × 10 mm. A film resistive heater is attached to each chip and is controlled by a voltage transformer that is connected in series. As such four similar voltage transformers are used for the four chips in the experiment. Variations in the heater powers between the different heaters are negligible. The resistors are attached to the underside of the chips with thermally conducting epoxy. Teflon is also used to isolate the module from the surroundings to minimize heat loss. A Teflon block is also threaded to accommodate four screws to ensure that the resistors are attached well enough to the chips.

Prior to performing the experiments, the chip surfaces are polished with a waterproof abrasive silicon carbide paper that has particles of average size 10 μm and should create a uniform surface texture on each chip. Two chromel-alumel thermocouples of the K-type are embedded along the chip centreline in the flow direction at a depth of 0.5 mm under the chip surface and are located 2 mm apart from upstream and downstream edges of the chip respectively. Before measurements were recorded, the wall temperatures of the simulated chips were allowed to reach steady state, typically in about 1 hour, after the power level and flow rate were set. The mean wall or surface temperature of the chip is the average of the temperatures measured by the two thermocouples. The procedure for obtaining data in the single-phase experiments is to start with a given heat flux and the flow rate ranging from 0.5 × 10-3 m3/h to 20 × 10^{-3} m^3/h. The increments of heat flux were made of the order of 0.1 W/cm2. When the surface temperature of a heater element increased sharply, it was assumed that the critical heat flux had been exceeded, and power to the heaters was immediately cut off. Heat flux was measured by measuring the voltage and resistance across the each heater by using a multimeter.

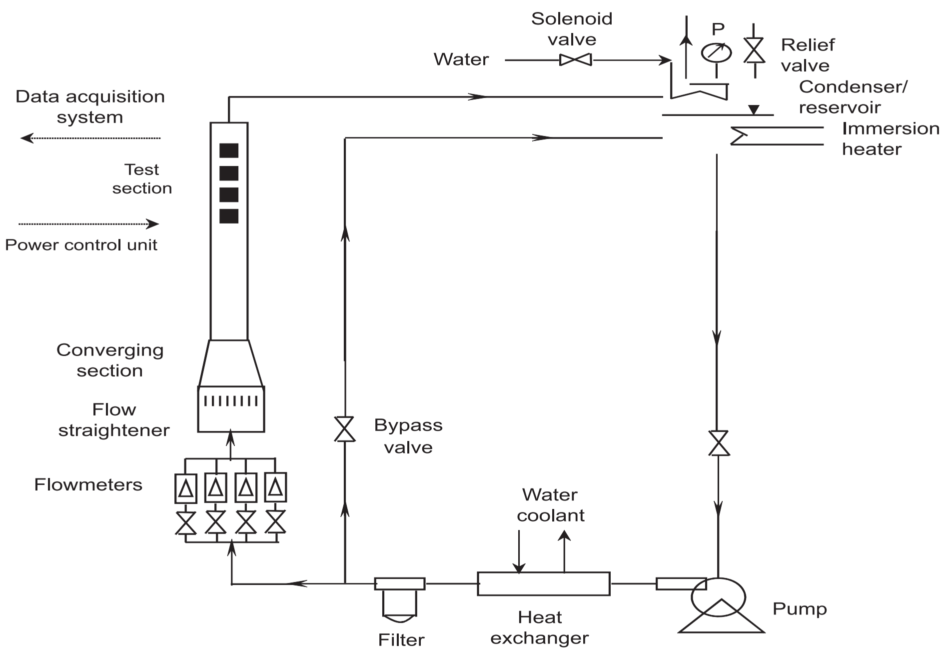

a) Schematic of the test facility

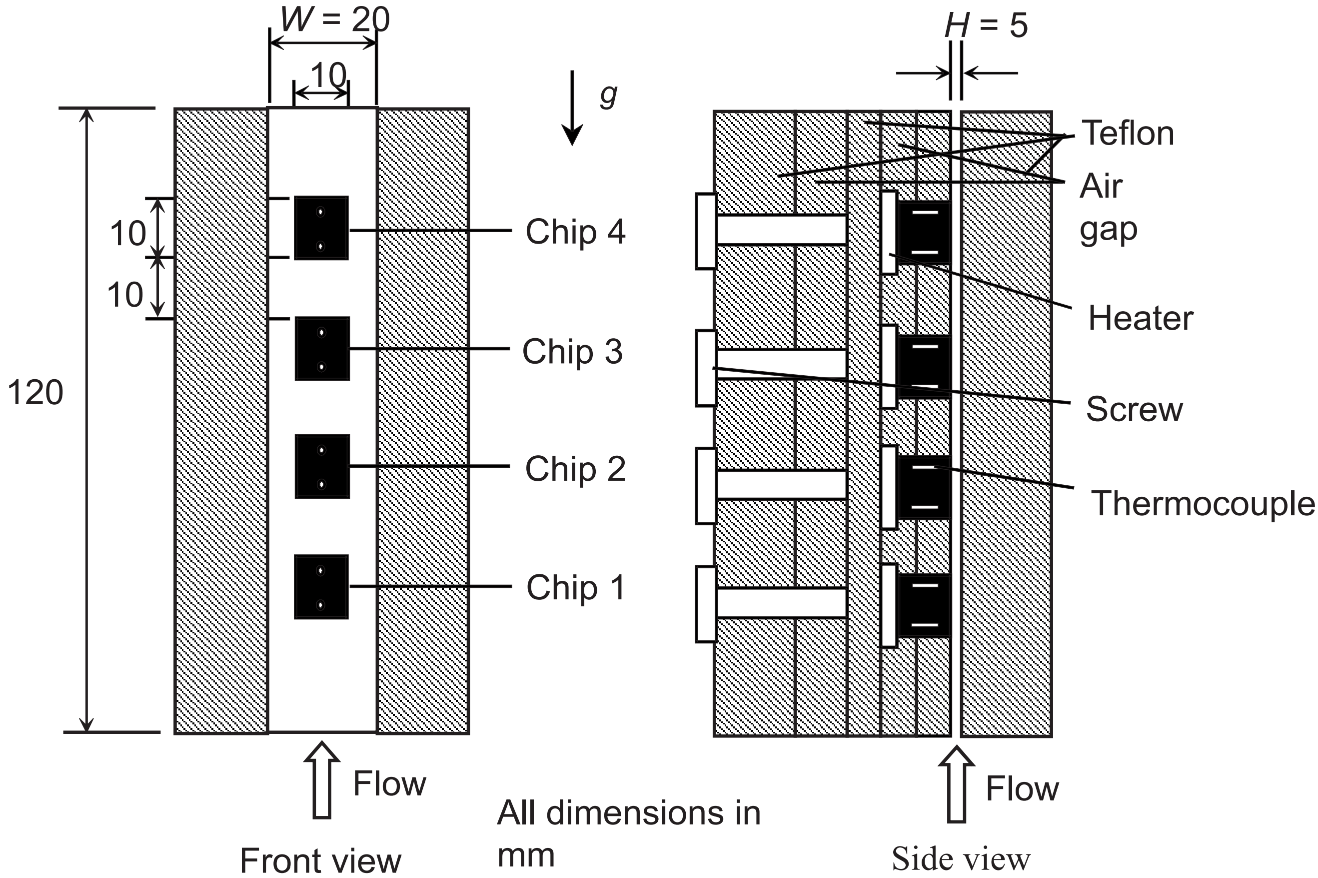

(b) Simulated chips mounted on one side of module

Fig. 1. Schematic of test facility and heaters details

All experiments with water are performed in a vertical upflow channel over an inlet temperature of $T_{in} \approx 24^{o}$C, and the heat flux ranging from 0.1 W/cm2 to 0.6 W/cm2. The configuration of simulated chips tested in this study is always flush-mounted and all the four chips are heated simultaneously at constant heat flux. The chip temperatures always remain less than 70oC. The heat losses are determined by measuring the surface temperature of Teflon exposed to the surroundings and the temperature of ambient air, and are based on the assumption that the heat losses by conduction in the multichip module are equal to the heat dissipation by natural convection from the surface of the multichip module to the surroundings, the contact resistance between the copper block and the Teflon insulation being negligible. The percentage of heat loss is estimated to be less than 5% of the total heat energy dissipated by the heater. Therefore, in light of the small heat losses, no correction is made for the power dissipated by the thick-film resistor in determining the chip heat flux. In general, heat losses for liquid cooling of simulated chips have been found to be negligible, such as in the studies of Incropera et al.[11], Willingham and Mudawar [12], and Heindel et al.[13]. An estimation of the overall uncertainly in the experimental data is made using standard techniques for single-sample measurements [14], and the propagation of the uncertainties into dimensionless parameters are then determined. The study reveals uncertainties in ΔT, q'', Nu_{ℓ}, Re_D, Re_{ℓ}, Gr_D, Gr_{ℓ}, to be less than 1.4%, 5.0%, 6.8%, 3.5%, 3.8%, 3.8% and 3.5% respectively. These values are based on the assumption of negligible uncertainty in the relevant fluid properties.

3. ANALYSIS OF EXPERIMENTAL DATA

The data were reduced in terms of Nusselt number based on heat source length as

$$Nu_{\ell} = \frac{h\ell}{k} = \frac{q\ell}{kA(T_{wall} - T_{in})} \quad (1)$$

where T_{wall} is the average of a chip wall temperature measured by two thermocouples attached on each chip, T_{in} is the inlet fluid temperature in the test section, and q is the input heater power. The chip length is ℓ =10 mm, providing exposed chip surface areas, A =100 mm2. All the thermophysical properties[15,16] are evaluated at the bulk fluid inlet temperature. The bulk temperature is defined as

$$T_b = \frac{T_{wall} + T_{in}}{2} \quad (2)$$

The temperature difference between chip and liquid inlet is defined as

$$\Delta T = T_{wall} - T_{in}. \tag{3}$$

Reynolds number based on hydraulic diameter and Reynolds numbers based on heat source length are calculated from Incropera et al. [11]

$$Re_D = \frac{\rho UD}{\mu} \tag{4}$$

$$Re_\ell = \frac{\rho U\ell}{\mu} \tag{5}$$

where the channel hydraulic diameter, D, is defined conventionally for the effective flow area. For flush mounted chip, and the velocity, U, is based on the cross sectional area of the empty space over heat sources, as the following

$$D = \frac{2(WH)}{W+H} \tag{6}$$

$$U = \frac{Q}{WH} \tag{7}$$

where Q, is the liquid flow rates

The Grashof number based on channel hydraulic diameter, and based on heat source length are defined as

$$Gr_D = \frac{g\beta q'' D^4}{k\nu^2} \tag{8}$$

$$Gr_\ell = \frac{g\beta q'' \ell^4}{k\nu^2} \tag{9}$$

4. EXPERIMENTAL RESULTS AND DISCUSSIONS

After the fluid flow and the inlet temperature reached steady state, the electrical power to the chips was turned on. The wall temperature of the simulated chips was allowed to reach steady state, typically in about 30 minutes. It was observed that in the last 3 minutes, the variation of the chip wall temperature less than 0.3oC. Thus, it can be assumed that the chip wall temperature has reached steady state at that time and all the readings have been taken at this point. The results obtained from the steady state were first analysed and compare with the results for forced convection condition with similar geometry. There is good agreement with the results of Tso et al.[9] and Shah and London [17] for overall data of the four chips. It is found a fare agreement of 5% discrepancy in Nusselt number values with the present results that ensured the test rig is in good working conditions.

The relative importance of free, mixed and forced convection is determined by the parameter (Gr_D/Re_D^2). However it also depends on the Prandtl number, which means that for a smaller Prandtl number, even with (Gr_D/Re_D^2) of the order of 0.1, one can observe considerable effect of mixed convection. It has been proposed that mixed convection occurrence of both natural and forced is to be considered when (Gr_D/Re_D^2) is of the order of unity (Incropera and Dewitt [18]; Lloyd and Sparrow [19]. For GrD/ReD2>>1, one can assume pure natural convection, and for Gr_D/Re_D^2<<1, it shows forced convection behaviour clearly. It can be seen that for a hot vertical plate the pure natural convection line merges with the mixed convection solution for Gr_D/Re_D^2>>1, also the pure forced convection merges with the mixed convection solution for Gr_D/Re_D^2<<1.

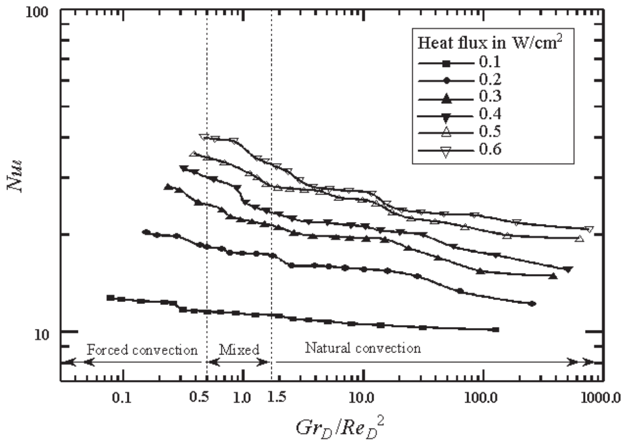

(a) At n = 0

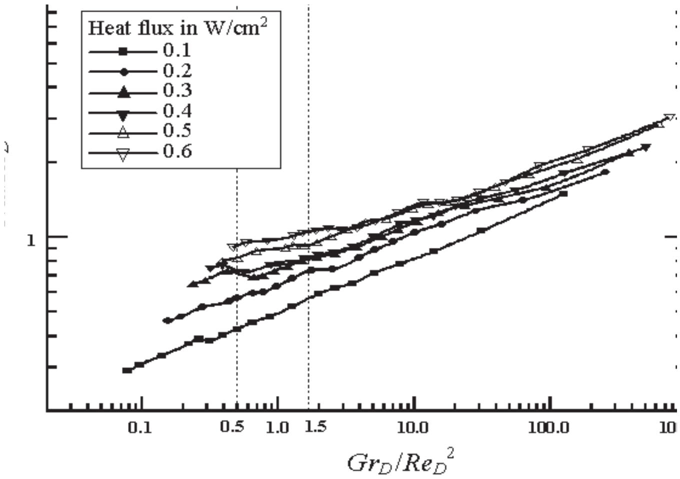

(b) At n = 0.5

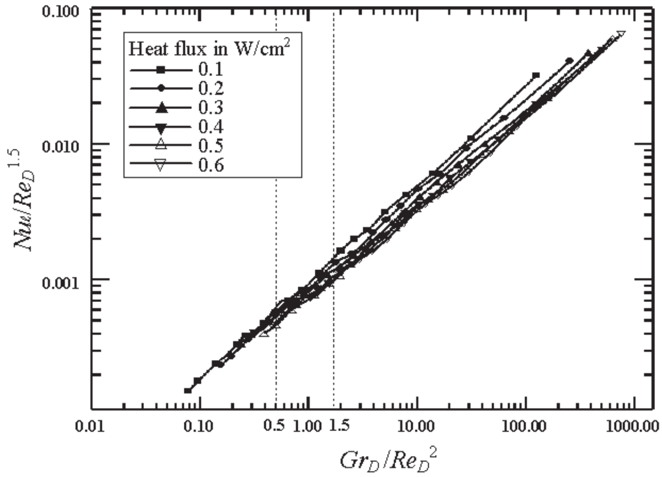

(c) At n = 1.5

Fig. 2. Variations of [Nu_ℓ/Re_D^n] with [Gr_D / Re_D^2] at different values of n

The experimental data obtained for all cases are then used for the development of an empirical correlation for mixed convection. The range of (Gr_D / Re_D^2) from 0.5 to 1.5 has been selected for the development of empirical correlations, as a range encompassing unity. It is proposed that the empirical correlation for mixed convection to be the following form

$$\frac{Nu_\ell}{Re_D^n} = C\left(\frac{Gr_D}{Re_D^2}\right)^m \tag{10}$$

The exponent n of Reynolds number of the left hand side of Eq. (10) has been selected from different test causes with different exponents, starting from 0.5 to 2.5. The standard deviation (SD) of C and m of Eq. (10) at different values of exponent n of Nu_ℓ/Re_D^n are plotted in Fig. 3. It is seen that the SD of C and m are minimum at the unique value, n = 1.25. Therefore the exponent for ReD is selected as 1.25. The variation of Nusselt number with Gr_D / Re_D^2 for average of the four chips are shown in Figs. 2(a), 2(b), and 2(c) for three values of n = 0, n = 0.5, and n = 1.5 respectively.

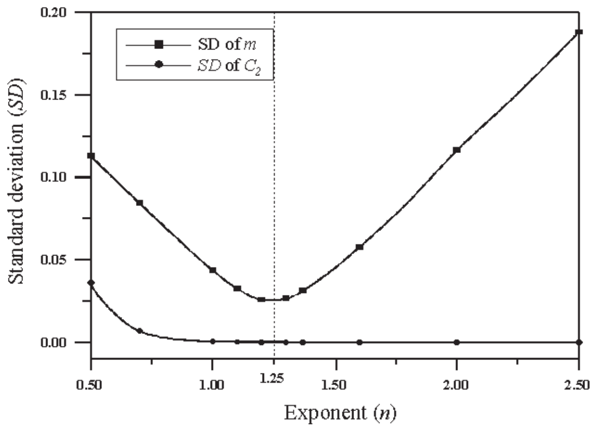

Fig. 3. Variation of exponents with standard deviation

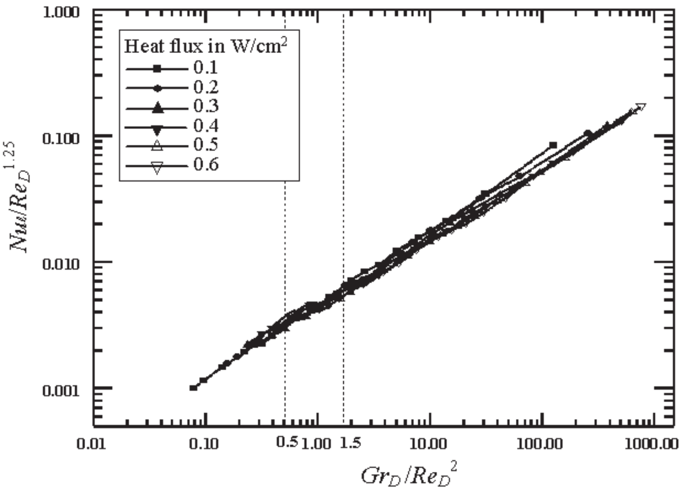

Fig. 4. Variation of [$Nu_\ell/Re_D^{1.25}$] with [Gr_D / Re_D^2]

The variations of ($Nu_\ell/Re_D^{1.25}$) with (Gr_D / Re_D^2) for all present experimental points for average of the four chips are shown in Fig. 4. Results show that all the data, which were represented by separate curves for different heat fluxes in previous plots, collapse into a single line when an appropriate value of n is chosen. Hence it is possible to represent the thermal behavior with a single correlation, without dependence on the heat flux.

From the survey, it is found that the conditions of Türkoğlu and Yücel[5] are nearer to our experimental conditions and hence our results are compared with their results on the new plot. For comparison, Grashof number and Reynolds number are re-calculated based on the heat source length as shown in Fig. 5. It is seen that even though the curves are not close to each other, they are of similar slope. In fact we do not expect good agreement with[5] because they are two-dimensional numerical results for single heat source with different channel aspect ratio, and the heat transfer coefficient is known to be a strong function of aspect ratio and method of heating[20]. Our Nusselt number is about 35% lower than that of the results of Türkoğlu and Yücel. Thus the correlation for mixed convection, Eq. (10), can be re-written in the following two forms,

$$\frac{Nu_\ell}{Re_D^{1.25}} = C_1\left(\frac{Gr_D}{Re_D^2}\right)^m \text{ (based on channel hydraulic diameter, D),} \tag{11}$$

$$\frac{Nu_\ell}{Re_\ell^{1.25}} = C_2\left(\frac{Gr_\ell}{Re_\ell^2}\right)^m \text{ (based on heat source length, } \ell\text{).} \tag{12}$$

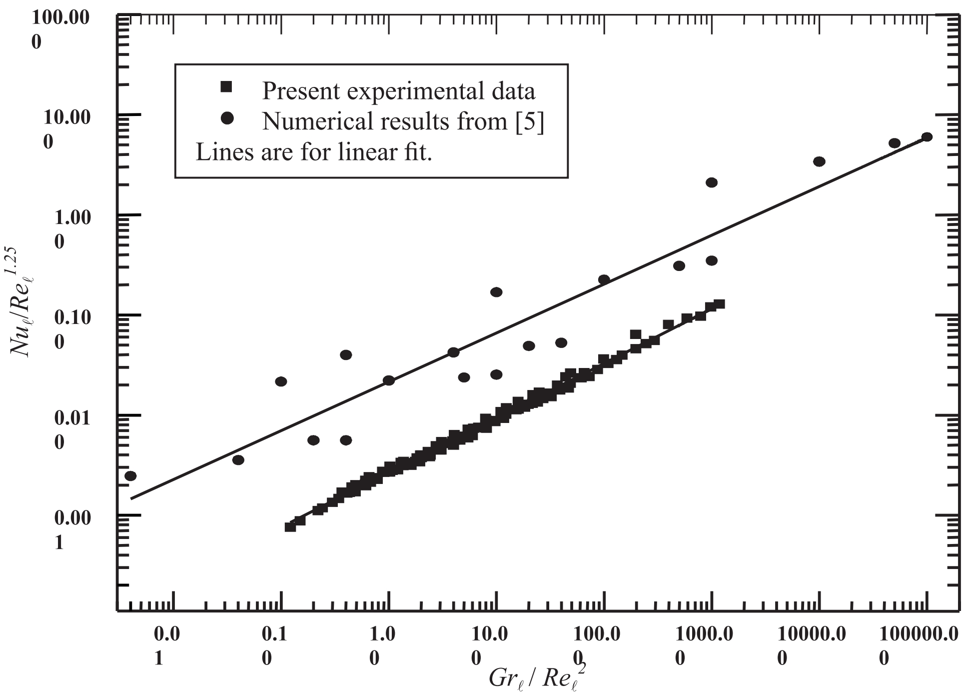

Fig. 5. Variation of [$Nu_\ell/Re_\ell^{1.25}$] with [Gr_ℓ / Re_ℓ^2)] for average experimental results

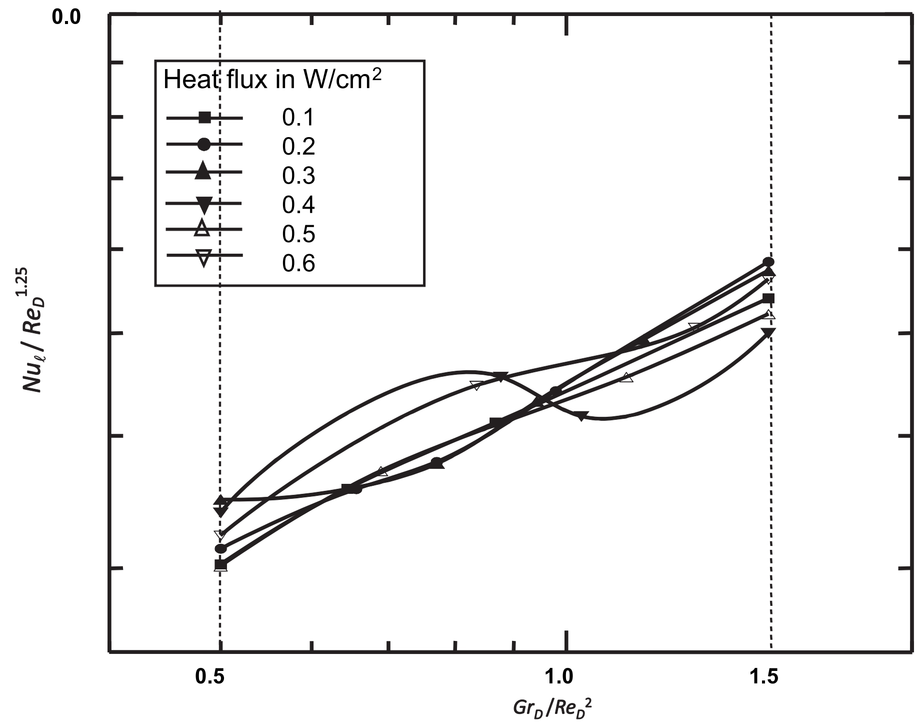

Fig. 6. Mixed convection region

This is done because in [5], ℓ is used to define the characteristic length, where m is same for both the two cases because only the constant ratio of D and ℓ is used in this experiment to convert D to ℓ. The variation of ($Nu_\ell/Re_D^{1.25}$) with (Gr_D/Re_D^2) at different heat fluxes for average of the four chips with the enlarge view of mixed convection region is shown in Fig. 6. The C1 and m in Eq. (11) for the four chips, where Grashof number and Reynolds number based on channel hydraulic diameter are determined by using linear fit method to correlate the laminar flow data within the mixed convection range is shown in Fig. 7(a). The data for the standard deviations for C_1 and m are given in Table 1. The results show that the average standard deviation of C_1 and *m* are within about 10%. The C_2 and m of Eq. (12) for the four chips are also determined by using linear fit method within the mixed convection range is shown in Fig. 7(b). The data for the standard deviations for C_2 and m are given in Table 2. The average standard deviation of C_2 and m are also within about 10%. The results obtained from the numerical results of Türkoğlu and Yücel [5] are also compared with the present form of equations and found that the average deviation of C_2 and m are within 18%. Therefore, the correlation equations for mixed convection are given in Eqs. (13) and (14) below:

$$\frac{Nu_\ell}{Re_D^{1.25}} = 0.0044\left(\frac{Gr_D}{Re_D^2}\right)^{0.5} \quad \text{(based on channel hydraulic diameter,}D\text{)}, \tag{13}$$

$$\frac{Nu_\ell}{Re_\ell^{1.25}} = 0.0027\left(\frac{Gr_\ell}{Re_\ell^2}\right)^{0.5} \quad \text{(based on heat source length, }\ell\text{)}, \tag{14}$$

$$\frac{Nu_\ell}{Re_\ell^{1.25}} = 0.0214\left(\frac{Gr_\ell}{Re_\ell^2}\right)^{0.5} \quad \text{(Türkoğlu \&Yücel, for single heater)}. \tag{15}$$

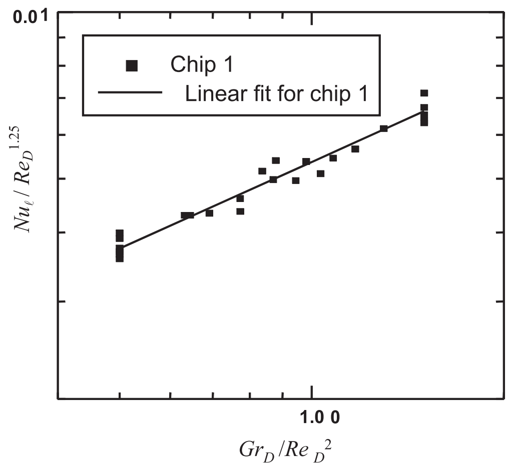

(i) Chip 1

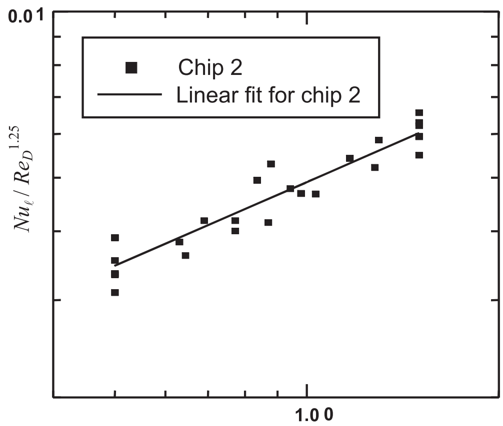

(ii) Chip 2

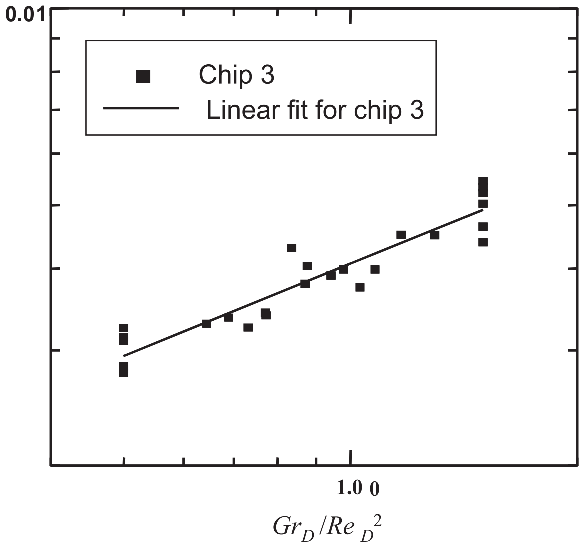

(iii) Chip 3

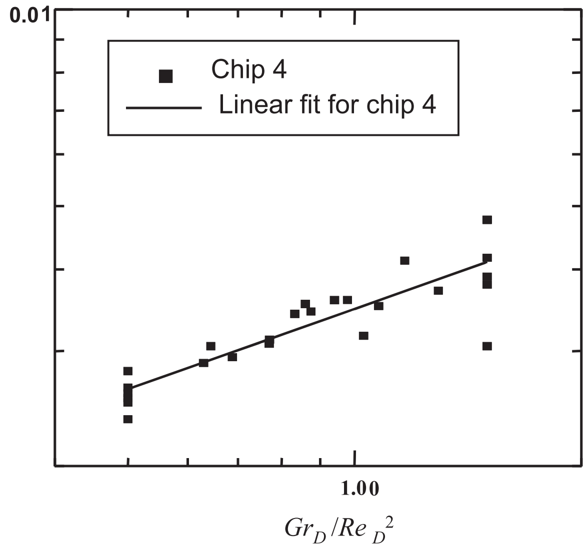

(iv) Chip 4

(a) [$Nu_\ell / Re_\ell^{1.25}$] versus [Gr_D / Re_D^2]

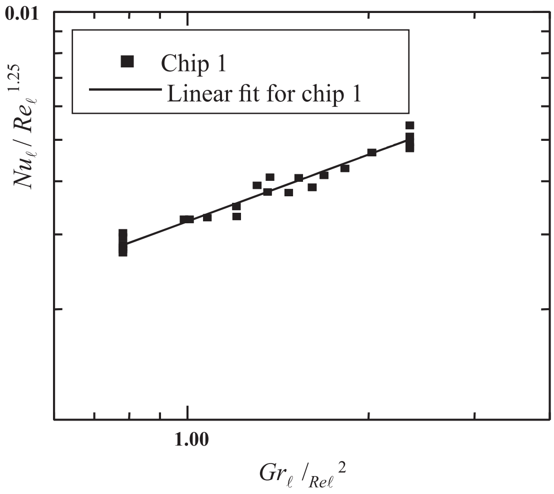

(i) Chip 1

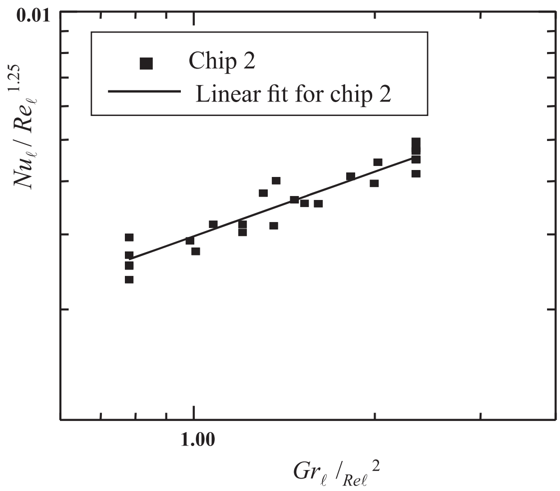

(ii) Chip 2

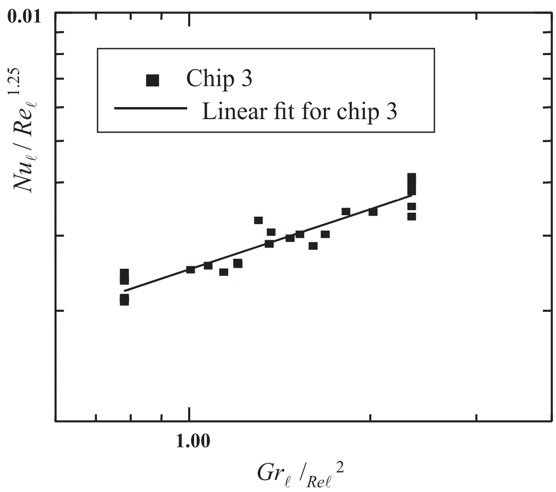

(iii) Chip 3

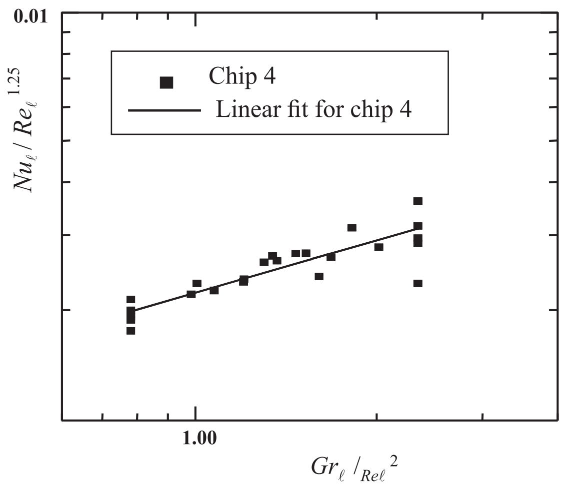

(iv) Chip 4

(b) [$Nu_\ell / Re_\ell^{1.25}$] versus [Gr_ℓ / Re_ℓ^2]

Fig. 7. Linear fit results for each chip

Table 1. The linear fit results based on channel hydraulic diameter for each chip

	C_1	*SD of* C_1	*m*	*SD of m*
Chip 1	0.00536	0.00005	0.5201	0.0207
Chip 2	0.00491	0.00007	0.5036	0.0337
Chip 3	0.00407	0.00006	0.4691	0.0319
Chip 4	0.00353	0.00005	0.4082	0.0313
Overall recommended	0.00441	0.00008	0.4766	0.0413

Table 2. The linear fit results based on heat source length for each chip

	C_1	*SD of* C_1	*m*	*SD of m*
Chip 1	0.00321	0.00003	0.5201	0.0207
Chip 2	0.00296	0.00005	0.5036	0.0336
Chip 3	0.00249	0.00004	0.4691	0.0319
Chip 4	0.00219	0.00005	0.4082	0.0431
Overall	0.00268	0.00006	0.4766	0.0429
Türkoğlu &Yücel [5]	0.0214	0.0039	0.4878	0.0339

5. NUMERICAL SIMULATION

Three-dimensional steady-state heat transfer is investigated numerically using the software Fluent [21]. The finite volume technique and the semi-implicit method for pressure-linked equation (SIMPLE) is used to solve the basic conservation equations [22]. The rectangular channel simulated for numerical simulation is shown in Fig. 8, same as the experiment and the first chip is located 700 mm downstream of the channel inlet, providing a minimum hydrodynamic entry length of 50 mm. This allows the fluid laminar boundary layer to be fully developed before the first chip.

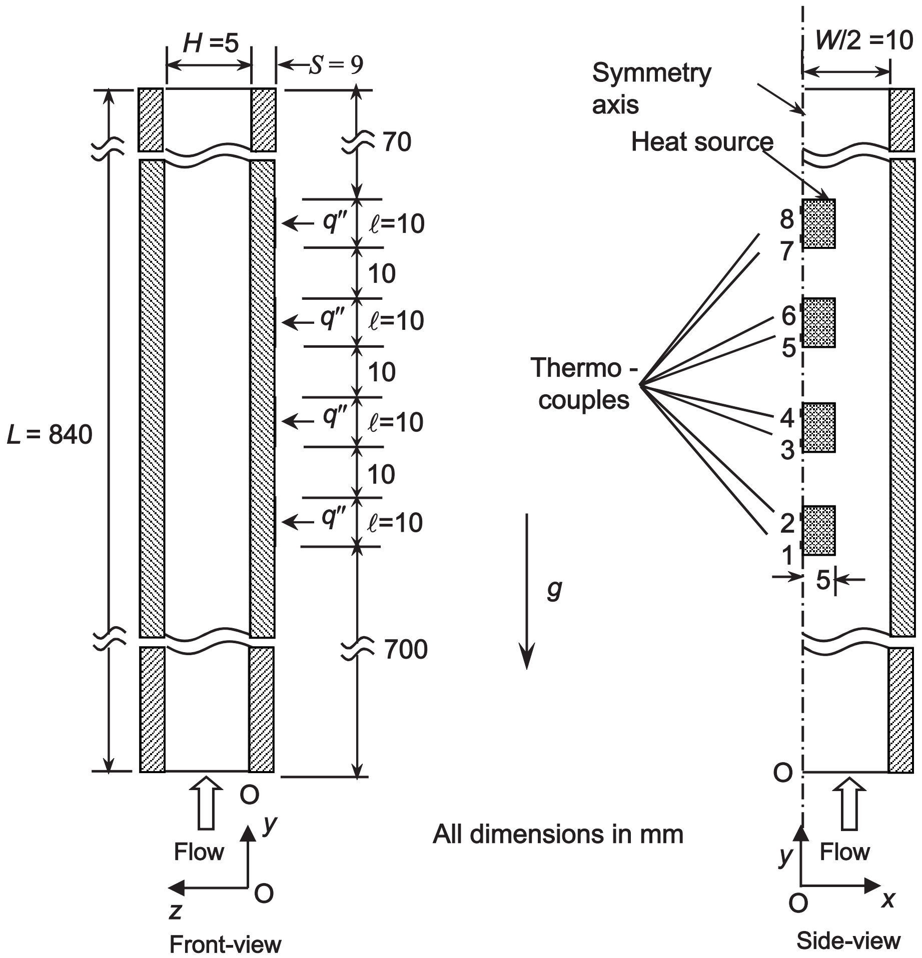

Fig. 8. Schematic diagram of the experimental set up

5.1. Governing Equations The numerical model is formulated based on incompressible, three-dimensional laminar flow heat transfer. The flow field and temperature field in the simulation satisfy the following governing equations.

The continuity equation

$$\frac{\partial(\rho u)}{\partial x}+\frac{\partial(\rho v)}{\partial y}+\frac{\partial(\rho w)}{\partial z}=0 \tag{16}$$

The convection-diffusions equations

$$\frac{\partial(\rho u\phi)}{\partial x}+\frac{\partial(\rho v\phi)}{\partial y}+\frac{\partial(\rho w\phi)}{\partial z}=\frac{\partial}{\partial x}\left(\Gamma\frac{\partial\phi}{\partial x}\right)+\frac{\partial}{\partial y}\left(\Gamma\frac{\partial\phi}{\partial y}\right)+\frac{\partial}{\partial z}\left(\Gamma\frac{\partial\phi}{\partial z}\right)+S_{\phi}. \tag{17}$$

In the above equation, $S\phi$ is the source term, the general variable ϕ represents *u, v, w or T*, where Γ represents the appropriate transport coefficients respectively as shown in Table 3.

5.2. Boundary Conditions for without conjugate Modelling All the surfaces are assumed to be adiabatic, except the embedded heaters that are heated with constant heat flux q". It is assumed that the surface outside the heat source is adiabatic. The boundary conditions are referred to Fig. 8 as follows. Eqs. (18d) and (18h) prescribe a uniform velocity and uniform temperature at the channel entrance, and Eq. (18i) assumes the stream wise energy diffusion flux to be negligible at the outlet.

At x = 0.5W,	$u = v = w = 0.$	(18a)
At x = 0 (symmetry plane),	$u = 0, \partial v/\partial x = 0.$	(18b)
At y = 0,	$u = w = 0.$	(18c)
At y = 0,	$v = v_{in}.$	(18d)
At z = 0, z = H,	$u = v = w = 0.$	(18e)
At x = 0.5W (insulated),	$\partial T/\partial x = 0.$	(18f)
At x = 0 (symmetry plane),	$\partial T/\partial x = 0.$	(18g)
At y = 0,	$T = T_{in}.$	(18h)
At the outlet, y = L,	$\partial T/\partial y = 0.$	(18i)
At z = H (insulated),	$\partial T/\partial z = 0.$	(18j)
At z = 0 (at the substrate, insulated),	$\partial T/\partial z = 0.$	(18k)
At z = 0 (at the heat sources),	$q'' = qo.$	(18l

Table 3. General variables and corresponding diffusion coefficients and source terms

ϕ	Γ	S_{ϕ}
u	μ	0
v	μ	$-(\partial P/\partial y)-\rho g$
w	μ	0
T	μ/Pr	0

5.3. Conjugate Modelling Conjugate heat transfer couples the heat transfer in the solid and fluid regions. The present problem considers heat transfer through the water and the side wall of thickness $S = 9$ mm as shown in Fig. 8. The convection effects due to the Teflon substrate is accounted for using natural convection boundary conditions with an assumed coefficient h = 2 W/m2K. The energy equation to the substrate region reduces to

$$\frac{\partial^2 T}{\partial x^2}+\frac{\partial^2 T}{\partial y^2}+\frac{\partial^2 T}{\partial z^2}=0 \tag{17}$$

The interface conditions are derived by performing an energy balance across the substrate-liquid interface. Using these equations, energy transport in the entire region, including substrate and liquid regions, are solved simultaneously.

The boundary conditions for conjugate modellings are same as the Eqs. (18a) to (18j) of without conjugate modelling and the following conditions are referred for conjugate modelling:

At z = -S (at the substrate)	$q'' = h(T_{Sub} - T\infty).$	(20a)
At z = -S (at the heat source)	$q'' = q_o.$	(20b

The computational domain is generated with non-uniform grid with various grid sizes, Grid independence is established when the change in chip wall temperature and the difference in Nusselt number are less than 3%, and for this purpose, several different non-uniformly spaced grid sizes were tried. The grid size was also selected considering the speed of the numerical simulation. The computation domain eventually selected consists of 25 grid lines in the x-direction, 350 grid lines in the y-direction and 15 grid lines in the z-direction. At the heat source, there are 5 grid lines in the x-direction and 10 grid lines in the y-direction. All the residuals for continuity, x-velocity, y-velocity, z-velocity are satisfied with the convergent criteria of 0.0001.

5.4. Numerical Results and Analysis Figure 9 shows a typical wall temperature distribution of the four in-line heat sources at Re_D = 1050 and q″= 0.6 W/cm2 with both with and without conjugate effects. It is seen for with conjugate effects the chip wall temperatures are sharply peaked at the leading edge of the heat source and maintain a uniform wall temperature on the chip. The chip temperature increases as the chip number increases from upstream to downstream. However Fig. 10 shows the favourable comparison of the numerical results with or without conjugate effects and the experimental results. It is observed that the experimental results agree well with the numerical results for conjugate effects with the differences of Nusselt number within 10%.

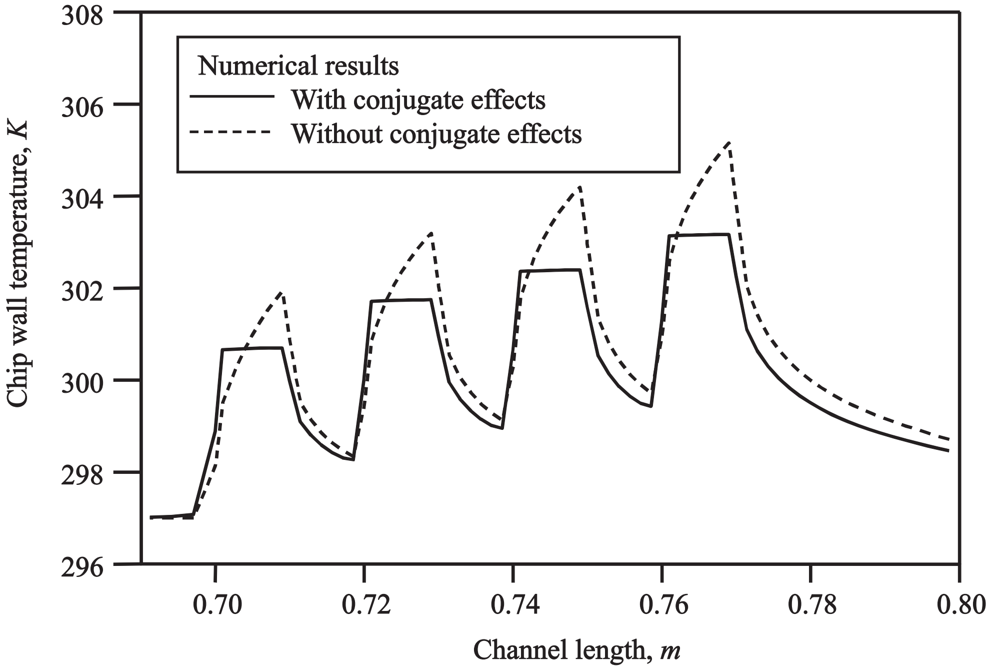

Fig. 9. Wall temperature distributions at x = 0 and z = 0

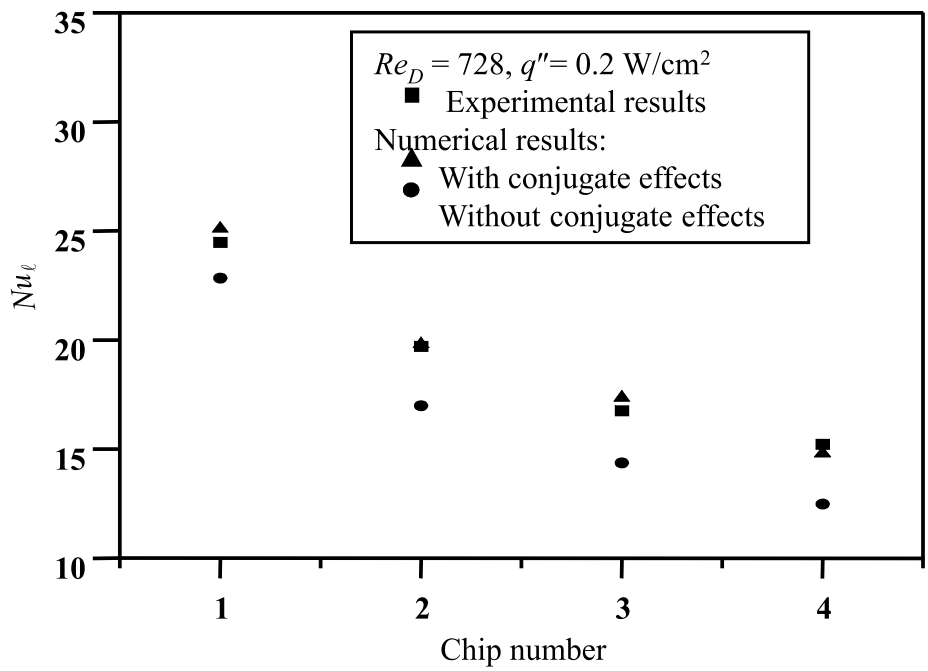

(a) Re_D = 728, q″ = 0.2 W/cm2

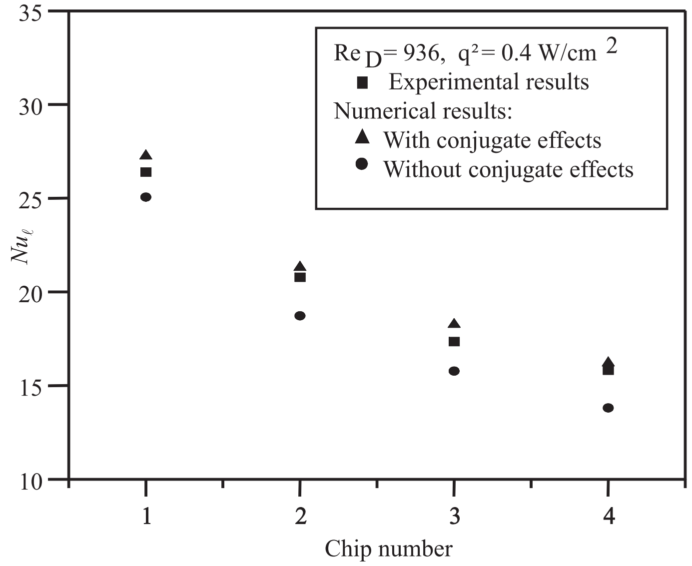

(b) Re_D = 936, q″ = 0.4 W/cm^2

Fig. 10. Comparison of numerical results with experimental results

Figure 11(a) shows the comparison of experimental results with numerical results without conjugate effects for four chips and overall data. The data for the standard deviations for C_3 and m_3 are given in Table 4. The correlation equation based on numerical results is given as

$$\frac{Nu_\ell}{Re_D^{1.25}} = 0.0069\left(\frac{Gr_D}{Re_D^2}\right)^{0.41} \tag{21}$$

Figure 11(b) shows the comparison of experimental results with numerical results with conjugate effects for four chips and for overall data. The data for the standard deviations for C_4 and m_4 are given in Table 5. The correlation equation based on numerical results is given as

$$\frac{Nu_\ell}{Re_D^{1.25}} = 0.0069\left(\frac{Gr_D}{Re_D^2}\right)^{0.5} \tag{22}$$

From the above two results it is found that the results with conjugate effects are close to experimental results compare to the results for without conjugate effects. It is found that the average standard deviations of C_3 and m_3 of Eq. (21) and the average standards deviations of C_4 and m4 of Eq. (22) are within about 36%. Table 6 shows the comparison of experimental results with numerical results with or without conjugate effects at Re_D = 1050 and q″ = 0.6 W/cm2 and the last column of the table shows the conjugate effects. It is obtained better results for with conjugate effects of the calculations. However it is seen that the effects of conjugate increases as the chip number increases. This may be due to the more heat loss by the conjugate effects at the chip of downstream compare to the chip at upstream.

Table 4. The results for linear regression for without conjugate effects for four each chip

	C_3	*SD of* C_3	*m*	*SD of* m_3
Chip 1	0.01053	0.00017	0.4157	0.0057
Chip 2	0.00756	0.00007	0.4129	0.0032
Chip 3	0.00599	0.00005	0.4113	0.0029
Chip 4	0.00495	0.00006	0.3997	0.0042
Overall recommended	0.00694	0.00037	0.4068	0.0187

Table 5. The results for linear regression for with conjugate effects for four each chip

	C_4	SD of C_4	m	SD of m_4
Chip 1	0.01005	0.00039	0.5053	0.0158
Chip 2	0.00745	0.00032	0.5044	0.0176
Chip 3	0.00609	0.00031	0.5033	0.0207
Chip 4	0.00504	0.00026	0.5029	0.0212
Overall	0.00691	0.00036	0.5021	0.0213

Table 6. Comparison of present experimental results with numerical results

Chip no	Experimental results	Numerical results				
		Without conjugate effects		With conjugate effects		Conjugate effects (°C)
	Wall temp. (°C)	Wall temp. (°C)	% deviation	Wall temp. (°C)	% deviation	
1	25.91	27.92	+ 7.19	27.59	+ 6.09	- 0.33
2	26.07	29.26	+ 10.88	28.56	+ 8.69	- 0.70
3	26.78	30.32	+ 11.68	29.39	+ 8.91	- 0.92
4	27.54	31.25	+ 11.88	30.20	+ 8.82	- 1.05

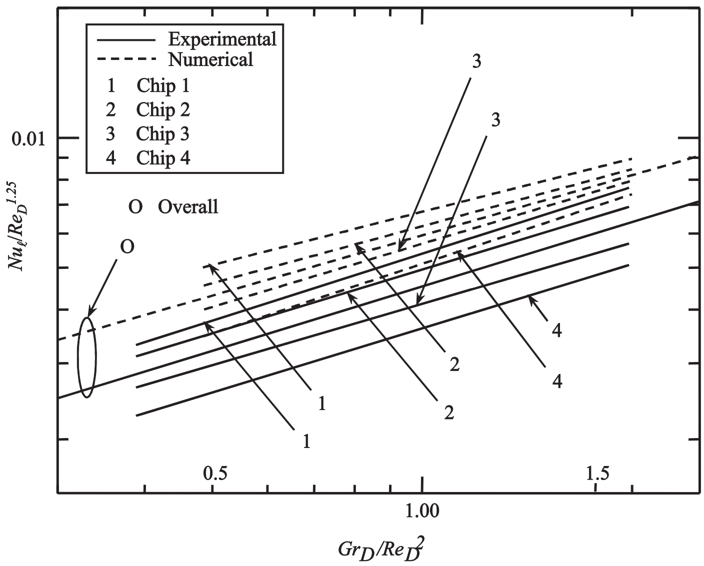

(a) Results without conjugate effects

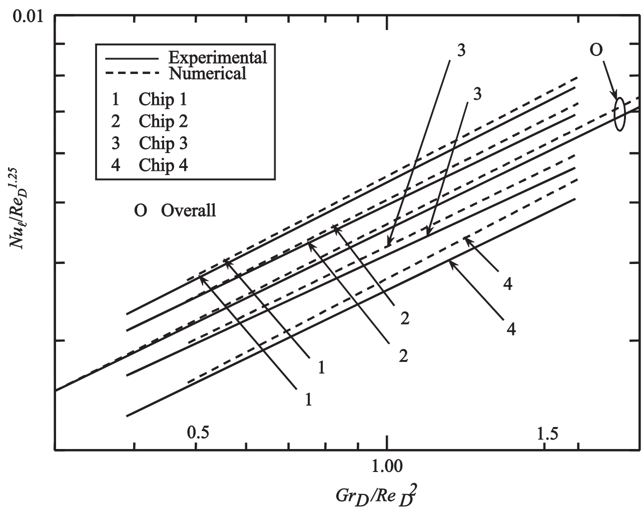

(b) Results with conjugate effects

Fig. 11. Comparison of present experimental results with numerical results for four chips

6. CONCLUSION

Experiments have been performed to study the mixed convection heat transfer characteristics on an array of four in-line, flush-mounted simulated chips in a vertical up-flow rectangular channel during steady state operation to determine the overall heat transfer coefficient. The effects of heat fluxes, coolant flow rates and chip numbers are investigated. By observing the experimental results on a Nu_ℓ versus $[Gr_D/Re_D^2]$ plot, around the unity value of the latter, a mixed convection regime is identified. By varying the exponent of Re_D, it is concluded that a unique value of the exponent exists, which is able to represent all the results of the experiment, for all heat fluxes tested. Comparison with single heater results in literature reveals similar slope in a plot of $[Nu_\ell/Re_\ell^{1.25}]$ versus $[Gr_\ell/Re_\ell^{2}]$ shown in Fig. 5. The overall correlation is Eq. (13) or Eq. (14).

Three-dimensional numerical analyses have been successfully performed on the problem for both cases of without conjugate effects and with conjugate effects. Conjugate effects reduce temperature of the heater surface by less than 5%, and conjugate results are closer to experimental results, as expected. The numerical correlations are shown in Eqs. (21) and (22).

REFERENCES

1. Xu, G. P.; Tso, C. P. & Tou K. W. A review on direct liquid cooling channel flow with single-phase for electronic systems, J. Electron. Manufact., 6 (2), 1996, p. 115-125.
2. Chu, R. C. Heat transfer in electronic systems, Proc. of the Eighth Int. Heat Transfer Conf., San Francisco, 1 1986, p. 293-305.
3. Hannemann, R.; Fox, L. R. & Mahalingam, M. Heat transfer in microelectronic components, Proc. of the Int. Symp. On Cooling Technology for Electronic Equipment, Hawaii, March 1987.
4. Braaten, M. E. & Patankar, S. V. Analysis of laminar mixed convection in shrouded arrays of heated blocks, Int. J. Heat Mass Transfer, 28 (9), 1985. p. 1699-1709.
5. Türkoğlu, H. & Yücel, N. Mixed convection in vertical channels with a discrete heat source, J. Heat Mass Transfer, 30, 1995, p. 159-166.
6. Wang, Y. & Vafai, K. Heat transfer and pressure loss characterization in a channel with discrete flush-mounted and protruding heat sources, Exp. Heat Transfer, 12, 1999, p. 1-16.
7. Meinders, E. R. Van Der Meer, T. H. & Hanjalic, K. Local convective heat transfer from an array of wall-mounted cubes, Int. J. Heat Mass Transfer, 41 (2), 1998, p. 335-346.
8. Du, S-Q., Bilgen, E. & Vasseur, P., Mixed convection heat transfer in open ended channels with protruding heaters, J. Heat Mass Transfer, 34, 1998, p. 263 – 270.
9. Tso, C. P., Xu, G. P. & Tou, K. W. An experimental study on forced convection heat transfer from flush-mounted discrete heat sources, J. Heat Transfer, 121, 1999, p. 326-332.
10. Tou, K. W., Xu, G. P. & Tso, C. P. Direct liquid cooling of electronic chips by single-phase forced convection of FC-72, Exp. Heat Transfer, 11, 1998, p. 121-134.
11. Incropera, F. P., Kerby, J. S., Moffatt, D. F. & Ramadhyani, S. Convection heat transfer from discrete heat sources in a rectangular channel, Int. J. Heat Mass Transfer, 29, 1986, p. 1051-1058.
12. Willingham, T. C. & Mudawar, I. Forced convection boiling and critical heat flux from a linear array of discrete heat sources, Int. J. Heat Mass Transfer, 35, 1970, p. 2879-2890.
13. Heindel, T. J., Ramadhyani, S. R. & Incropera, F. P. Liquid immersion cooling of a longitudinal array of discrete heat sources in protruding substrate: 2-Forced convection boiling, J. Electron. Packaging, 114, 1992, p. 55-62.
14. Kline S. J. & McClintock, F. A. Describing uncertainties in single-sample experiments, Mech. Engg., 75, 1953, p. 3-8.
15. Perry, J. H. Ed., Chemical Engineer's Handbook, 4th ed. McGraw-Hill, New York, 1963.
16. Greankoplis, C. J. Massa Transport Phenomena, Holt, Rinehart & Winston, New York, 1972.
17. Shah, R. K. & London, A. L. Laminar flow forced convection in ducts, Advances in Heat Transfer, Supplement No. 1, Academic Press, New York, 1978.
18. Incropera, F. P. & Dewitt, D. P. Fundamentals of heat and mass transfer, John Wiley and Sons, New York, 1998.
19. Lloyd, J. R. & Sparrow, E. M. Combined free and forced convection flow on vertical surfaces, Int. J. Heat Mass Transfer, 13, 1970, p. 434-438.
20. MacGregor, R. K. & Emery, A. P. Free convection through vertical plane layers: Moderate and high Prandtl number fluids, J. Heat Transfer, 91, 1969, p. 391-403.
21. Fluent Inc., Computational Fluid Dynamics Software, Lebanon, NH, USA, 1995.
22. Patankar, S. V. Numerical Heat Transfer and Fluid Flow, Hemisphere Publishing Company, New York, 1980.

Nomenclature

A	exposed chip surface area (m^2)
C	coefficients in correlations
c_p	specific heat at constant pressure, (kJ/kg K)
D	channel hydraulic diameter (m)
Gr_D	Grashof number defined in Eq. (8)
Gr_ℓ	Grashof number defined in Eq. (9)
g	gravitational acceleration (m/s^2)
H	height of the channel (m)
h	heat transfer coefficient (W/m^2 K)
k	thermal conductivity of fluid (W/m K)
L	characteristic length of the channel (m)
ℓ	length of heat source (m)
m	exponent
Nu_ℓ	Nusselt number defined in Eq. (1)
n	exponent
P	pressure (N/m^2)
Pr	Prandtl number = ν/α
Q	flow rate (m^3/s)
q	heater power (W)
q''	heat flux (W/cm^2)
q_o	prescribed heat flux (W/m^2)
Re_D	Reynolds number defined in Eq. (4)
Re_ℓ	Reynolds number defined in Eq. (5)
$0SD$	standard deviation
S_ϕ	source term
T_b	bulk fluid temperature (K) defined in Eq. (2)
T_{in}	channel inlet temperature (K)
T_{sub}	temperature at the substrate (K)
T_{wall}	chip wall temperature (K)
T_∞	surrounding temperature (K)
ΔT	temperature difference (K) defined in Eq. (3)
U	velocity of flow (m/s) defined in Eq. (7)
u, v, w	velocity at the x, y, z directions respectively (m/s)
W	width of the channel (m)

Greek symbols

α	thermal diffusivity = k /(ρc_p), (m^2/s)
β	co-efficient of thermal expansion (1/K)
Γ	diffusion coefficient
ϕ	general variable
ρ	density of fluid (kg/m^3)
ν	kinematic viscosity (m^2/s)

Subscripts

b	bulk fluid
in	inlet
sub	substrate
wall	chip wall
1,2,3,4	correlation index

PREVAILING STRESS PATTERN IN THE INDO-MYANMAR REGION DERIVED FROM FOCAL MECHANISM DATA USING MULTIPLE INVERSE METHOD AND ITS DEPTH VARIATION

Minakshi Devi*
Professor
Department of Physics, Gauhati University, Guwahati, Assam, India.
E-mail: md555@sify.com
Corresponding author

Aditya Kalita, Santanu Baruah, Saurabh Baruah
Geoscience Division, CSIR-North East Institute of Science & Technology
Jorhat-785006, Assam, India
Email: saurabhb_23@yahoo.com
Contact no: 09864253284

ABSTRACT

A multiple inverse method has been used to separate stresses from a set of focal mechanism data of Indo-Myanmar region. Four parameters are determined by the inversion; one for the shape of the stress ellipsoid and three for the direction of principal stress axes. Most prominently, the area is affected by a stress state with a horizontal NE-SW directed maximum compression with low stress ratio which has induced thrust and strike-slip faulting in the region. Study of variation of stress pattern in three different depths ranges (0-45 Km, 45-90 Km and 90-150 Km) in the study region shows rotation of maximum principal stress axis towards North at higher depths.

Keywords: *Fault–slip data, stress tensor, parameter space, focal mechanism solution, principal stress axis.*

1. INTRODUCTION

Stress tensor inversion of fault slip data is a useful tool to understand palaeo-stress in the upper crust (Angelier, 1979) [1]. Several numerical techniques have been proposed for separating stresses from heterogeneous fault slip data (Angelier, 1994; Nemcock and Lisle, 1995; Fry, 1999; Shan et al. 2003, Shan et al. 2004; Yamaji, 2003; Yamaji et al. 2006) [2] to [8]. Multiple inverse method of Yamaji (2000)[9] is one of those methods which distinguish stresses from heterogeneous fault-slip data. This method is an extension of the right dihedral method (Angelier and Mechler, 1977)[10] which is able to indicate not only possible stress orientation but also possible stress ratios (Yamaji, 2003)[7]. Main criteria for determination of stress pattern are the orientation of optimal stress axes subjected to the ratio of principal stress differences. This requires careful consideration of both the differences in mechanisms according to faulting modes and the regional changes that depend on the pattern of major seismotectonic units of the studied region (Wallace, 1951)[11]. Sometimes it is difficult for conventional inverse methods to separate out stresses specifically when the fault is activated by different stresses. The usage of multiple inverse method iteratively resample k-element subsets from a set of fault slip data and determines optimal stress tensors for the subsets. Significant stresses are identified by clusters on stereograms that show principal stress orientations and stress ratio.

In this study, we aim at reconstructing and interpreting the separation of deviatoric stresses from heterogeneous focal mechanism data of the earthquakes originating in the Indo-Myanmar region, based on the improved multiple inverse techniques developed by Yamaji (2000)[9], and modified by Otsubo et al. (2008)[12] for the use of focal mechanism solutions.

2. TECTONIC SETTING

The Indo-Myanmar ranges (Figure 1), comprising from north to south the Naga Hills, Chin Hills and Arakan Yoma Hills, pass northeastward into a belt of northwest trending structures linking them with the eastern Himalayas. Southward the ranges pass into the Andaman and Nicobar Islands. The region in the present study covers only the SW-NE trending Naga Hills and the N-S trending Chin Hills. The Naga Hills are 250 km wide with maximum elevation of 3500m (Vanek et al. 1990) [13]; it contains ophiolites and lack exotic blocks in the Flysch and in the Miocene strata. The Chin Hills are 700 km wide with maximum elevation of 3000 m (Vanek et al. 1990) [13]; ophiolites are absent but exotic blocks occur in the Flysch and are unknown in the Miocene strata (Brunnschweiler, 1974) [14]. The Indo-Myanmar ranges represent a complex orogenic belt composed of Upper Cretaceous-Eocene folded and faulted flysch strata surrounded by post Eocene molasse strata of the Central Myanmar molasse basin in the east and of the outer molasse basin in the west. Main folding, faulting and uplifting occurred in the middle to Upper Pliocene. Convergence and subduction of the Indian plate occur along the Indo-Myanmar arc (Mitchell and Mckerrow, 1975; Mitchell, 1981) [15],[16]. A slab of the Indian plate dips eastwards below the Burmese arc as observed in several studies (Das and Filson, 1975; Mukhopadhayay and Das Gupta, 1988; Rai et al. 1996; Ravi Kumar et al. 1996; Satyabala, 1998) [17],[18],[19],[20],[21].

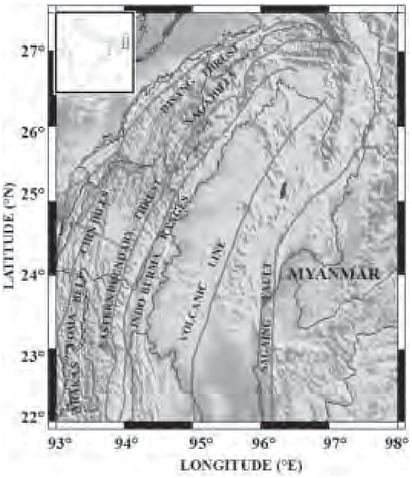

Fig.1. Tectonic setting of the study region (adapted from Kayal, 1998; Nandy, 2001; Baruah and Hazarika, 2008)[22],[23],[24]. Thick lines in the map shows the major thrusts and faults in the study region namely Naga Thrust, Disang Thrust, Eastern Boundary Thrust and Sagaing Fault etc.(Inset the study region)

3. DATABASE AND SEISMICITY

In this study we have used 100 focal mechanism solutions of earthquakes which comprise the data recorded by local networks and CGMT data for the period 1977 to 2010. The focal mechanisms are illustrated in the form of beach ball in figure 2. The magnitudes (Mw, moment magnitude) of the events range from 3.5 to 7.2. All the foci were located in the depth range of 7-152 km. Out of 100 earthquake events, 27 events occurred at depths greater than 100 km.

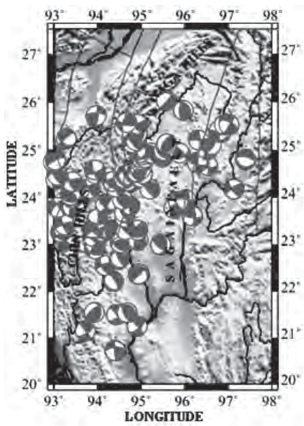

Fig. 2. Map distribution of epicenters of 100 earthquakes considered in this study. All earthquakes are shown with the conventional illustration as 'beachballs' (Schmidt's equal area stereoplot, lower hemisphere, with extentional quadrants black and compressive quadrants left white).

In Indo-Myanmar region, the earthquake epicenters are highly concentrated and as many as 10 large earthquakes Mw >7.0 occurred during the last 100+ years. The seismic activity in this belt is intense and uniform to a depth of 200 km and the earthquakes are highly concentrated along the strike of the Indo-Myanmar ranges but beyond the latitude 26º N in the region of Naga hills the seismicity become shallow due to the collision process (Mitchell and McKerrow, 1975; Kayal, 1996; Radha Krishna and Sanu, 2000) [15], [25], [26]. The mode of faulting is predominantly strike-slip down to a depth of 90 km, and thrust below this depth. In the Burmese arc region, the predominance of seismic activity of strike-slip (55%) followed by reverse faulting (40%) and normal faulting (5%), is a typical of subduction zones which are generally characterized by a predominance of reverse fault mechanism of up to 75% (Rao and Kumar, 1999) [27]. In addition, studies of P- and T-axis orientations indicate that the stress pattern in the subducted slab is different from that farther east (Ravikumar et al. 1996) [20].

4. METHODOLOGY

The multiple inverse method (MIM) is a numerical technique that separates stresses from heterogeneous fault-slip data; the method is an adaptation of the generalized Hough transform (Ballard, 1981)[28] to stress tensor inversion. It is to be noted that the optimal stress determined by the stress inversion is represented by a four dimensional parameter space, because the principal stress orientations are represented by three Euler angles and the stress ratio is the remaining parameter. The method (Otsubo and Yamaji, 2006) [29] utilizes computational grid distribution in the four dimensional parameter space. The method iteratively applies Angelier's (1979) [1] inversion scheme for all combination of k-fault subsets from a dataset. The k-fault is the k numbers of faults in a subset created from N numbers of faults. The optimal stress for such a subset is determined by maximizing the summation

$$S = F(d^{(1)})+.................. + F(d^{(k)}) \tag{1}$$

where, $d^{(1)}$ is the angular misfit of the ith fault and F (d) is the piece-wise linear function given by:

$$F(d) = \begin{cases} 1-\dfrac{d}{d_T}.............(dd \leq {}_T) \\ 0.....................(d_T < d) \end{cases} \tag{2}$$

where, d_T is the threshold. Owing to the more or less large d_T, it is possible to find out the stresses that simultaneously match to several fault slip data.

The number of resulting subsets is given by the binomial coefficients

$${}_N C_k = \frac{N!}{k\ !(N-k)!} \tag{3}$$

where, N is the number of fault slip data, or equals

$${}_{2N} C_k = \frac{2N!}{k!(2N-k)!} \tag{4}$$

where N is number of focal mechanisms. Usually the value 4 or 5 is assigned to the parameter k. The inverse method determines four variables i.e. three Euler angles (θ, φ and ψ) for the principal stress axes and the stress ratio $\Phi = (\sigma_2 - \sigma_3)/(\sigma_1 - \sigma_3)$ (Angelier, 1984)[30]. Therefore, the optimal stress for a subset is represented by a point in the four dimensional parameter spaces. This method defines an attribute of dataset and utilizes attributes based on fault/tensor compatibility (Nemcock and Lisle, 1995)[3]. A stress tensor is adjudged compatible with a fault if the theoretical slip direction calculated with tensor lies within the threshold from the observed slip direction. Previous researchers used the threshold in the range between 10º and 30º (Angelier, 1979; Nemcock and Lisle, 1995; Liesa and Lisle, 2004) [1], [3], [31]. Multiple inverse method applies an enhancement factor (with $0 \leq e \leq 99$) which defines a minimum of solutions at a computational grid point; and it is required for the particular state of stress to appear in the stereogram. It determines the best-fitting stress tensor for a group of faults by minimizing the sum of associated misfit angles with the misfit angle β being defined as the angle between the calculated maximum shear stress and the measured slip direction for an individual fault plane. Finally, all reduced stress tensors i.e. one for each 4-fault subsets are plotted in a pair of lower hemisphere. Not much study on the stress properties in the Indo-Myanmar region have been made except the recent study by Angelier and Baruah (2009) [32] for Northeastern India based on the Right Dihedra Method and the study of the crustal deformation in the Burmese arc and the adjacent regions by Radha Krishna and Sanu (2000)[26]. Simultaneously Rajendran and Gupta (1989)[33] studied the seismicity and tectonic stress field of a part of the Myanmar- Andaman- Nicober arc based on the spatial distribution of the earthquakes and their focal mechanism solutions. The usage of MIM a new and reliable technique developed by Otsubo et al. (2008)[12] for identifying the stress pattern as applied in the Indo-Myanmar region, ascertains the prevailing stress condition in the region. The results of the present study have been discussed below.

5. RESULTS AND DISCUSSION

The average orientation of maximum and least principal stress axes that prevails in the Indo-Myanmar region are precisely determined using the inversion of double couple fault plane solutions of earthquakes through application of the multiple inverse method. The result indicates heterogeneity of the fault slip data as illustrated by clusters of stress oriented differently. To find the most relevant stress state for a homogeneous subset, two series of stress state simulation are performed; the first of which yields a preliminary solution while in the second simulation series we access the relevance of the stress states by testing each preliminary stress state against the entire fault population. A single simulation implies the designation of the parameters σ_1, σ_3 and R and the calculation of associated misfit angle for each fault slip data. For fully designated stress state, we obtain a list of misfit angles β for the complete dataset which is linked to both fluctuation histogram and tangent lineation plot. Each subset is related to the determined stress state by low misfit angles.

Figure 3(a) shows the orientations of the different fault planes as well as the auxiliary planes and associated slip directions under the state of stress. Figure 3(b) is the paired stereograms showing the principal orientation of stresses by lower hemisphere equal area projection. The left stereogram shows the orientation of σ_1 (maximum principal axis) axis while the right stereogram shows the orientation of σ_3 (least principal axis) axis (Fig. 3b). Each of the symbols that have heads and tails like tadpoles plotted on the stereograms represents a state of stress. The clusters of tadpole symbols with same colors, same directions and the same lengths which are appearing in the stereograms represent significant stresses for a given set of focal mechanism data. The color represents the stress ratio. The stress ratio varies from 0 to 1 with color scale ranging from violet to red as shown in the figure 3(b). On the left stereogram, position of the head of a tadpole symbol indicates a σ_1 orientation, and the azimuth and plunge of the σ_3 orientation is designated by its tail (Fig. 3b). The length of a tail is drawn proportional to the difference between 90º and the plunge of the σ_3 axis. The steeper the σ_3 axis, the shorter the tail is. The correspondence between the length and plunge is shown by the ten grey tadpole symbols plotted between the stereograms, where the tadpoles with the longest and shortest tails indicate plunges at 0º and 90º. The roles of the head and tail of each tadpole symbol are inverted on the right stereogram. That is, the position of the head of a tadpole symbol on the right stereogram indicates σ_3 the orientation; and the length and the direction of the tail denoting plunge and azimuth of σ_1 orientation.

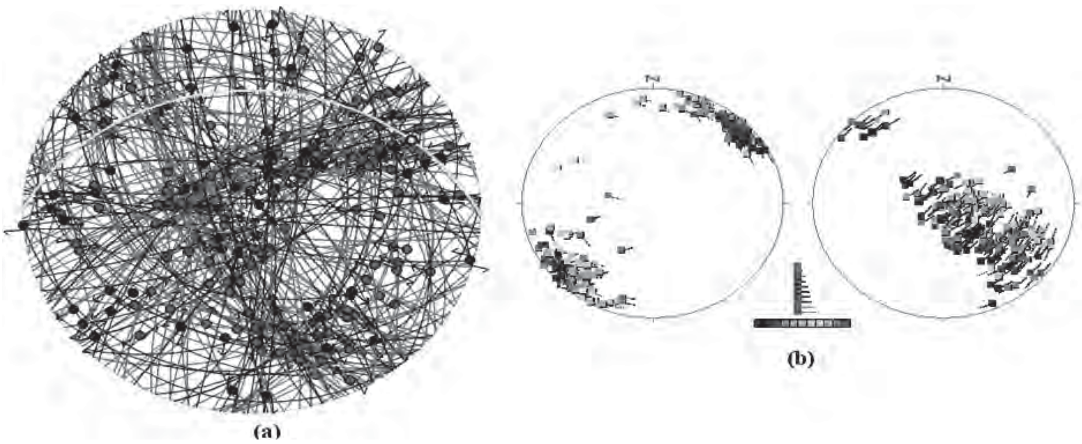

Fig. 3

Fig. 3. (a): Orientations of different fault planes and the auxiliary planes along with associated slip vectors. Fault planes with blue color represent normal faults while with red color represents reverse faults. Fault planes having slip vectors with two bars associated with them are the strike slip faults. **(b)** Stress states significant are visualized as clusters on the paired stereograms; principal orientations of the stresses are denoted by lower hemisphere, equal area projection. Each of the symbols that have heads and tails like tadpoles plotted on the stereogram represents a state of stress whose color represents the stress ratio. Values of stress ratio are indicated by 11 colors with an interval of 0.1 with a color bar under the stereograms. Clusters of tadpoles with similar colors and similar attitudes on the stereograms represent significant stresses for a given fault-slip data.

Figure 4(a) shows the orientations of σ_1 (i.e. the maximum principal axis) with azimuth 47.7º and plunge 11.5º, and σ_3 (i.e. least principal axis) with azimuth 160.0º and plunge 61.7º. The σ_1 and σ_3 axes are represented by ▲ & ★ respectively (Fig. 4). On an average, the maximum principal stress axis is directed NE-SW. Figure 4(b) is the illustration of the misfit angles between the theoretical and observed sip directions of the fault planes known as the tangent lineation diagram of the focal mechanism datum with small arrows plotted on the stereonet. In the diagram a focal mechanism datum is represented by a small arrow plotted in the stereonet. The position of the arrow in the diagram is the pole to the fault plane and the arrow points the slip direction of the footwall block. The arrows colored red, violet and blue represents misfit angles of 0º, 10º and 20º respectively. The values written in the lower left corner of each figure represents the corresponding azimuth and plunge of the stress axes as well as the stress ratio. The first column represents the azimuth of σ_1 and σ_3 axes and the stress ratio while the second column represents their plunges. In figure 5, the histogram, which is the another representation of the tangent lineation diagram in figure 4(b) shows the frequency of angular misfits between the observed and theoretical slip directions of the fault planes with a bin width of 10º. Bars of first three bins are colored red, violet and blue respectively having misfit values 0º, 10º and 20º respectively. We used the threshold angle d_T =30º and those subsets for which the stress tensor is not compatible with the entire members of the subset are left out from the inversion process. While computing the stress direction parameters for the region, the stress ratio is chosen to be 0.5 with enhancement factor (e.f) as 8 and dispersion factor (d.f) as 2.

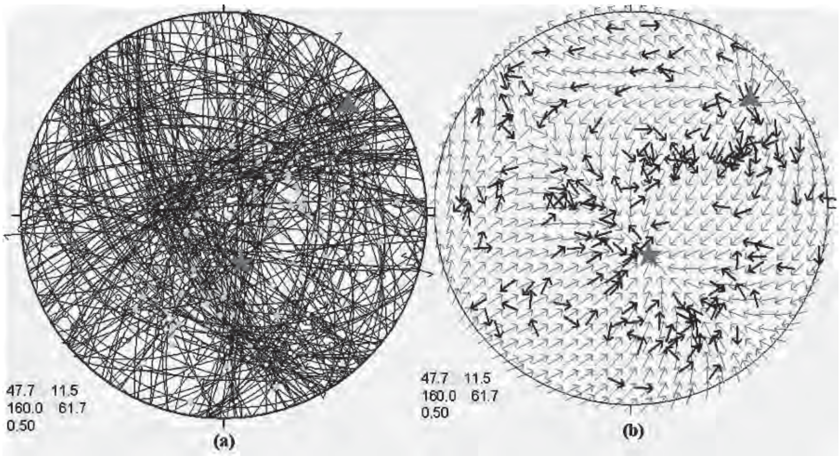

Fig. 4

Fig. 4. (a) Orientations of σ_1 and σ_3 axes indicated by symbols ▲ and ★ respectively, on the stereonet. The orientations and stress ratios are shown by their azimuths and plunges at the lower left corner of the net of the figure. (b) Tangent lineation diagram showing the theoretical slip directions for the stresses with principal orientations and stress ratio as shown in the lower left corner of the net. Thick arrows represent the computed slip directions. Arrows colored red, violet and blue represents slip vectors having angular misfits of 0º, 10º and 20º respectively.

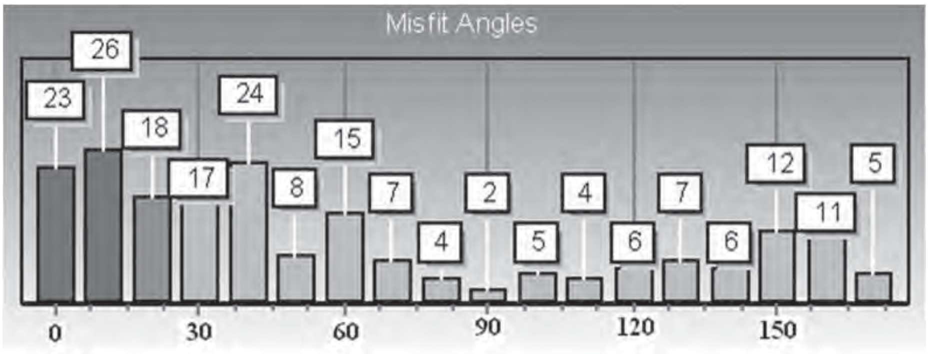

Fig. 5

Fig. 5 : Histogram for angular misfits between the theoretical and the observed slip directions with the bin width of 10º. The numbers shown at the top of each histogram represents the number of faults for that particular angular misfit value. Misfit angles smaller than 30º is highlighted by colors in the figure. The first three bins of the figure which are colored red, violet and blue represents misfit angles of 0º, 10º and 20º respectively.

The multiple inverse method was originally devised for geological fault slip data; its re-sampling scheme has been adapted to focal mechanism data to cope with the nodal plane ambiguity problem (Otsubo et al. 2008) [12]. There is a problem in dealing with the focal mechanism solutions as to know which of the two nodal planes is the fault plane. In the present method the nodal planes of entire data are assumed as fault planes and thus we have 2N fault-slip data. Then from 2N fault slip data k-element subsets are generated followed by some screening process to avoid the identical focal mechanisms in the inversion process. The stresses compatible with a dataset are recognized as the clusters of reduced stress tensors. It is important to consider the significance of the clusters and once they are determined the correspondence between the stress and the data is important as well. For the fully designated stress state, we obtain a list of misfit angles for the complete dataset which is directly linked to both a fluctuation histogram and a tangent lineation plot. The later displays the stress state specific to theoretical slip pattern and the measured slip directions. However the tangent lineation diagram in figure 4(b) indicates that many of the given faults are parallel to the principal stress planes, which are defined by two principal stress axes. The proximity of the fault and principal stress planes indicates low slip tendency of the faults (Morris et al. 1996) [34].

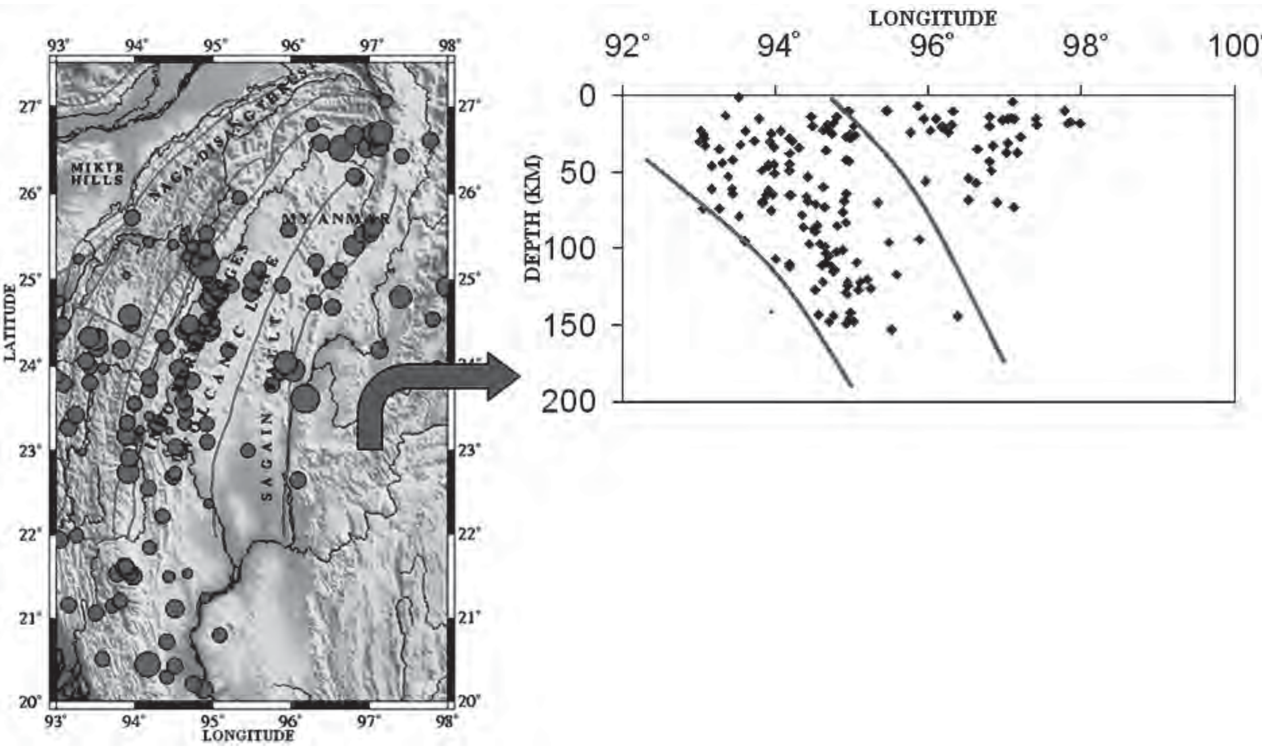

Fig. 6. Subduction of the Indian plate beneath the Burmese plate.

The result suggests existence of two distinct stresses trending approximately 47.7º and 160.0º for σ_1 and σ_3 respectively (Fig. 4). These stresses may be explained by decoupling of the overriding Burmese plate over the Indian plate and might be due to oblique plate convergence (Radha Krishna and Sanu, 2000) [26]. LeDain et al. (1984) [35] suggest that convergence along the Indo-Myanmar ranges was active at least until 1 Ma, while Satyabala (1998) [21] inferred active subduction even at present below the Burmese arc. Ravikumar and Rao (1995) [36] observed P-axes for most of the mechanisms within the subducted slab are oriented in a NNE direction. Ni et al. (1989) [37] and Le Dain et al. (1984) [35] also suggest that the overriding plate is getting mechanically dragged northward along with the Indian plate, and the present day convergence is accommodated by transcurrent movement along the Sagaing fault. Our stress result reveals trends of compression around N-S (NNW-SSE to NNE-SSW). From an analysis of borehole breakouts and focal mechanism solutions Gowd et al. (1992) [38] found a NNE-SSW compression. Chen and Molnar (1990) [39] also believed that the Indian-Myanmar ranges decoupled from the Indian plate and the orientation of compression has changed form E-W to NNE-SSW since 1 Ma. Study of stress inversion of focal mechanism solutions by Angelier and Baruah (2009) [32] revealed a complex stress pattern in the Indo-Myanmar region. The Burmese arc and its underlying lithosphere, however, experience nearly arc perpendicular extension with ESE-WNW trends in the northernmost, NE trending segment and ENE-WSW trends in the middle segment of the arc (Angelier and Baruah, 2009) [32]. Such extensional stress, documented from many arcs, is likely a response to pull from and bending of the subducting plate (Angelier and Baruah, 2009) [32]. Rajendran and Gupta (1989) [33] from the study of seismicity and tectonic stress field of a part of the Myanmar- Andaman- Nicobar arc also obtained the direction of maximum compression in NE-SW to N-S compatible with the postulated motion of the Indian plate. Hence the results obtained in this study are in good agreement with all other previous studies made. Not only does this stress regime undergoes NE-SW directed compressive stress as a result of active under thrusting of the Indian plate beneath the Myanmar plate (Fig. 6), it experiences at the same time a back-arc extension (i.e. tensile stress) in an approximately E-W direction.Study of the variation of prevailing stress pattern in the three selected depth sections (0-45km, 45-90km and 90-150km) shows rotation of maximum principal stress axis from ENE-WSW direction towards NS direction at higher depths (fig. 7). In terms of stress, this variation reveals a typical transition from heterogeneity in the upper lithosphere to relative homogeneity at larger depths. The dominating stress regime varies with depth, from ENE–WSW compression above 45 km depth to NNE–SSW compression for earthquakes deeper than 45 km. A single stress regime, thus, accounts for earthquakes deeper than 90 km, which is not the case at shallow depths. As the NNE–SSW compression is poorly represented in the upper lithosphere (Fig. 7) whereas it is the single major regime at higher depths, a plausible origin of this compression beneath the Indo–Burma Ranges is the pressure exerted on the dipping slab by both its eastward-concave bending that induces arc-parallel contraction in the lithosphere and the regional N–S compression.

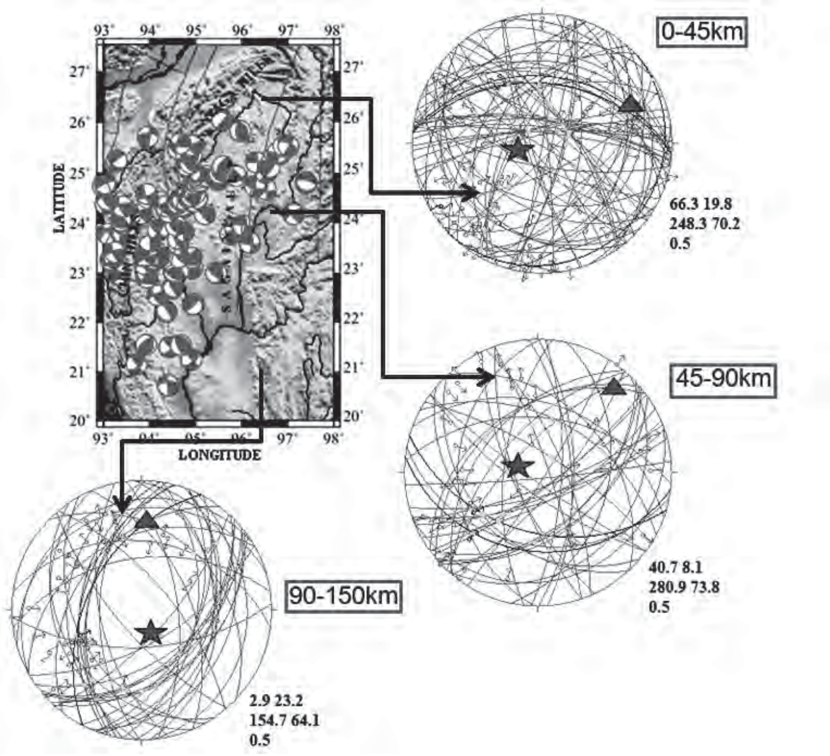

Fig. 7. Variation of stress pattern in the three selected depth ranges showing the rotation of the maximum principal stress axis towards North at higher depth ranges

ACKNOWLEDGEMENT

The authors are grateful to Dr. P. G. Rao, Director North-East Institute of Science and Technology (NEIST)-Jorhat, Assam for his constant encouragement to pursue the research. We thank Prof. H.K.Gupta, Chairman, Research Council, NEIST for his support. We are also grateful to Prof. J.R. Kayal, Emeritus Scientist (CSIR), Jadavpur University, Kolkata for his guidance and support. We acknowledge Dr. Atsushi Yamaji for providing the software to carry out the work. This study is supported by MoES and Department of Science and Technology, New Delhi vide reference number no. DST/23(533)/SU/2005.

REFERENCES

1. Angelier, J. Determination of the mean principal stresses for a given fault population, Tectonophysics, 56, 1979, p.T17-T26.
2. Angelier, J. Fault slip analysis and paleostress reconstruction, In: Hancock, P.L., (Ed.). Continental Deformation, Pergamon, 1994, p.53.
3. Nemcok, M. & Lisle, R. J. A stress inversion procedure for polyphase fault/slip datasets, Journal of Structural Geology, 17, 1995, p.1445.
4. Fry, N. Striated faults: visual appreciation of their constraint on possible paleostress tensor, Journal of Structural Geology, 21, 1999, p.7.
5. Shan, Y.; Suen, H. & Lin, G. Separation of polyphase fault/slip data: an objective-function algorithm based on hard division, Journal of Structural Geology, 25, 2003, p.829.
6. Shan, Y.; Li, Z. & Lin, G. A stress inversion procedure for automatic recognition of polyphase fault/slip datasets, Journal of Structural Geology, 16, 2004, p.919.
7. Yamaji, A. Are the solutions of stress inversion correct ? Visualisation of their reliability and the separation of stresses from heterogeneous fault-slip data, Journal of Structural Geology, 25, 2003, p.241.
8. Yamaji, A.; Otsubo, M. & Sato, K. Palaeostress analysis using the Hough transform for separating stresses from heterogeneous fault slip data, Journal of Structural Geology, 28, 2006, p. 980.
9. Yamaji, A. The multiple inverse method: a new technique to separate stresses from heterogeneous fault –slip data, Journal of Structural Geology, 22, 2000, p.441.
10. Angelier, J. & Mechler, R. Sur une methode graphique de recherche contraintes principales egalement utilizable en

tectonique et en seismologie: la methode des diedres droits, Bulletin de la Societe Geologique de France, 19, 1977, p.1309.

11. Wallace, R. E. Geometry of shearing stress and relation to faulting, J. Geol., 59, 1951, p.118.

12. Otsubo, M.; Yamaji, A. & Kubo, A. Determination of stresses from heterogeneous focal mechanism data: an adaptation of the multiple inverse method, Tectonophysics, 457, 2008, p.150.

13. Vanek, J.; Hanus, V. & Sitaram, M.V.D. Seismicity and deep structure of the Indo-Myanmarn plate margin, Journal of Southeast Asian Earth Sciences, 4, 1990, p.147.

14. Brunnschweiler, R.O. IndoMyanmar ranges. In: Mesozoic-Cenozoic Orogenic Belts (Edited by Spencer, A.M.), The Geological Society of London, Special Publication No.4, Scottish Academic Press, Edinburgh, 1974, p. 279.

15. Mitchell, A. H. G. & Mckerrow, W. S. Analoguous evolution of the Myanmar orogene and the Scottish caledonides, Geol. Soc. Am. Bull., 86, 1975, p. 305.

16. Mitchell, A.H.G. Phanerozoic plate boundaries in the mainland SE Asia, the Himalaya and Tibet, J. Geol. Soc. Lond., 138, 1981, p.109.

17. Das, S. & Filson, J.R. On the tectonics of Asia, Earth Planet. Sci. Lett., 28, 1975, p.241.

18. Mukhopadhayay, M. & Das Gupta, S. Deep structures and tectonics of Burmese arc: Constraints from earthquake and gravity data, Tectonophysics, 149, 1988, p.299.

19. Rai, S.S.; Srinagesh, D. & Sarma, P.V.S. S.R. Morphology of the subducted Indian plate in the Indo-Burmese Convergence zone, Proc. Indian. Acad. Sci. (Earth Plan.Sci.), 105, 1996, p. 441.

20. Ravi Kumar, M.; Rao, N. P. & Chalam, S. V. A seismotectonic study of the Myanmar and Andaman arc regions using centroid moment tensor data, Tectonophysics, 253, 1996, p.155.

21. Satyabala, S. P. Subduction in the IndoMyanmar region. Is it still active? Geophys. Res.Lett, 25, 1998, p.3189.

22. Kayal, J.R. Seismicity of North East and surrounding-development over the past 100 years, J. Geophysics, 29, 1998, p. 31.

23. Nandy, D.R. Geodynamics of Northeastern India and the Adjoining Region. ACB Publication, Kolkata, 2001, p.209.

24. Baruah, S. & Hazarika, D. A GIS based tectonic map of northeastern India, Current Science, 95, No.2. 2008, p.176.

25. Kayal, J. R. Earthquake source processes in northeast India: a Review, J. Himalayan Geol., 17, 1996, p.53.

26. Radha Krishna, M. and Sanu, T.D Seismotectonics and rates of active crustal deformation in the Burmese arc and adjacent regions Journal of Geodynamics, 30, 2000, p. 401.

27. Rao, N.P. & Kumar, M.R. Evidences for cessation of Indian plate subduction in the Burmese arc region, Geo-phys. Res. Lett, 26, 1999, p.3149.

28. Ballard, D.H. Generalizing the Hough transform to detect arbitrary shapes, Pattern Recognition, 13 (1), 1981, p.111.

29. Otsubo, M. & Yamaji, A. Improved resolution of the multiple inverse method by eliminating erroneous solutions, Computers & Geosciences, 32, 2006, p.1221.

30. Angelier, J. Tectonic analysis of fault slip datasets, J. Geophys. Res., 89,1984, p.5835.

31. Liesa, C.L. & Lisle, R.J. Reliability of methods to separate stress tensors from heterogeneous fault-slip data, Journal of structural geology, 26(3), 2004, p. 559.

32. Angelier, J. & Baruah, S. Seismotectonics in Northeast India: a stress analysis of focal mechanism solutions of earthquakes and its kinematic implications, Geophys. J. Int., doi: 10.1111/j.1365-246X.2009.04107x, 2009.

33. Rajendran, K & Gupta, H.K. Seismicity and tectonic stress field of a part of the Myanmar-Andaman-Nicobar arc, Bulletin of the Seismological Society of America, 79, 1989, p 989.

34. Morris, A.; Ferrill, D.A. and Henderson, D.B. Slip-tendency analysis and fault reactivation, Geology, 24, 1996, p. 275.

35. Ledain, A.Y.; Tapponnier, P. & Molnar, P. Active faulting and tectonics of Myanmar and surrounding regions, J. Geophys. Res. 89, 1984, p. 452.

36. Ravikumar, M. & Rao, N.P. Significant trends related to the slab seismicity and tectonics in the Burmese arc region from Harvard CMT solutions, Phys. Earth Planet. Inter., 90, 1995, p. 75.

37. Ni, J.F.; Guzman-Speziale, M.; Bevis, M.; Holt, W.E.; Wallace, T.C. & Seager, W. Accretionary tectonics of Myanmar and three dimensional geometry of the Myanmar subduction zone, Geology, 17, 1989, p.68.

38. Gowd, T.N.; Srirama Rao, S.V. & Gaur, V.K. Tectonic stress field in the Indian subcontinent, J. Geophys. Res., 97, B8, 1992, p. 11,879.

39. Chen, W.P. & Molnar, P. Source parameters of earthquakes and intraplate deformation beneath the Shillong Plateau and northern Indo-Myanmarn ranges, J.Geophys. Res. 95, 1990, p. 12527.

INTERNATIONAL JOURNAL OF ENGINEERING SCIENCES AND MANAGEMENT (ISSN: 2231-3273)

International Journal of Engineering Sciences and Management is a bi-annual journal of Dronacharya Group of Institutions, Greater Noida, UP, India.

1. SCOPE OF THE JOURNAL

To publish full-length research papers in any one or more of the following disciplines:

Computer Science & Engineering, Information Technology, Electrical, Electronics & Communication Engineering, Mechanical Engineering, Civil Engineering, Physics, Mathematics, Economics, and Management.

2. PURPOSE OF THE JOURNAL

To keep the academic community abreast of the research and technical scenario in the stated disciplines in the world.

3. CHERISHED AIM OF THE JOURNAL

To excite and ignite the young minds and to motivate them for involving themselves in research and development activities. This will empower our manpower in the context of fast changing technologies across the globe.

4. GUIDELINES FOR AUTHORS

SUBMISSION OF MANUSCRIPTS: Soft copy of the manuscript for consideration of publication should be sent (as MS Word Windows 2007 attachment) by Email to the Executive Editor at advisor.r&d@gnindia.dronacharya.info

All papers, received for consideration of publication and complying with the below-mentioned format will be sent for review to at least two referees. In accepting the paper for publication, the Editors and reviewers will give special weight to readability and interest value for a wide readership besides the originality and the high-standard of its contents. The Executive Editor's decision is final in case of non-unanimity of opinion of referees. Under normal circumstances, the authors will be informed about the status of their papers by the Executive Editor within eight weeks of their submission.

PREPARATION OF MANUSCRIPTS:

- **Manuscript:** Manuscript should be in English, the preferred spelling being that of the Concise Oxford Dictionary. It should be in 'Times New Roman', single-spaced, and typed on 8.5" x 11" or A4-size paper with margins of 1" (25 mm) on each side. Manuscript should be typed in single column only (and not in double or triple columns).
- **Title of Paper:** Font size 16, ALL CAPITALS, bold, centered, and not underlined. The title must be 12.5 mm below the top of the page (in addition to the standard 25 mm margin). The Title should adequately describe the contents of the paper
- **Full names of all Authors,** with * as superscript with corresponding author's name and his/her Email ID (Font size 12, centered) and also the contact number. A blank line should be left between the title and the author's name(s).
- **Full postal address** along with affiliations (Font size 10, centered).
- **Abstract** (Font size 10, centered) All papers must have a non-mathematical abstract of not more than 200 words. The abstract should indicate the general scope of the paper, the important findings and the conclusions drawn. The abstract should include only text. It should be specific about the methodologies used and the conclusion drawn of the

work reported. Please avoid the use of abbreviations and references. (Text of the Abstract: Font size 9, single-space, justified).

- **Keywords:** Include up to six keywords that describe your paper for indexing and for web searches. The more discriminating your keywords are, the greater is the likelihood that your article will be found and cited. (Font size 9, italics, left-justified).
- **Text:** (Font size 10, Justified). The paper must be divided into sections starting preferably with "Introduction" and ending with "Conclusion". The main sections should be numbered 1, 2, 3 etc and subsections as 2.1, 2.2 etc. Main headings should be typed in capitals, subheadings in lower case. Both types of heading should be underlined and left-justified. Footnotes should be avoided. Equations should be typewritten and with the equation number placed in parentheses at the right margin. Reference to the equation should use the form 'Eq. (3)'. Use extra line spacing between equations, illustrations, figures and tables. The use of SI units is strongly recommended
- **Tables and Figures:** Tables and Figures should be integrated with the text (and not sent separately at the end of the manuscript) and numbered consecutively in the order in which reference is made to them in the text of the paper. All captions must be centrally located above a Table and below a Figure (Font size 10). All tables and figures must be numbered consecutively in Arabic numerals (not Roman) (e.g., Table 3 or Fig. 3) in the order of appearance in the text. Tables & Figures should be reproduced in the exact format and at the exact place as desired to appear in the journal
- **Conclusion:** A conclusion section must be included and should indicate clearly the advantages, limitations and possible applications of the paper. Authors may also discuss about the scope of future work.
- **Acknowledgements:** An acknowledgement section may be included after the 'Conclusion'.
- **References:** It is mandatory for references to be quoted in the text and be placed at the end of the text. They should be numbered consecutively in order of their citation in the text and be indicated by superscripts in the text of the manuscript. Examples of different citations as References are given below:

(i) In case of referring to an Article in a Journal

Kuebel, D.; Lahiri, M. & Wolf, E. *An Inverse Problem in the Theory of Stochastic*

Electromagnetic Beams, Opt. Commn., 282, 2009, p.141.

(ii) In case of referring to a Book/Monograph

Rao, C.N.R. & Raveau, B. (Eds.). Transition Metal Oxides, Wiley-VCH, 2nd Edition, 1998, Ch. 2.

(iii) In case of referring to a Conference Paper

Ctvrtnickova, T.; Mateo, M; Yanez, A. & Nicolas, G. Characterization of Coal Fly Ash Components by Laser-Induced Breakdown Spectroscopy. Presented at the Fifth International Conf. on Laser-Induced Breakdown Spectroscopy, Berlin, Adlershof, Germany. Sep 22-26, 2008, CP-15, p. 67-68.

(iv) In case of referring to a Report

Marine, R.E. & Iliff, K.W. *Application of Parameter Estimation to Aircraft Stability and Control.* NASA, USA, 1986, Report No. NASA-RP-1168.

Papers quoting the LATEST references from the referred journals will be preferred for publication unless the original contribution from the author/s is of a very high standard.

UNDERTAKING

Authors must include, in the covering Email that their paper has not been published//accepted/submitted for publication/ presentation to any other journal/ book/conference in any form and the work submitted by them is their own and original. The same 'Undertaking' should also be attached, on a separate page, along with the manuscript. This ethical policy of the Journal will be strictly adhered to.

Note: Manuscripts not in conformity with these 'Guidelines' will not be forwarded to the experts for review.

IJESM SIGHTINGS

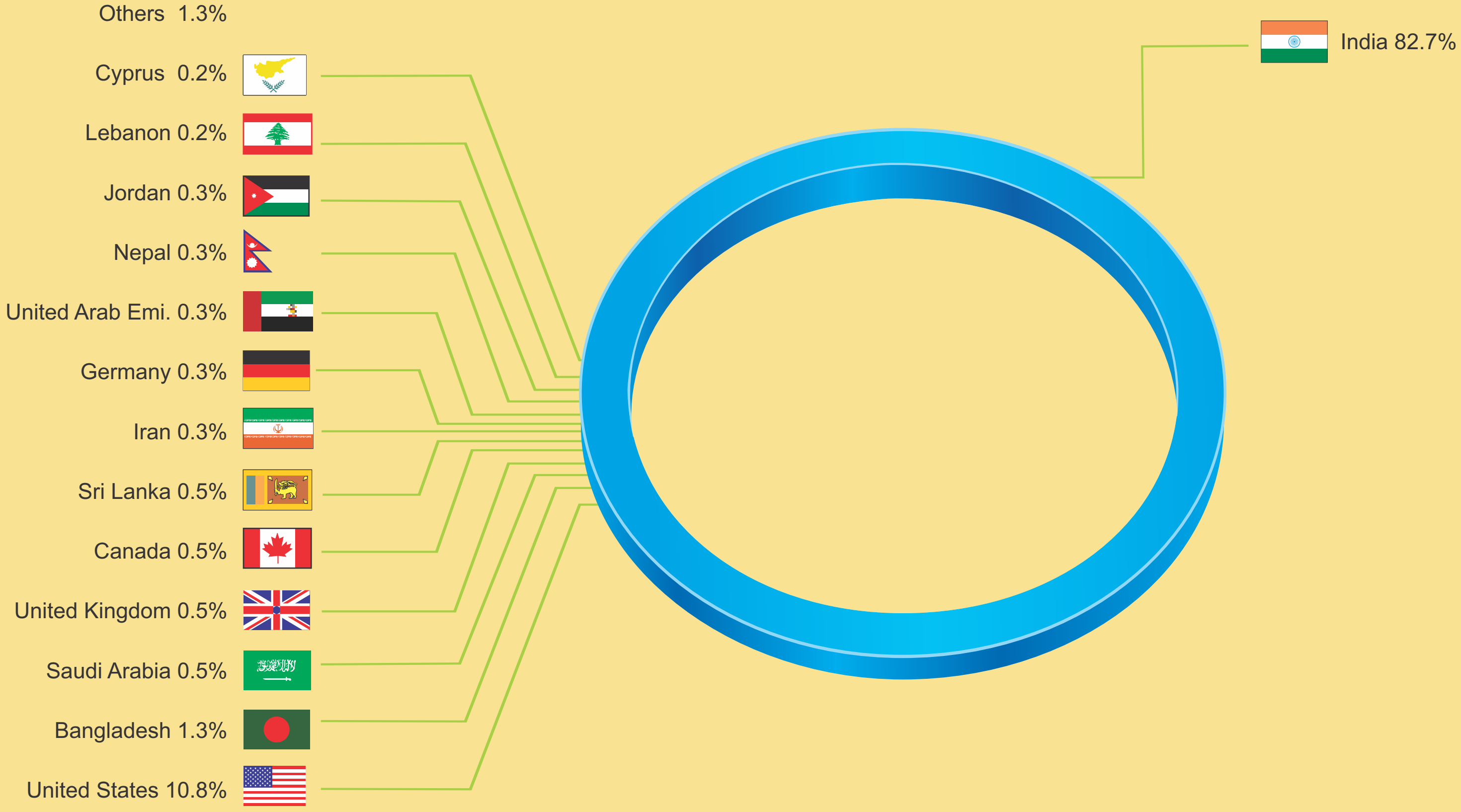

www.dronacharya.info

Approved by
All India Council for Technical Education, New Delhi

Affiliated To:
Mahamaya Technical University, Noida

Campus:
#27, Knowledge Park-III, Greater Noida (U.P) – 201308,
Phone: 0120-2323854-58, Email: director@gnindia.dronacharya.info

Corporate Office:
76P, Part-III, Sector-5, Gurgaon, 122001, Haryana (India)
Phone: 0124-2251602, 2253144, Email: info@dronacharya.info